The Fluid Dynamic Study of Ducted And Unducted Wells Turbines in Unidirectional And Oscillatory Flows

Ruediger Volker Buttgereit

December 1997

A thesis submitted for the degree of
Doctor of Philosophy
of the
University of London
and for the
Diploma of Imperial College

Department of Aeronautics
Imperial College of Science, Technology and Medicine
London, UK

The Fluid Dynamic Study of Ducted And Unducted Wells Turbines in Unidirectional And Oscillatory Flows

Ruediger Volker Buttgereit

December 1997

A thesis submitted for the degree of
Doctor of Philosophy
of the
University of London
and for the
Diploma of Imperial College

Department of Aeronautics
Imperial College of Science, Technology and Medicine
London, UK

Abstract

This thesis reports on experimental and numerical studies of the fluid dynamic performance characteristics of ducted and unducted Wells turbine rotors in unidirectional and bi-directional fluid flows. The studies of the ducted Wells turbine performance in unidirectional, steady air flow have relevance for existing prototype wave power devices in which the turbine is used to convert energy from a alternating air flow driven by an oscillating water column. The studies of the performance of unducted Wells turbines in oscillatory flow relate to a novel application of the Wells turbine in which the turbine rotor is placed in an oscillatory flow beneath waves.

The aerodynamic characteristics of a 0.75 [m] diameter ducted mono plane Wells turbine rotor having from two to eight constant chord blades have been studied in steady, incompressible, unidirectional flow by measuring the chord wise surface pressure distributions and hence the blade forces at a number of radial stations on a rotating NACA0015 sectioned blade. Particular attention was paid to the steady stall behaviour of the rotating blade. It was found that the stall behaviour of the rotating blade is dramatically different from that of the static blade section and in steady flow is strongly affected by the stall delay phenomenon which is known to also occur on wind turbine rotors. This part of the thesis work also provided evidence of strong non-linear post-stall interactions between cascade and stall-delay effects.

A theory similar to the existing actuator disc theory for unidirectional steady flow was developed as part of the thesis work to assess the ideal fluid-dynamic efficiency of the Wells turbine in unducted small to moderate KC oscillatory flow. The theory which modelled the rotor wake by concentrated vortex rings revealed that the peak cyclic efficiency of the rotor is inversely proportional to KC and due to the action of the rotor wake can attain values greater than unity if the rotor efficiency (power coefficient) is based on the peak axial energy flux through an area equal to the swept area of the turbine rotor that would occur in the undisturbed free stream. The wake idealisation chosen for the numerical model was justified by flow visualisation studies which showed that in small KC oscillatory flows the wake roll-up is a defining feature of the wake development.

A number of water tank experiments were designed and carried out to measure the shaft power of unducted Wells turbine rotors in small to moderate KC oscillatory flow at small scale to provide some validation for the theoretical performance analysis developed. These experimental investigations confirmed that the cyclic efficiency of an unducted Wells turbine rotor is inversely proportional to KC and that power coefficients greater than unity can be achieved due to the induced back flow of the rotor wake.

Acknowledgements

This work was funded by the UK Engineering and Physical Sciences Research Council whose support is gratefully acknowledged.

The inspiring support and encouragement recieved from J.M.R Graham under whose competent supervision to work it has been a pleasure and a privilege is sincerely acknowledged.

The author wishes to thank the departmental technical staff who have contributed to the project in many ways. Particular thanks are due, amongst others, to J.Meggesy, A.Smith, I.James, E.Turner, J.Coles, R.Carter and J.O'Leary whose assistance in the flow visualisation studies and all photographic work is acknowleged.

Thanks are also due to P.Mackwood whose consistent help in all matters of experimental set-up is gratefully acknowledged.

Special thanks to my family and Dorit who supported me in times of severe crises and self-doubt.

Last but by no means least I wish to express my gratitude to all my friends at Imperial College Aeronautics - in particular the E256 boys.

to Mum and Dad

Contents

Chapter 1

Introduction

1.1 Wave Power

Seen against the background of the technically more matured conversion processes of renewable energy sources such as wind or solar power, the conversion of wave energy is a fairly young technology posing an entirely new field of R&D. Though, wave power was strongly promoted in the late 1970s and early 1980s funding was subsequently reduced due to pessimistic assessments of economic competitiveness. Some increase in funding has been apparent in the 1990s, particularly for oscillating water column (OWC) devices. In 1991 the European DG XII-Renewable Energy Division initiated a review of research into wave energy conversion in order to incorporate this into their JOULE energy research programme. A preliminary budget of 1.2 mio. ECU was made available for the exploration of R&D scope of wave energy conversion. The findings of the resultant research report submitted in 1993 were included in the JOULE II programme for consideration of further funding of wave power.

The interest in wave power is stirred by the large amount of energy stored in the waves. Also, the energy density of the waves is roughly a factor of 100 higher than the energy density for wind so that in theory wave power devices for a given energy capture can be much smaller than equivalent wind energy converters. The total gross energy in waves along the European coastline has been assessed to be of the order 1.000 TWh/a, of which approximately 75% is received along the Atlantic west coast (Lewis (1993)). Of this total it is estimated that the technically achievable output is around 120 TWh/a (this corresponds to roughly 12% of increase in estimated total energy demand in the EEC up to the year 2050).

A relatively large variety of competing devices are currently being researched in a number of countries inside and outside the EEC. Since these costly prototype devices are relatively high risk projects, research has mainly been carried out at

universities and research institutes.

1.2 The Wells Turbine

One device widely used for power take off in wave energy converters is the so called Wells turbine named after its inventor Prof. A.Wells of Queens University in Belfast. The Wells turbine is an axial flow turbine, which for a bi-directional

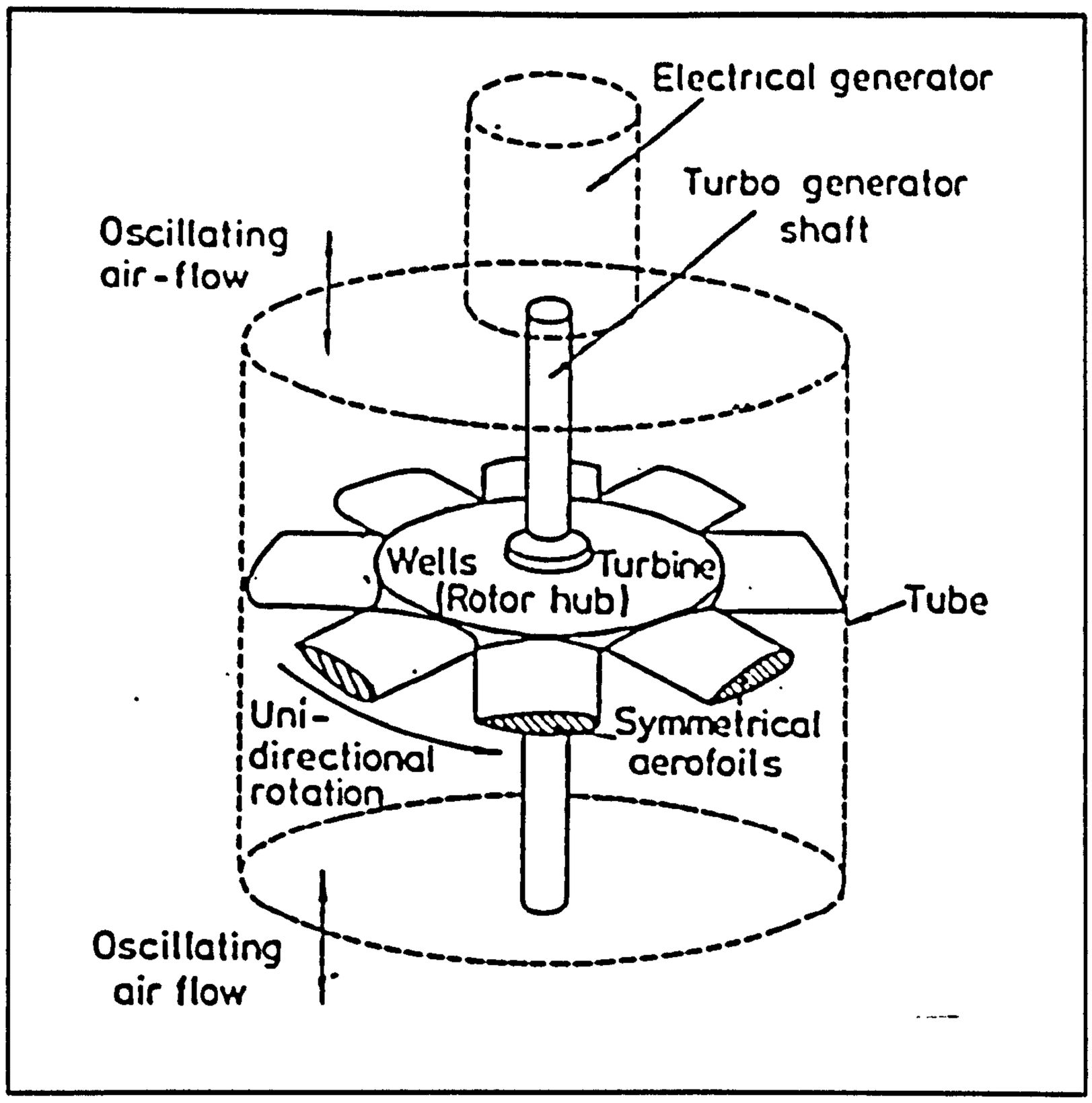

Figure 1.1: Wells Turbine Arrangement

incident fluid flow inherently produces unidirectional rotation. Its main geometric features as conceptually shown in figure (1.1) (Ragunathan (1983)) are untwisted blades employing symmetrical profiles. The acting blade forces are shown in figure (1.2) and it can be seen that in oscillatory flow the axial force changes sign with flow direction, but the action of the tangential force which provides the rotation is always in the same direction.

The Wells turbine is commonly used in wave power devices which generate an

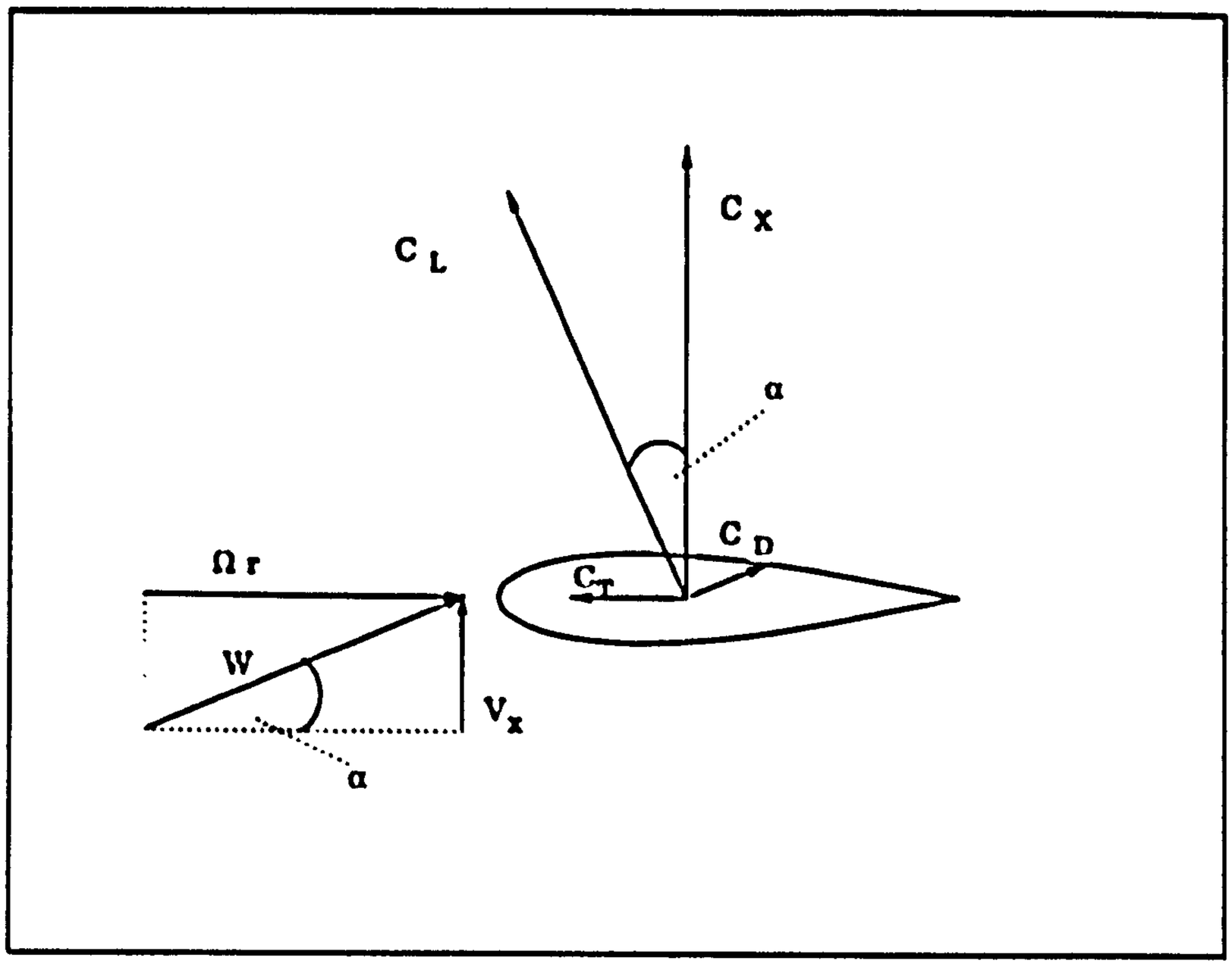

Figure 1.2: Blade Forces

oscillating water column (OWC) due to wave motion. It is usual to operate the Wells turbine in an airflow driven by the OWC. As shown in figure (1.3) this allows pneumatic gearing of the flow from high force, low speed to low force, high speed. The turbine can, therefore, be operated at high RPM which is compatible with conventional a/c generators with no need for gearing. Furthermore, high Keulegan-Carpenter number (KC) flows can be generated in which the turbine for a large part of a flow cycle is exposed to quasi-steady flow. The KC number is defined as $KC = (\pi A)/(D_T)$ where A is the amplitude of displacement of the oscillating flow and D_T is the turbine diameter.

Figure (1.4) (Whittaker (1992)), presents a schematic view of a 75 kW (rated) shoreline OWC power plant, which is run by Queens University, Belfast as a pilot project on the island of Islay. Concepts also exist, however, for offshore OWC devices where the available energy is significantly greater than at shoreline locations. One such device, the OSPREY, is described by Thorpe (1995).

As discussed by Bishop (1981) more conventional turbines such as Francis or Kaplan which have peak efficiencies in excess of 90% (-compared to theoretically predicted cyclic efficiencies of around 70% for the Wells turbine-) can be used in an OWC. These, however, require complicated rectifying valve mechanisms to provide unidirectional pulsating flow through the turbine from the alternating flow due to the captured wave motion.

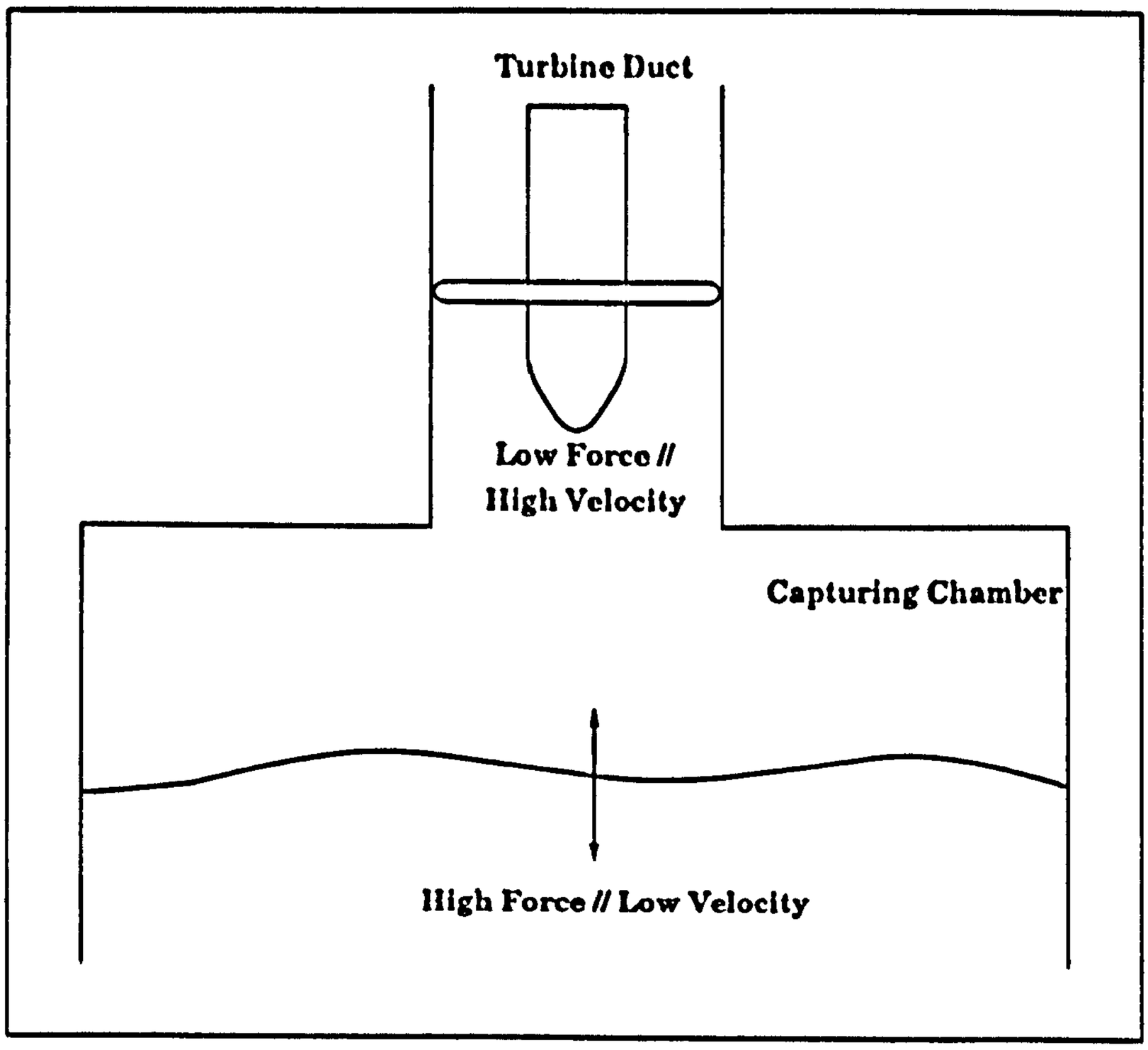

Figure 1.3: Flow Gearing

The Wells turbine has no need for flow rectification in that sense and is hence structurally comparatively simple and compact. Some workers argue that guide vanes are needed to enhance the start-up characteristics of the Wells turbine, which undermines the devices' main advantage of structural compactness. Evidence of tests carried out at Queens University (Ragunathan (1982)), however, suggests that paying attention to relevant design parameters such as the solidity and hub/tip ratio of the rotor, the turbine may be configured to be self starting. In addition to being inherently self-rectifying, aerodynamic considerations indicate that the Wells turbine is also self governing in that at high rotational speeds the compressibility drag of the blades expected to arise at tip Mach numbers well below unity would reduce the net torque, thus preventing turbine run-away. It has been shown (Ragunathan (1981)) that additional turbine control required as protection from alternator over-speed or for the case of turbine shut-down may be provided on the Wells turbine by installing a conventional mechanical brake.

To date the Wells turbine has mainly been used in a ducted arrangement as a power take-off mechanism in shoreline OWC devices described above. Since

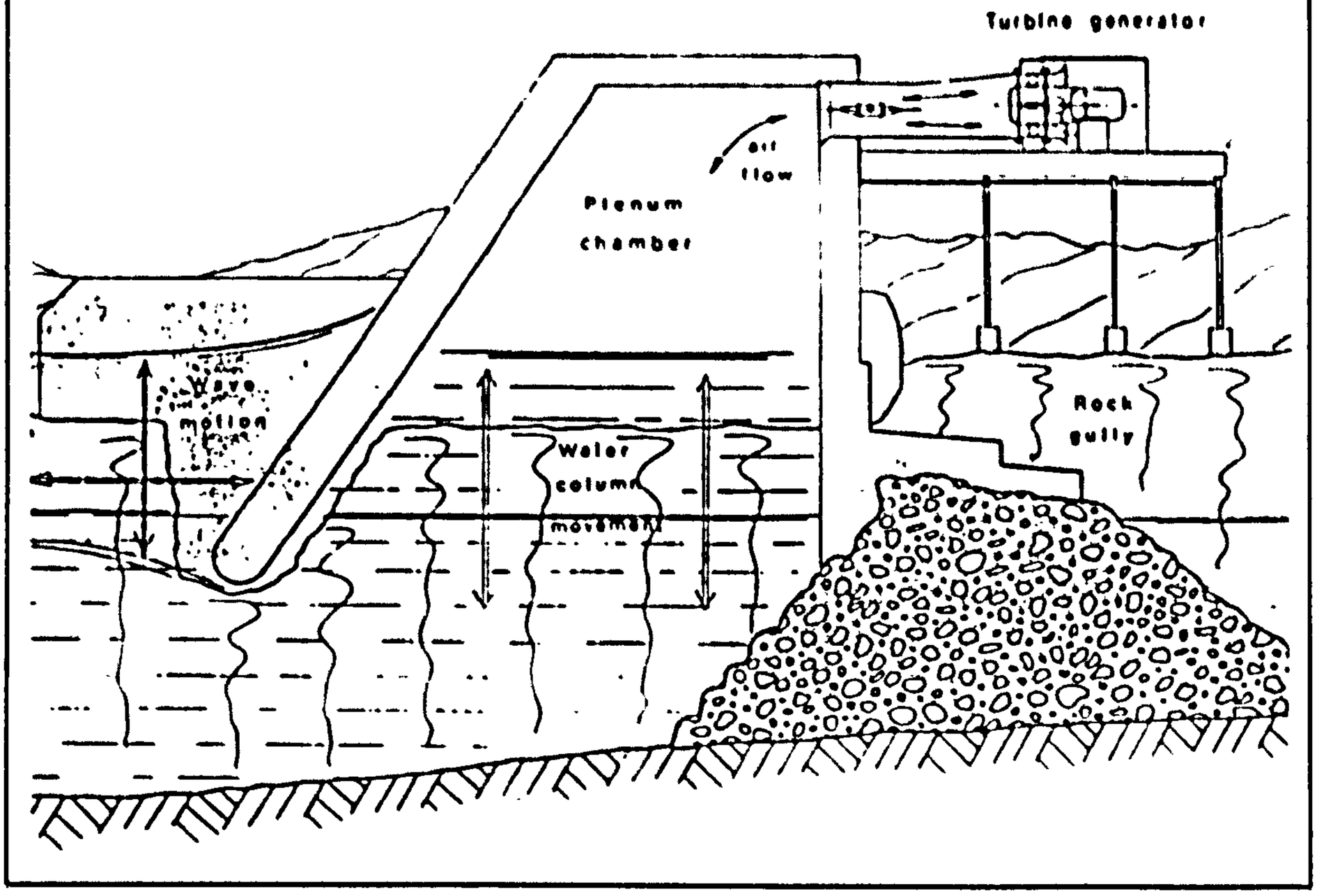

Figure 1.4: Islay 75 [kW] Wave Power Device

waves retain only a fraction of their initial energy as they reach the shore, it seems attractive to place wave energy converters offshore. The performance of a number of such devices has been studied to date. Grant (1987) for example has investigated the performance characteristics of a distress beacon which derived its power from surface waves by means of a low-head reversible flow turbine suspended below a float. Whittaker (1991) has explored the performance of a wave activated navigation buoy which used a ducted Wells turbine to convert the energy generated by the heaving motion of the buoy. In some of these cases the comparatively large, weighty structure associated with the capturing chamber of an OWC may be costly to build and install. A more cost effective set up might be to place the Wells turbine directly into the water flow beneath the waves. In this application the turbine is likely to operate in an unducted configuration. This is a novel use of the Wells turbine, which has apparently not been studied previously in any great detail and is the subject of part of the present work.

1.2.1 The Performance of The Wells Turbine in Ducted Flow

The Wells turbine performance is conventionally studied in terms of non-dimensional quantities for the shaft power W_S and the pressure drop across the rotor dp as well as the turbine efficiency η. In general, these quantities are related to the flow rate through the turbine duct Q, which is given by the axial flow velocity V_x and the cross sectional area of the duct. From this the so called flow coefficient Φ, which is defined as the ratio of V_x to the rotor blade tip speed $U_t(tip)$ and is, therefore, the inverse of the tip speed ratio Λ, can be deduced. All of the above performance quantities are strong functions of Φ and most theoretical and experimental studies aim to quantify this dependency.

To date theoretical performance prediction methods developed for the Wells turbine have mainly described the turbine operation in an OWC type set up. This, generally, implies that the turbine is mounted in a close fitting duct. The first theoretical aerodynamic performance analysis for this arrangement was developed by Sturge (1977) at the CEGB Marchwood Engineering Laboratories (MEL). Most subsequent theoretical Wells turbine performance studies have followed his method which was based on a blade element theory (BET) approach and is outlined in the following.

In the theoretical analysis given by Sturge the non-dimensional quantities for W_S, dp and η are related to the blade forces and various geometric parameters of the rotor. The method treats the duct flow as consisting of a number of concentric annular stream tubes. On the assumption of stream tube independence for the flow through the rotor the blade span is divided into a number of sections for which the flow is considered to be two dimensional. This is the conventional approach of BET which was derived by Glauert (1947) and argues that the flow over a particular blade section is not affected by that over the adjacent blade sections.

Assuming that for each blade element the axial force on all blades is balanced by the pressure force on an equivalent annulus and that the change in angular momentum of the flow passing through the rotor is equal to the blade elements' contribution to the rotor torque, the performance quantities W_S, dp and η can be expressed in terms of the tangential and normal blade forces F_T, F_N and the local blade incidence α. The related force coefficients C_T and C_N are determined from isolated airfoil data which is modified to account for effects due to the fact that the blades are operating in a cascade with 90 degrees stagger angle.

Ragunathan (1995) has discussed conventionally applied theoretical models developed by e.g. Weinig (1935) and the so called Martensen methods, which are

singularity methods and provide an inviscid analysis of 2D static cascade flow. In general, it is assumed that the static cascade data can for attached flow be applied to rotating blades and no account of rotational effects is explicitly given in the analysis. The methods mentioned above propose a correction factor k that can be applied to the lift coefficient of an isolated flat plate aerofoil C_{L0} to estimate the sectional lift coefficient of an aerofoil C_L in a static cascade. This correction factor can also be derived from general cascade theory given by Horlock (1958) and, for a cascade with a stagger angle of $\pi/2$, is given by:

(1.1) $$C_L = k\, C_{L0}$$

and

(1.2) $$k = \left(\frac{2s}{\pi c}\right) tan\left(\frac{\pi c}{2s}\right)$$

where c is the chord and s is the pitch.

The inviscid influence between aerofoils in a static cascade which causes this increase in C_L is due to the velocities mutually induced on each other by neighbouring aerofoils and is related to the bound circulation Γ. Ragunathan (1995) gives numerically computed and experimentally measured pressure distributions for NACA0012 and NACA0021 aerofoil sections in a cascade at pre-stall angles of attack (AOA). These results show that for an aerofoil operating in a static cascade the leading edge suction is significantly increased and that the differences in aerodynamic loading between leading and trailing edges is reduced .

In their basic form these potential flow methods cannot predict cascade effects on drag, so that in the absence of any better information it is sometimes assumed that the drag coefficient of an aerofoil is unaffected when operating in a cascade. Ragunathan (1995) has also presented results of computations in which the potential flow results of a basic Martensen method were combined with a boundary layer analysis to investigate cascade effects on C_T. Alternative approaches for quantifying the cascade effects, which are important to the performance of a Wells turbine rotor have been based on experimental investigations. In these the correction factors applicable to the isolated aerofoil data were deduced by correlating mean blade force coefficients with direct shaft power measurements.

In order to be able to evaluate the variation of the local blade incidence α along the blade span some assumptions are usually made about the radial variation of the axial inflow velocity in the rotor plane. Ragunathan (1983) has explained the so called radial equilibrium approach and the constant velocity approach which are usually applied in the theoretical performance prediction methods available for the Wells turbine. The former approach assumes that Δp is constant between

the rotor hub and the rotor tip so that no radial pressure gradients exist in the flow ahead and aft of the rotor. This assumption leads to an iterative procedure in which α is adjusted locally to satisfy the condition of a radially constant pressure drop across the turbine. In contrast, the second approach assumes that V_x is radially invariant in the rotor plane, which for a given rate of rotation allows the incidence to be computed directly as

$$\tan \alpha = \frac{V_x}{U_t} \tag{1.3}$$

where U_t is the tangential velocity seen by the turbine blade and is related to the rate of rotation Ω. Figure (1.5) below illustrates this relationship. Results of experimental measurements presented by Ragunathan (1983) suggest that both approaches make valid assumptions and that the differences in performance estimates derived from the two methods are, in general, for most flow rates negligible. However, experimental data recorded by Ragunathan (1986) for a model Wells

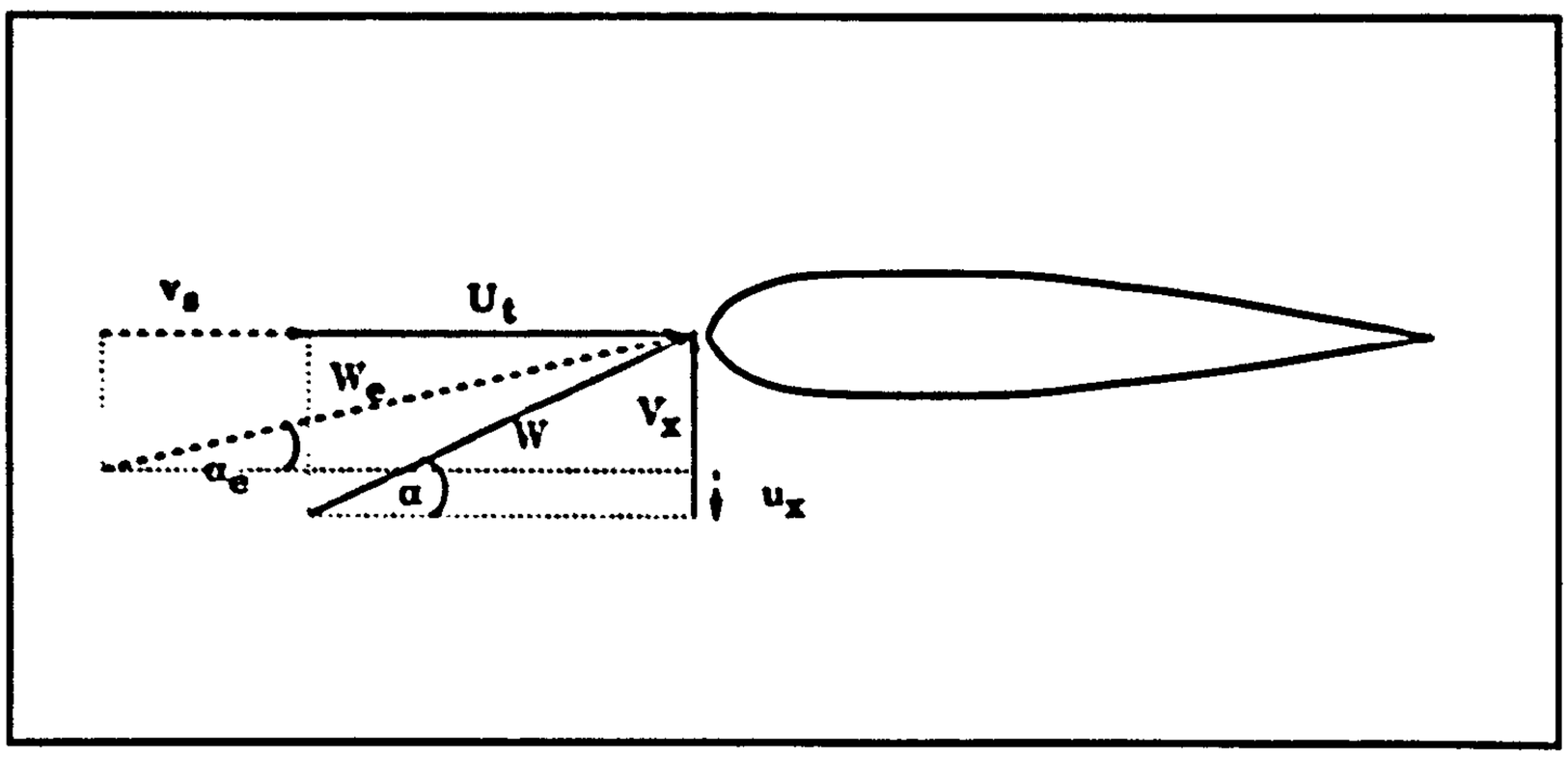

Figure 1.5: Incident Velocities

turbine which had a solidity σ of 0.75 and a hub/tip ratio h of 0.62 suggests that for high solidity rotors there is considerable radial variation of V_x downstream of the rotor. For a tip speed ratio of approximately 8.5 the published data revealed that downstream of the rotor V_x was increased by almost 80% at the blade tip while towards the blade root V_x was reduced by around 60%. Ragunathan concluded, therefore, that for high solidity rotors the concept of radial equilibrium is questionable.

Neglected in most published theoretical and experimental performance analyses of the Wells turbine are the effects of the rotor wake. The rotor wake induces axial and circumferential velocities u_x and v_θ in the plane of rotation as also indicated in figure (1.5).

These induced velocities vary radially as discussed in the following and cause an effective blade incidence α_e given by

$$\tan \alpha_e = \frac{V_{xe}}{U_{te}} \tag{1.4}$$

where $V_{xe} = V_x + u_x$ and $U_{te} = U_t + v_s$

Assuming that for each blade element dr the total axial force F_N acting on all of the n rotor blades is balanced by the pressure force acting on the swept annulus and the local change in axial momentum due to u_x the following relation may be derived:

$$n F_n \, dr = u_x \rho V_{xe} \, 2\pi r \, dr + \Delta p \, 2\pi \, dr \cdot r \tag{1.5}$$

Introducing the axial force coefficient $C_N = F_n/(1/2 \rho W_e^2 c)$ where $W_e = (V_{xe} + U_{te})^{1/2}$ is the total velocity and c is the blade chord equation(1.5) may be rearranged to give:

$$u_x = \frac{n (c/r)}{4\pi} C_N \frac{W_e^2}{V_{xe}} - \frac{\Delta p}{\rho V_{xe}} \tag{1.6}$$

This equation must be solved subject to the requirements of mass flow continuity in the annulus between the rotor tip r_t and the rotor hub r_h, i.e.:

$$\int_{r_h}^{r_t} 2\pi r \, u_x \, dr = 0 \tag{1.7}$$

By integrating equation(1.5) and substituting equation(1.7) assuming that $(\partial \Delta p/\partial r) = 0$ it can be shown that

$$\Delta p = 1/2 \, \rho \frac{nc}{\pi r_t (1 - h^2)} \int_h^1 C_N W_e^2 \, d(r/r_t) \tag{1.8}$$

The swirl velocity v_s acts in the circumferential direction and is induced by the vortex wake of the rotor, which is sustained by the vorticity shed from the n rotor blades, each of which carry a bound circulation Γ. The continuously shed hub and tip vortices form axially symmetric spiral vortex sheets downstream of the turbine rotor. On the inside of such a vortex sheet the swirl is zero, because an infinite spiral sheet does not induce any swirl velocity at radii smaller than its own within the sheet region. The swirl velocity field outside, however, is not zero and is, in fact, equal to that induced by an axial vortex filament of equivalent strength. From this it is apparent that the tip vortex does not contribute to

the swirl which, therefore, is most strongly related to the shed hub vortex. This result does not account for the effect of the rotor duct, which can be modelled by image vortex sheets for the tip and hub vortices. It can be seen, however, that they do not cause any swirl at the rotor, because the latter lies inside these image vortex sheets and, therefore, the same argument applies to these vortex sheets as for the tip vortex.

If the hub vortex is approximated as a semi-infinite axial vortex filament which originates at the centre of the rotor and has a strength $n\Gamma$ then the swirl velocity induced by this filament far downstream of the rotor at a distance r from the axis of rotation is:

$$v_s = \frac{n\Gamma}{2\pi r} \tag{1.9}$$

where according to the Kutta-Joukowski theorem Γ for each blade is related to the blade lift coefficient C_L by

$$\Gamma = 1/2\, W_e\, c\, C_L \tag{1.10}$$

so that

$$v_s = \frac{n(c/r)}{2\pi} W_e C_L \tag{1.11}$$

It can be seen that v_s increases in direct proportion with the local lift coefficient and the chord to radius ratio (c/r). This suggest that as C_L increases with α, the blade would, due the action of v_s which causes a reduction in the effective incidence α_e, at high incidences tend to 'unstall' itself.

On the assumption that ahead of the rotor v_s is nominally zero the value of v_s in the plane of rotation is taken to be exactly half its value downstream of the turbine rotor. If for high Λ the resultant velocity W_e is approximated by $v_s + \Omega r$ in equation (1.11) then:

$$\frac{v_s}{\Omega r} = \frac{n\,(c/r)\,C_L}{4\pi}\,\frac{W_e}{\Omega r} \tag{1.12}$$

so that,

$$\frac{v_s}{\Omega r} = \frac{n\,(c/r)\,C_L}{4\pi}\left(1 + \frac{v_s}{\Omega r}\right) \tag{1.13}$$

and finally,

$$\frac{v_s}{\Omega r} = \frac{n\,(c/r)\,C_L}{4\pi - n\,(c/r)\,C_L} \tag{1.14}$$

Clearly, the assumptions made in the derivation of equation(1.14) are invalid at

high local angle of attack i.e. lower tip speed ratios.

Barnsley and Wellicombe (1991) performed LDA measurements of mean and instantaneous axial and circumferential velocities ahead and aft of an unducted model wind turbine rotor in steady axial flow. Their measurements revealed that while the mean induced axial velocity well ahead of the rotor was nominally zero there was a small non-zero mean value of the circumferential velocity v_1 ahead of the rotor which was near constant up to $0.25\%D_T$ upstream, which suggests that the assumption of zero swirl ahead of the rotor is not strictly true. Closer to the blade the time history traces of the circumferential velocity showed strong local influences of the blade circulation.

The above numerical performance analysis treats the flow through the Wells turbine rotor as quasi steady. In general, no explicit account of the oscillatory nature of the incident flow generated in an OWC in which the Wells turbine conventionally operates is taken in these performance prediction methods. Ragunathan (1995) outlines the commonly accepted view that the non-dimensional frequencies of the airflow driven by the captured wave motion in typical wave climates are low enough to justify the steady flow approximation. Experimental studies performed in oscillatory flow by Ragunathan and Ombaka (1985) for different Wells turbine geometries showed that the non-dimensional pressure drop, the shaft power and the rotor efficiency over a fairly wide range of flow coefficients are not a strong function of the reduced flow frequency. Further, it is clear that in an OWC relatively high KC number flows occur due to the pneumatic gearing of the airflow. For the Islay prototype Wells turbine typical operational KC numbers were estimated to be of the order of 100. For these high KC number flows the turbine indeed operates in quasi steady flow for a large part of the flow cycle.

On the whole, performance predictions for ducted Wells turbines made from the unidirectional, steady flow theory approach described above seem to agree reasonably well qualitatively and quantitatively with experimental data measured in steady unidirectional and unsteady alternating flows (see e.g. Grant (1979) ,Ragunathan (1986)). Model scale experiments carried out in unidirectional steady flow by Grant (1979), however, indicated that for the larger flow coefficients the theoretically predicted turbine power was significantly lower than the measured shaft power. This was explained by the differences between the test Reynolds number and that relating to the aerofoil data used in the prediction method. More recently, Koola (1995) has carried out larger scale wind tunnel investigations in which the shaft power measured for a Wells turbine operating in unsteady randomly alternating flow was compared to numerical predictions using conventional theory. From the data presented it was clear that, while there was good agreement between theory and experiment for the lower flow rates, at

the higher flow rates the theory dramatically underpredicted the turbine shaft power. It was concluded that the theoretical model does not accurately predict the onset of turbine stall.

In order to comply with the stringent requirements of the electric grid the Wells

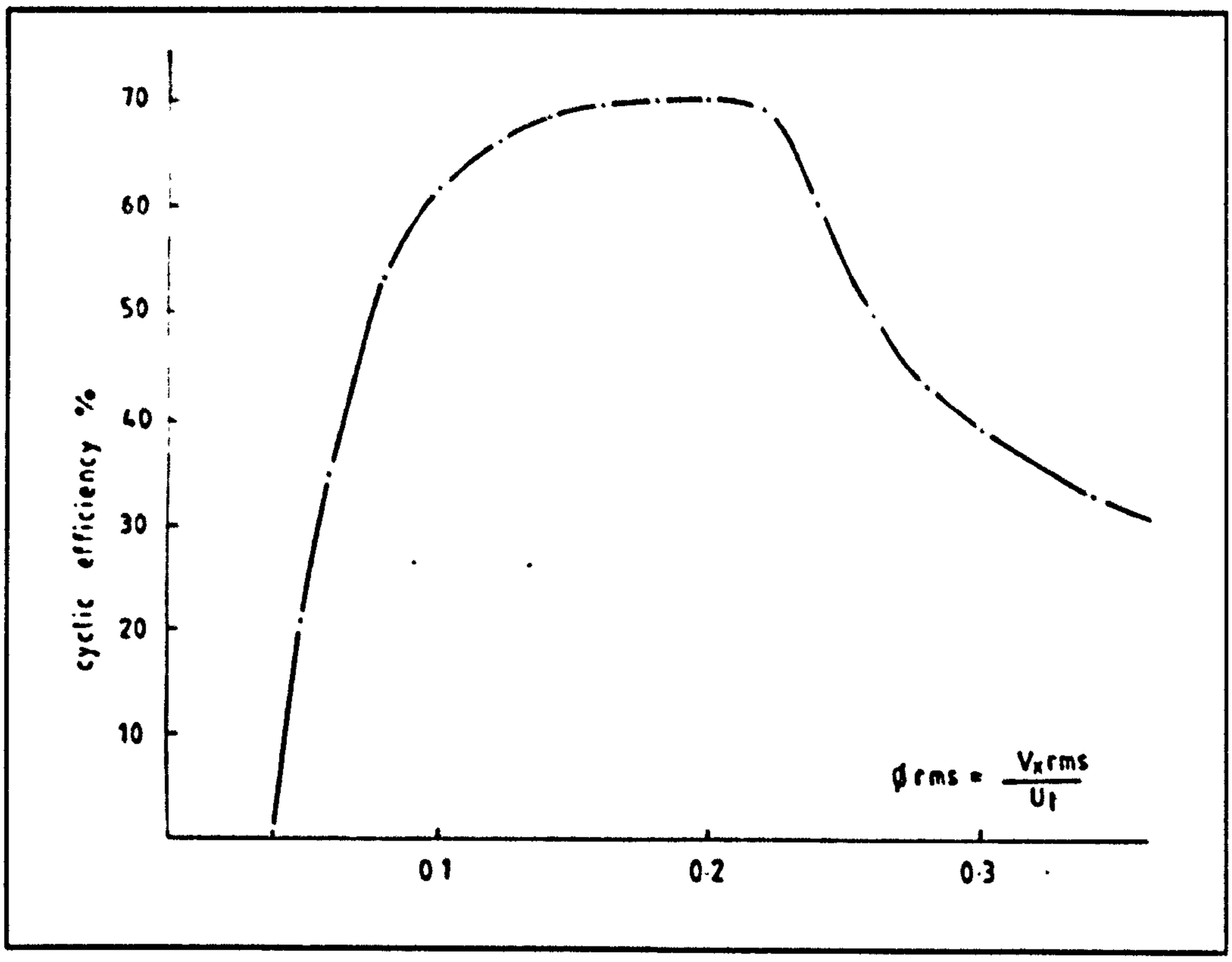

Figure 1.6: Wells Turbine Cyclic Efficiency

turbine, attached to an induction type generator of AC power, would conventionally be operated at nominally constant RPM. For the Wells turbine operation in OWC wave power devices it can be seen that during a wave flow cycle the turbine blades will operate at a range of incidences due to variations of the axial inflow velocity. Figure (1.6) (Whittaker (1992)) shows a typical variation of cyclic turbine efficiency with flow coefficient Φ which for constant RPM is proportional to the inflow velocity V_x. It can be seen from this that at low values of Φ (i.e.high Λ) the efficiency is reduced due to profile drag effects. Further it may be noted, that for large values of V_x the turbine efficiency and, therefore, the energy capture of the device is low. This is associated with rotor stall. Clearly, from a designers point of view it seems desirable to configure the turbine so that it operates out of stall for a possibly large part of a flow cycle for a typical spectrum of inflow velocity fluctuations. Unfortunately, for the Wells turbine, stall of rotating blades and its dependency on geometric rotor parameters is currently not well understood nor theoretically described.

There is evidence from a number of full scale measurements of rotor power carried out for wind turbines such as those performed on a 55 [kW] VESTAS 15 [m] rotor at the Riso Laboratories in Denmark (Viterna (1982)) that for low TSR (i.e. high wind speeds) performance estimates made from BET lead to significant underpredictions. This is usually ascribed to the so called stall delay effect, which was first reported by Himmelskamp (1945), who had documented it in an experimental study of a fan blade performance, and it is consequently also known as the Himmelskamp effect. It describes the phenomenon that on a rotating blade stall doesn't occur locally until higher angles of attack (AOA) than would be expected from 2D sectional aerofoil data. Figure (1.7) (Schlichting (1979)) shows sectional C_L data measured by Himmelskamp on a rotating fan blade.

More recently, stall delay has been investigated by a number of researchers in

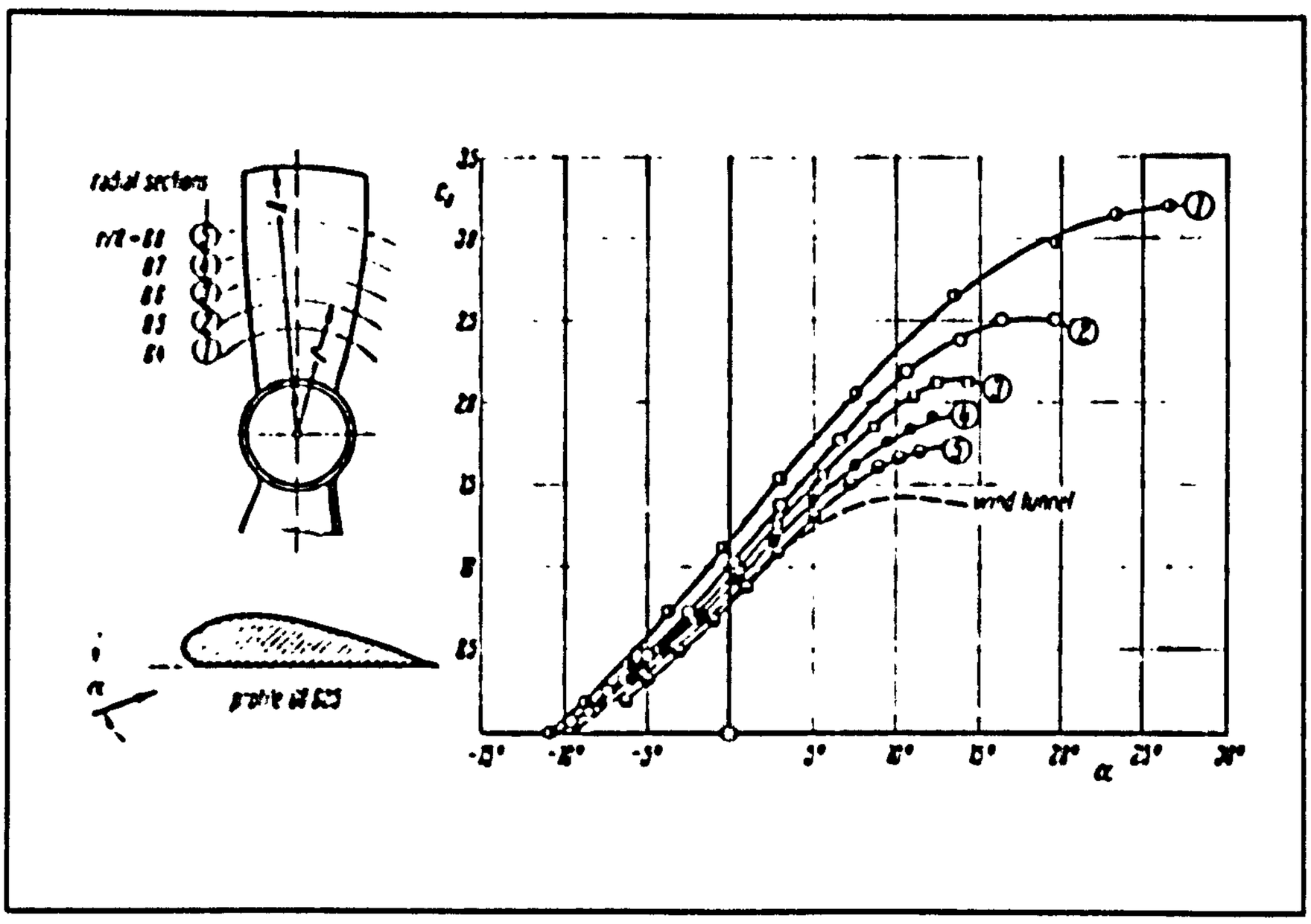

Figure 1.7: The Himmelskamp Effect

controlled wind tunnel experiments in which chord wise surface pressure distributions were measured at various radial positions on a rotating wind turbine blade and subsequently compared to either measured or computed data for the 2D characteristics of the blade profile section. From these static pressure distributions local normal and tangential force coefficients were deduced by integration using estimated values for the local blade incidences.

The results of measurements performed on a rotating blade of a 2.7[m] diameter wind turbine rotor presented by Graham (1989) showed that the data

recorded at a number of span wise positions for the C_L variation with the local blade incidence α agreed fairly well with data taken for the non-rotating blade while the blade incidences α were well below the stall angle α_{max} of the static blade. At higher blade incidences at which the measured pressure distributions of the static blade signalled stalled flow, however, the C_L versus α curves derived for the rotating blade showed rather different characteristics from that of the static blade. The main difference was that while the static blade showed the expected reduction in post-stall lift the rotating blade sections in comparison revealed significantly increased values of C_L and a much higher value of α_{max}. Correspondingly, the values of C_{Lmax} were much larger at all radial stations than those established for the static blade. Further, a strong dependency of C_{Lmax} on radial position was noted, as a result of which C_{Lmax} at the blade root was significantly higher than near the blade tip. These results qualitatively resemble those originally measured by Himmelskamp for rotating fan blades. It was further reported in this study that the data deduced for the blade profile drag coefficient C_{D0} varied to a lesser extent along the blade span.

Similar wind tunnel measurements were carried out by Ronsten (1991) on a two bladed, 2.4[m] diameter wind turbine rotor. His findings agreed qualitatively with those of Graham and Brown and he concluded from this study that rotational effects suppress the loss of the leading edge suction peaks at high angles of attack (AOA) across a large portion of the blade span. It was observed from the recorded chord wise pressure distributions that for the inboard blade sections the eventual loss of the leading edge suction peak on the upper surface of the rotating blade was far more gradual than for the static blade. In contrast to the behaviour of the static blade, which subsequent to the sudden loss of the leading edge suction peak showed a 'flat top' pressure distribution signalling stalled flow conditions, the distributions observed by Graham as well as Ronsten at high AOA indicated that over a significant part of the upper blade surface the flow was still attached as a result of which the blade was generating a considerable amount of lift. Figure (1.8) below shows an example of such a pressure distribution measured in a steady flow wind tunnel study at model scale by Graham (1989) at high AOA on a rotating wind turbine blade. Interestingly, these studies also found that the differences in the *Cp*-distributions on the lower surfaces of the rotating and non-rotating blade sections were comparatively small.

Barnsley and Wellicombe (1991) discovered in experiments carried out on a 1.0[m] diameter wind turbine rotor that a sudden drop in the derived rotor shaft power occurred at values of Λ for which the outer part of the blade, where the bulk of the driving torque is generated, had shown no signs of stall. From this they concluded that the decrease in rotor power was due to a rapid increase in the blade drag coefficient, which they associated with the loss of the leading edge suction peak. In this context, attention was drawn to the importance of scale effects due to which the post-stall reduction in shaft power at model scale may

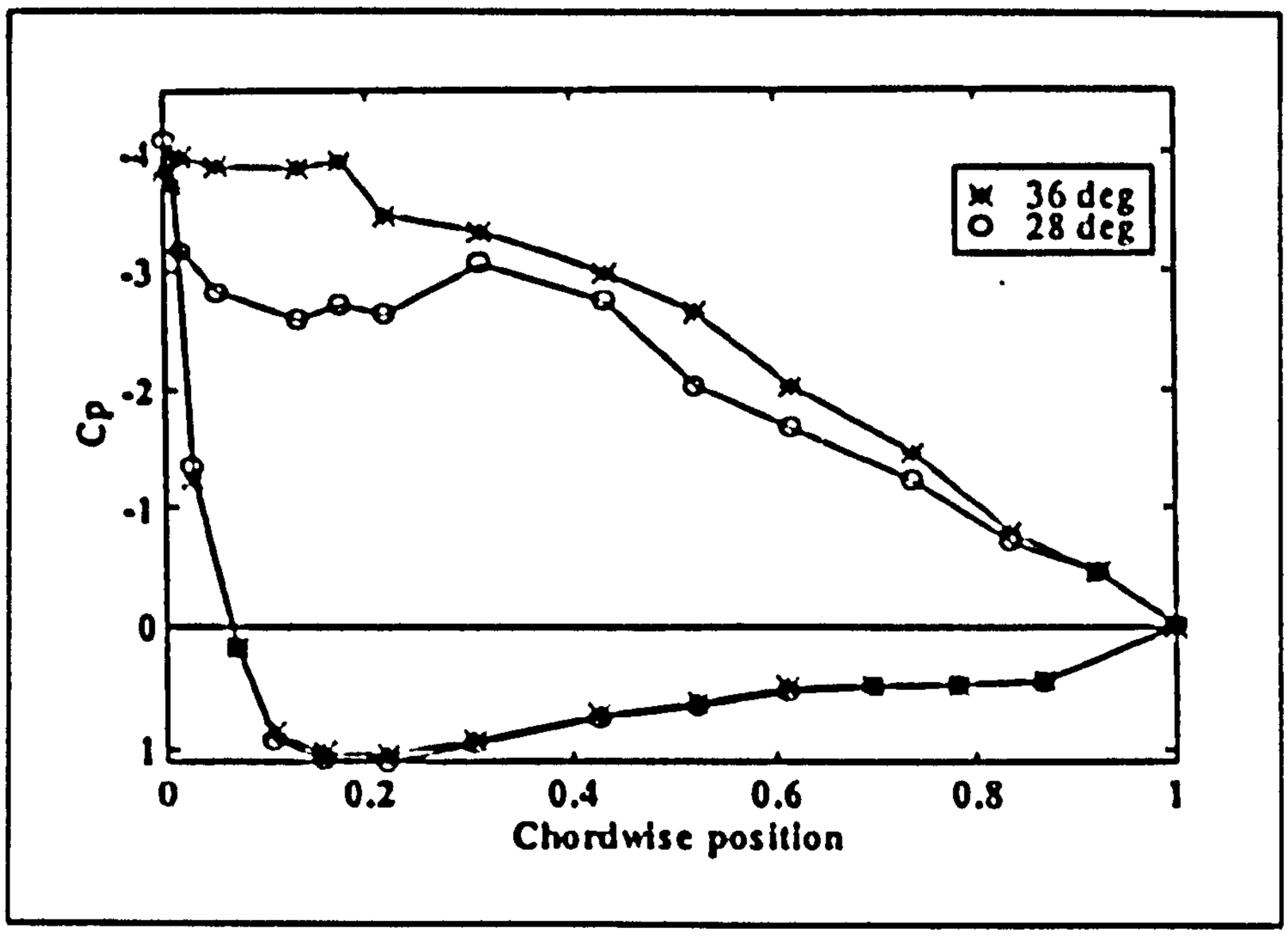

Figure 1.8: Stall Delay Pressure Distributions

be expected to be higher than for full scale machines operating at much higher Reynolds numbers.

From the literature survey conducted in preparation for the research work which is a main subject of this thesis, it would seem that for some time there was no common consensus among the researchers working in the field for the explanation of the stall delay phenomenon described above.

Wood (1991) presented results of 3D potential flow calculations and argued from these that the apparent stall delay could be explained from purely inviscid flow analysis and was due to cascade effects. His computations were set up for a ducted rotor geometry with low aspect ratio blades and they produced chord wise pressure distributions which showed a reduction in the leading edge suction peaks in comparison to the relevant 2D section characteristics even for pre-stall AOA. As a result of this Wood concluded that the adverse pressure gradient on the upper blade surface was reduced and a consequent delay in boundary layer separation was inferred.

McCroskey (1971) carried out surface flow visualisation studies of the boundary layer transitional behaviour on helicopter blades at model scale. The results of his work strongly suggested that while the boundary layer remains attached it is governed by chord wise pressure gradients rather than by Reynolds number, rotational or 0 effects. It was found, however, that there were appreciable cross

flows in regions near the leading edge when laminar separation bubbles occurred or in separated flow regions near the trailing edge. McCroskeys work did not produce any conclusive evidence of stall delay. However, as is discussed in more detail below the extent of stall delay that occurs on a rotating blade depends the local ratio of blade chord to radius (c/r), which for typical helicopter blades is small.

Rawlinson and Smith (1990) attempted to model the flow over rotating blades computationally by using a first order panel method which was coupled to a 3D integral method boundary layer solver and a prescribed wake model. Generally, the published results of this numerical study showed acceptable qualitative agreements for the predicted power of a wind turbine rotor when compared to experimental results at low Λ. However, the computed chordwise pressure distributions did not agree well with the corresponding experimental data at the blade leading and trailing edge regions. At pre-stall AOA the computations showed smaller lift curve slopes than measured in experiments and it was suggested that this may be due to the relatively low aspect ratio of the blades used for the study and that the agreement may improve for higher aspect ratio blades. Generally, this study did not allow conclusive statements on the nature of the stall delay effect, though some features were qualitatively well reproduced by the numerical method, since there was ambiguous quantitative agreement with experimental data.

On the whole, however, the majority view among researchers was in agreement with the explanation offered originally by Himmelskamp that stall delay is effected by radial flows which exist in the boundary layer of the upper blade surface and are driven by Coriolis forces. As a consequence of these radial flows the boundary layers become thinned out so that the adverse pressure gradients that cause the flow to separate are locally reduced thereby postponing the stall.

Milborrow (1985) provided a relatively simple theoretical analysis of the centrifugal forces acting on fluid particles in the boundary layer and the resulting radial mass flows of a rotating blade. This analysis leads to expressions relating the local radial and stream wise velocity components of the surface flow. In qualitative agreement with results of wool tuft flow visualisation studies carried out on a 1.2[m] diameter fan, which showed signs of delayed stall, the derived theory suggested that radial velocities on the blade suction surface increase with chord wise distance, chord to radius ratio (c/r) and lift coefficient C_L. Further, Milborrow drew attention to the existence of a span wise pressure gradient that promotes outward flow and is due to the increase of the dynamic pressure with radius. In his interpretation of these results it is argued that since the bulk of the flow near the hub is diverging -either under the action of pressure gradients or to clear the rotor hub or both- these blade sections operate effectively in yaw.

In 1994 the 'dynamic stall and 3D effects' research project for wind turbine aerodynamics was initiated under JOULE II funding. This project aimed to improve the understanding of the three-dimensional and unsteady effects which govern the stall behaviour of rotating wind turbine blades. It was intended to conclusively document the parameters on which the stall of wind turbine blades depends by conducting model as well as full scale experimental and numerical investigations. These were carried out at a number of European research organisations. Key results of the project were summarised by Bjoerck (1996): Theoretical analysis performed at NLR using a quasi 3D viscous/inviscid matching procedure which successfully modelled the stall delay phenomenon confirmed that the main effects of rotation scale with (c/r). The chord wise pressure distributions which were produced in full 3D Navier-Stokes computations carried out at the Denmark Technical University for a constant chord untwisted blade revealed strong stall delay effects at the inner parts of the rotating blade. These pressure distributions were in good qualitative and quantitative agreement with those experimentally measured on a rotating blade model at post-stall AOA. The study concluded that the increased post-stall lift coefficients computed for the inboard blade sections were related to rotational effects and were due to Coriolis forces acting on fluid particles in the separated 3D boundary layer flow.

Although the Wells turbine operates in much the same way as wind turbines do, geometrical quantities such as the rotor solidity σ, blade aspect ratio AR and hub/tip ratio h are usually considerably different from those of a typical wind turbine rotor. As a result, the aerodynamic behaviour of a Wells turbine rotor is in some respects different from that of a wind turbine.

Current Wells turbines which operate in OWC wave power devices are essentially high solidity machines with h typically ranging between 50% to 70%. Consequently, the rotor solidity is more sensibly described in terms of the swept annular area between the rotor tip and hub rather than the swept area of the blade tips alone which defines the tip solidity of the rotor σ_t usually applied to wind turbine rotors. To this extent the aerodynamic performance of the Wells turbine may be expected to be more similar to that of conventional high solidity axial flow turbomachinery. As discussed above, the cascade effects strongly influence the pre-stall performance of the rotating blades on a Wells turbine. Since the predominantly inviscid prediction methods applied to date to the analysis of the Wells turbine performance are not very useful in the study of separated cascade flows little published data which documents the post-stall effects of σ is available.

Further differences to the aerodynamic behaviour of wind turbine rotors arise because of the fact that typically the blades of a Wells turbine rotor are of fairly low AR due to the comparatively large values of h. In this context Ragunathan

(1995) has commented qualitatively on the importance of effective leading and trailing edge sweep angles for the stall behaviour of the low AR, rectangular plan form Wells turbine blades. These sweep angles result from the fact that the leading and trailing edge lines are not on a radial line through the centre of rotation and are more severe for low AR blades.

It can be seen from these considerations that at the start of the current research work it was not obvious to what extent the in the meantime well documented understanding of the important steady flow mechanisms that govern the stall of wind turbine rotors were transferable to the Wells turbine and, thus, exactly to what extent the stall delay phenomenon would be important on a Wells turbine operating in steady flow.

1.2.2 The Performance of The Wells Turbine in Unducted Flow

As mentioned above novel offshore applications of the Wells turbine might place the device directly in the sea waves. Typically in these applications the turbine might be arranged as a single- or multistage buoy type device in which the turbine rotor is suspended vertically from a float and would be driven by the orbital flows beneath the waves.

In contrast to ducted applications in an OWC there is no pneumatic gearing of the flow in this arrangement and flows would tend to be of low to moderate KC. The main difference between the flows for the ducted and unducted turbine rotors is that in the latter case the vortex wake has a greater effect on the performance, since the flow can pass around as well as through the turbine rotor. The flow structure for the unducted turbine operating in low to moderate amplitude oscillatory flow may be anticipated to have similarities to low KC flow past non-porous flat plates, which shed a peripheral vortex ring that generates appreciable back flow on each half cycle (de Bernardinis (1981)).

The hydrodynamic performance of the Wells turbine in such flows and the flow structures on which it depends have not been studied previously and as a result there is no performance data available.

Also in the case of the flow around the unducted turbine, where interactions with the returning wake of the previous half cycle are important, no theoretical analysis similar to the BET or the actuator disc theory for turbine rotors in unidirectional flow has been developed to predict the rotor performance.

Though, the wake structure in the case of an unducted Wells turbine operating in small KC oscillatory flow is considerably different from that of a ducted Wells turbine operating in quasi-steady, large KC oscillatory flow, the fluid mechanic behaviour of the local blade sections is comparable for the two applications. If it is assumed that in both cases the unsteady flow effects are comparable, then the aerodynamic characteristics of the rotor blades for an unducted Wells turbine are governed by the same phenomena as those of the ducted Wells turbine. It is clear, therefore, that the stall delay and cascade effects discussed above for a ducted Wells turbine arrangement are also important for the aerodynamic performance of the blades of an unducted Wells turbine.

Research Objectives

The aims of the thesis work were:

- To experimentally measure the stall of a rotating blade operating in a typically configured ducted Wells turbine arrangement in steady, unidirectional flow.

- To, from these measurements, gain an improved understanding of the steady stall behaviour of the Wells turbine and, in particular, establish the importance of the stall delay effect.

- To develop a physical understanding of the Wells turbine performance in unducted oscillatory flow.

- To document the Wells turbine performance through numerical and experimental study.

Chapter 2

The Wells Turbine Performance in Ducted Flow

The research work reported on in this chapter was intended to contribute to the understanding of the aerodynamic performance of the Wells turbine in a ducted arrangement which is typical for current prototype shoreline and off-shore OWC wave power plants.

Much research of the Wells turbine performance in such an arrangement has already been performed by other researchers as discussed earlier using mainly blade element theory, which predicts the aerodynamic performance of the turbine rotor from the relevant 2D-aerofoil data, as well as model scale experimental measurements of the turbine shaft power. As also discussed in the introduction of this report, the agreement between the experimental data and the theoretical predictions of the power of a Wells turbine for low rates of airflow through the turbine duct on the whole has been found to be fairly good. For this operational regime, therefore, the Wells turbine aerodynamic behaviour is considered to be fairly well described by the blade element theory which is usually applied without modifying the aerodynamic characteristics of the blade sections for rotational effects.

For wind turbines it is known that the aerodynamic performance is under predicted by blade element theory in high winds (i.e when the rotor is operating at a low tip speed ratios) for which the resultant flow incident to the local blade sections would, from the known aerofoil characteristics, be expected to separate from the blade surface. The numerical and experimental research work by a number of researchers which has been discussed in detail above has shown that this discrepancy is caused by the so-called stall delay effect which relates to radial flows in the boundary layers of the rotating blade.

For the Wells turbine operating in quasi-steady flow through a close fitting

duct no experimental work equivalent to that performed for unducted wind turbine rotors has been carried out to date. Since in most experimental work carried out for the Wells turbine to date the turbine shaft power has been measured directly, the radial variation of the aerodynamic characteristics of the rotor blades has had to be inferred from blade element theory. This approach does not allow a direct experimental validation of the basic blade element theory and the linear cascade theories used for the performance prediction of the ducted Wells turbines. Further, there is evidence that the stall behaviour of the Wells turbine is not well predicted by the conventional theory.

In analogy to the experimental work carried out for wind turbine rotors the work reported on in this chapter was, therefore, aimed at providing a more direct documentation of the radial variation of aerodynamic characteristics of a rotating Wells turbine blade paying particular attention to the stalling behaviour. Generally, therefore, this work was intended to allow more detailed comments on the validity of the conventional theoretical approaches to the performance prediction of ducted Wells turbines to be made.

2.1 Research Objectives

The main research objective of the work reported on in this chapter was to experimentally study the span wise variation of aerodynamic performance characteristics of a rotating blade of a typically configured ducted Wells turbine rotor in unidirectional, steady airflow. The effects of rotor solidity and hub to tip ratio were also to be studied. In particular, the turbine stall previously not well understood was to be investigated at a number of radial stations along a rotating blade and was to be compared to the stalling behaviour of the static blade.

2.2 Experimental Procedure

2.2.1 General

Efforts to optimise the performance of the Wells turbine have led researchers to incorporate a number special features into the rotor design such as guide vanes, blade taper, blade thickness taper, as well as blade sweep. The effect of these on the Wells turbine performance has been studied in a number of single and multistage arrangements. For the current study, which mainly aimed to establish some fundamental aerodynamic characteristics of the Wells turbine rotor by focusing on the stall behaviour, it was felt that there was no particular merit in including any of the above features. In fact, there was a strong feeling that

their inclusion would only complicate the interpretations of the test results. It was decided, therefore, that the experimental work should be conducted on the simplest Wells turbine configuration.This is represented by a mono plane rotor comprising straight, constant chord blades, which are unswept about the mid chord line.

In line with the conventional approach chosen by numerous researchers for the experimental study of the Wells turbine performance at model-scale the wind tunnel experiments were designed and carried out for steady, incompressible, uni-directional flow conditions. Effects due to the oscillatory nature of the incident axial flow as encountered by the Wells turbine in an OWC were thus not explored in the wind tunnel study.

Following the example of the experimental investigations of the stall delay phenomenon on model wind turbine rotors mentioned in the previous report section it was decided to document the local flow conditions for a range of tip speed ratios by recording the chord wise pressure distributions at various radial stations on one rotating blade. The corresponding normal and tangential force coefficients could then be derived by integration of the local pressure distributions. This experimental method was favoured over rotor torque measurements, because it allowed a more direct analysis of the contribution of individual blade sections to the shaft power.

2.2.2 Wind Tunnel Set-Up And Flow Calibration

The turbine was configured and designed mechanically as described below to be compatible with the cross sectional dimensions of the test section of a number of the low-speed wind tunnel facilities of the Imperial College Aeronautics department.

The flow blockage posed by the turbine was anticipated to be rather high. Consequently, there was some concern about the ability of the departmental closed circuit wind tunnels to generate stable axial flows against these high levels of blockage. It was felt, that in the worst circumstances the turbine might even cause the tunnel fan to become stalled. Further disadvantages of the closed circuit tunnels related to the test section accessibility. This was carefully considered in the context of the potentially rather extensive turbine and duct rigging procedures.

Eventually, a blow-down tunnel was chosen, which is usually set-up with an 18 inch square test section. This particular tunnel was chosen because of its powerful backward aerofoil centrifugal blower, its accessibility and not least because testing time was easily available. The blower was fully controllable at low as well

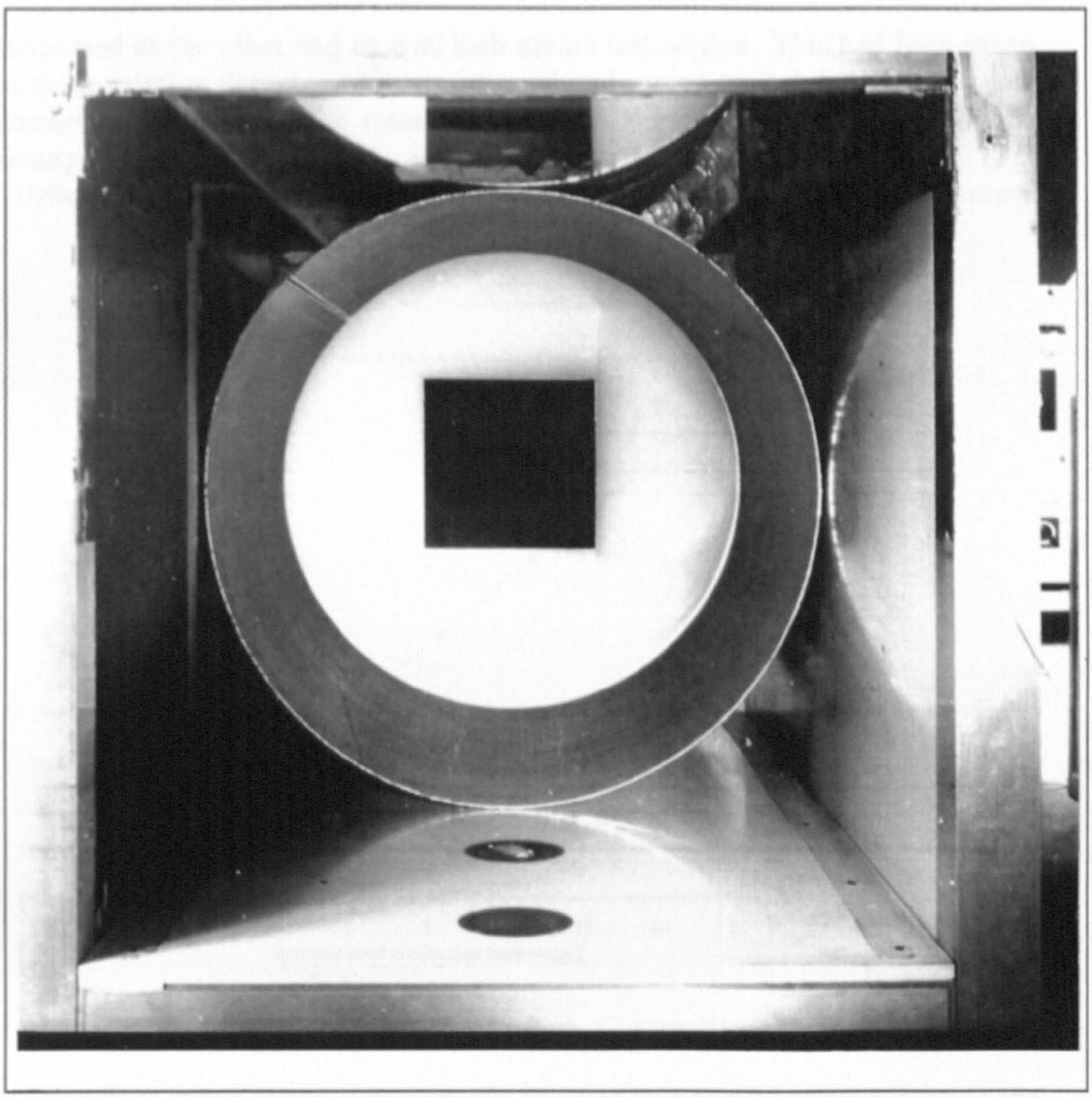

Figure 2.1: Blow Down Wind Tunnel Arrangement

as high wind speeds and capable of generating a high pressure low speed flow without stalling.

The rotor diameter of nominally 0.74 [m] of the Wells turbine designed for the experiment was too large for the 18 inch square test section. This was removed and was replaced by a purposely designed and built diffuser/duct arrangement. The straight tapered inside walls of the diffuser were inclined at nominally 4 degrees and created a cross sectional transition between the diffuser inlet and outlet faces from 18 inch square to 30 inch diameter round. While at one end the aluminium turbine duct was flanged and cantilevered from the diffuser, it was

supported at the other end by a 30 inch square test section. This had been taken from an existing departmental wind tunnel and served to stabilise the exit flow downstream of the turbine rotor. Figure (2.1) shows an upstream view of the arrangement.

Using a pitot-static probe the velocity profile was traversed inside the empty

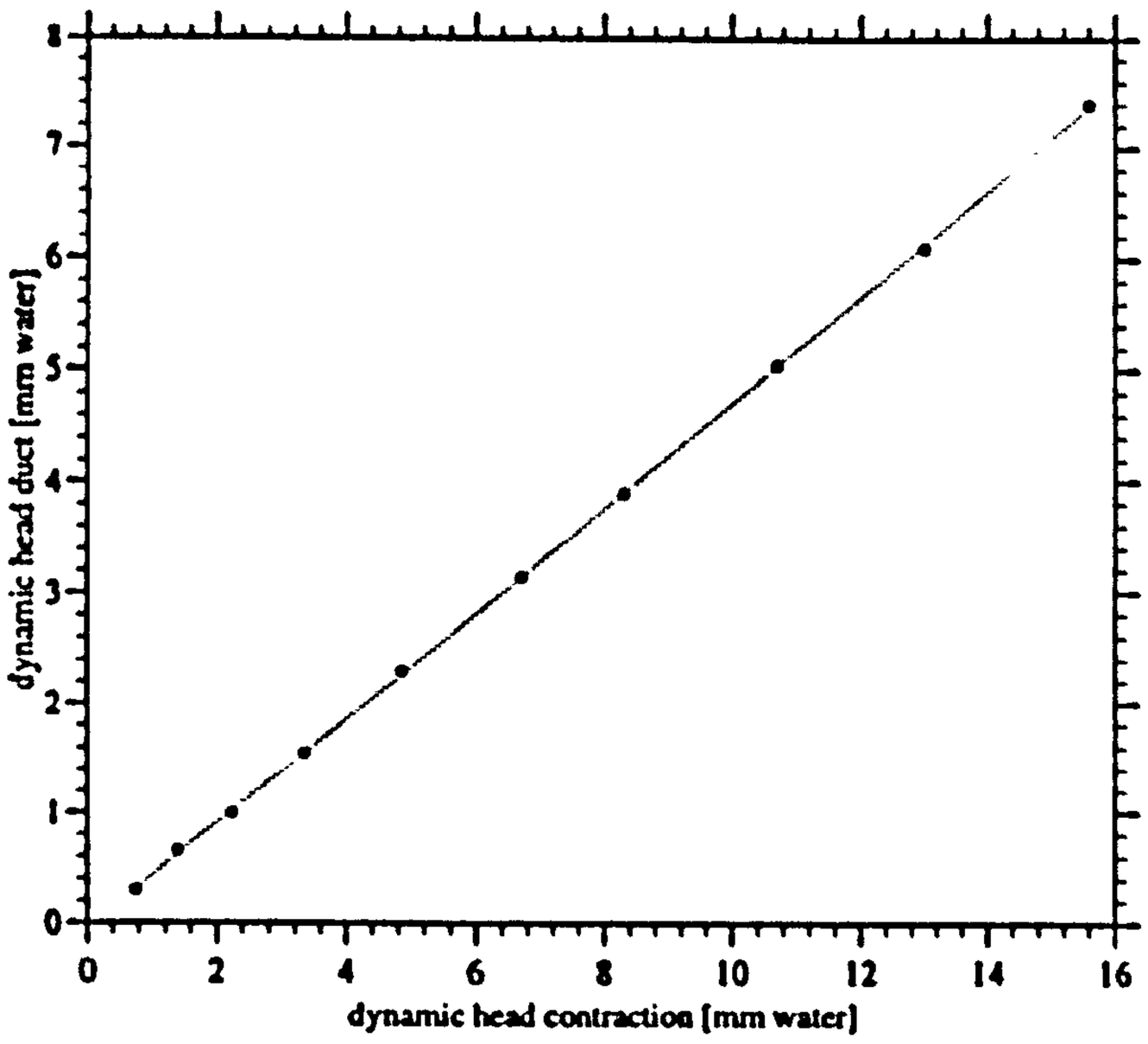

Figure 2.2: Duct Dynamic Pressure vs. Contraction Dynamic Head

turbine duct over a range of flow speeds and was found to be uniform outside the wall boundary layers to within nominally 2%. The boundary layer thickness on the duct walls from these measurements were estimated to be less than 30[mm]. As further part of the tunnel calibration the flow in the annulus between the duct and the turbine nacelle was monitored with the blade-less turbine in position. Figure (2.2) shows the ratio between the dynamic head in the rotor plane and the dynamic head in the exit plane of the tunnel contraction. The former was measured on the centre line of the flow annulus in the rotor plane while the latter was deduced from a measurement of the static pressure drop across the tunnel contraction.

It is evident that over the range of wind speeds shown the dynamic head ratio was constant. The corresponding ratio of flow velocities was approximately 3% higher than expected from continuity of mass flows between the contraction exit

and the plane of rotation. This suggested that friction losses in the diffuser were small and that the associated boundary layers on the tunnel walls and turbine nacelles were thin.

Previous to the actual turbine testing the blower performance was verified in blockage tests. In these the centre line duct velocity that the blower could generate against a uniform resistance was measured. The resistance was generated by a number of gauze screens placed normal to the flow. It was found that for a resistance ratio of 2.5, which relates the pressure drop across the resistance to the dynamic pressure of the flow ahead of it, the blower could sustain the test speeds of 13 [m/s] at approximately 50% of its maximum power. This was regarded as more than adequate for the envisaged tests.

2.2.3 Turbine Conceptual Design

In the conceptual design stage of the turbine model a number of defining geometric quantities - such as the rotor diameter D_T, the number of blades n, the blade chord c, the rotor solidity σ, the hub/tip ratio h and the blade profile- and operational parameters -such as the design RPM, the tip speed ratio Λ, tip Mach number Ma_t and the blade Reynolds number- needed to be decided upon in order to arrive at a suitable turbine configuration and turbine operation that allowed all experimental aims to be achieved. Since these geometric and performance parameters are interrelated and they needed to be harmonised in trade-off studies. Generally, the configurational design aimed to produce a rotor lay-out and turbine operational characteristics that were typical for the prototype machines currently being researched by other institutes (eg. the shoreline OWC device at Islay run by Queens University, Belfast).

The rotor diameter was chosen to be compatible with the cross sectional dimensions of a number of low-speed wind tunnel test sections of the Aeronautics department of Imperial College. In the design process diameters between 0.50 [m] and 1.50 [m] were considered to be realistic. From a survey of published Wells turbine model scale performance data it was apparent that typical operational values of Λ for OWC devices range between approximately 10 and 3. Allowance was made for the fact that in the current experiment Λ values of less than 3 possibly needed to be achieved in order to comprehensively illustrate any anticipated stall delay effects in the blade root region.

In an effort to promote stable interactions between the tunnel blower performance and the turbine operation it was decided to run the rotor at constant RPM throughout the tests so that the required variation of Λ was achieved by adjusting the wind speed generated by the tunnel blower. Subsequent design

iterations which compromised the value of RPM, D_T and design wind speed V_x ensured that at the highest values of Λ the tip Mach number was incompressible. Further, the RPM was chosen so that at the lowest design Λ the required wind speed was not excessive, thereby avoiding extreme demands on the available tunnel blower power. At the highest values of Λ the required tunnel speed was to be well within the stable range of the tunnel blower control.

Since it was intended to vary σ during the experiments by changing the number of rotor blades a possibly large number of blades seemed desirable, which would allow σ to be adjusted within a sensible range. The maximum number of blades and the blade chord were, eventually, also chosen to produce model rotor geometries that were typical for current prototype Wells turbines. In order to maximise the test Reynolds number for the chosen design RPM a large blade chord was favoured. Also, on a more practical level, this design choice enabled a greater number of pressure tappings to be installed on the instrumented blade.

The NACA0015 section was chosen as the blade profile, since its two dimensional characteristics have been extensively documented over a wide range of Reynolds numbers in computational and experimental studies and its aerodynamic behaviour is, therefore, well understood. In particular, this profile was chosen because it is used in the Wells turbine rotor of the Islay wave power device.
Summarised below are the main geometric and operational parameters which define the model mono plane Wells turbine and its design performance in the experiment.

Turbine Geometry:

turbine diameter D_t:	740.00 [mm]
blade profile:	NACA0015
blade chord c:	120.00 [mm]
hub/tip ratio h:	0.560/0.650
number of blades n:	2 / 4 / 8
tip clearance:	nom. 3 [mm]

n	h	σ_t	σ
8	0.560	0.412	0.529
	0.650		0.500
4	0.560	0.206	0.264
	0.650		0.250
2	0.560	0.103	0.132
	0.650		0.132

where $\sigma_t = (nc)/(\pi D_t)$ and $\sigma = (nc)/[\pi r_{tip}(1 + h)]$

Performance/Operation:

RPM = 1200 = constant
TSR_{min}= 3
TSR_{max}= 10
$V_{X min}$= 4.5 $[m/s]$
$V_{X max}$= 15 $[m/s]$

2.2.4 Turbine Control

The turbine needed to be controllable over the full range of experimental tip speed ratios. On the one hand, this required the turbine to be driven, when the power extracted from the airflow was insufficient to sustain rotation at design RPM. However, when the turbine was operating at high efficiency the shaft power produced was potentially such that, if left uncontrolled, the turbine may have tended to accelerate beyond the design RPM. To prevent this so called turbine 'run-away' a method of braking the turbine was required.

In previous experimental work by Graham and Brown (1991) carried out in the Aeronautics department of Imperial College a 3 [hp] controllable dc- electric motor, the maximum output shaft RPM of which was reduced to 400 by a 4/1 ratio gear box was used to drive a 2.5 [m] diameter wind turbine rotor at 200 RPM. It was found in the course of this work that the inherent gear box resistance provided adequate protection against over speeding for most wind speeds at which the turbine was tested. By introducing a 1/3 gearing this motor could be used to provide driving power to the Wells turbine at the design RPM of 1200 and also provide some means of controlling potential over speeding. The maximum shaft power estimated for the Wells turbine model was found to be similar to that extracted by the wind turbine model rotor in the experiments conducted by Graham and Brown. Though, this suggested that the gear box resistance would suffice as a control mechanism, a LUCAS 12-V car alternator, by means of which regenerative braking could be exercised was incorporated in the turbine design as an independent control device.

2.2.5 Mechanical Design And Manufacture

Generally, the mechanical design process was driven by requirements of structural strength, component accessibility for purpose of configurational modifications during testing, ease of manufacture/assembly and low cost. Figure (2.3) shows the general arrangement of the main mechanical turbine components.

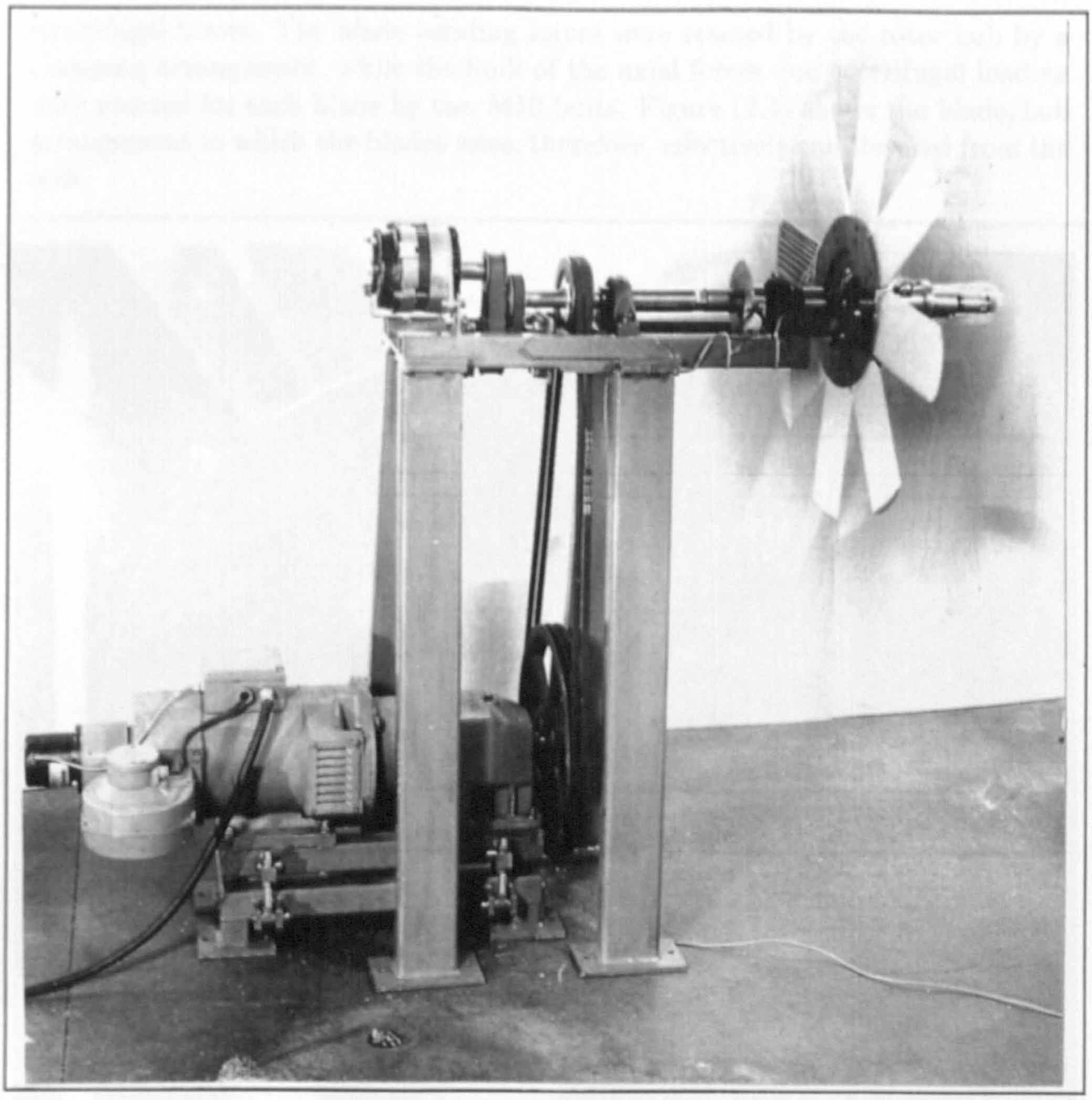

Figure 2.3: Turbine Component General Arrangement

The main structural frame was designed in steel with support legs which are bolted directly to the floor of the test laboratory to uncouple the turbine mechanically from any vibrations of the tunnel itself. Since the drive motor would not fit inside the turbine nacelle it was mounted beneath the turbine and the tunnel test section on a separate support frame and was connected to the turbine drive shaft via a 3/1 belt drive system. The 30 [mm] diameter steel drive shaft was stressed for whirling and a worst case quasi static loading resulting from imbalanced radial forces which would occur in the case of a sudden blade fracture at maximum RPM. The turbine blades where stressed for bending forces which were estimated from a blade element computation and for the significantly greater

centrifugal forces. The blade bending forces were reacted by the rotor hub by a clamping arrangement, while the bulk of the axial forces due centrifugal loading were reacted for each blade by two M10 bolts. Figure (2.4) shows the blade/hub arrangement in which the blades were, therefore, effectively cantilevered from the root.

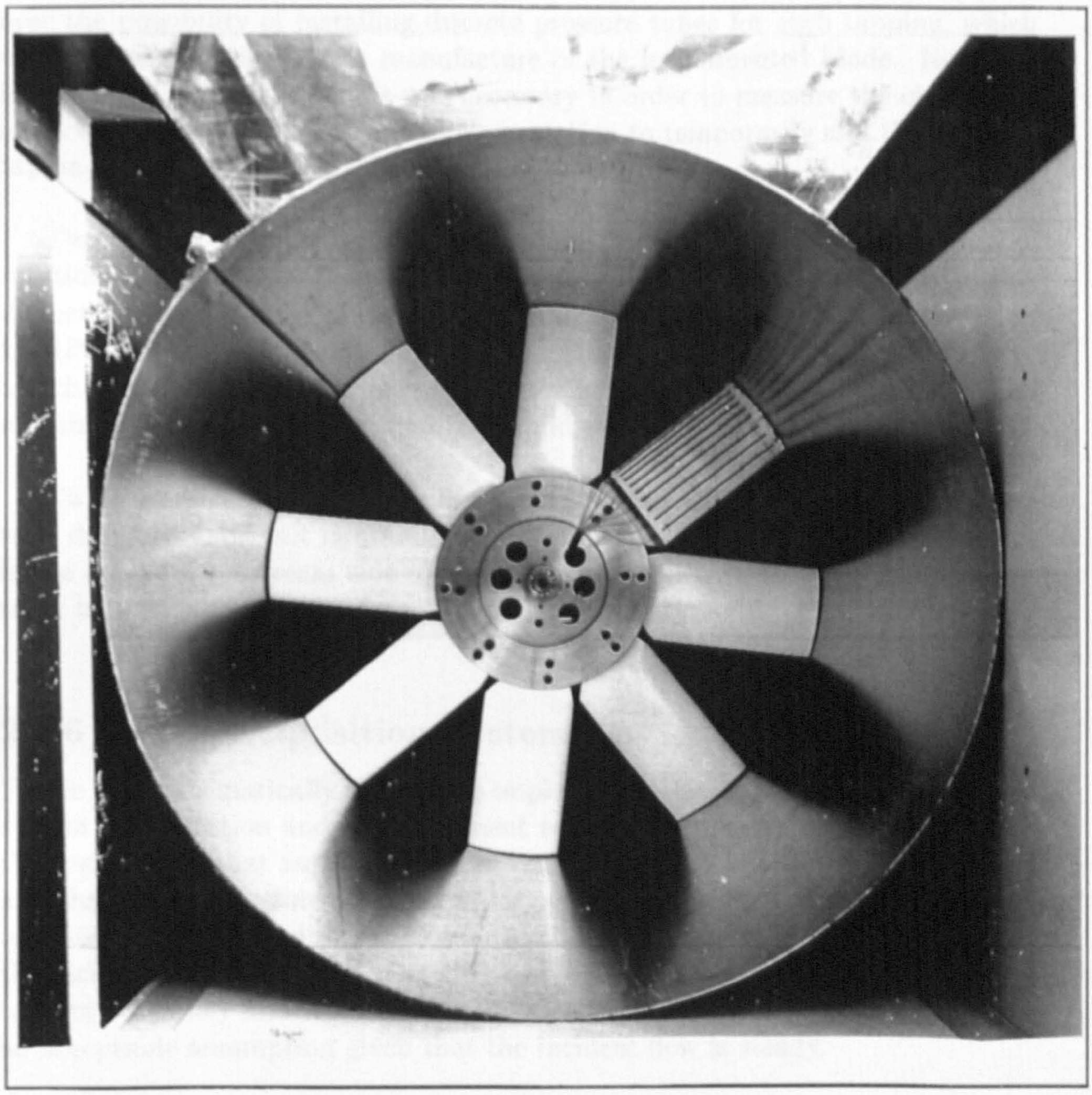

Figure 2.4: Blade / Hub Arrangement

The blades were designed to be lightweight and were constructed for stiffness with a GFRP skin and a tapered CFRP spar which was bonded to the skin directly. Using two female GFRP half-moulds, which were shaped from a wooden master blade, the upper and lower blade surfaces were manufactured separately and were subsequently bonded together at the leading and trailing

edges. One of the blades had 20 copper tubes of 0.145 [in] diameter, which were embedded in the GFRP skin during the lay-up process at specified chord wise positions. Subsequent to the curing process the copper tubes were visible through the transparent polyester resin and static surface pressure tappings were drilled at 6 radial stations. This arrangement for the pressure tappings was favoured over the possibility of installing discrete pressure tubes for each tapping, which would have complicated the manufacture of the instrumented blade. However, in this tapping arrangement it was necessary in order to measure the chord wise surface pressure at only one radial blade station to temporarily seal the pressure tappings at all other radial positions.

Two nose cones which were half-ellipsoids in cross section along the axis of rotation and which had a 0.48 [m] and a 0.42 [m] diameter respectively giving diameter to length ratios D_h/L_h of 1.1 and 0.9 were designed and constructed in GFRP. A wooden attachment ring was designed via which the nose cones were attached to the metal rotor hub. The rotor hub was designed in detail for CNC machining and was manufactured from mild steel.

Two cylindrical nacelles equal in diameter to that of the respective nose cones were designed and built in aluminium. They were attached to the main turbine frame on the downstream side of the rotor leaving a clearance gap between the rotor hub and the nacelle edges of nominally 3 [mm].

2.2.6 Data Acquisition System

Figure (2.5) schematically depicts the implemented data acquisition system. The system configuration and the equipment selection were crucially determined by the assumption that surface pressures on the rotating blade were quasi-steady and that, therefore, time-averaged static pressure measurements meaningfully illustrate local flow conditions. Similar model-scale wind tunnel studies in which the incident flow speed was controlled have been carried out for wind turbine rotors (eg. Barnsley and Wellicome (1989)) and have shown that this is, generally, an acceptable assumption given that the incident flow is steady.

The hub mounted pressure scanning system comprised of a 48-port scanivalve and a RDP electronics MLP 75 [mbar] differential pressure transducer, which has a specified repeatable linearity of +/- 0.25 %, a gain temperature coefficient of +/- 0.002% per degree C and a frequency response of 150 [Hz]. The scanivalve was triggered externally by a 5 [V] pulse generated by a computer driven controller and acted as a pneumatic multiplexer transmitting incident blade surface pressures to the pressure transducer. A support arrangement was designed and manufactured to allow the scanivalve and the pressure transducer to be mounted

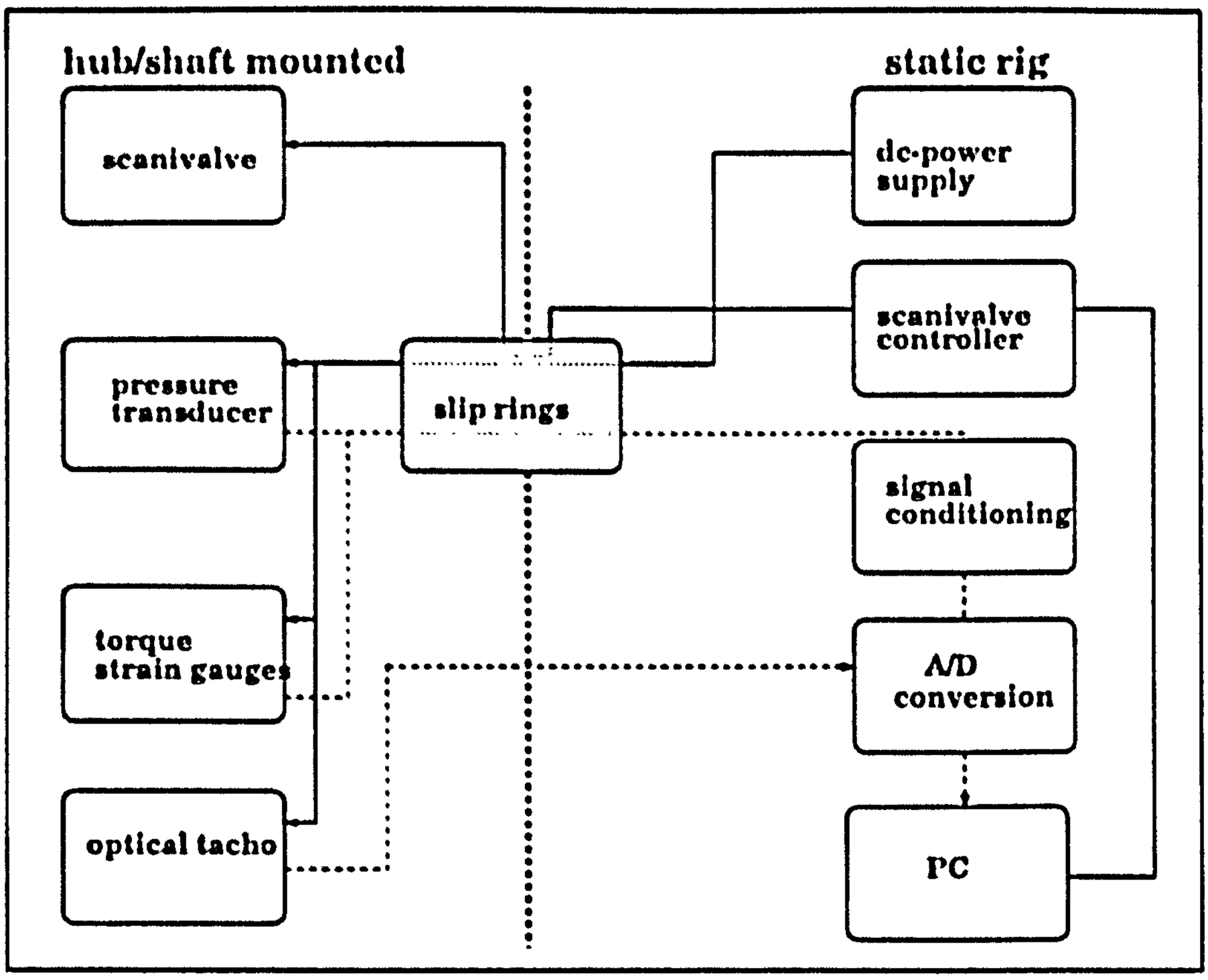

Figure 2.5: Data Acquisition System

on the rotor hub in line with the rotational axis so that they were not subjected to any centrifugal loading. Care was taken in the design of this mounting arrangement that the resultant orientation of the transducer membrane was perpendicular to the axis of rotation as a result of which there was no transducer output due to any forces other than those acting due to the transmitted pressure. Figure (2.6) shows the general arrangement of the pressure scanning system.

The +/- 15[V] dc power supply and the discrete 5 [V] trigger pulse required for operating the pressure transducer and the scanivalve were transmitted to the rotating hub through an IDM R/B08-20 silver plated 8 channel slip ring/brush assembly. The low noise performance of this slip ring system, specified by the manufacturers as nominally 60 [μ V] per [mA] current at 10.000 RPM allowed the transducer output to be passed through the slip rings without significant distortion of the means signal. The use of the slip rings for all required input/output signals and power supply transmissions to and from the rotating hub meant that the number of hub-mounted components was kept to a minimum and that all signal conditioning was performed using standard laboratory equipment on a static test rig. As a result, the achieved system reliability was extremely high throughout the experimental work and required no further maintenance or calibration

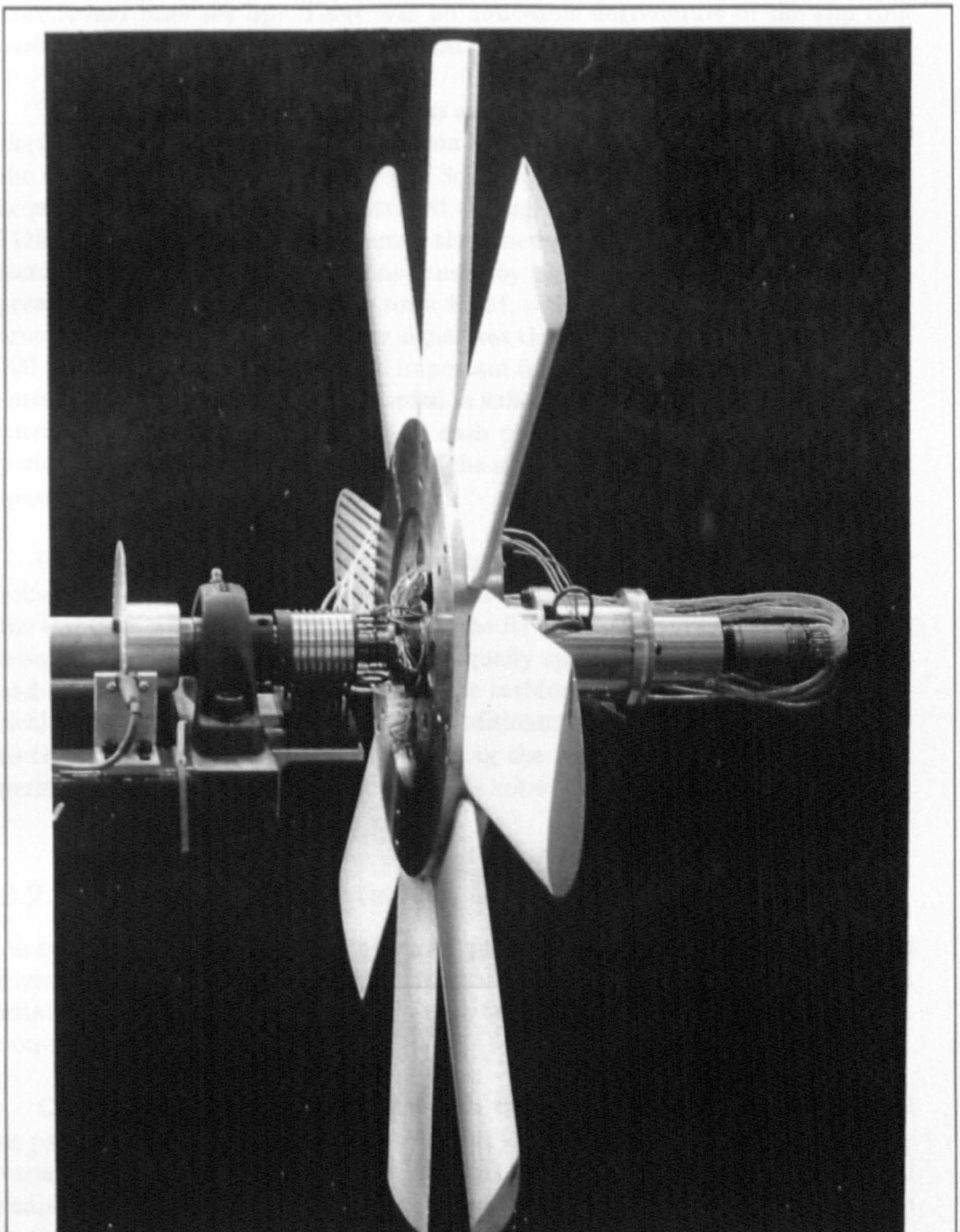

Figure 2.6: The Instrumented Rotor

once it had been set up. There was no noticeable degradation of the slip ring performance due to wear over the period of testing.

The analogue transducer output was amplified at gains of up to 50, filtered for electrical noise and digitally recorded on a Dell 386-PC. The A/D conversion of the filtered signal was performed by a Scientific Solutions Inc. 'Labmaster' data acquisition board which was controlled through the PC using specially written FORTRAN routines. It was assumed that the highest frequencies of any significant transducer signal fluctuations caused by unsteadiness in the blade surface pressures would be related to the rotor RPM, which in the tests was constant at around 13-15 [Hz]. The transducer signal was thus recorded at a sampling rate of 100 [Hz] in order to ensure that all important features of the instantaneous blade surface pressure variation were recorded in sufficient detail. Typically, in the tests carried out the transducer output for each pressure tapping was recorded for a period of 5 [sec], so that 500 readings of the instantaneous blade surface pressures were recorded.

For the measurement of the turbine shaft RPM and hence the blade angular velocity an optical tacho was installed that generated a sequence of $4[V]$ pulses the length of which was in proportion to the RPM. The tacho consisted of a shaft mounted rotary disc that had 50 holes equally spaced around its circumference and a static optical device attached to the turbine frame. The output of the optical tacho required no further signal conditioning and was transmitted directly to the A/D conversion board. By counting the number of pulses over a known period of time the pulse frequency and the rotor RPM were deduced.

2.2.7 Experimental Method

As stated in the introduction to this chapter the main aim of the experimental investigation was to establish the radial variation of the stall characteristics of a rotating NACA0015 sectioned Wells turbine blade and compare it to those of a non-rotating blade.

On an aerofoil section or finite AR wing the stall, which is associated with full or partial separation of the boundary layer, is usually studied in terms of the C_L variation with flow incidence α. In particular, the stall for conventional aerofoil shapes such as NACA0015 is usually identified by the occurrence of a maximum in the C_L vs. α curve and a rapid rise in the drag coefficient C_D.

The study of the stall of the rotating blade, therefore, required the measurement of C_L and C_D over a range of incidences. These force coefficients are related to the local tangential C_T and normal force coefficients C_N through α by

equations (2.1) and (2.2) .

$$C_L = C_N sin\alpha - C_T cos\alpha \tag{2.1}$$

$$C_D = C_N cos\alpha - C_T sin\alpha \tag{2.2}$$

C_T and C_N may be obtained from the chord wise Cp distributions by integral equations, which are given below in their finite difference form for a trapezium rule integration:

$$C_N = -0.5 \sum_{n=1}^{ntaps} (Cp_{n+1} + Cp_n)(x_{n+1} - x_n) \tag{2.3}$$

$$C_T = -0.5 \sum_{n=1}^{ntaps} (Cp_{n+1} + Cp_n)(y_{n+1} - y_n) \tag{2.4}$$

where *ntaps* is the number of pressure tappings and x, y are the coordinates of the blade surface pressure tappings in a blade frame of reference.

It is important to note that C_D estimated from the static surface pressures does not account for the component of drag which is due to surface friction. Therefore, the derived C_D values are not really expected to be a quantitatively satisfactory measure of the profile drag coefficient until there are large flow separations.

The experimental error inherent in this method of deriving the local force coefficients is to a large extent dependent on the number of pressure taps as well as their location. In particular, failure to record the peak suction pressure Cp_{min} close to the leading edge may lead to appreciable underestimation of C_L. The values of C_D are also very sensitive to the trailing edge pressure, which was not recorded in the experiment because of the impracticality of fitting pressure taps into the very thin trailing edge of the blade. As a compromise, in the numerical integration the trailing edge Cp was artificially set to a value midway between the values recorded for the rear most taps on the upper and lower blade surfaces.

The sectional characteristics of the static turbine blade, in contrast to which the aerodynamic behaviour of the rotating blade was to be studied were measured experimentally using the actual turbine blade in a static arrangement. This data provided a more valid basis for comparison than published NACA0015 aerofoil data resulting from numerical or experimental studies.

It was shown earlier that for a blade section located at a radial distance r from the axis of rotation the local 'geometric' incidence α is related to the axial inlet velocity V_x and the tangential velocity $U_t = \Omega r$, incident on the rotating blade by $tan\alpha = V_x/U_t$. The geometric incidence α was therefore determined

according to the above expression from direct measurements of mean values for V_x ahead of the turbine rotor and U_t.

However, the effective incidence α_e seen by the blade must include the effect of the swirl velocity v_s which acts in the circumferential direction and is induced in the plane of the blade rotation by the rotor wake and any induced changes in axial velocity. The variation of the induced axial velocities and the constraints to which this is subject has already been discussed in the introduction chapter. As pointed out earlier in the report, the main effect of the v_s is to reduce α so that the blade sees an effective effective incidence α_e. Some theoretical analysis was also given earlier which related v_s to C_L and (c/r) and the downstream variation of v_s was briefly discussed. The swirl effect is difficult to quantify without conducting an extensive experimental investigation due to the complexity of the rotor wake structure. Nevertheless, subsequent to the basic pressure measurements on the rotating blade, some attempts were made to experimentally measure v_s to establish the importance of swirl to the pressure measurements. These experiments are discussed separately later.

The dynamic head of the incident flow was measured using a pitot-static probe,

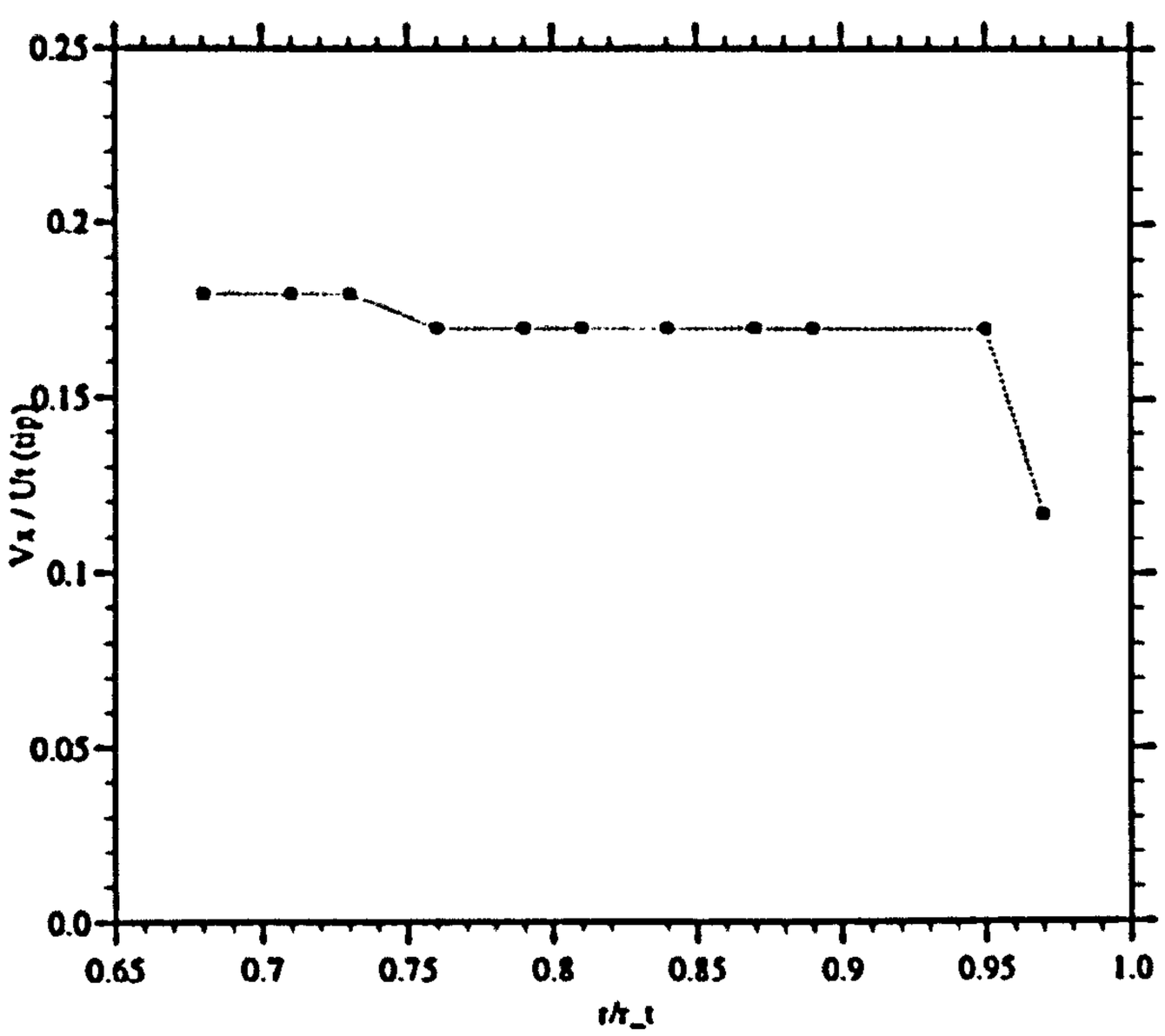

Figure 2.7: Axial Inflow Velocity Profile

which was placed approximately 4 blade chord lengths upstream of the rotor at the inlet of the turbine duct. The output of the probe was read on a Betz manometer and was calibrated against the contraction pressure drop over a range

of flow rates. The calibration was carried out for rotor configurations comprising 0, 2, 4 and 8 blades, which ascertained that the reading was not influenced by the local blade circulation. V_x was deduced from the probe reading by assuming continuity of mass flows between the duct and the rotor annulus. Figure (2.7) illustrates the radial variation of $V_x/U_t(tip)$ measured ahead of the 8 bladed rotor using a pitot-static tube. The rotor was operating at a nominal tip speed ratio of 5.9 and it can be seen that except near the tip the flow is approximately uniform. It can be noted from this figure that closer to the rotating hub ($r/r_t = 0.650$) the values of $V_x/U_t(tip)$ are increased by approximately 5 %. This increase may relate to the rotating boundary layer of the rotor hub. U_t was deduced directly for a given radial location r from a measurement of Ω.

The blade surface pressures p_{blade} were measured sequentially using the scanivalve/differential pressure transducer arrangement, mounted centrally on the rotating hub. The reference pressure port of the transducer was left unconnected, so that all pressures were measured relative to the ambient pressure inside the nose cone during testing ie. $\Delta p = p_{blade} - p_{cone}$. It should be realised that the choice of reference pressure does not affect the derived values for C_L and C_D. In any case, an attempt was made to approximately measure p_{cone} by placing a pressure tube close to the open rear face of the rotating hub inside the turbine nacelle. A differential pressure was formulated to the static pressure just ahead of the rotor, which was measured by static pressure tappings in the duct wall. This differential pressure $\Delta p_2 = p_{cone} - p_{stat}$ was added to Δp. In this way p_{blade} was nominally referenced to the free stream static pressure, which allowed a definition of the pressure coefficient Cp, which is compatible with that for the static blade tests: $Cp = (p_{blade} - p_{stat})/(1/2\rho V^2)$.

As pointed out by Graham and Brown (1991) the pressure sensed by the transducer in this arrangement consists actually of two components. One of these is due to the blade static surface pressure p_{blade} while the other is of opposite sign and is due to the centrifugal pressure p_z acting on the column of air in the pressure tube connecting the blade tapping and the transducer port. It can be shown that $p_z = (1/2)\rho(\Omega(r-r_0))^2$, where r is the radial distance of the pressure tap from the centre of rotation and r_0 is that of the transducer. For the chosen experimental set up r_0 was nominally zero, so that, in this case, p_z is approximately equal to the local dynamic head. In the experiment p_z was calculated for each radial station and added to p_{blade} before formulating the blade surface pressure coefficient Cp as

$$Cp = \frac{(\Delta p + \Delta p_2 + p_z)}{1/2\rho V^2} \tag{2.5}$$

2.2.8 Sequence of Measurements

Before each measurement the pressure taps at all radial stations were covered using chord wise continuous 19 [mm] wide strips of sello tape, which was 0.0635 [mm] in thickness. Leak tests, which confirmed that all taps had been adequately sealed, were performed by spinning the rotor at 800 RPM in a nominal axial air stream and recording the transducer output for all taps. Subsequently, the tape was removed at the radial station at which flow measurements were to be carried out.

When all pre-test checks of the turbine apparatus and measurement system had been completed the turbine was run up to operational RPM with the tunnel blower switched off. The tunnel was then activated and a low wind speed was set. The pressure drop across the tunnel contraction and the dynamic head measured by the pitot-static probe in side the rotor duct were monitored to judge when incident flow conditions had settled.

Once the tunnel conditions were stable the scanivalve was homed and a zero differential pressure reading was taken from the pressure transducer. The airflow temperature in the tunnel contraction and the ambient pressure in the laboratory were recorded and used to compute the density of the airflow. When the rotor RPM and the dynamic head of the airflow in the duct had been recorded the pressure measurement was initiated and was controlled by specially written FORTRAN 77 software, which operated in conjunction with the 'Labmaster' hardware.

For each pressure tap the gain of the pressure transducer output amplification was adjusted to give the highest possible signal within the +/- 10 [V] range acceptable to the A/D hardware in order to optimise the sensitivity of the pressure measurement. At the end of the pressure scan further reference readings of the zero differential pressure transducer output p_0 were taken to allow any drift of experimental conditions to be accounted for.

The above testing sequence was repeated without stopping the turbine which ran at constant RPM during a particular set of pressure measurements for discrete increases in wind speed. By increasing the wind speed in subsequent pressure scans the turbine tip speed ratio was progressively reduced and the blades were gradually taken into the stalled flow regime. When the highest wind speed setting had been reached it was gradually reduced in successive measurements, which aimed to establish any stall hysteresis effects.

2.2.9 Data Analysis

A number of FORTRAN 77 routines were written to handle all primary data analysis at the end of each individual pressure scan were incorporated into the data acquisition program which was run on a Dell-386 PC in conjunction with the Scientific Solutions Ltd. 'Labmaster' A/D conversion hardware.

On the assumption that the electrical drift of the transducer signal varied linearly between the beginning and the end of a particular pressure scan, the code formulated an average value for the p_0 readings taken before and after each pressure scan. From the measured instantaneous transducer outputs mean voltages were calculated for each pressure tapping.

The measured transducer calibration factors were applied by the data analysis code which included the averaged values of p_0 as an offset voltage to obtain the measured surface pressures p_{blade} in [mbar]. Further, p_s was calculated from the measured rotor RPM and Cp values were formulated according to equation(2.5) above and saved as an ASCII data file .

From the derived Cp values and the tapping coordinates the local normal and tangential force coefficient C_N and C_T were computed by numerical integration according to equations (2.3) and (2.4) and written to an ASCII data file.

2.3 Results

2.3.1 Pressure Measurements on The Static Blade

The turbine blade was tested in a static arrangement in the 3 [ft] x 2 [ft] rectangular test section of one of the closed circuit wind tunnels of the Imperial College Aeronautics department. The tests were carried out at a number of different Reynolds numbers $Re = (V_\infty c)/\mu$ ranging between 0.2e6 to 0.3e6. In order to avoid any 3-dimensionalities of the incident flow, which might have occurred due to non-uniform test section blockage posed by the low aspect ratio blade, a vertical dividing wall (end plate) was fixed in the test section close to the blade tip. This dividing wall extended approximately 4.5 blade chords upstream and downstream of the blade. The arrangement is schematised as an upstream view in figure (2.8) . While the blade surface pressures were measured at the mid span position for AOA between 0 degrees and 28 degrees using a multi-tube alcohol manometer, the blade AOA was measured with an inclinometer placed on the flat surface of the blade attachment. The data was not corrected for any blockage effects since these were estimated to be negligible due to the low blockage area

ratio of the blade ($c/h = 0.13$).

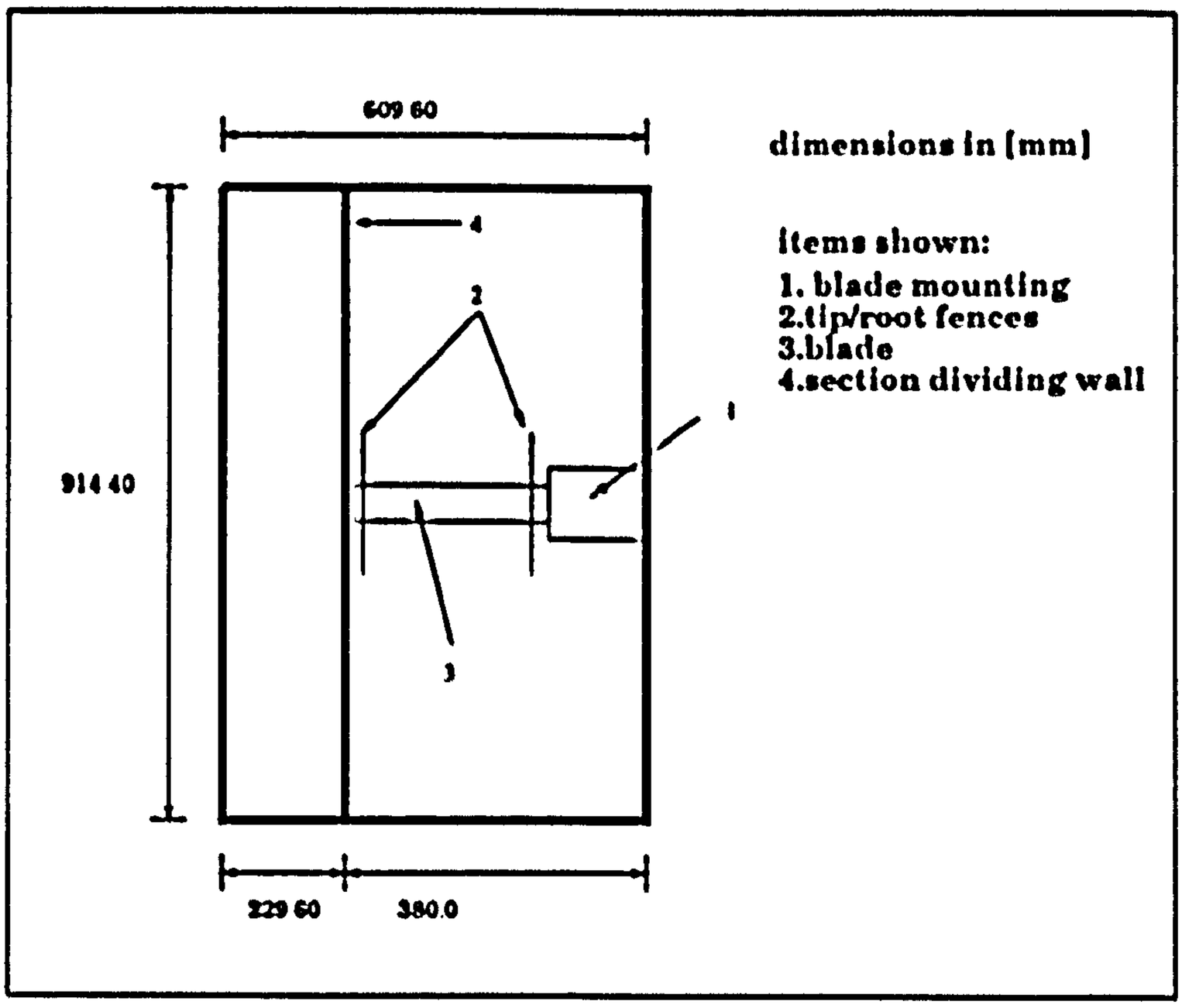

Figure 2.8: Static Blade Wind Tunnel Arrangement

Figure (2.9) compares the Cp distribution for $Re = 0.25e6$ measured at nominally 0 degrees AOA to the potential flow Cp distribution for a NACA0015 section given by Abott and von Doenhoff (1959). The evident differences are due to the boundary layer effects which are not accounted for in the inviscid potential flow result. There is an indication that the actual blade incidences are slightly less than zero degrees for the experimental data shown.

Figures (2.10)-(2.13) below show the measured variation of chord wise Cp distributions with AOA. These figures illustrate clearly the 'peaky' type pressure distributions, which are typical for the NACA0015 aerofoil section and which for high pre-stall AOA have a distinct minimum value Cp_{min} close to the leading edge in a very localised high suction region on the upper blade surface. At the tested Re the blade sections sustained fully attached flow up to nominally 12 degrees AOA for which approximately $\hat{Cp}_{min} = -3.4$. It is clear in figures (2.10) and (2.11) that for most AOA Cp_{min} and the leading edge stagnation pressure were not quite recorded with the chosen distribution of pressure taps. As a result, it may be expected that the C_L data derived from the measured Cp distributions underestimate the sectional blade lift.

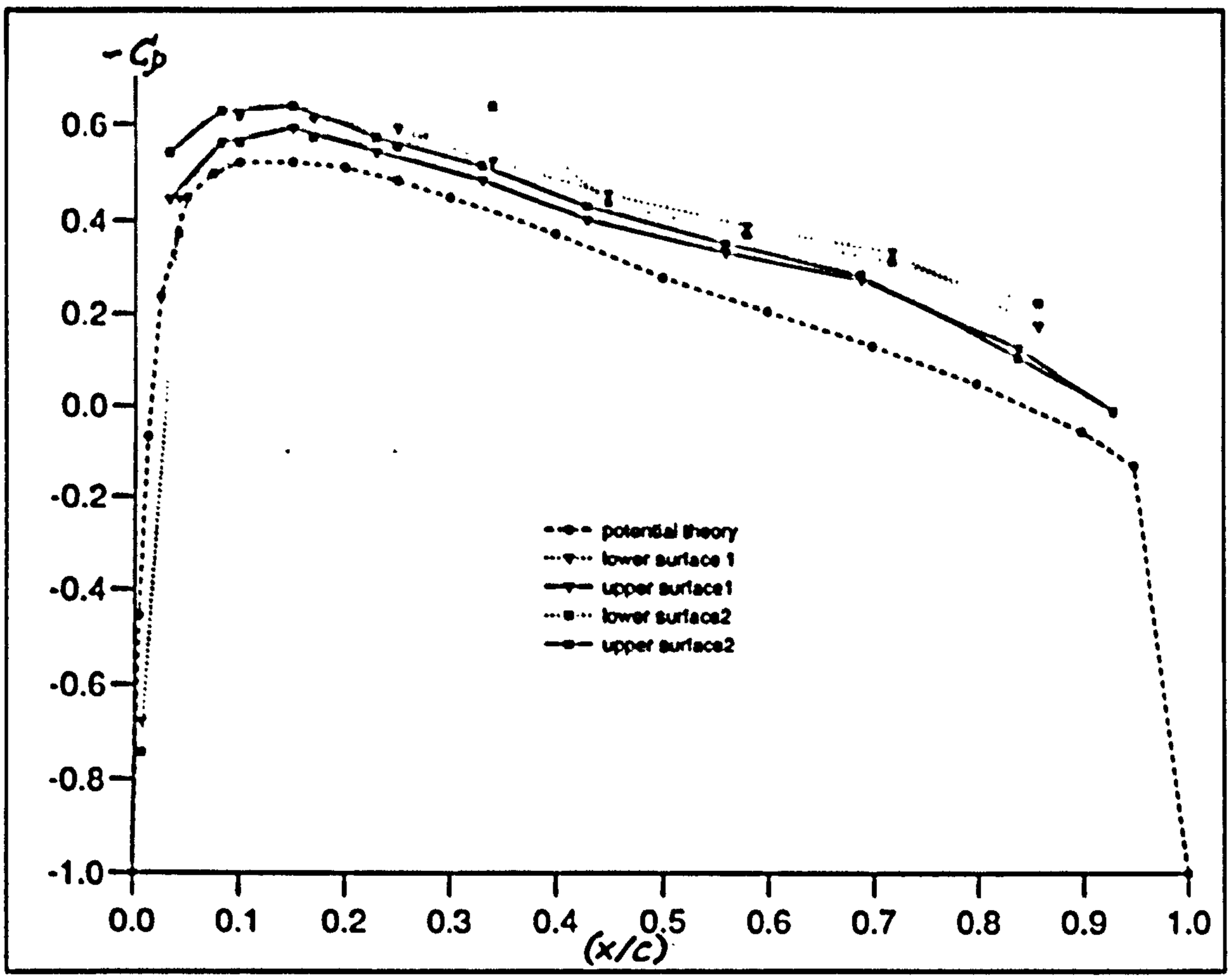

Figure 2.9: Zero Degrees Experimental And Potential Flow Cp-Distributions

Between 13 degrees and 14 degrees the blade suddenly stalled, which resulted in a region of near constant Cp over the entire upper surface and remains virtually unchanged for any further increases in AOA. This stall behaviour is symptomatic of a strong laminar leading edge separation, which would be expected for a NACA0015 section operating in the tested range of Re from published classical aerofoil theory and experimental data given by eg. Abott and v.Doenhoff. Though, it is apparent that the leading edge separation dominates at these Re, the Cp distributions suggest that, to a lesser extent, there is also some trailing edge stalling due to the thickening of the blade boundary layer.

Figures (2.14) and (2.15) show the variation of the sectional force coefficients C_L, C_D, C_T and C_N derived by integration of Cp according to equations (2.1) - (2.4) .

The lift curve slope $a_0 = \partial C_L/\partial\alpha$ indicated in figure (2.14) is 4.8$[/rad]$, which is somewhat lower than the theoretical value of 2π given by thin aerofoil theory. This may partly be explained from boundary layer effects, which for pre-stall AOA cause the C_L to be reduced from values given by potential theory. Further,

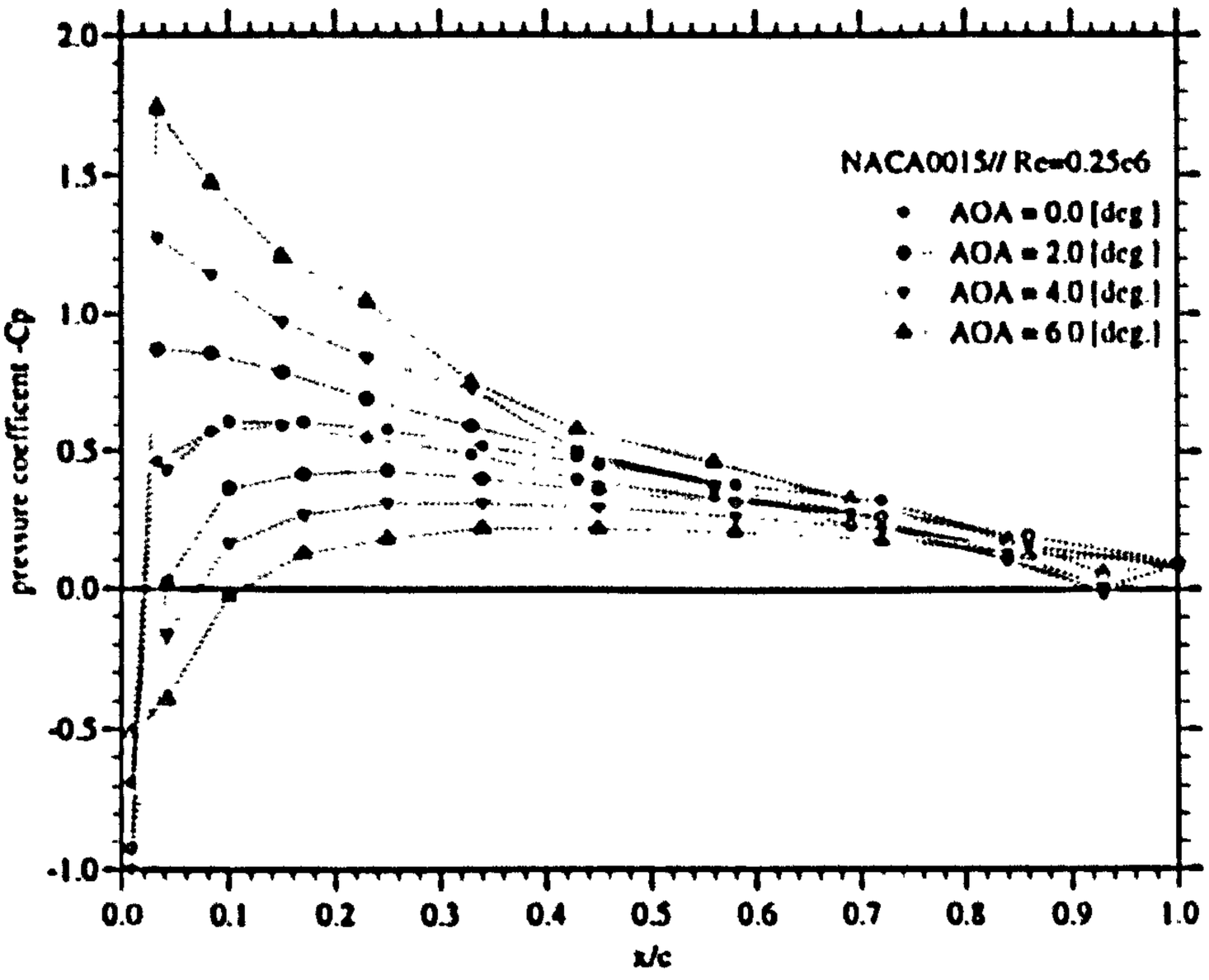

Figure 2.10: Static Blade Sectional Cp-Distribution

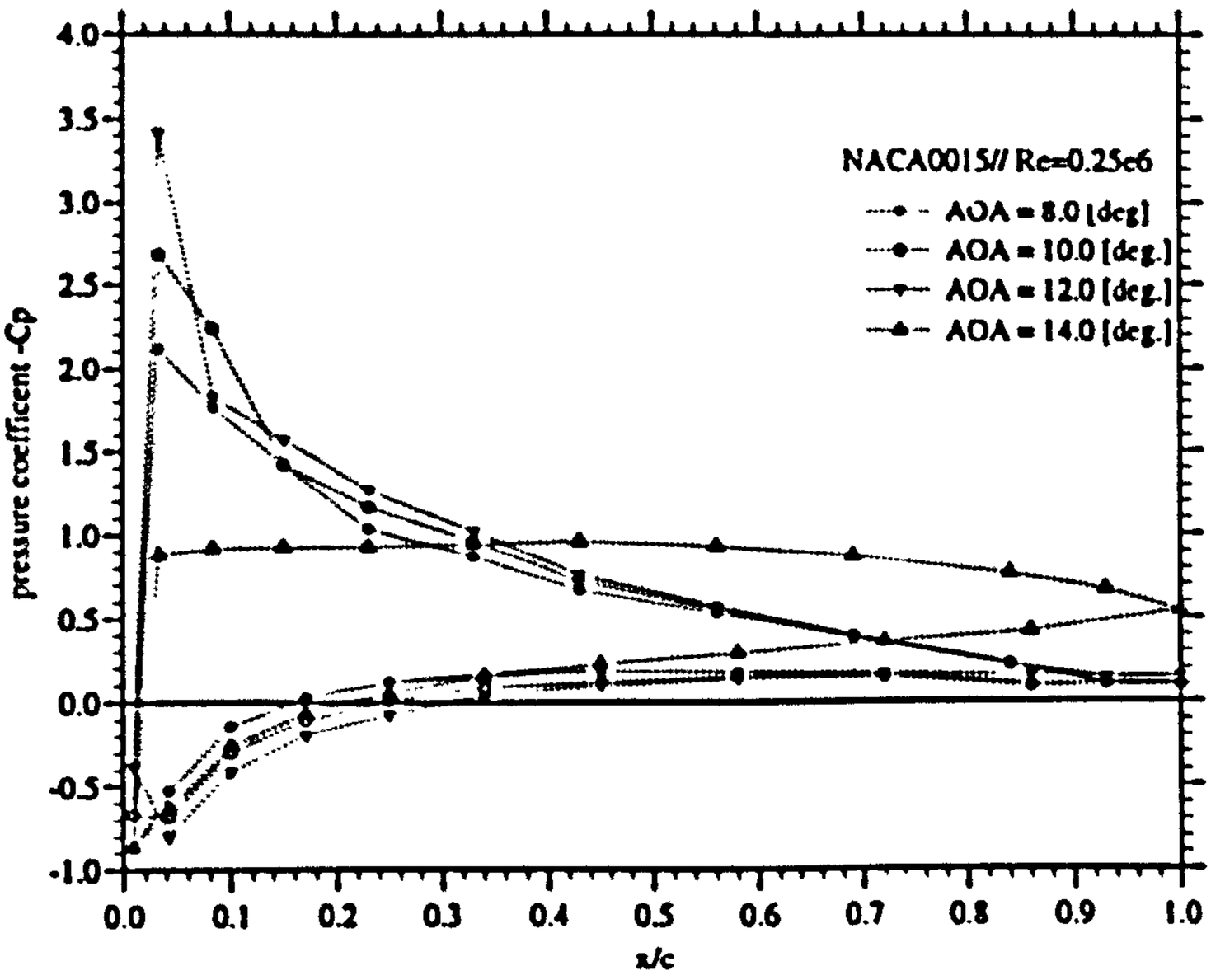

Figure 2.11: Static Blade Sectional Cp-Distribution

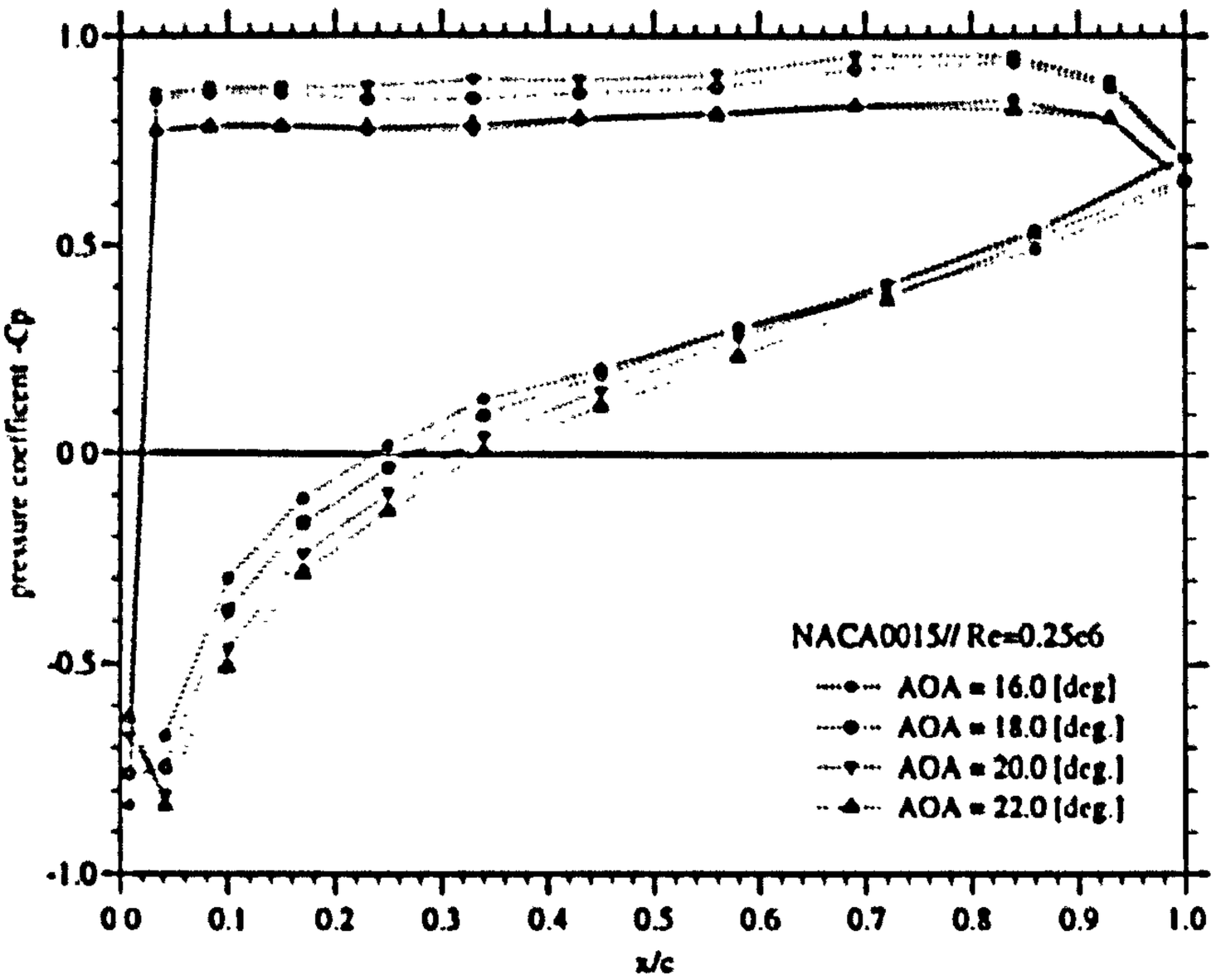

Figure 2.12: Static Blade Sectional Cp-Distribution

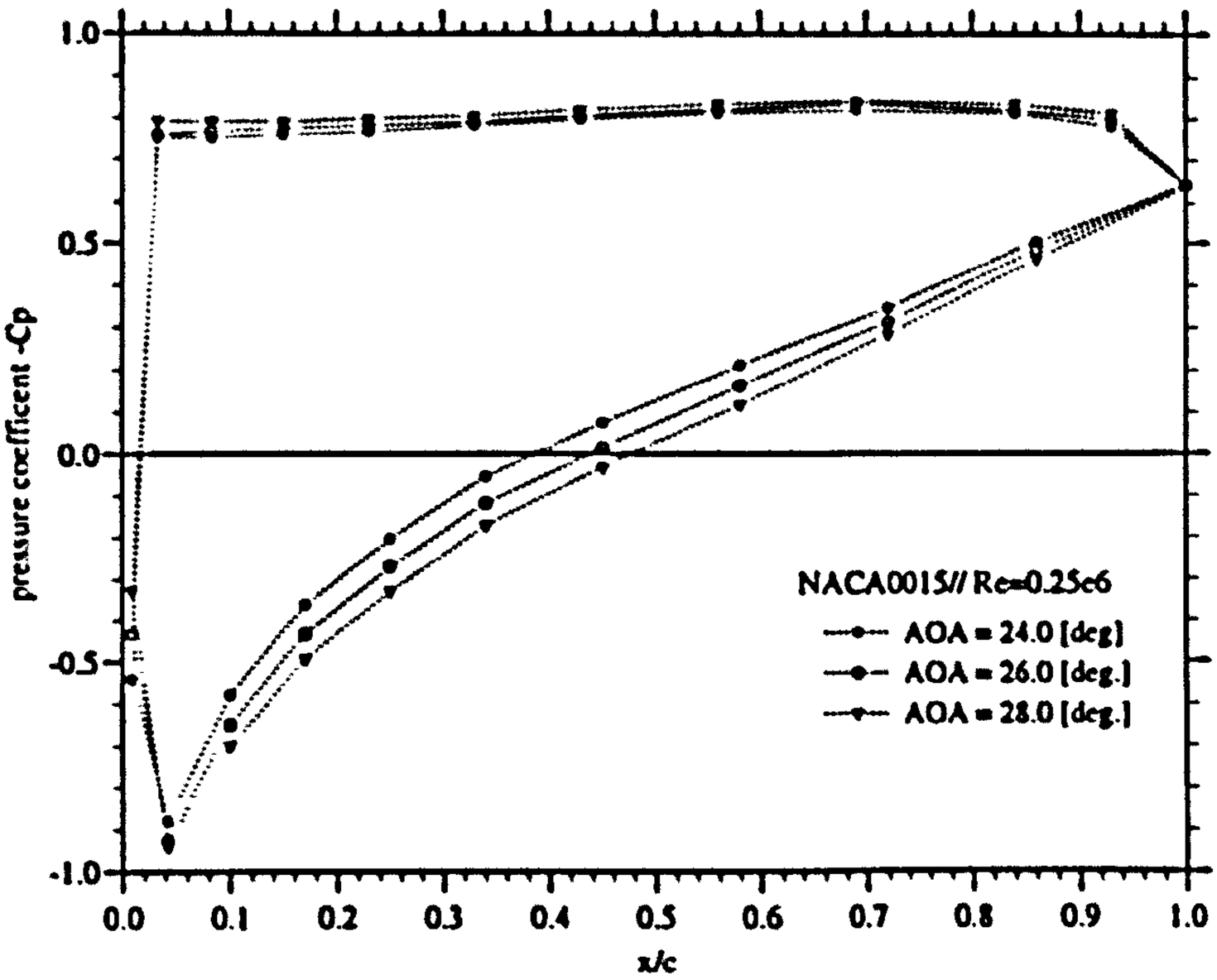

Figure 2.13: Static Blade Sectional Cp-Distribution

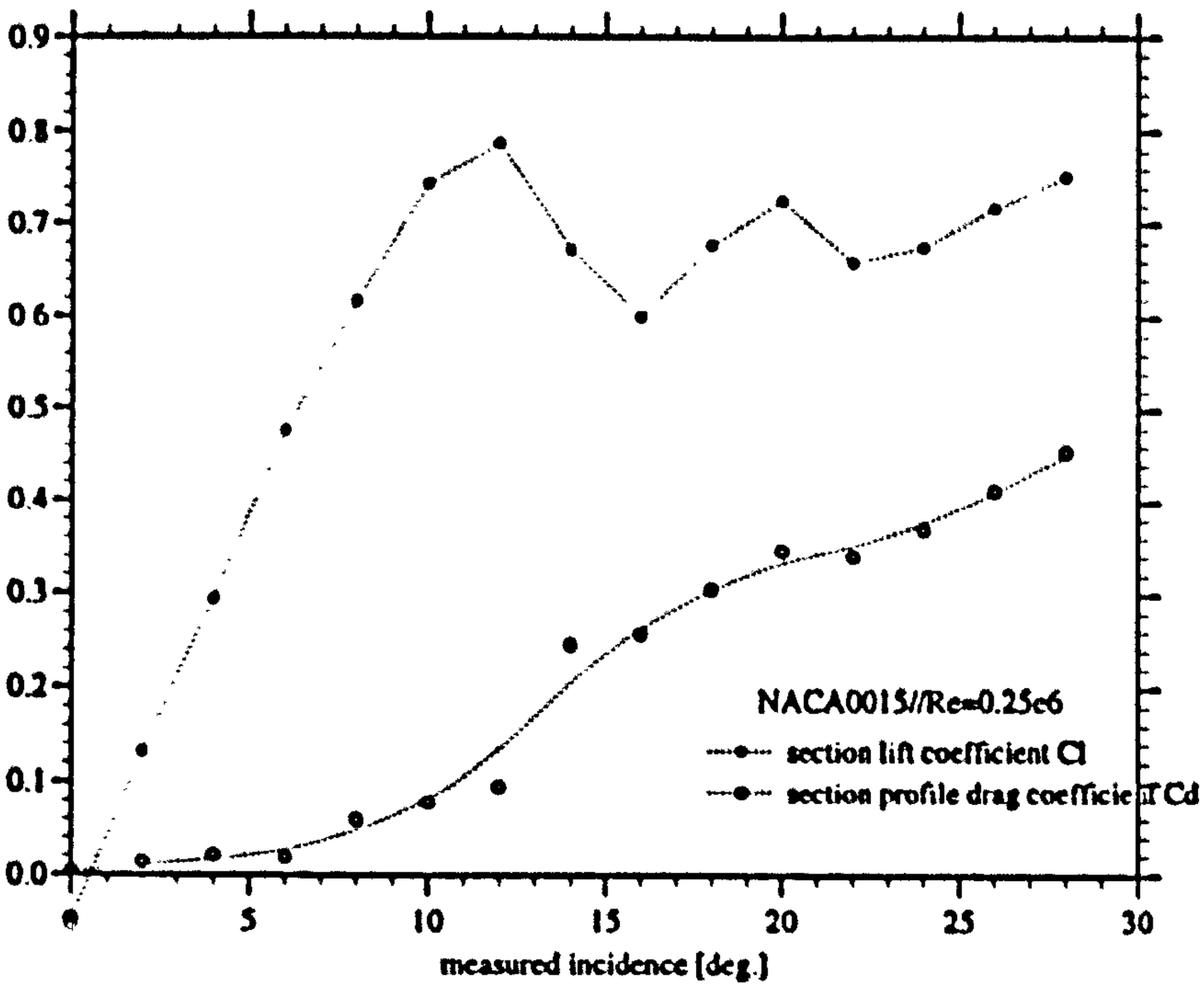

Figure 2.14: Measured Sectional C_L And C_D

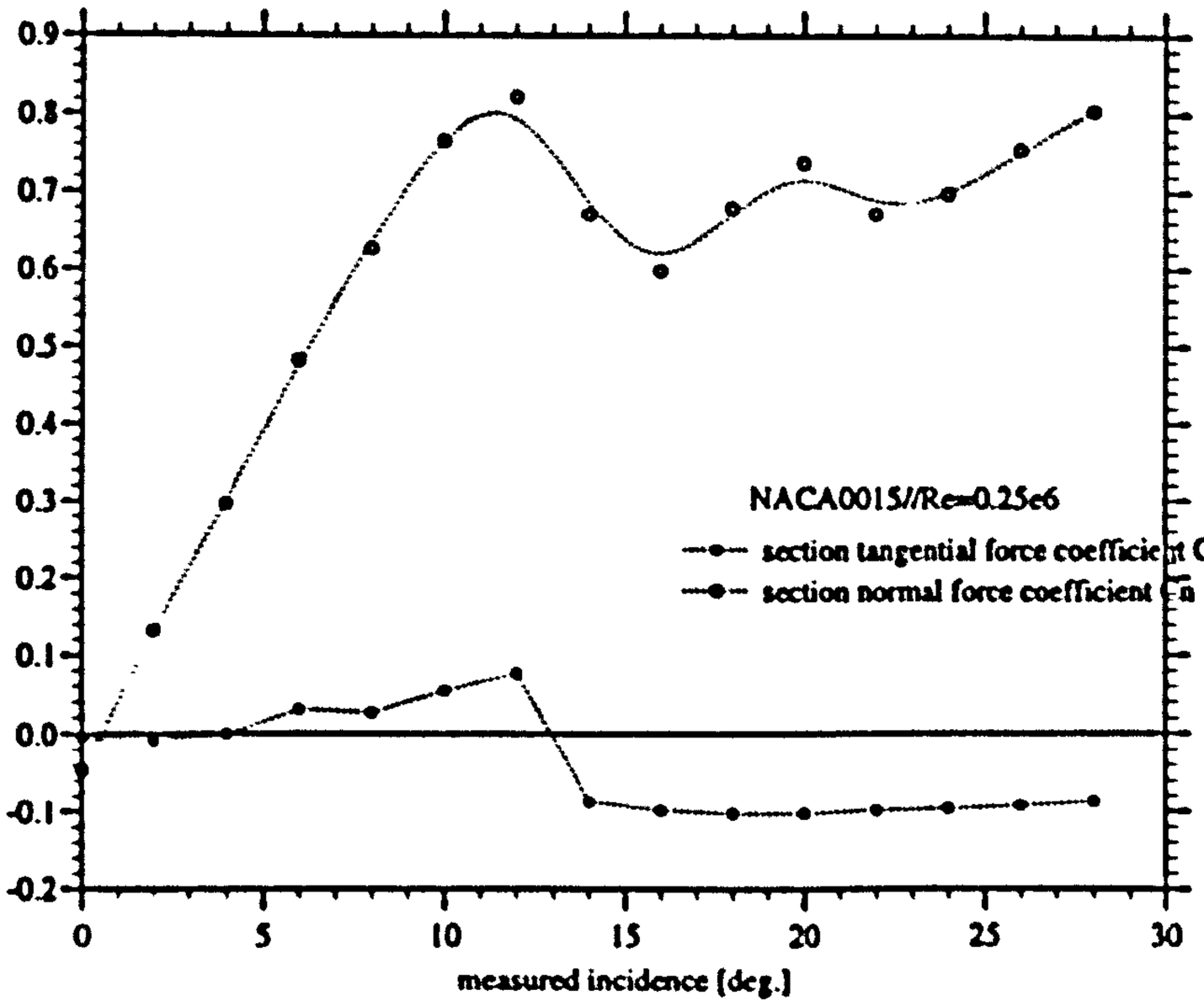

Figure 2.15: Measured Sectional C_T And C_N

as mentioned above, the experimentally deduced C_L values are expected to be low because of the failure to record Cp_{min}. However, experimental data given by Eastman (1937) revealed that, for Re less than approximately 0.4e6, a_0 is a strong function of Re and varies significantly from 2π. For Re between 0.2e5 and 0.4e6 this data suggests that for NACA0015 a_0 varies between approximately 5.2 $[/rad]$ and 4.9$[/rad]$. This is not too dissimilar to the values of a_0 recorded in the static blade measurements and gives some confidence in the data.

The maximum lift coefficient C_{Lmax} recorded at an AOA of 12 degrees is approximately 0.80 and, due to the effects discussed above, is slightly lower than given by the data of Eastman et al. From this C_{Lmax} would be expected to be around 0.90 to 1.00 for Re between 0.17e6 and 0.33e6 .

2.3.2 Rotating Blade Tests

On the whole, the experimental set-up was very successful and provided a high level of system reliability. Because the preliminary tunnel calibrations had shown that the wind tunnel blower could easily generate flow speeds in the test section which were in excess of the original design test speeds it was decided to run the rotor at a constant RPM of 800 rather than the intended 1200 RPM. When fitted with the larger of the two nose cones which were tested the levels of vibration due to force imbalance of the rotating masses were sufficiently low for the rotor to be run without any balancing masses. For the smaller nose cone, however, significant vibrations occurred at around 600 RPM. As a result, this rotor needed to be dynamically balanced using additional masses which were attached to the hub. Once balanced correctly the maximum RPM of 1200 could be achieved free of significant vibrations for this rotor configuration. However, for the pressure measurements it was run at 800 RPM to ensure that the Re were compatible between the measurements for the two nose cones.

Figure (2.16) shows the unamplified zero differential pressure transducer output measured at a sampling frequency f_{samp} of 100 [Hz] for an RPM of 800. This figure gives an indication of the electrical signal distortion due to the slip ring noise at this RPM. The maximum slip ring noise shown is of the order of +/- 300 [μ V] but on average is probably closer to +/- 150 [μ V] , which, as will be seen in the following, is small compared to the mean pressure transducer signals recorded in the experiments.

Figure (2.17) shows the pressure transducer signal fluctuations recorded at $f_{samp} = 100[Hz]$ for a single pressure tap located near the blade root and close to the leading edge on the downwind surface of the rotating blade for a number of AOA cases . The signal traces for all AOA cases contain high frequency fluctuations, which occur at a frequency corresponding to the rotor RPM of approximately 13 [Hz] . For the AOA cases shown up to the 16.40 degrees the

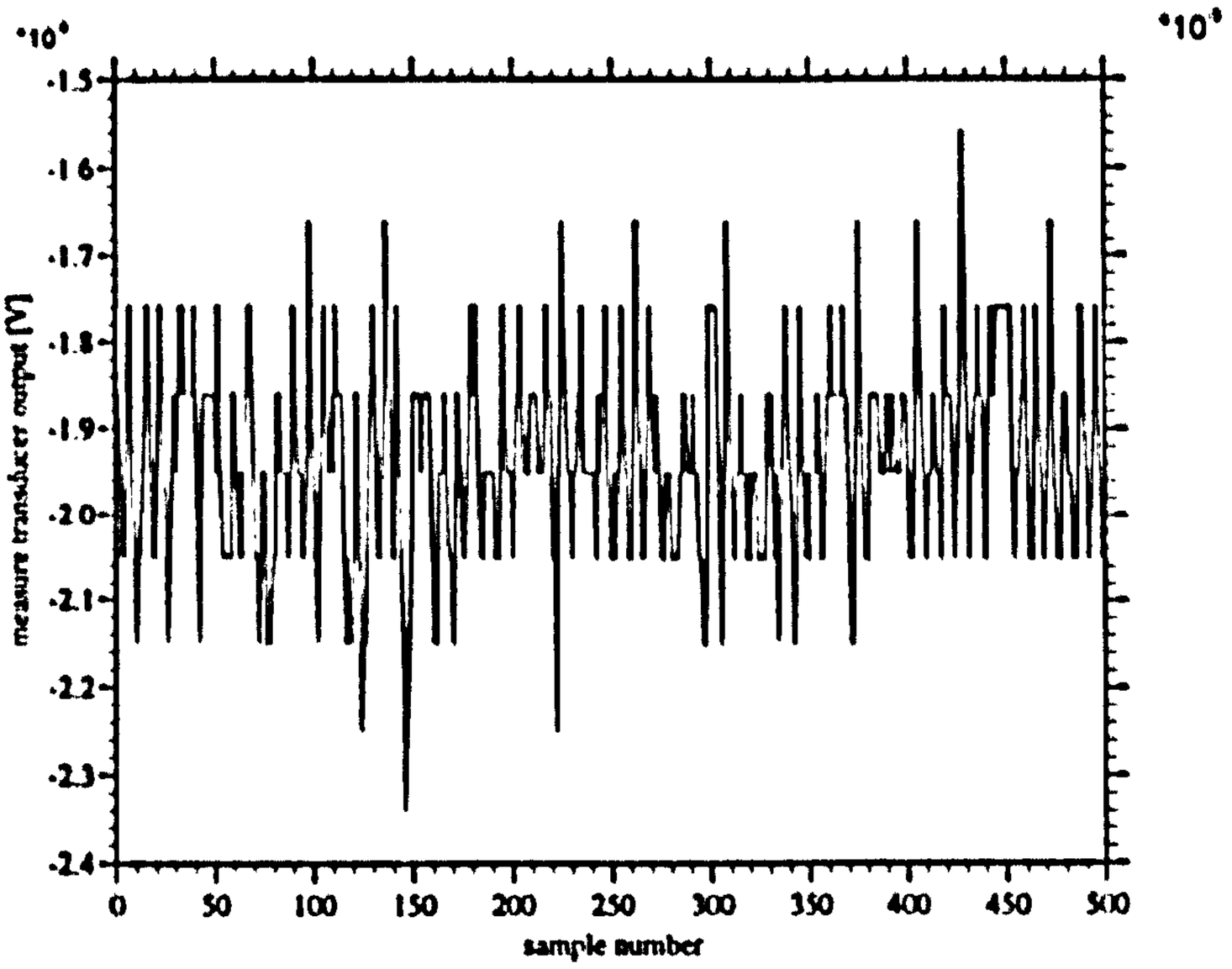

Figure 2.16: Slip Ring Noise at 800 RPM

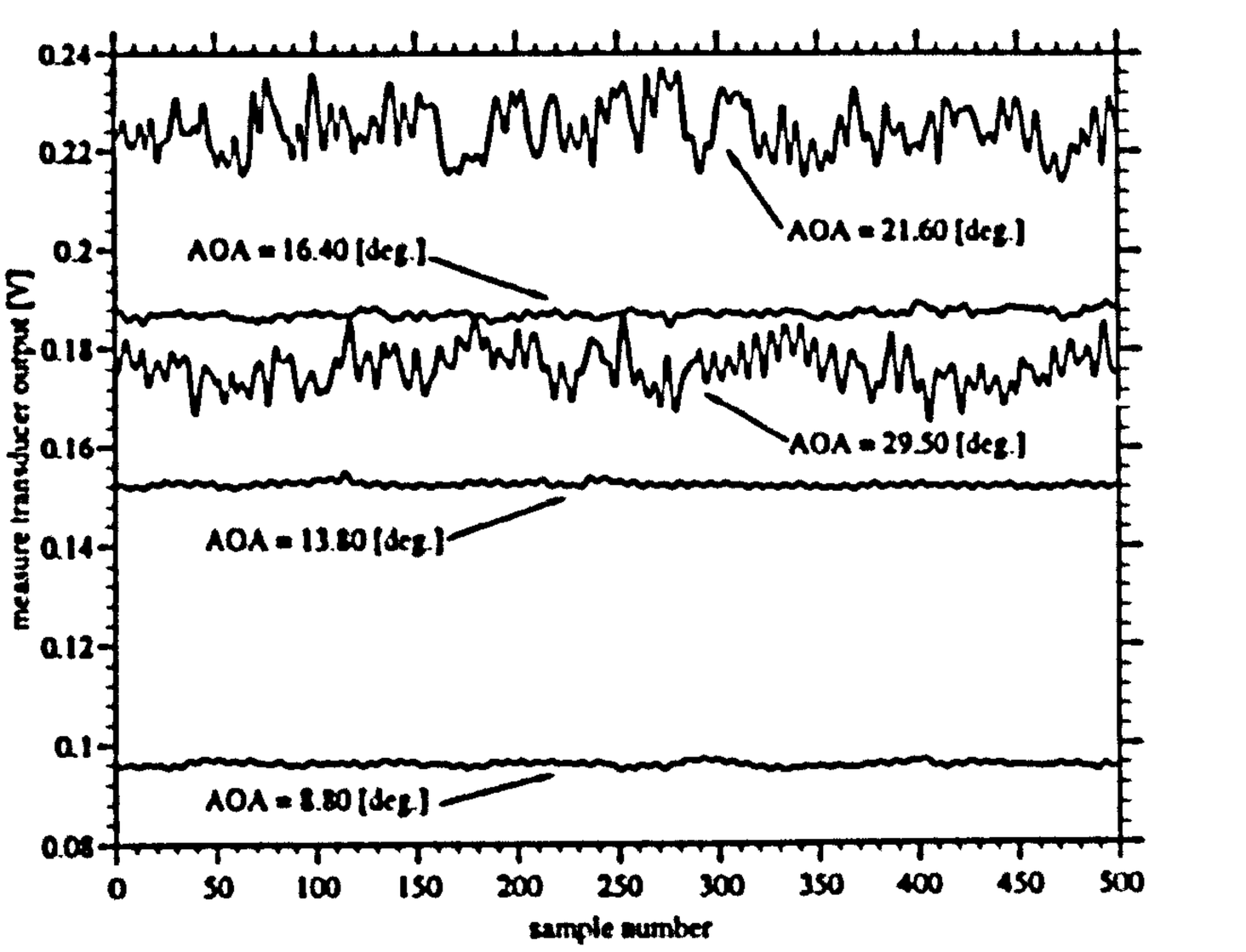

Figure 2.17: Pressure Fluctuations

magnitude of these fluctuations is of the order of the slip ring noise shown above. It, therefore, seems reasonable to assume that any surface pressure fluctuations at this frequency are small. Clearly, the measured pressures at these AOA are

extremely steady. In addition to the high frequency fluctuations the signal traces shown for 21.6 degrees and 29.5 degrees AOA reveal fluctuations at lower frequencies. The amplitude of these fluctuations is around +/-5% of the mean transducer output voltage. These fluctuations give an indication of the typical levels of unsteadiness of the blade surface pressures, which were measured for the inboard blade stations in the tests for higher AOA. Though, these pressure fluctuations are obviously increased for the higher AOA compared to the low AOA cases. They are not significant enough compared to the mean signal to suggest that there are gross instantaneous deviations from the mean local flow pattern. In fact, it may be argued from the evidence presented that the mean flow is, even at the high AOA, largely steady. This justifies the assumption that time averaged pressure measurements provide a meaningful indication of the physical flow over the rotating blade at all AOA, which was fundamental to the design of the sequential pressure scanning system. Further, the data suggests that the stall behaviour of the blade was steady and that the so called rotating stall which can occur on axial flow turbomachinery is not an important consideration for the interpretation of the test results presented in the following.

Blade Cp-Distributions

Figures (2.18) - (2.25) show the effect of the local 'geometric' incidence α on the chord wise Cp distributions measured at radial stations $r/r_t = 0.940$ / 0.840 / 0.760 / 0.680 (for which the corresponding (c/r) ratios shown in the figures are 0.340 / 0.380 / 0.420 / 0.470) for an 8 bladed rotor configuration with a hub/tip ratio h of 0.65 and a solidity σ of 0.53. The Cp values derived by the method described above in some cases did not quite achieve the expected value of +1.0 near the leading edge stagnation point but were in fact somewhat lower (- typically the maximum Cp values derived near the leading edge were in the range +0.6 to +0.9 but never greater than +1.0 -), which suggests that the hub reference pressure was in some cases not recorded accurately. In order to allow better comparison between the individual measurements the Cp distributions have in the presentation been unilaterally shifted so that the maximum recorded leading edge pressure corresponds to $Cp = 1.0$ as would be expected for the leading edge stagnation point. This somewhat arbitrary shift is physically inaccurate since the pressure distributions suggest that the stagnation point lies in between the two pressure taps closest to the leading edge and causes some degree of uncertainty about the absolute values of C_{pmin}. However, since this does not distort the pressure distributions as such it does not affect the derived force data.

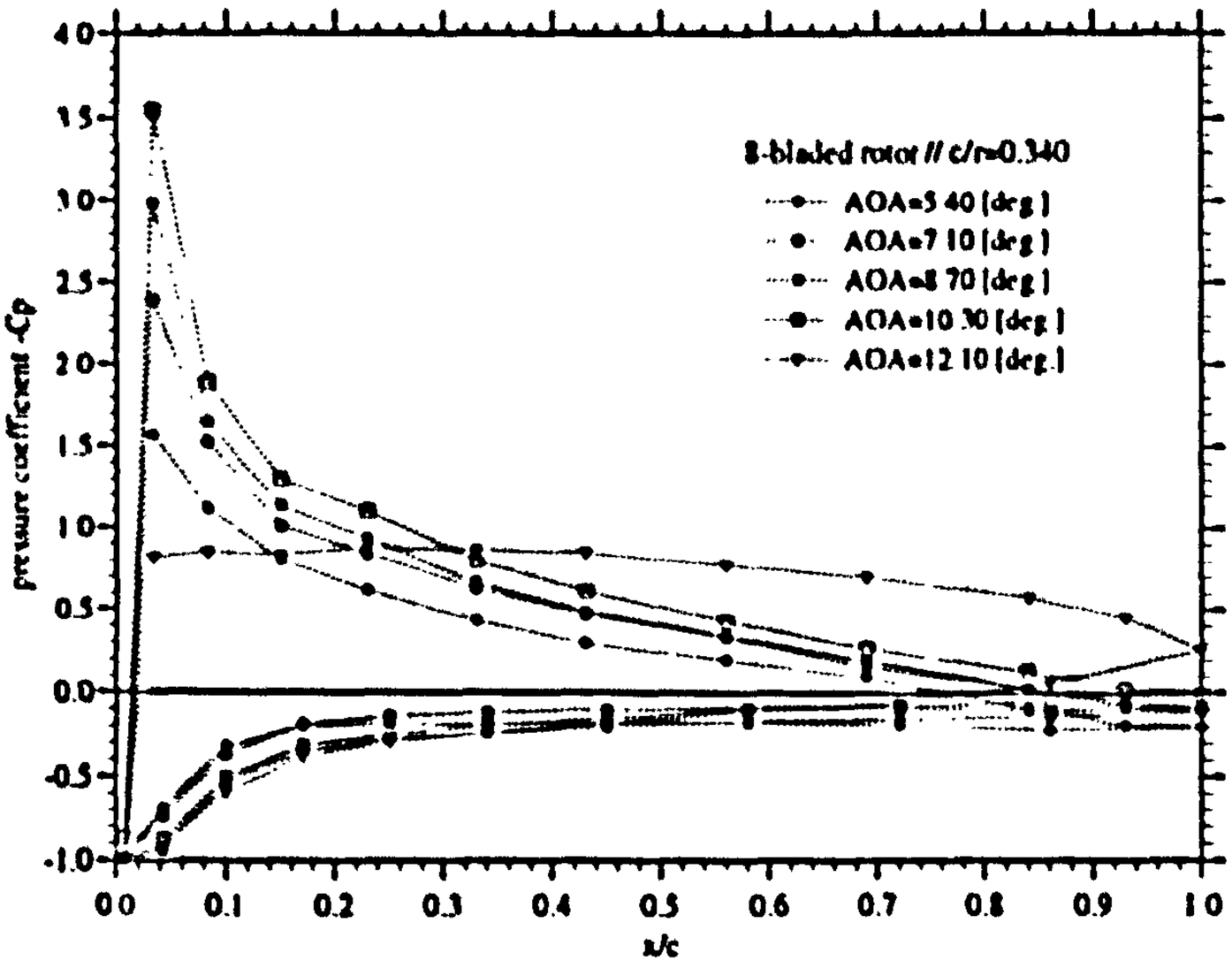

Figure 2.18: Rotating Blade *Cp*-Distributions

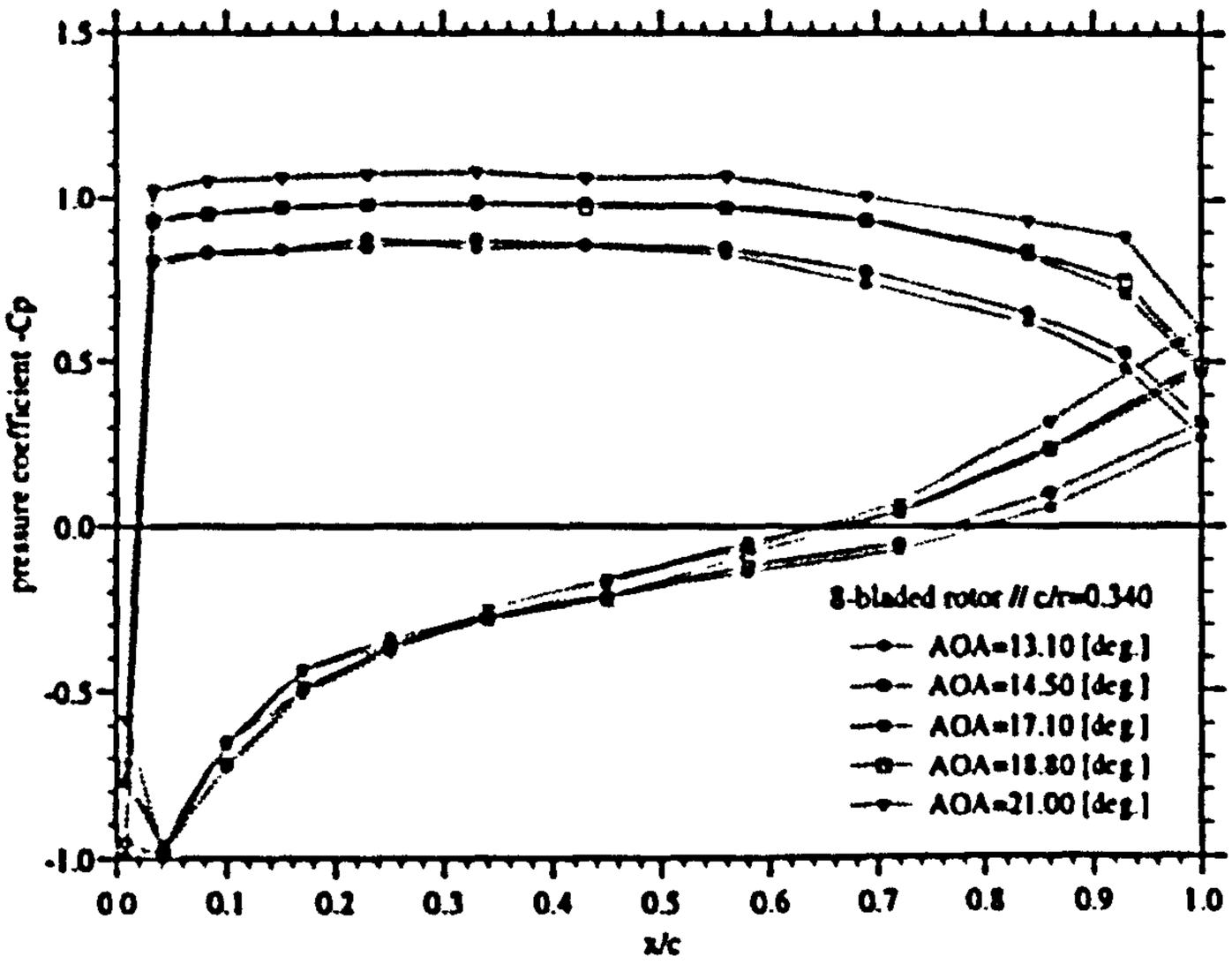

Figure 2.19: Rotating Blade *Cp*-Distributions

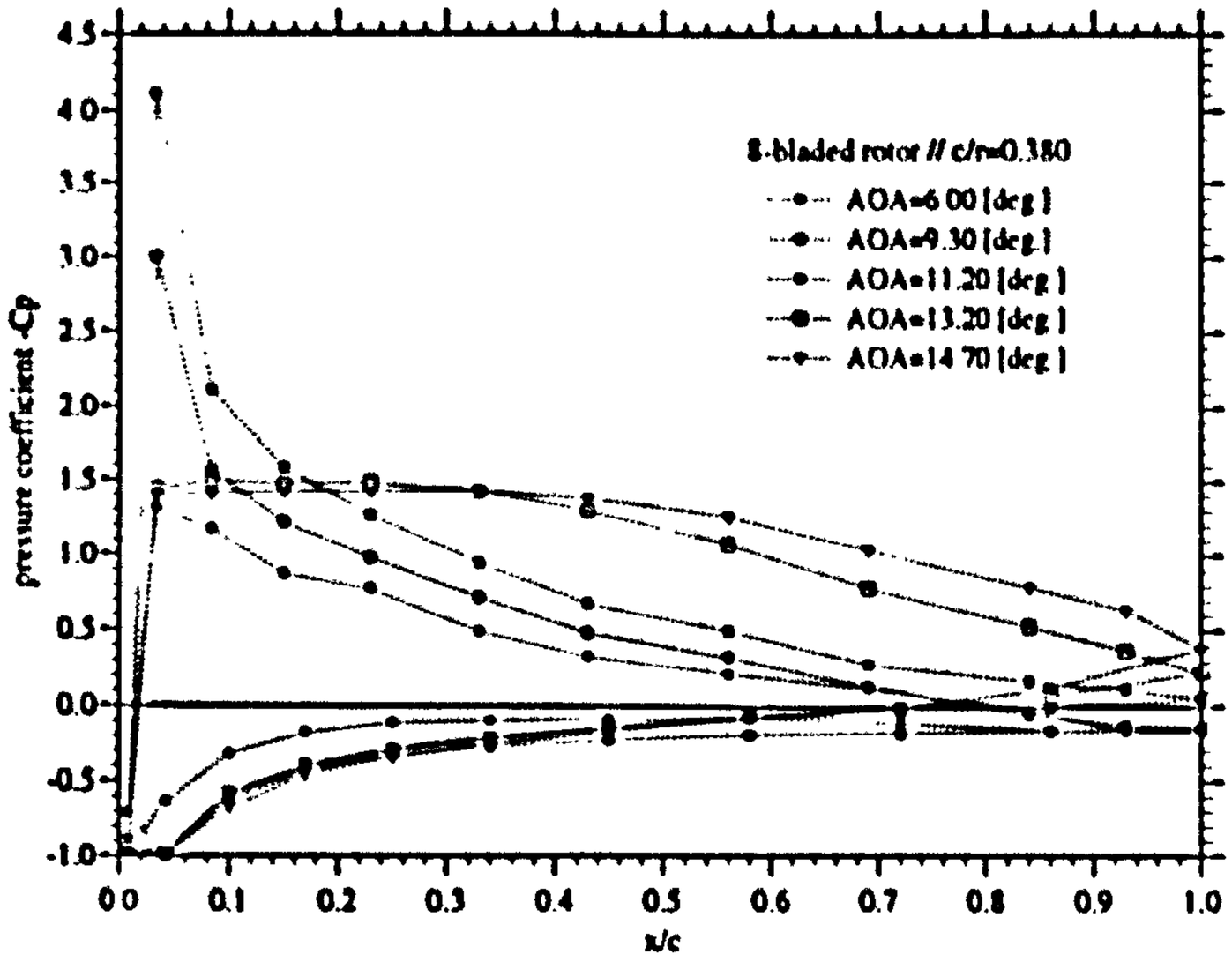

Figure 2.20: Rotating Blade *Cp*-Distributions

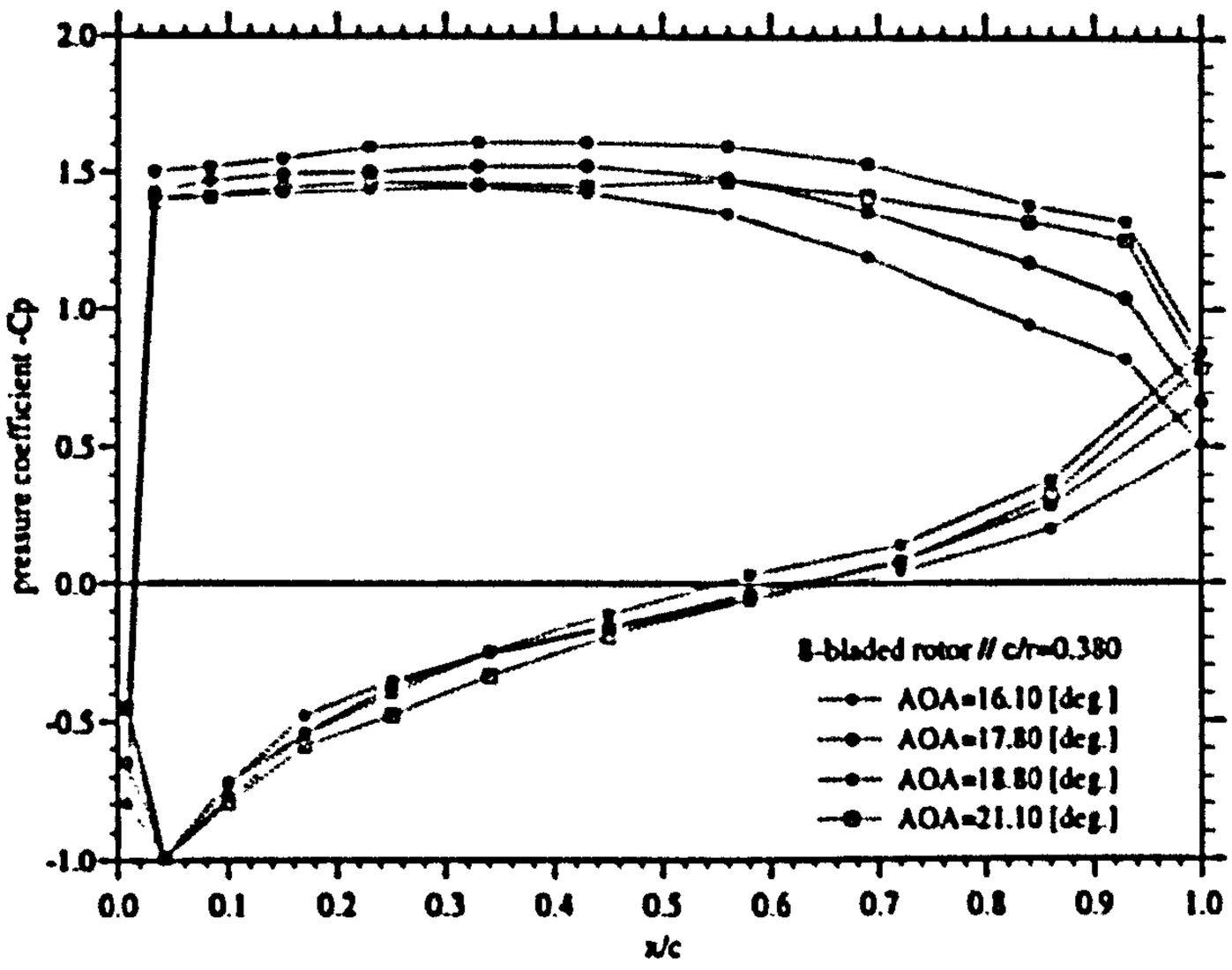

Figure 2.21: Rotating Blade *Cp*-Distributions

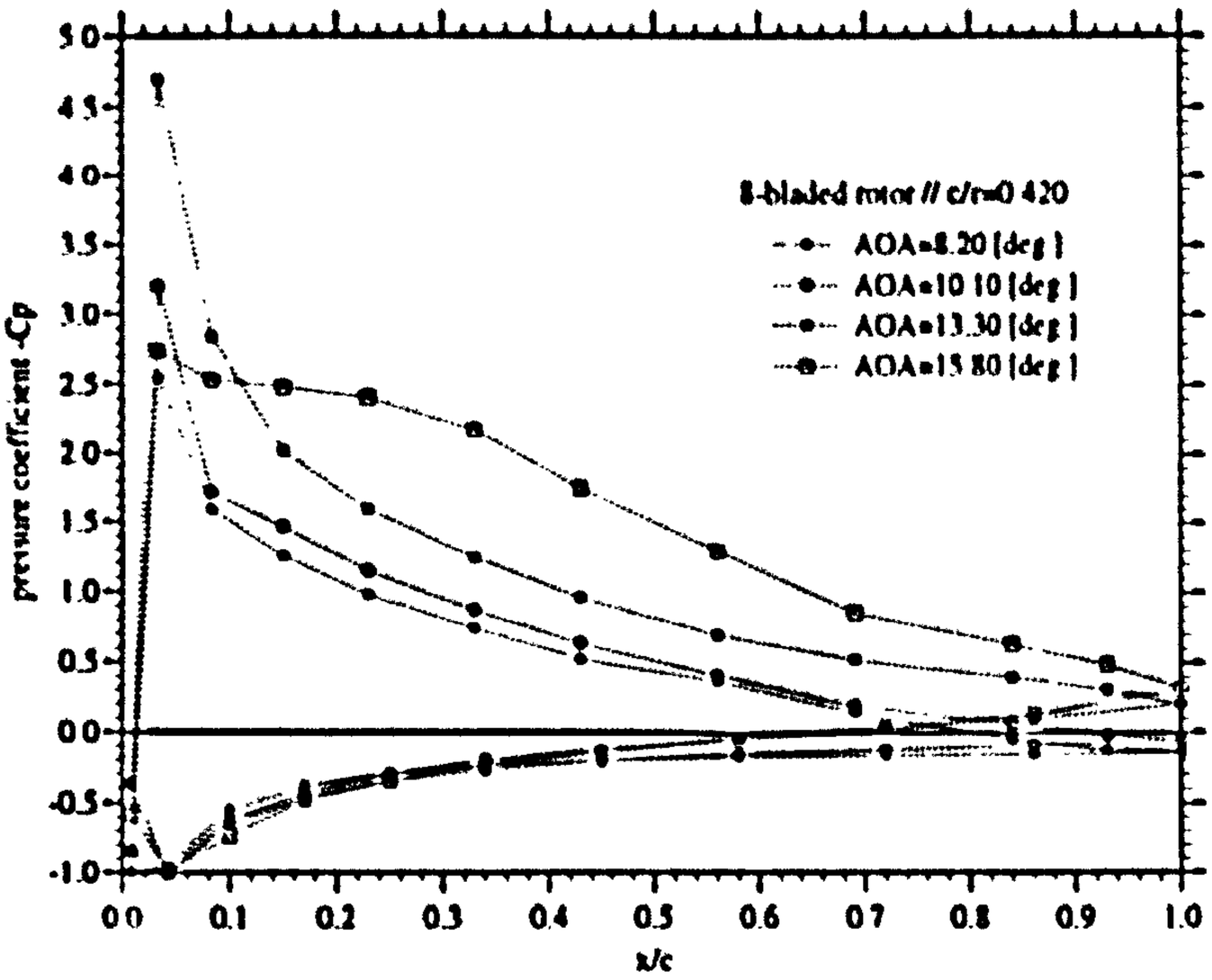

Figure 2.22: Rotating Blade *Cp*-Distributions

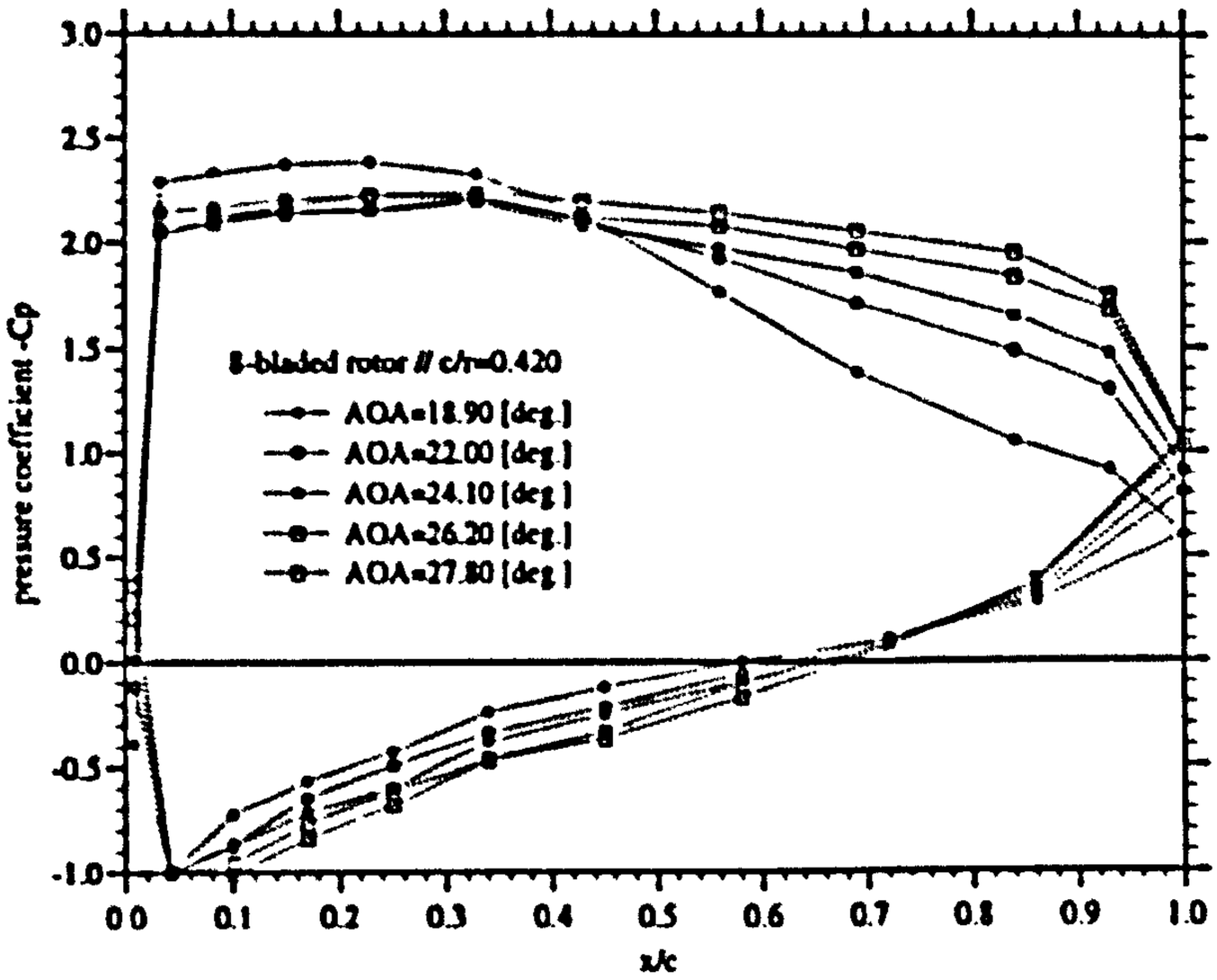

Figure 2.23: Rotating Blade *Cp*-Distributions

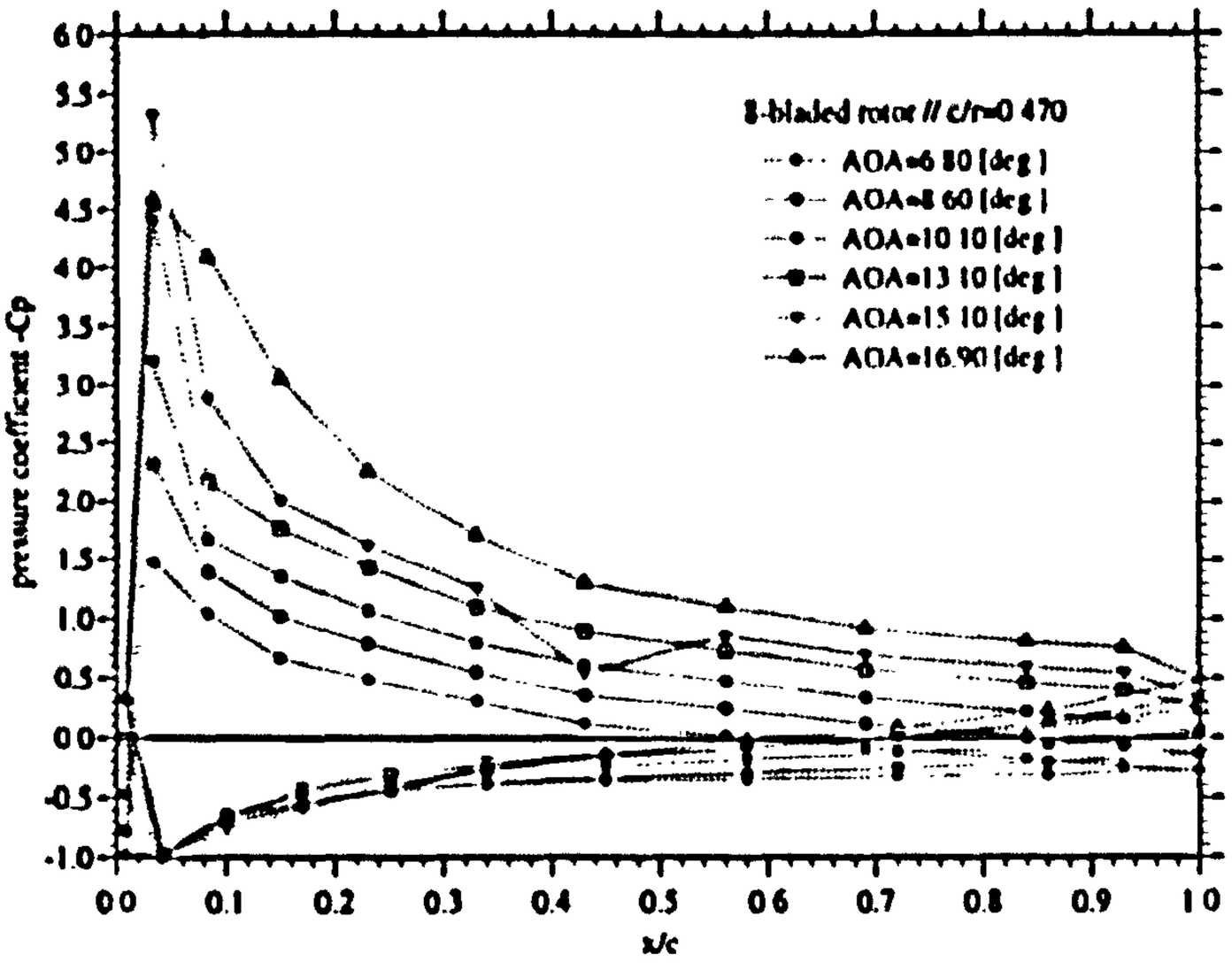

Figure 2.24: Rotating Blade *Cp*-Distributions

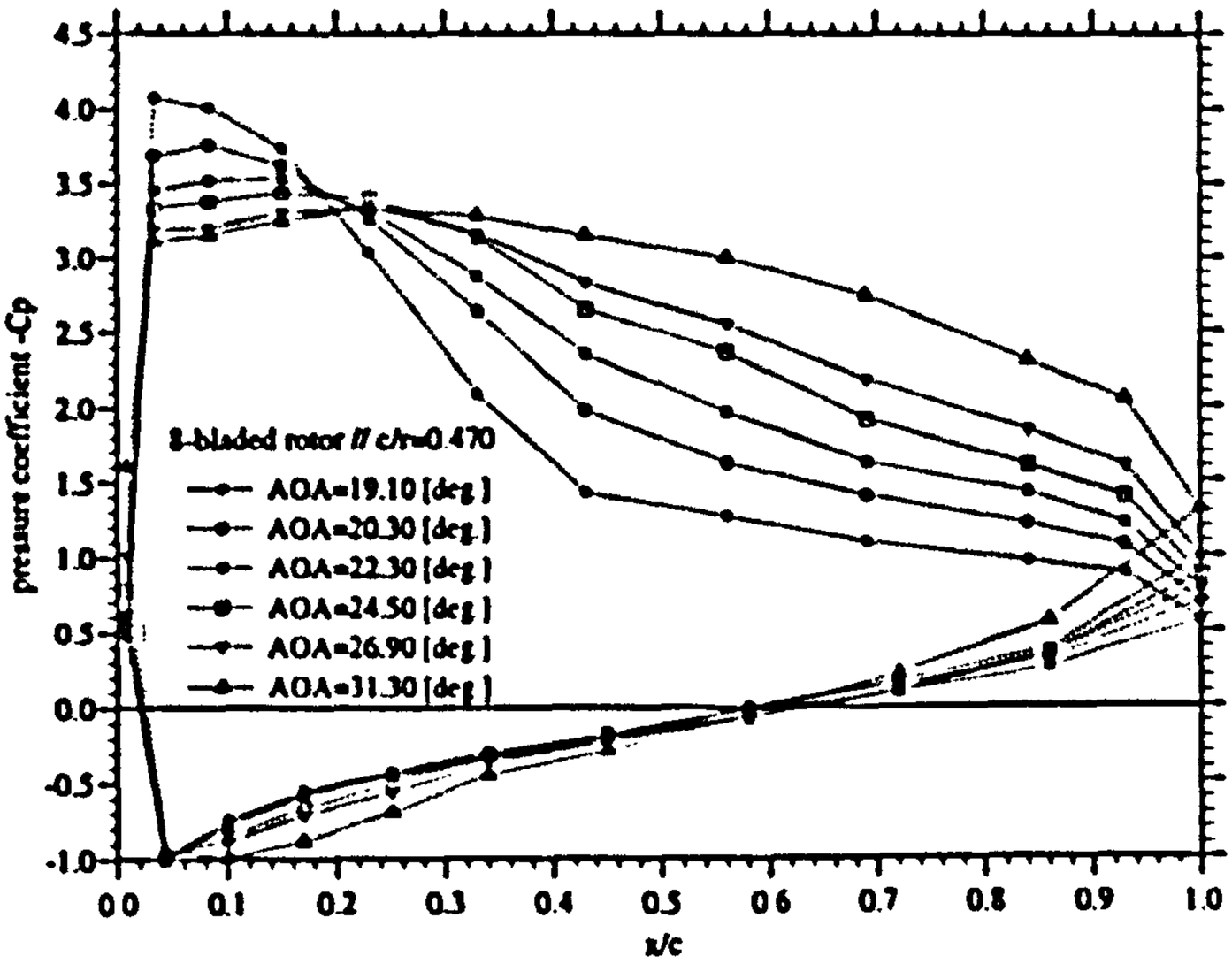

Figure 2.25: Rotating Blade *Cp*-Distributions

The stated values of α do not account for the swirl effects of the rotor wake. These effects are treated separately later in the report. It will be seen, however, that, as has been commented earlier, they locally reduce α. This reduction was found to be particularly strong for blade sections near the root.

Over the range of local incidences shown, the tip Re based on the total velocity W' varies between approximately 0.24e6 and 0.26e6. At $r/r_t = 0.680$ the Re varied between 0.170e6 and 0.20e6. These Re variations are not expected to be significant enough to cause substantially different boundary layer behaviour between the blade tip and root regions for any chord wise flow over the NACA0015 blade section. Consequently, it may be concluded with some confidence that Re effects were not an important cause of any radial variations of the blade aerodynamics noted in the current experimental work.

For low to moderate values of α the chord wise suction surface Cp distributions qualitatively show close resemblance to the peaky distributions measured on the static blade. Notable, however, is the fact that there is a strong radial variation of the maximum values of leading edge suction peaks denoted in the following by $\hat{Cp}_{min}$, which as presented increase in magnitude from $\hat{Cp}_{min} = -3.6$ at $r/r_t = 0.940$ to $\hat{Cp}_{min} = -5.4$ at $r/r_t = 0.680$. Further, the data suggest that as r decreases the AOA at which $\hat{Cp}_{min}$ occurs $\alpha_{\hat{Cp}min}$ increases. For a r/r_t value of 0.940 Cp_{min} occurs just before local blade stall at nominally 12 degrees while at $r/r_t = 0.680$ $\hat{Cp}_{min}$ is reached at around 15 degrees incidence. By comparison, the Cp distributions on the pressure surface of the blade do not deviate strongly between the tip and root regions of the blade.

In principle, the radial variations of $\hat{Cp}_{min}$ noted above can qualitatively be inferred from the inviscid theory for static 2 dimensional cascades discussed in the introduction to this report chapter. From this it would seem that the increase in $\hat{Cp}_{min}$ towards the rotor hub for a given α is due to a reduction in the local chord to pitch ratio as a result of which the influence of the bound circulation of the neighbouring blades increases. However, this cascade theory cannot predict any radial variation of $\alpha_{\hat{Cp}min}$ as indicated by the measurements on the rotating blade. It must be assumed, therefore, that the noted dependence of $\hat{Cp}_{min}$ on r is not a linear cascade effect but is due to other flow phenomena. In fact, it will be shown later that this variation is strongly related to the swirl effects which progressively decrease the effective α towards the blade hub.

For higher α the suction surface Cp distributions differ more radically along the blade span. In general, the data measured at high α for $r/r_t = 0.940$ and $r/r_t = 0.840$ shows great qualitative similarity to the static blade data. As α is increased beyond approximately 10 degrees at $r/r_t = 0.940$ and 12 degrees at

r/r_t = 0.840 there is a sudden transition from the peaky type Cp distribution to a flat type. At r/r_t = 0.940 any further increases in α have little systematic effect on Cp values and the blade may be assumed to be completely stalled in this region. The stall angle $\alpha_{Cp_{min}}$ as defined by the loss of the leading edge suction peak at this radial station is somewhat lower than that for the static blade and may be due to local three dimensionalities associated with the tip flow. Further, it is evident that the Cp levels on the suction blade surface at post-stall α in this region are slightly higher than for the static blade. This may be related to the static pressure drop across the turbine rotor which in causes the static pressures on the downstream surface of the rotating blade to be lower than those for the static blade at an equivalent AOA. On the whole, though, the evidence strongly suggests that the stall of the rotating blade sections close to the tip is governed by the same flow mechanisms as those for the static blade, which relate to chord wise pressure gradients. It may hence be concluded that the tip regions of the rotating blade experience a leading edge stall as would be predicted by the blade element theory using the static blade data.

At r/r_t = 0.840 the value of $\hat{Cp}_{min}$ is closer to that recorded for the static blade. However, the post-stall Cp distributions are not as flat as those at r/r_t = 0.940 and it is evident that the aerodynamic rear loading of the blade section is sensitive to further increases in α.

Further inboard from the tip at r/r_t = 0.760 the sudden loss of the leading edge suction peak does not result in a flat top Cp distribution typical for fully stalled flow at high α, but leads to some intermediate 'bulky' type Cp distribution. It is evident that there is a significant low pressure region, which extends over approximately 50% of the local blade chord and in which the Cp levels are appreciably higher than at equivalent values of α for the blade stations closer to the tip. This low pressure region is stable for further increases in α, which cause a gradual increase in the Cp values that could be recorded over the rear half of the blade. As a result the aerodynamic loading at this radial station becomes more evenly spread between the front and the rear of the blade. Eventually, as α is increased even further, a flat pressure distribution stabilises at the Cp level set by the leading edge flow.

At r/r_t = 0.680 the Cp distributions measured at high α show a rather different behaviour yet. This is characterised by a more continuous reduction of the very localised pre-stall leading edge suction, which only very gradually loses its' peakyness and spreads rear wards over the blade section at a lower Cp level, which, however, is significantly higher than the Cp levels further away from the hub at equivalent values of α. Interestingly, at very large values of α the leading edge Cp values stabilise at a certain level and for further increases in α only the aerodynamic loading towards the rear of the blade section increases similarly to

the noted behaviour at $r/r_t = 0.740$.

Clearly, the stall behaviour of the blade sections closer towards the rotor hub is very different from that of the static blade. The 'bulky' Cp distributions measured at high α for $r/r_t = 0.680/0.740$ show a strong resemblance to those recorded by a number of researchers (see introduction to this report chapter) for high AOA on the inboard blade stations of wind turbine rotors. These were explained by the stall delay phenomenon. This, as discussed earlier in the report, relates to radial flows in the blade boundary layers which are caused by the action of Coriolis forces. Since these forces scale on the (c/r) parameter they increase in strength towards the rotor hub for constant chord blades. It is, therefore, reasonable to assume that the Cp distributions recorded in the current experiments for the Wells turbine rotor are also caused by stall delay. For the rotor configuration tested the evidence suggests that significant stall delay occurs for blade sections with $(c/r) \geq 0.420$ while blade sections for which $(c/r) \leq 0.380$ do not seem to experience any great extent of stall delay.

The Cp distributions recorded for high AOA at $r/r_t = 0.680$ indicate that the radial flows associated with the stall delay initially build up in a fairly localised region near the leading edge of the suction surface of the blade. Further, it would seem that as α increases the leading edge radial flows gradually reduce in intensity and spread out towards the trailing edge.

By comparison, the radial flows occurring at high α near the leading edge at $r/r_t = 0.76$ are evidently never as localised as they initially are close to the rotor hub at $r/r_t = 0.680$. The less gradual initiation of the radial flows at this span wise location may be strongly affected by radial flows that have already established themselves at blade stations closer to the rotor hub, which for a given Λ are operating at a higher AOA. It seems acceptable to more generally conclude from this argument that when the Wells turbine operates at low Λ the flow over a significant portion of the span is affected by the radial boundary layer flows that emanate from sections closer to the blade root.

Blade Force Coefficients

Section lift force coefficient C_L, drag force coefficient C_D, normal force coefficient C_N and tangential force coefficient C_T were derived by integration according to equations (2.1) - (2.4) from the measured pressure distributions, which have been discussed above. Their variation with α is illustrated in figures (2.26) - (2.29) below for all radial stations, which are denominated in the figures by their respective values of (c/r).

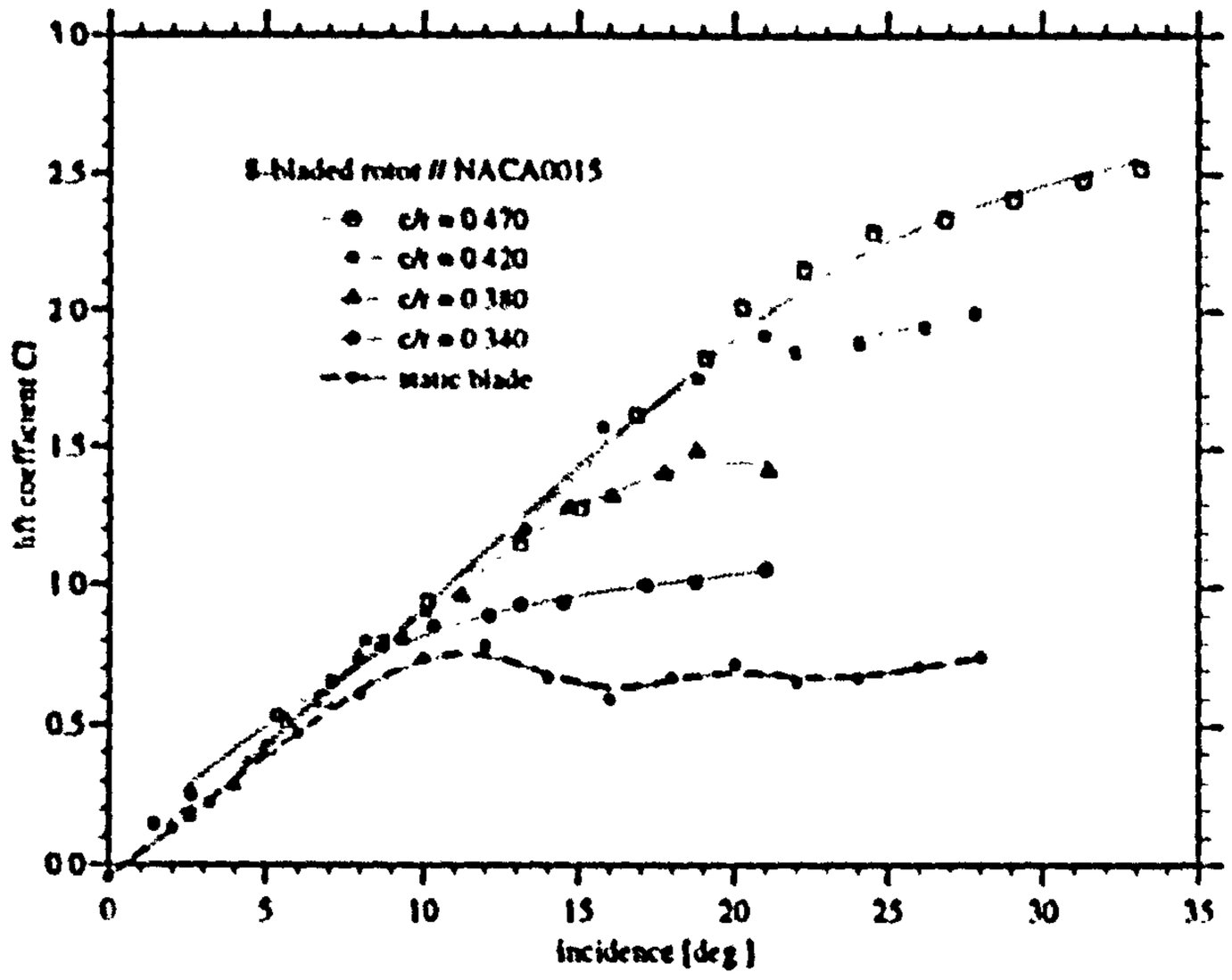

Figure 2.26: Sectional Lift Coefficients

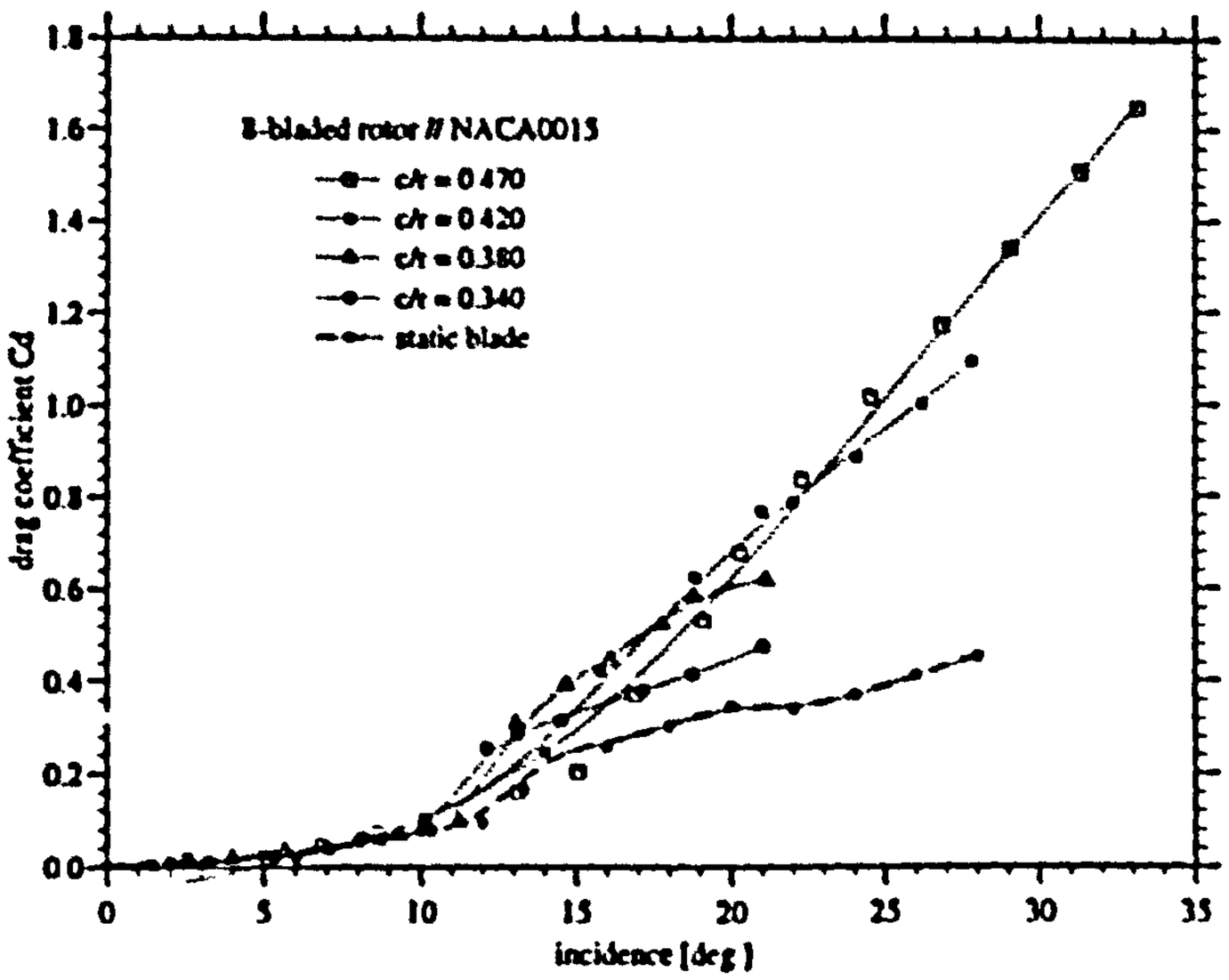

Figure 2.27: Sectional Drag Coefficients

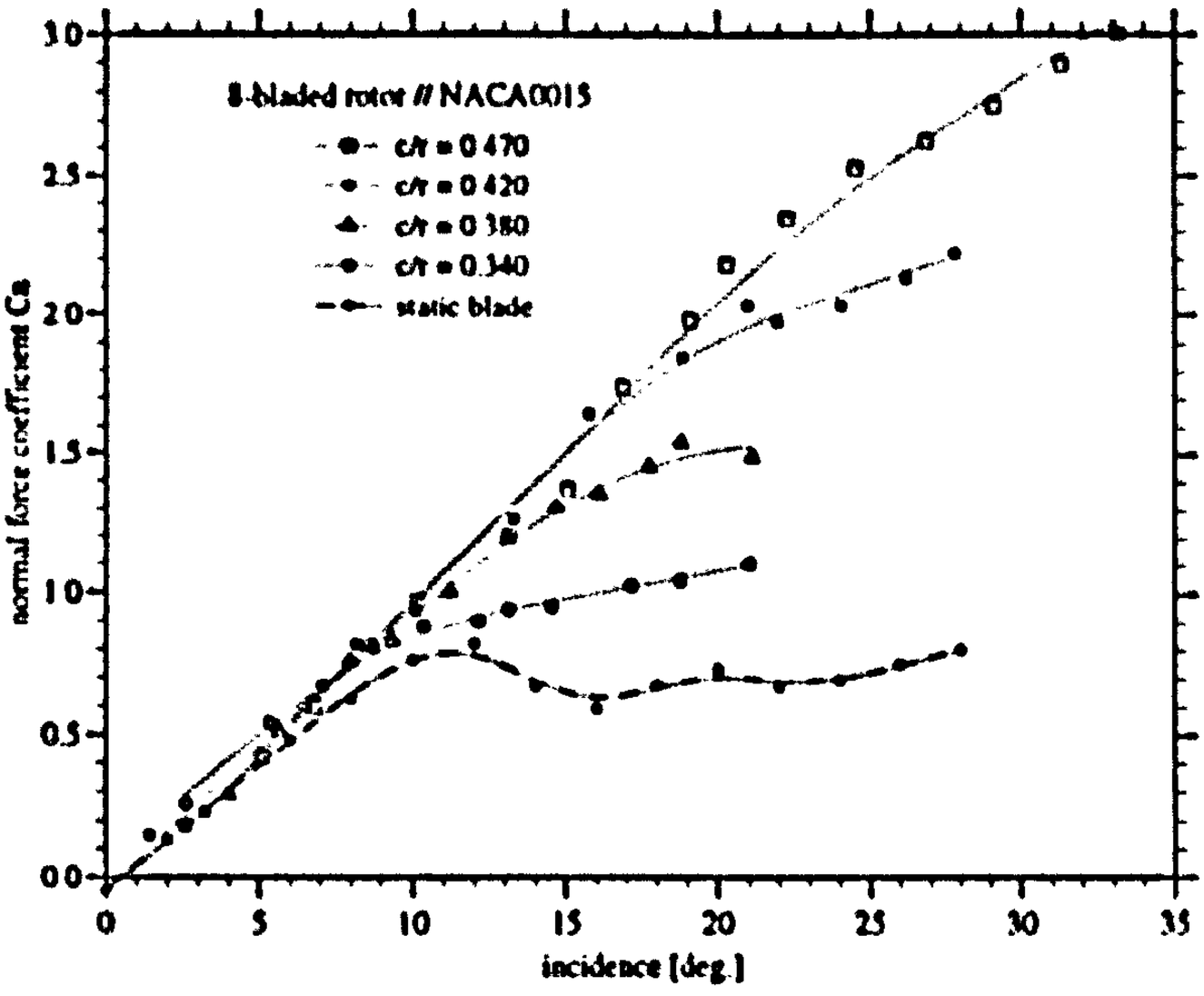

Figure 2.28: Sectional Normal Force Coefficients

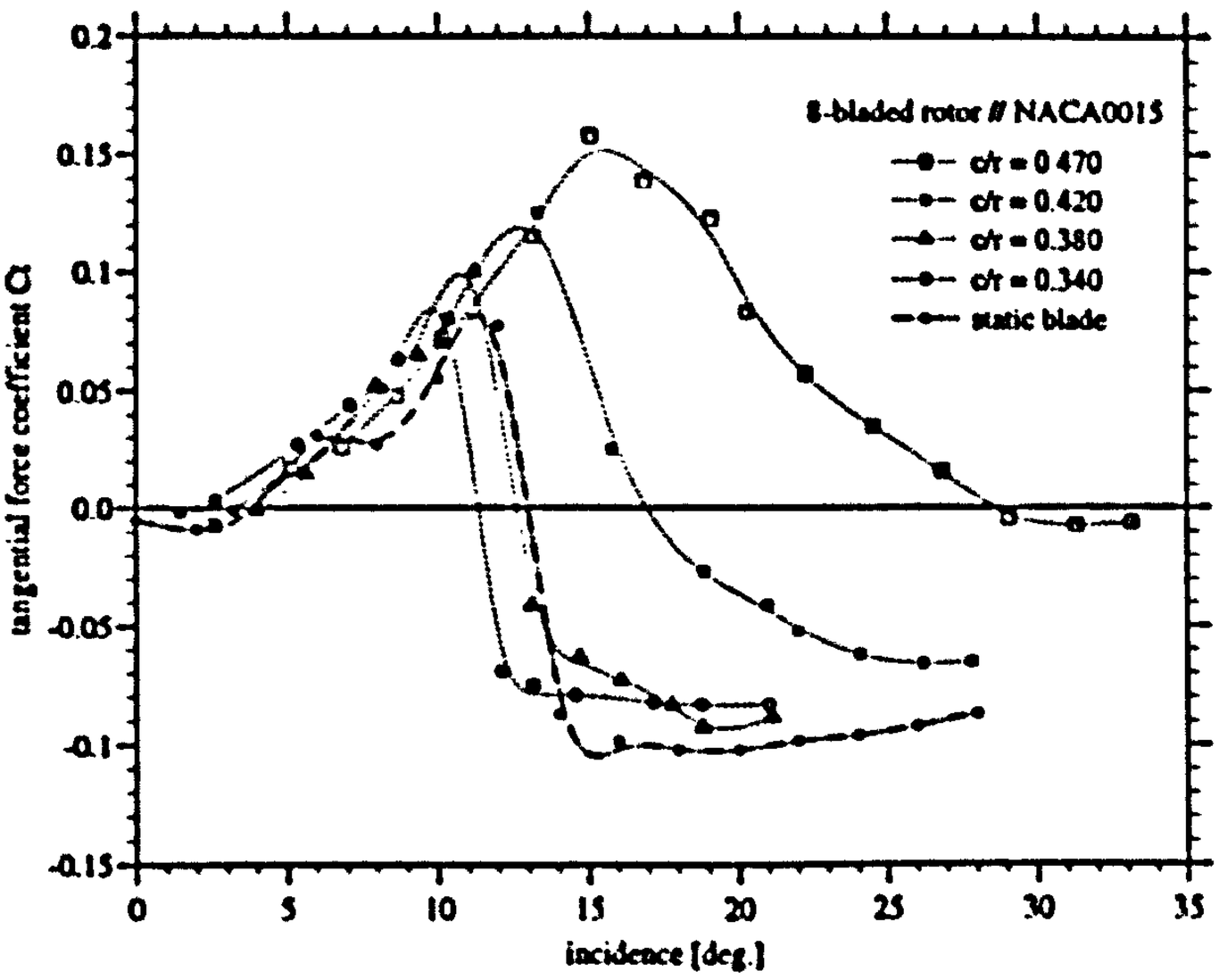

Figure 2.29: Sectional Tangential Force Coefficients

Within the data scatter of the presentation no clear trend is discernible for any radial variation of the lift curve slope a_0 and it must be assumed that this is nominally constant. a_0 for the rotating blades in this rotor configuration is somewhat higher than the static blade value, which is an indication of the linear cascade effects which are known to be important at pre-stall incidences.

For higher values of α, though, the C_L curves reveal a strong variation with (c/r). This relates to the deviations noted above in the Cp distributions for the different radial stations, which are caused by the the radial flows that occur in the boundary layers of the blade. Due to these flows C_L continues to increase near linearly with α even after the fairly localised leading edge suction has broken down, which is associated with the pre-stall attached flow dominated by chord wise pressure gradients. Significant for the rotor shaft power is the dramatic non-linear increase in notional C_{Lmax} and the associated incidence at which it occurs α_{max} with (c/r). In fact, it is evident that for blade stations close to the rotor hub α_{max} was not reached for the range of flow rates tested. In this context it should be noted that the depicted radial variation of th C_{Lmax} is unlikely to be due to opposite to Re effects since it is in the opposite direction. As was established for the Cp distributions earlier, the C_L curves reveal a strong qualitative similarity to data published for studies of the stall behaviour of rotating blades of wind turbine rotors, which were subject to stall delay.

As discussed in the introduction of the thesis, the extent of stall delay has, for wind turbine rotors, been shown to depend on (c/r). Snel (1993) derived an empirical equation to relate the lift coefficient of the rotating blade sections (C_{L3D}) to the basic 2D sectional lift coefficient (C_{L2D}), which provides a measure of the stall delay:

(2.6) $$C_{L3D} = C_{L2D} + k\,(c/r)^2\,\Delta C_L$$

where k is a constant and ΔC_L is given by

(2.7) $$\Delta C_L = C_{L(linear)} - C_{L2D}$$

with

(2.8) $$C_{L(linear)} = 2\pi\,sin\alpha$$

Snel proposed that for typical wind turbine rotors k is approximately equal to 3. Effectively equation (2.6) expresses the local extent of stall delay as a proportion of the difference between the actual post-stall lift produced by the static blade and a hypothetical C_L value obtained as a linear extrapolation of the pre-stall lift curve slope.

Snel's equation was applied to the C_L data presented in figure (2.26) to derive values of k applicable to the 8 bladed Wells turbine rotor tested. The results are shown in figure (2.30). Within the data scatter the is no clear trend in the

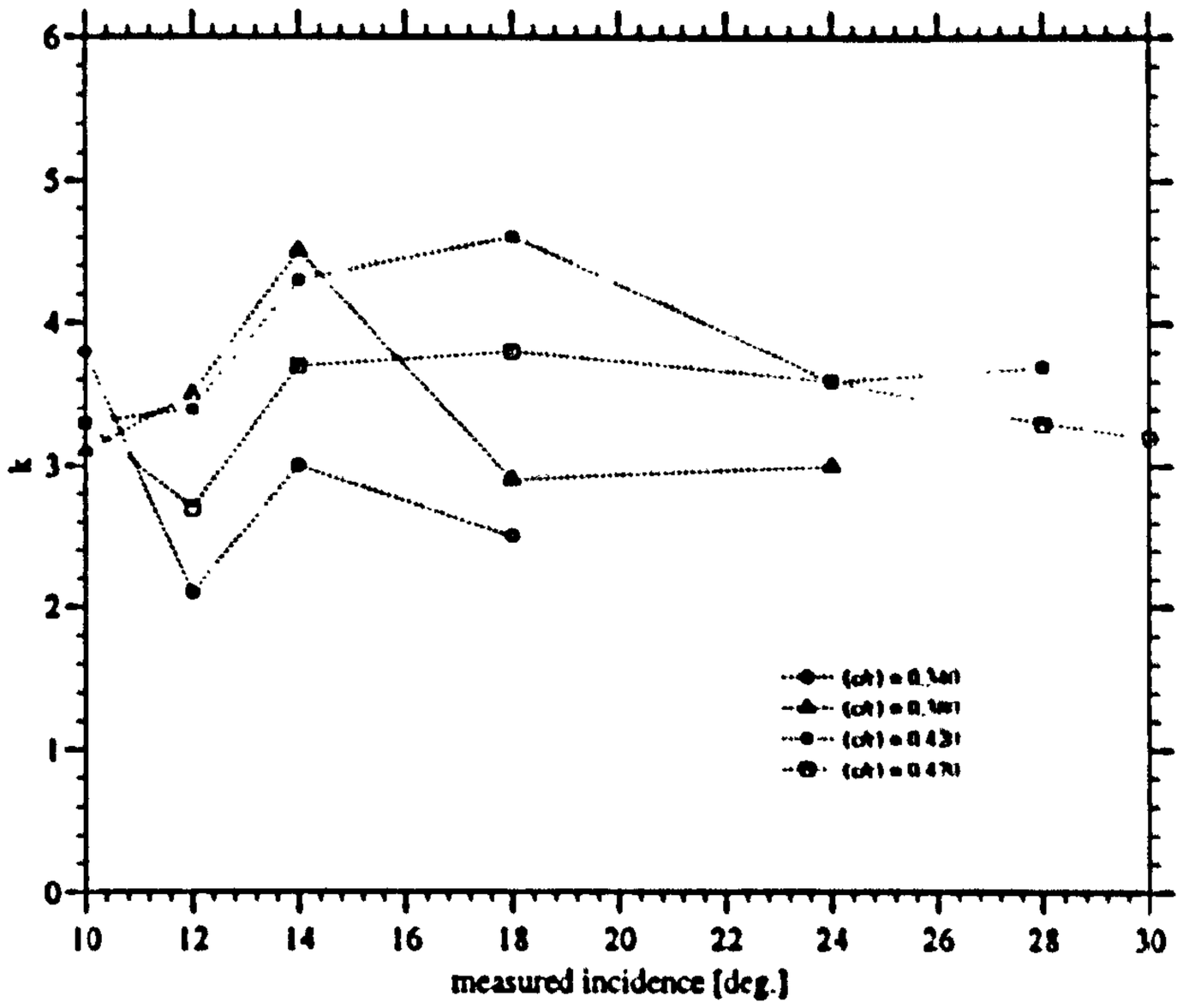

Figure 2.30: Stall Delay Coefficient k

radial variation of k, though there is a suggestion that the value of k increases somewhat towards the blade root. It is apparent from the data that for the 8 bladed rotor the value of k (- averaged over the range of post-stall incidences achieved for respective blade sections -) is of the order 3 - 3.8 . This seems slightly higher than the value quoted by Snel for wind turbine rotors. To some extent this may be expected because the above equation does not account for cascade effects which, as will be discussed in the following thesis section, are important (particularly) for the 8 bladed rotor even at post-stall incidence and would tend to reduce the values of k . Stricly, for the Wells turbine equation (2.6) should contain a factorisation for the cascade effects:

$$C_{L3D} = f_c \left[C_{L2D} + k\,(c/r)^2\, \Delta C_L \right] \tag{2.9}$$

where f_c is a cascade effect factor, which for pre-stall incidences is equal to the factor given by linear cascade theory but at post-stall incidences is likely to be a function of the local blade incidence since for, the high solidity rotor, there are strong interactions between the cascade and stall delay effects (nb. for pre-stall incidences ΔC_L is zero and equation (2.9) reduces to the usual equation given by linear cascade theory). Further, the above result does not account for the effects of axial and swirl velocities induced by the rotor wake, which may introduce a more pronounced radial variation of k and are discussed seperately later. In any case, this result suggests that the extent of stall delay present on the 8 blade

rotor at post-stall incidences is comparable to that noted for wind turbine rotors.

The C_D curves show comparatively insignificant radial variation for low to moderate α and all data points seem to collapse onto a single curve. There is some radial variation, however, once there is an appreciable drag rise, which is associated with the loss of the leading edge suction peak. Again this finding is reminiscent of what is reported in the literature on the aerodynamics of wind turbine rotors.

Since C_N is most strongly dependent on C_L the curves shown in figure (2.28) show a similar variation with (c/r). The apparent near-linear increase of C_N with α, at high AOA, which is sustained longer close to the blade root, is thus directly related to the stall delay phenomenon. This result goes some way to explaining the approximately linear relationship that exists between the pressure drop across the Wells turbine rotor and Λ^{-1} at high axial flow rates for which from conventional theory the rotor blades would be expected to be stalled (see e.g. Sturge et al. (1977)).

From the data presented in figure (2.29) there seems to be no strong influence of (c/r) on the C_T curves for low AOA. However, for higher AOA the curves show distinct maxima C_{Tmax} which are strong non-linear functions of (c/r). The occurrence of C_{Tmax} is associated with the steep drag rise at high AOA which in turn is initiated by the loss of the leading edge suction peak on the down-wind blade surface. Correspondingly, the curves for (c/r) values between 0.340 and 0.420 exhibit quite sharp decreases in C_T at fairly discrete values of α. For $(c/r) = 0.470$ it was seen earlier that the suction peak reduces more gradually at high AOA. Consequently, the associated C_T curve has a much more rounded maximum and does not decrease as rapidly at higher AOA.

Since the contribution of a blade section to the overall rotor power is directly proportional to $C_T \times r^3$ the above curves have strong implications for the turbine performance. It is clear that due to the apparent stall delay at blade stations close to the rotor hub, these stations may be expected to produce significantly higher levels of power at lower values of Λ than would be predicted by the conventional BET approach, which uses basic aerofoil data. Because, however, the bulk of the shaft power is produced by blade sections near the tip, the more global effect of the noted stall delay on the overall turbine power is likely to be less dramatic.

Effects of Rotor Solidity

The effects of rotor solidity σ on the local force coefficients was studied by varying the number of rotor blades. Figures (2.31) - (2.38) show comparative plots of C_L

and C_D data which was recorded for 2,4, and 8 bladed rotor configurations which had a constant hub/tip ratio of 0.650 and respective solidities of 0.12, 0.25 and 0.49.

On the whole, there is little difference over the full range of tested Λ between the curves for the 2 and 4 bladed rotors within the data scatter. From this it can be concluded that cascade effects are negligible for these rotor configurations. This is in agreement with the cascade theory given earlier according to which the C_L values for both of these rotor configurations for a given local blade incidence should be only approximately 3% higher than that of an isolated aerofoil section at an equivalent AOA.

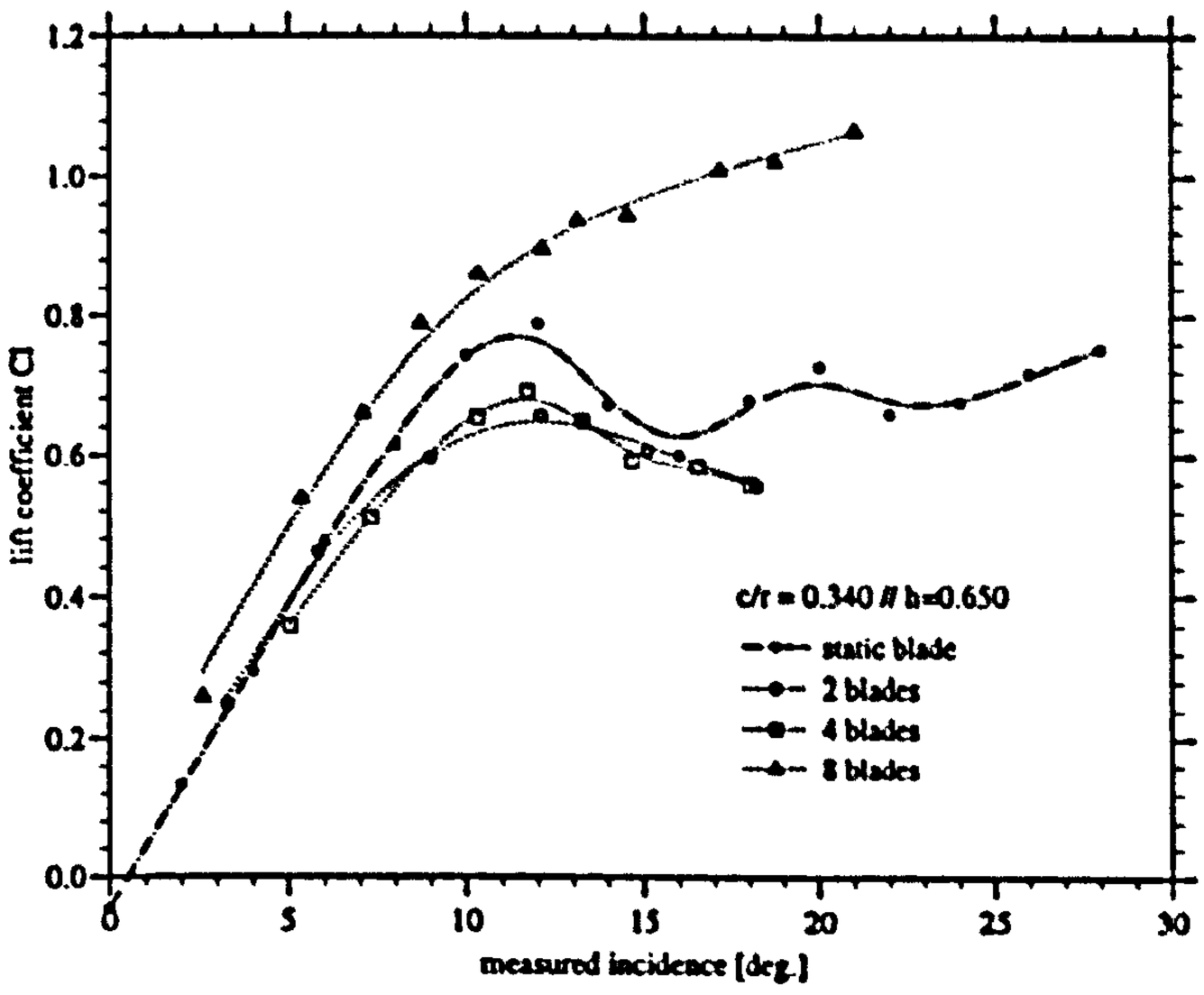

Figure 2.31: Effect of Rotor Solidity on C_L at $(c/r) = 0.340$

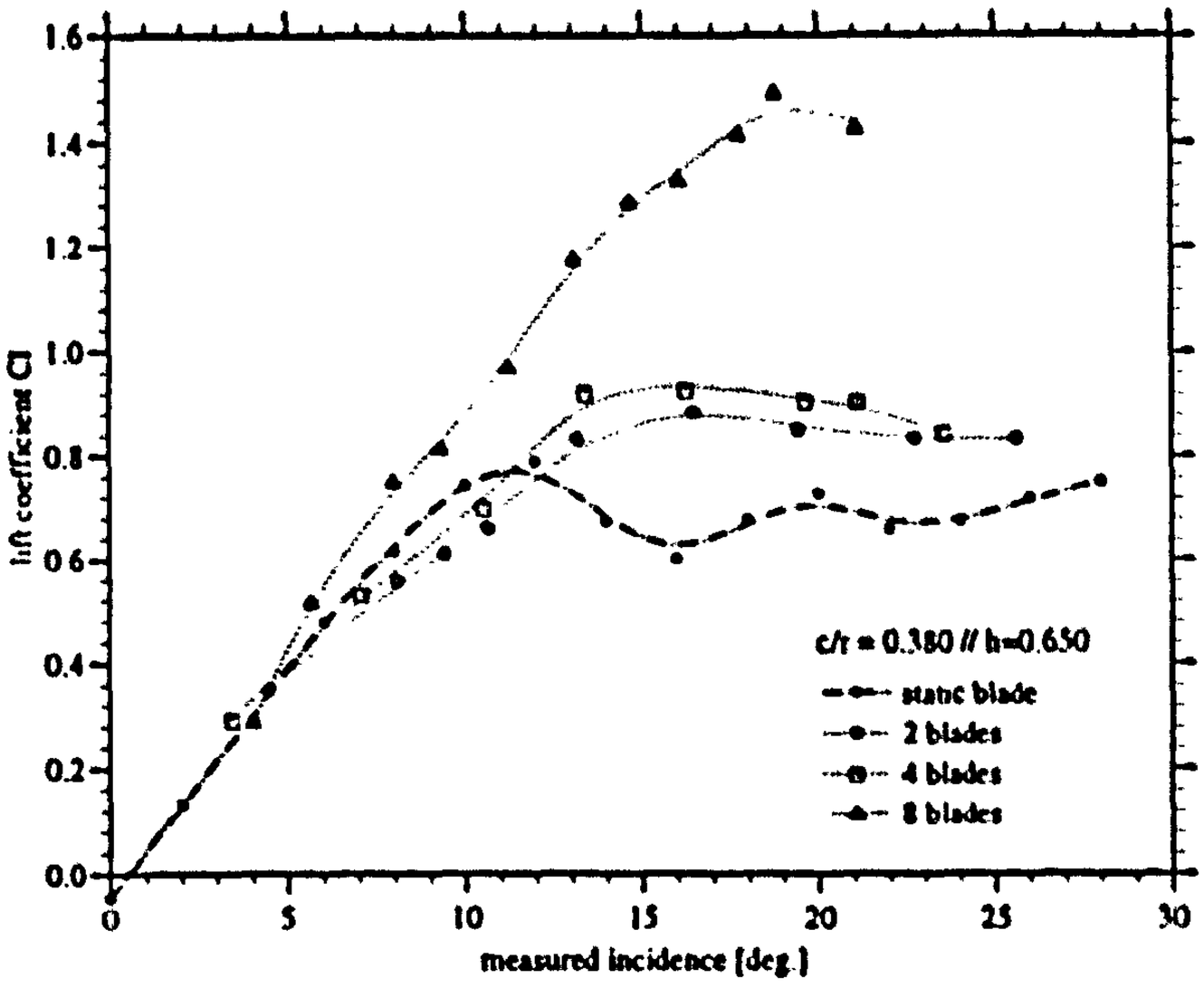

Figure 2.32: Effect of Rotor Solidity on C_L at $(c/r) = 0.380$

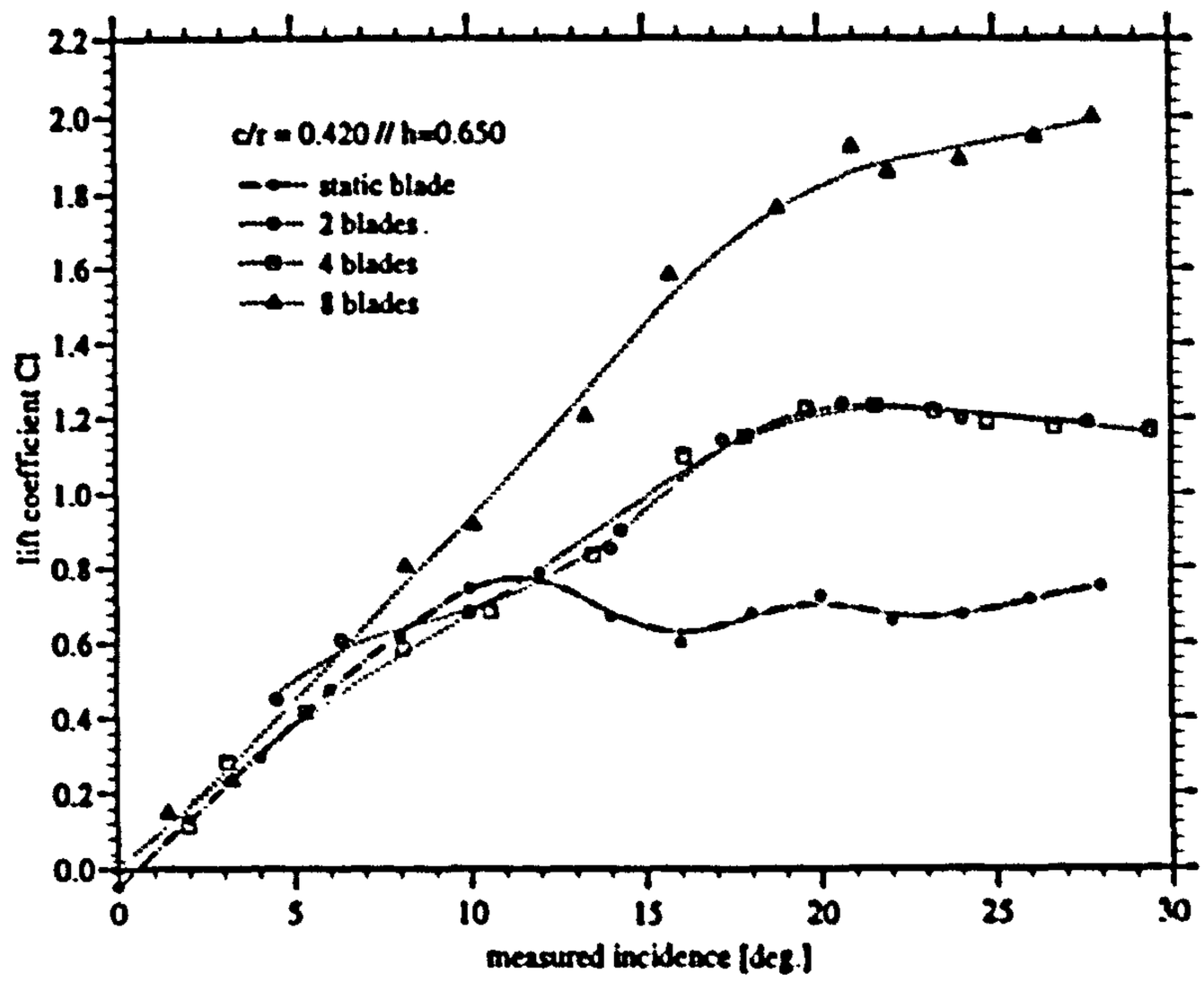

Figure 2.33: Effect of Rotor Solidity on C_L at $(c/r) = 0.420$

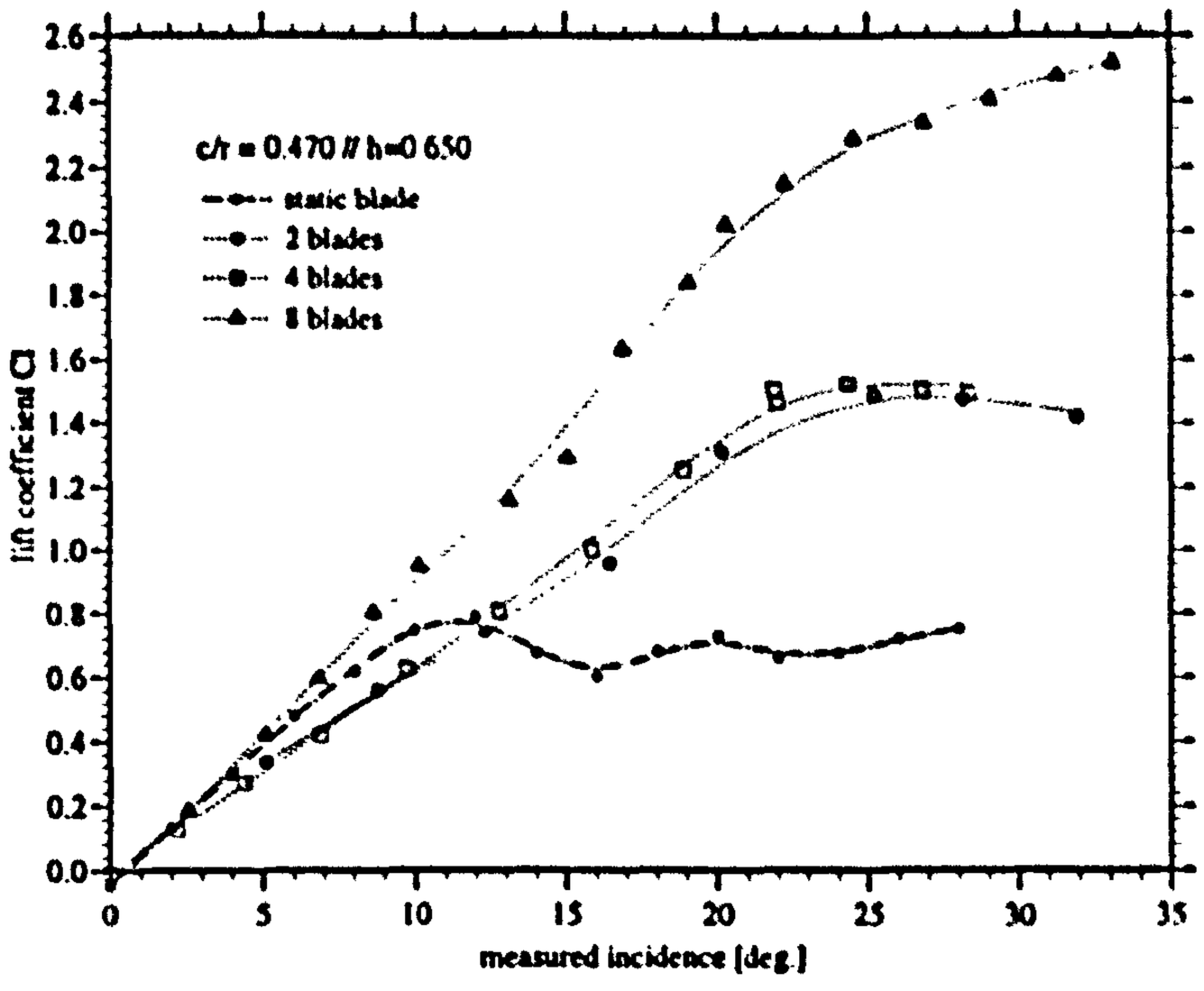

Figure 2.34: Effect of Rotor Solidity on C_L at $(c/r) = 0.470$

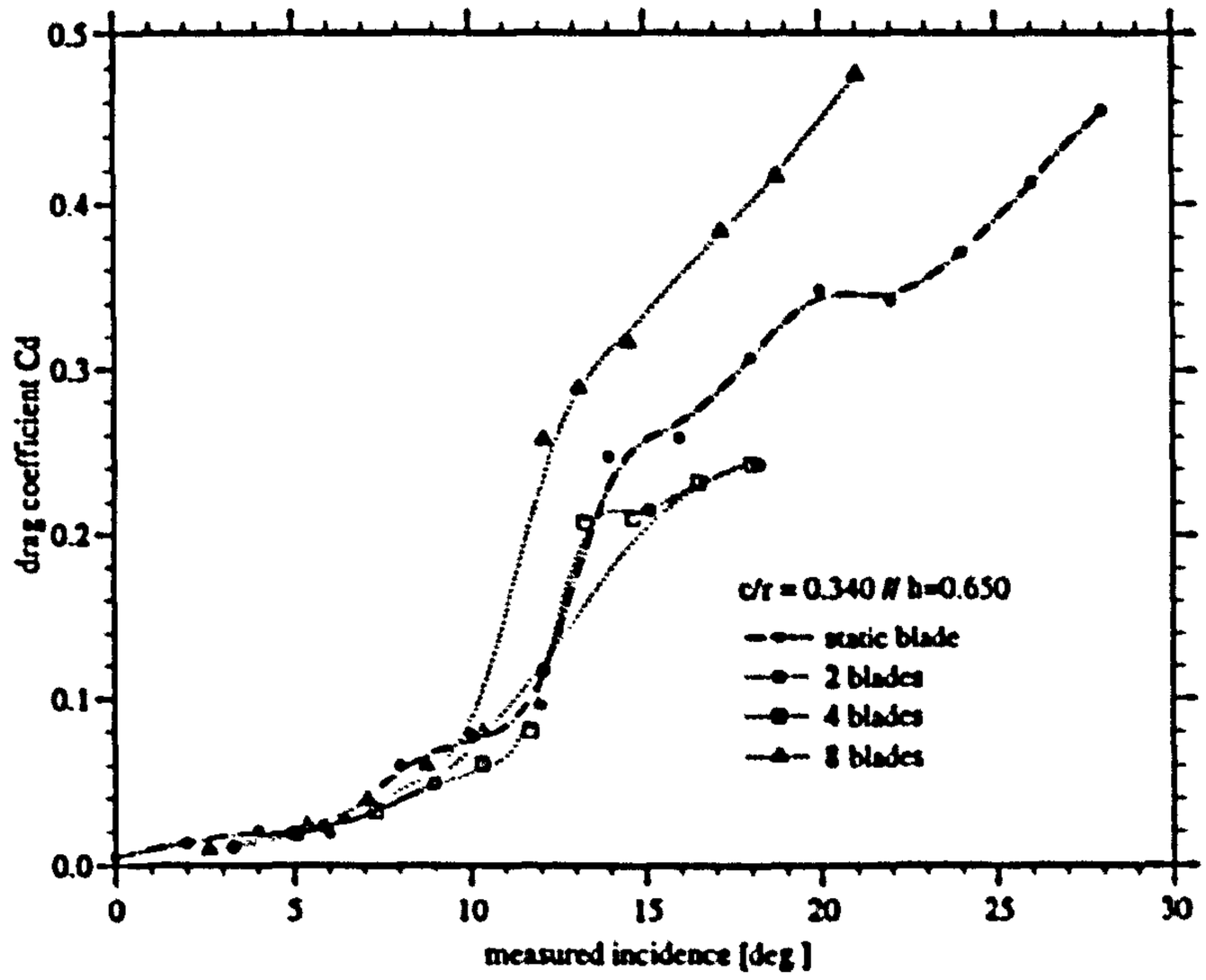

Figure 2.35: Effect of Rotor Solidity on C_D at $(c/r) = 0.340$

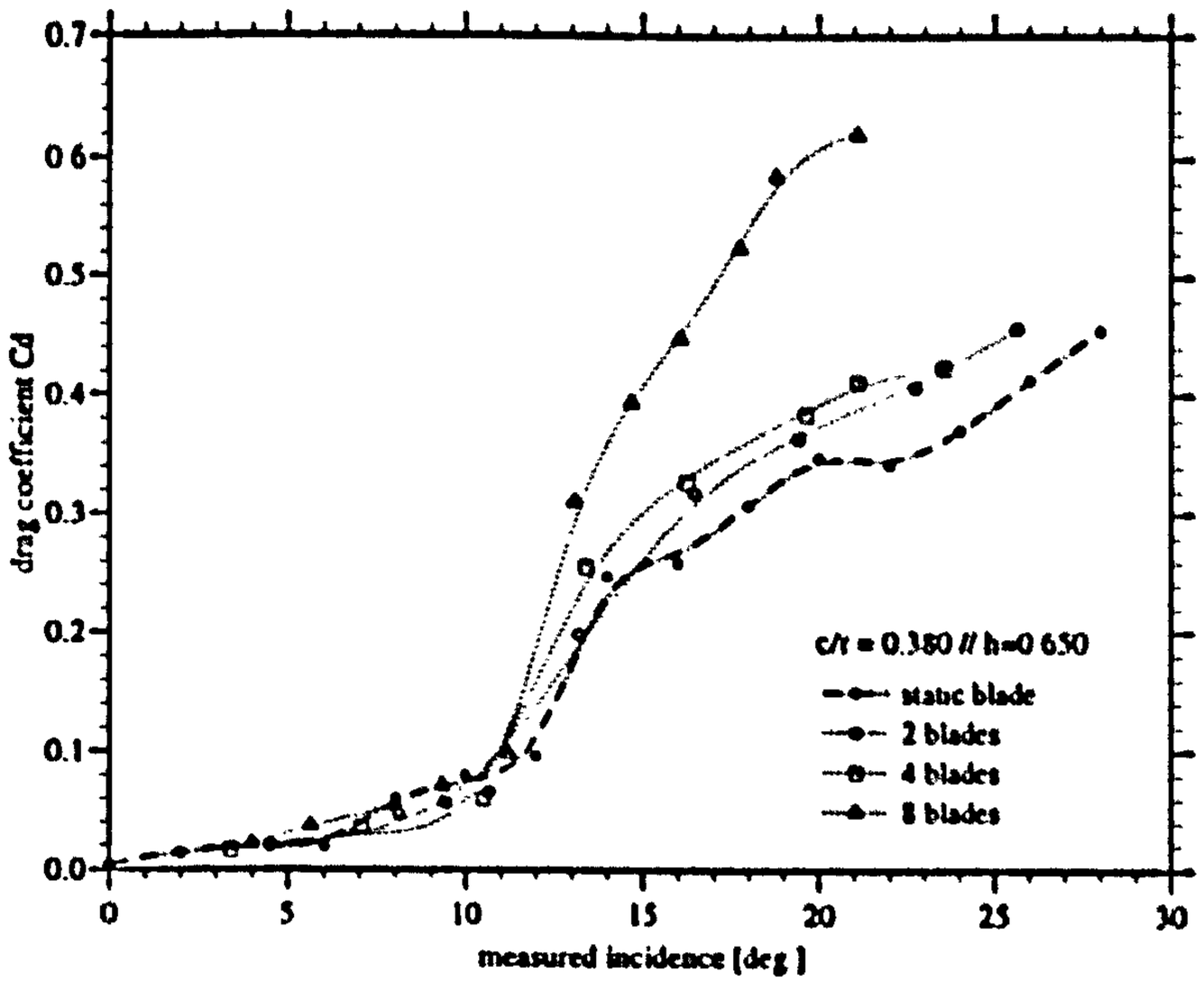

Figure 2.36: Effect of Rotor Solidity on C_D at $(c/r) = 0.380$

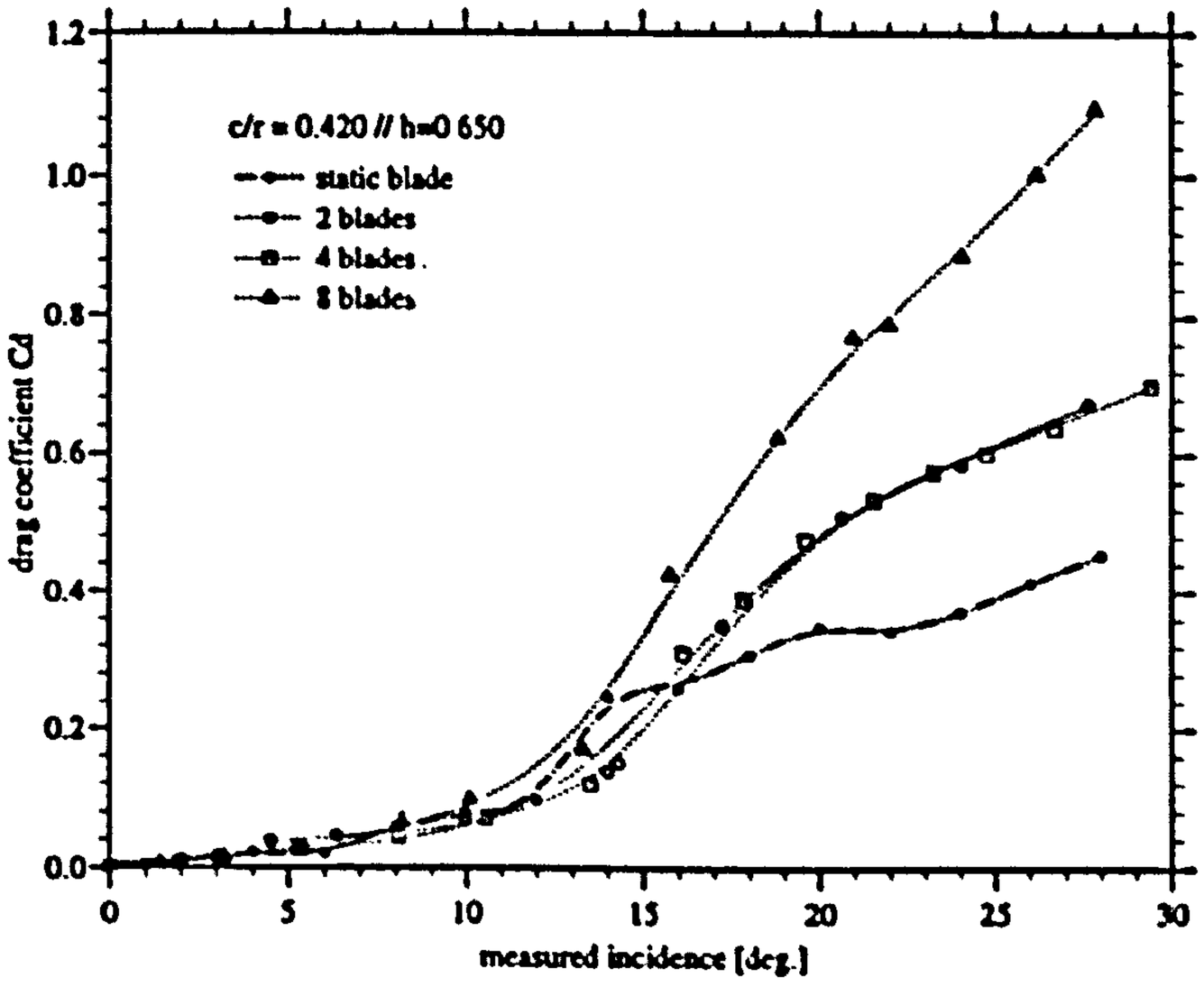

Figure 2.37: Effect of Rotor Solidity on C_D at $(c/r) = 0.420$

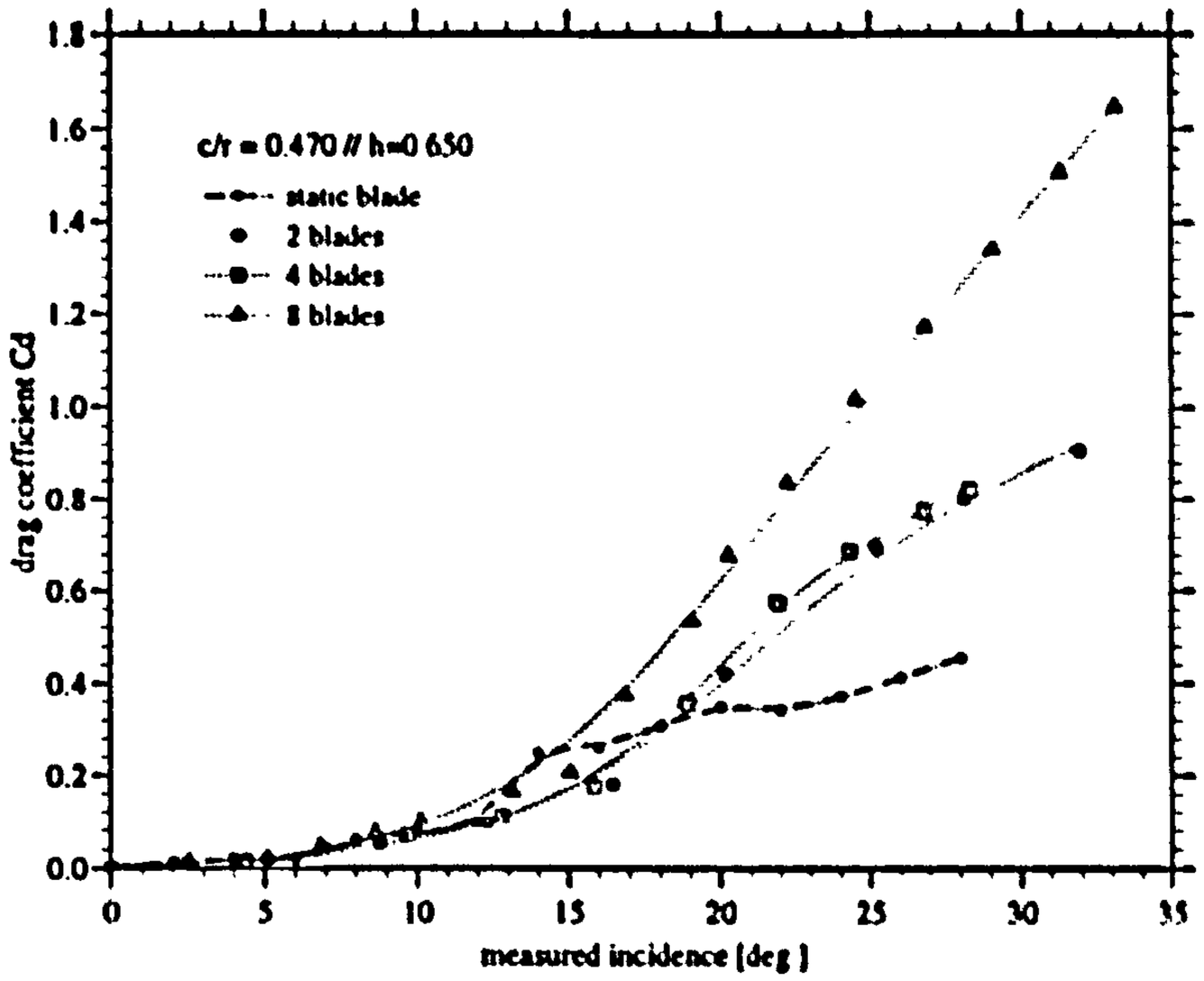

Figure 2.38: Effect of Rotor Solidity on C_D at $(c/r) = 0.470$

For these rotor configurations, therefore, any differences noted in comparison to the static blade characteristics are an indication of rotational effects only. On the other hand, this also implies that differences between the data recorded for the two lower solidity rotors tested and the 8 bladed rotor relate mainly to cascade effects. These were shown to be important for the interpretation of test results taken for the 8 bladed rotor.

As was discussed above for the 8 bladed rotor, the C_L curves for the 2 and 4 bladed rotors reveal that for the rotating blade C_{Lmax} and α_{max} are strong non-linear functions of (c/r). The values for these are significantly increased along the whole blade span except near the blade tip, compared with the static blade values. Since, C_{Lmax} and α_{max} are a measure of stall delay it is clear from the 2 and 4 bladed rotor data, that this effect is important for the aerodynamic performance even of low solidity Wells turbine rotors. As far as the physical explanation of the stall delay effect is concerned, the data presented above lends weight to the argument that the radial boundary layer flows by which it is caused are related to Coriolis forces rather than inviscid solidity effects.

Linear approximations to the presented pre-stall C_L curves suggest that for the rotating blades of the two lower solidity rotors the lift curve slope a_0 is around 3.9 $/rad$ while for the 8 bladed rotor it is around 5.3 $/rad$, a factor of 1.35 higher. This is in good agreement with the inviscid cascade theory, which applied to the respective mean solidities of the three rotor geometries predicts an increase of

a_0 by a factor of 1.3 . However, the the C_L curves also show that at high AOA the data recorded for the 8 bladed rotor is subject to solidity related effects, which are not described by the conventional cascade theory: While for the two low solidity rotors the C_L values do not increase for AOA higher than α_{max} the curves for the 8 bladed rotor show a steady increase for further increases in AOA and in the experimental range. In the above discussions of the recorded chord wise pressure distributions this was related to the increase in the rear loading of the local blade section at high AOA. Further, it was speculated earlier that this increase in rear loading was due to an increasing extent of radial flows in the boundary layer near the trailing edge of the rotating blade. However, the above comparison of the C_L curves recorded for the three rotor configurations suggests that this effect is caused by mutual influence of neighbouring blades and is likely to depend on the local blade circulation, which due to the stall delay effect at high AOA is considerable close to the rotor hub (- though, it is important to note that for these highly 3-dimensional flows the local circulation cannot be inferred from the Joukowski theorem and hence there is some ambiguity about the precise value of the circulation -) . From this it would be expected that chord wise rather than span wise velocity perturbations are induced due to this influence. To this extent the solidity effects at high AOA noted for the rotating blades might be interpreted in a manner similar to that described for static cascades by Ragunathan for pre-stall AOA, which in addition to an increase of the leading edge suction peaks also predicted an increase in the aerodynamic loading towards the trailing edge. In any case it is clear that at high local AOA for the high solidity rotor there are strong indications of interactions between the cascade effects and the radial flows with which the stall delay phenomenon is associated.

Figures (2.35) - (2.38) show that at low blade AOA the rotor solidity does not appreciably influence C_D. While the curves for the two low solidity rotors follow the static blade data fairly well at (c/r) values of 0.340 and 0.380 the curves also show that at larger AOA the C_D values at (c/r) values of 0.420 and 0.470 are increased over the static blade data. It is further evident from these figures that at high AOA there is a solidity effect on C_D.

Effects of Hub/Tip Ratio

Measurements were also carried out for 2,4 and 8 bladed rotor configurations which comprised a smaller nose cone for which $h = 0.560$. For the smaller nose cone measurements could be taken at an additional radial station given by $(c/r) = 0.55$. The solidities σ for the three rotor configurations with the reduced value of h were only slightly increased to 0.53, 0.26 and 0.13. Because h was changed by changing only the hub diameter D_h the tip solidity σ_t remained unchanged compared to the tests with the larger nose cone. The blade aspect

ratio $AR = (c/r_t)/(1-h)$ was reduced from 0.90 for the larger nose cone to 0.73. As a result, any differences in the C_L data between the two configurations is due to changes in h and AR.The C_L data recorded for the two different values of h is compared in figures (2.39) - (2.41) below.

It is apparent that for all three rotor configurations the C_L values at high local AOA are significantly increased for the smaller nose cone for all values of (c/r) except $(c/r) = 0.34$. This suggests that by reducing h the extent of radial flow occurring at high AOA on the down wind blade surface is increased at a given value of (c/r). Consequently, it may be concluded that the presence of the hub wall limits the extent of radial flow in the root region of the blade.

The pre-stall effect of h on C_L seems smaller by comparison and is related to the fairly insignificant change in σ. Within the data scatter it is assumed that a_0 is not affected by h for the three rotor configurations.

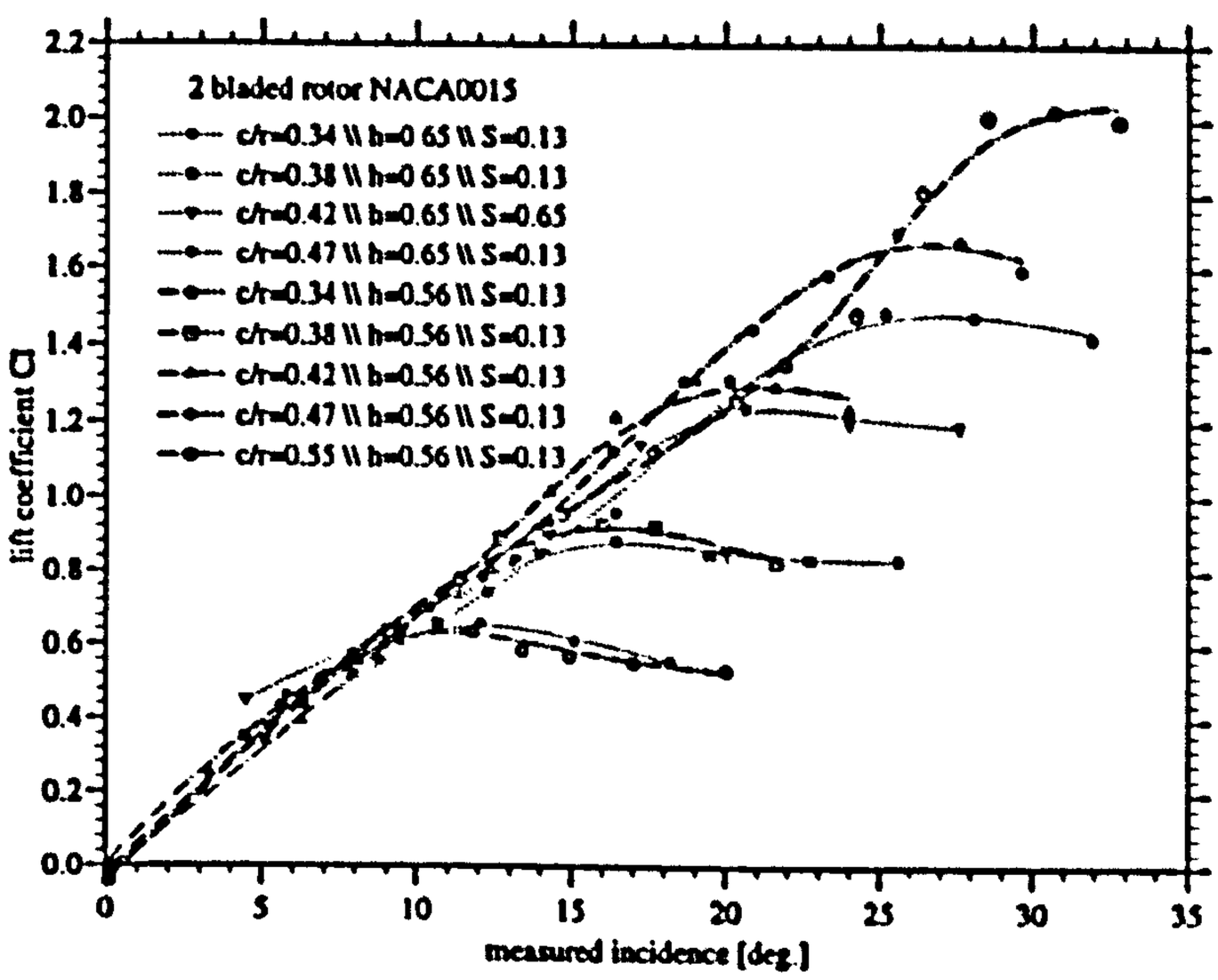

Figure 2.39: Effect of h on C_L For The 8 Bladed Rotor

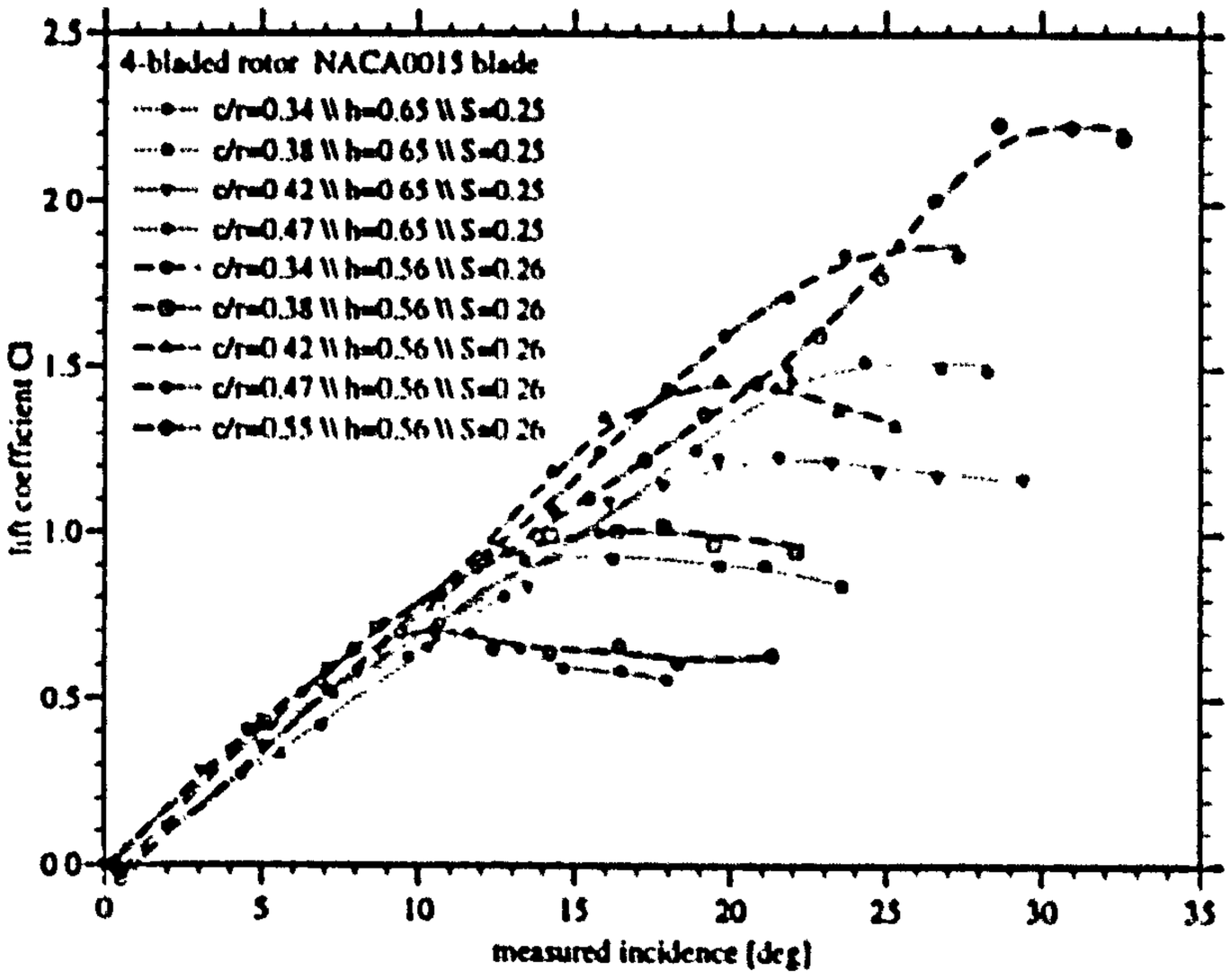

Figure 2.40: Effect of h on C_L For The 4 Bladed Rotor

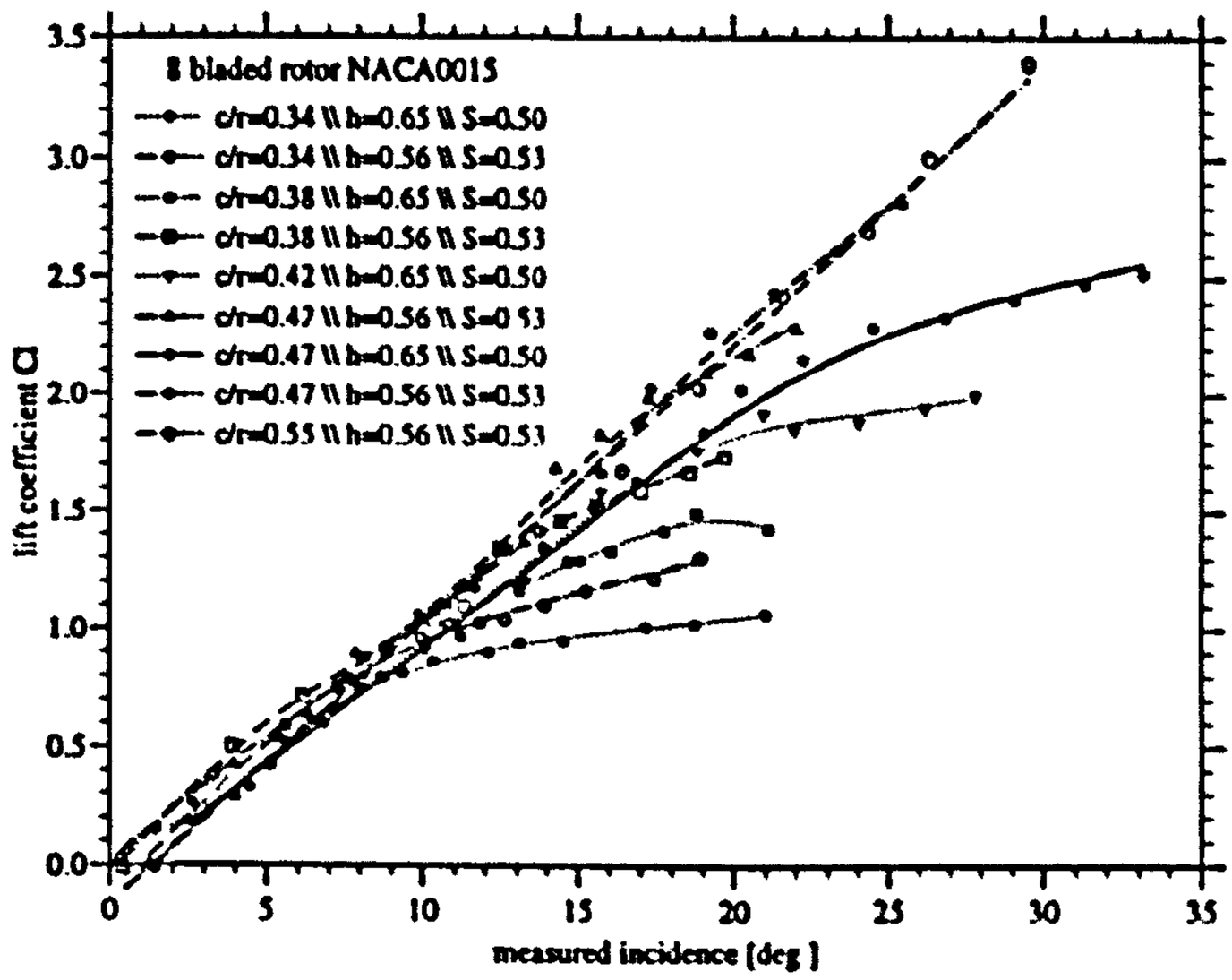

Figure 2.41: Effect of h on C_L For The 2 Bladed Rotor

Effects of Induced Velocities

In the previous report pages the variations of the blade surface pressure and the force coefficients were presented as a function of the geometric incidence α. As mentioned in the introduction to this section the rotor wake induces axial and circumferential velocities u_x and v_s in the plane of rotation due to which the blade sees an effective incidence α_e.

Swirl Velocity

In the introduction a theoretical analysis of the induced circumferential swirl velocity was given. This showed that locally the swirl velocity increases with the non-dimensional parameter (c/r) and with the blade lift coefficient C_L. Strictly, this theory is only applicable to attached flow and low angles of attack and there is considerable ambiguity about the swirl when the blade is operating at low values of Λ i.e. high local incidence. In particular this ambiguity arises because of the radial flows which occur in the separated boundary layers of the rotating blade.

Using equation(1.14) together with the experimentally measured local force coefficients and local blade incidences the swirl velocities and hence the effective blade incidences α_e were theoretically derived in an iterative procedure for each radial blade station. The results of these swirl calculations are summarised for the 8-bladed rotor with the larger nose cone for which $h = 0.650$ in figure (2.42) . This figure compares the measured C_L data versus uncorrected incidence α to the swirl-corrected C_L data versus the effective blade incidence. No corrected data is presented for higher blade incidences because, as pointed out in its derivation equation(1.14) only holds for lower incidences.

The figure suggests a certain extent of radial variation of the swirl effect. In particular it appears that at the outboard blade stations the induced swirl velocities are smaller than at the inboard blade sections.

It can further be seen that for pre-stall incidences the lift curve slopes at all radial stations are appreciably increased for the swirl corrected data compared to the values derived neglecting the swirl effects. It is also interesting to note that when including the swirl effects there seems to be a more pronounced radial variation of $\partial C_L/\partial\alpha$ between the tip and root regions of the blade. The depicted variation would suggest that $\partial C_L/\partial\alpha$ increases towards the blade root which may be expected from linear cascade theory.

Attempts were also made to experimentally determine the swirl velocity v_s

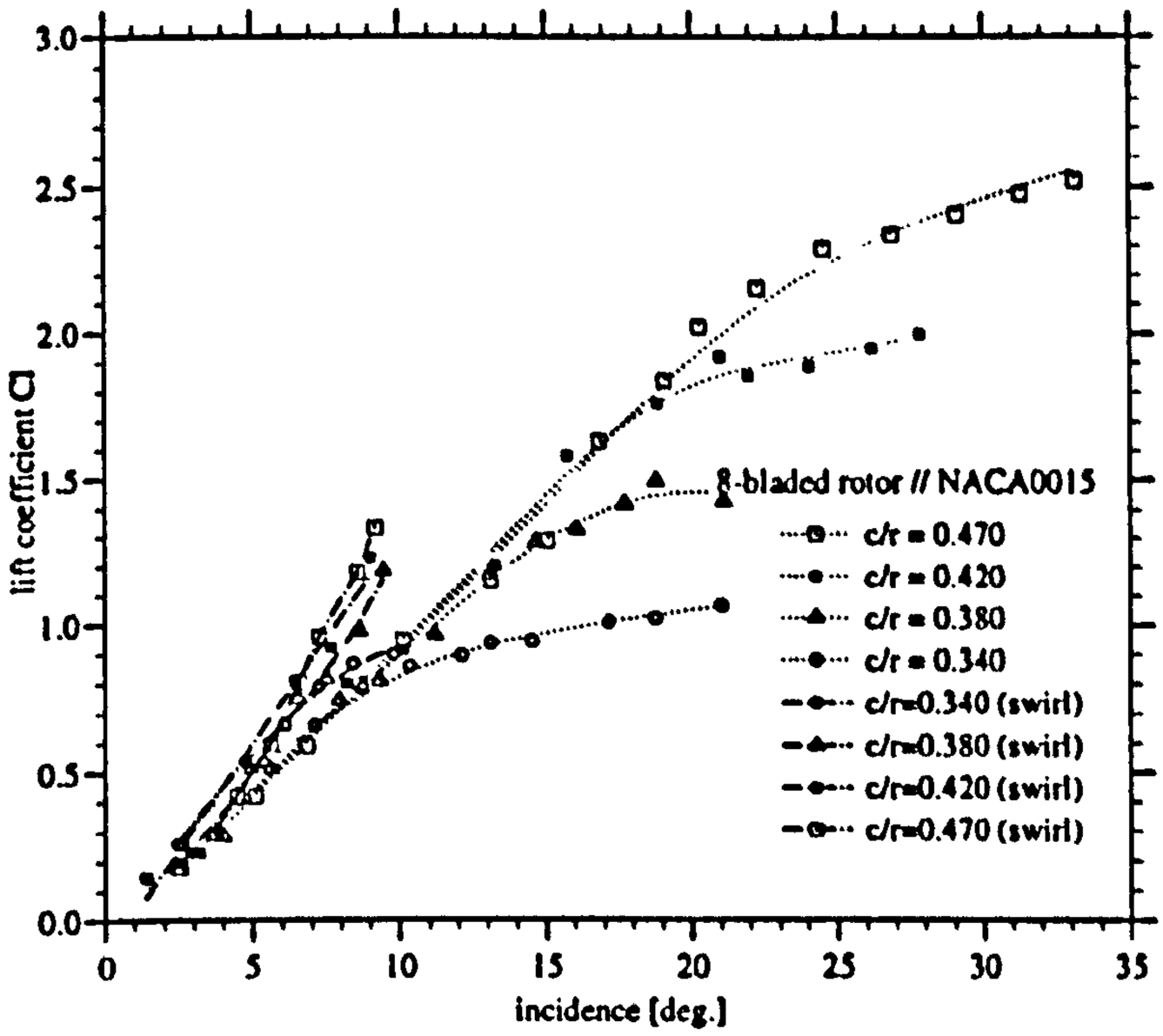

Figure 2.42: Swirl Corrected And Uncorrected C_L Data

applicable to the tested rotors by measuring the swirl angle γ_s. These measurements are briefly described in the following and were not intended as an exhaustive study of the wake flow but as an indicative exploration of the swirl effects, which are particularly important to the measurements for the 8 bladed Wells turbine rotor. As such, the experimental set-up implemented for this investigation was comparatively simple and the results presented in the following are not considered to be quantitatively very accurate.

A 5 hole probe was used to approximately measure γ_s nominally 1/2 D_T downstream of the turbine rotor. The probe was supported in the turbine duct from a rod which was adjustable in length so that the swirl could be measured at a number of span wise stations. At one end of the support rod an inclinometer was attached. The rod could be manually rotated from the outside of the tunnel test section thereby allowing the probe orientation to be adjusted in pitch. The experimental objective was to align the 5-hole probe with the local flow direction by progressive pitch adjustment and hence to obtain a reading for γ_s from the inclinometer for different flow rates and radial positions of the probe. By connecting two opposing total pressure tubes of the 5 hole probe to the two ports of a differential pressure transducer the probe could be judged to be aligned with the local flow direction when the transducer output voltage, read on a voltmeter, corresponded to the zero differential pressure voltage, which was registered pre-

vious to a particular test run.

Figure (2.43) shows the swirl angle measured for the 8 bladed rotor with $h = .650$ at three radial stations corresponding to $(c/r) = 0.340$ / 0.370 / 0.420 as a function of the local geometric (measured) blade incidence $\alpha = atan(V_x/U_t)$.

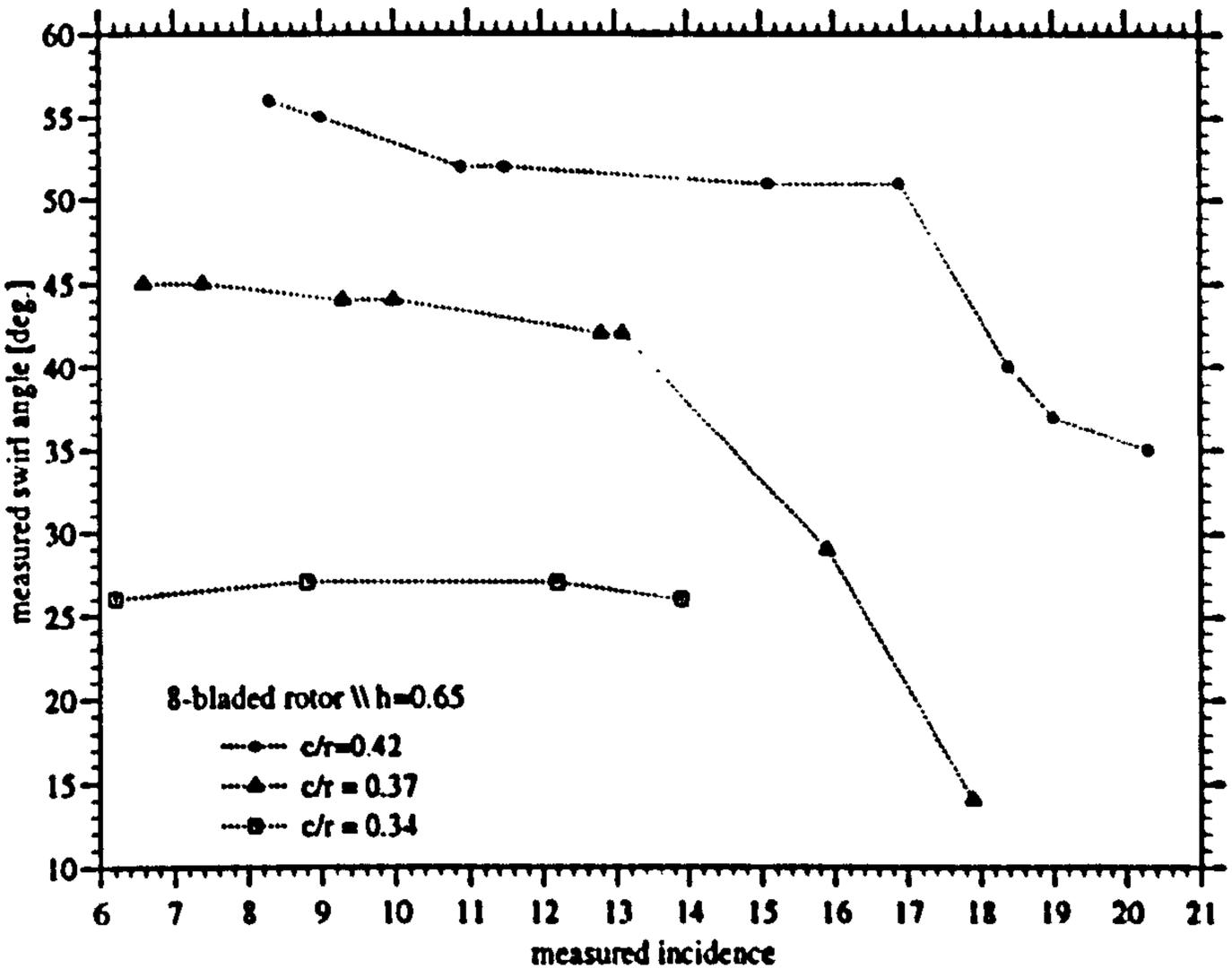

Figure 2.43: Variation of The Swirl Angle γ_s

Clearly this figure suggests that there is a strong non-linear dependency of γ_s on (c/r). It is evident that γ_s for a given value of α increases from the rotor hub to the tip. Also, it is interesting to note that within the data scatter $\partial\gamma_s/\partial\alpha$ is near constant at lower values of α. At higher values of α the curves for $(c/r) = 0.37$ and $(c/r) = 0.42$ signal a sharp decrease of γ_s. This indicates a strong change in the wake structure. By cross reference to the corresponding measured C_L vs α curves shown earlier it can be seen that the decrease in the γ_s curves coincides roughly with the onset of a decrease in the local $\partial C_L/\partial\alpha$. This feature of these curves was associated with the loss of the leading edge suction peak and the emergence of strong local radial flows on the downwind surface of the blade profile producing the stall delay effect.

The swirl velocity v_s is related to the swirl angle γ_s by

$$tan\gamma_s = \frac{v_s}{U_x} \tag{2.10}$$

Figure (2.44) shows the variation of v_s non-dimensionalised by the local tangential velocity of the blade U_t with α derived from the measured values of γ_s (noting that $\gamma_s|_{rotor} = (1/2)\gamma_s|_{wake}$).

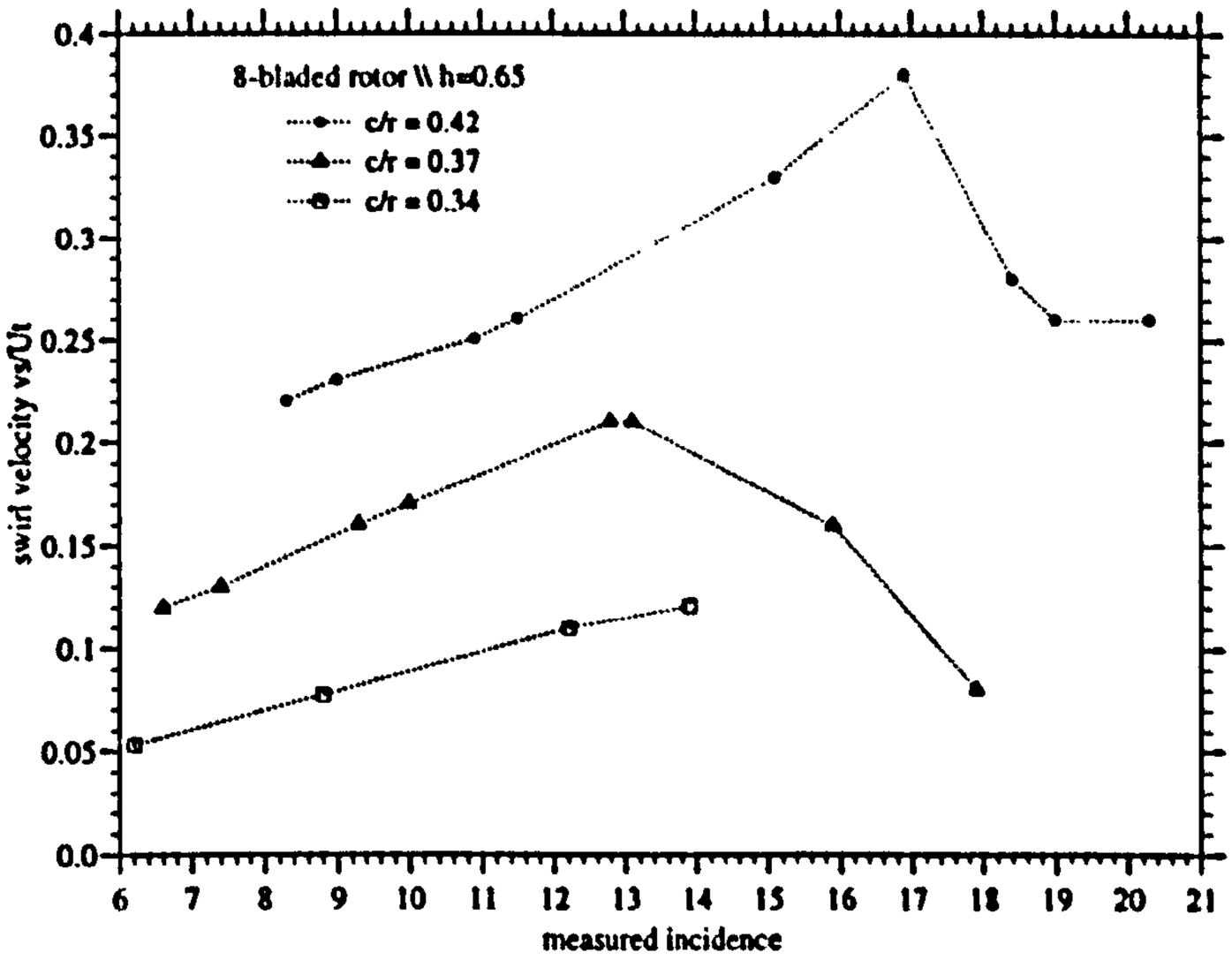

Figure 2.44: Variation of The Swirl Velocity v_s

It can be seen that the swirl velocities for the 8 bladed rotor configuration are considerable, particularly at $(c/r) = 0.42$ where the derived values of v_s reach almost 40% of the tangential speed of the blade. As would be expected from the theory given earlier it is apparent from these curves that for lower local blade incidences v_s increases with (c/r) and C_L. However, eventhough it was found earlier that due to the stall delay effect locally the blade can sustain high values of C_L at post stall incidences, the swirl velocity reaches a distinct maximum, which occurs just before the recorded blade surface pressures indicate the loss of the leading edge suction pressure. It is clear, therefore, that once the radial flows are established on the rotating turbine blades the theoretical analysis relating v_s to C_L is no longer valid.

Figure (2.45) below shows the incremental corrections $\Delta\alpha$ which need to be applied to the geometric incidence α to account for the effect of v_s which acts to locally reduce the blade incidence. It is evident that while at the tip the required correction is fairly small (at max. 0.5 [deg]) towards the rotor hub $\Delta\alpha$ is significantly higher and reaches up to approximately 2.5 [deg] at $(c/r) = 0.42$.

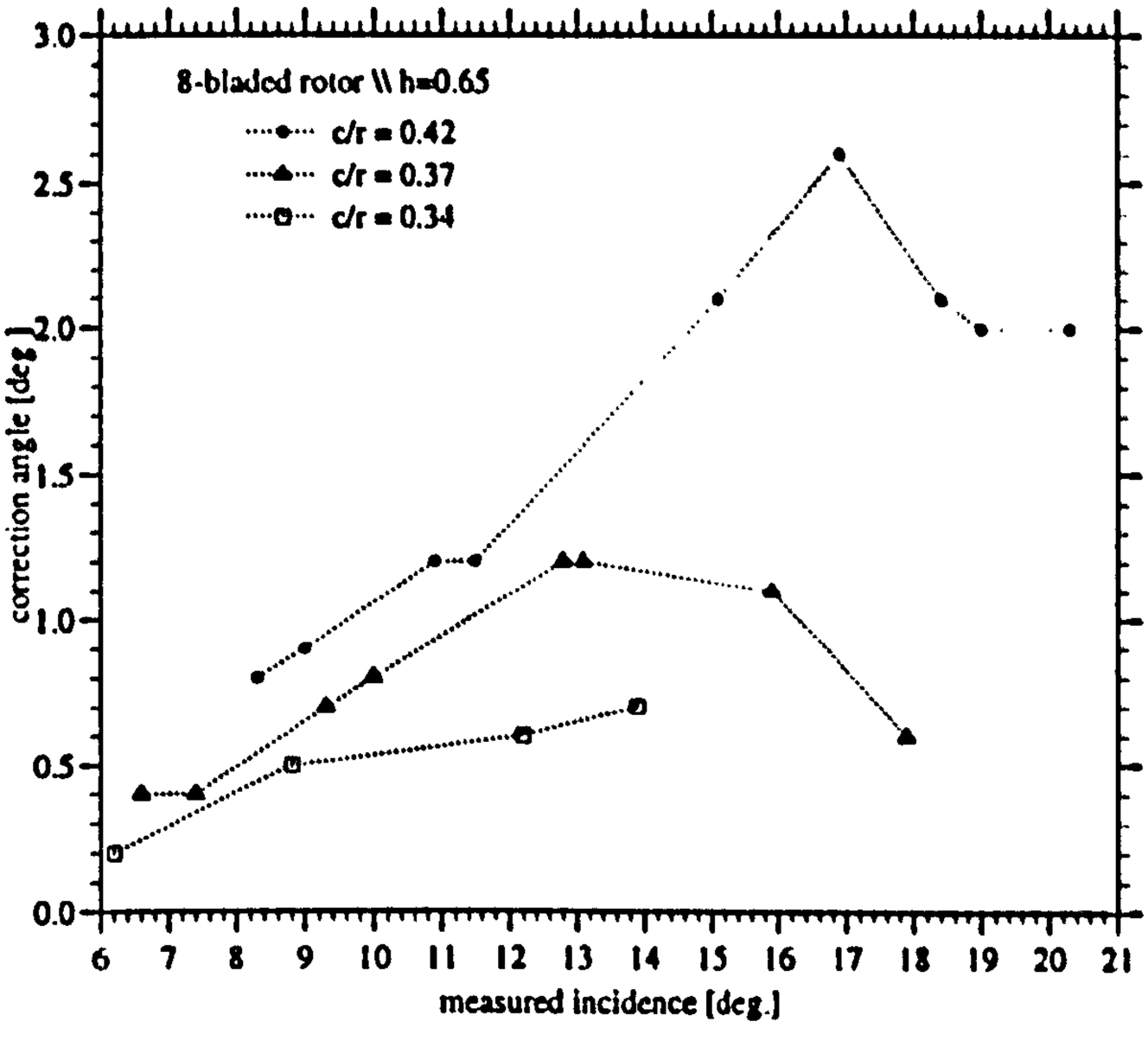

Figure 2.45: Variation of The Correction Angle $\Delta\alpha$

The measured radial variation of the swirl correction angle $\Delta\alpha$ explains the radial variation of $\alpha_{\hat{C}pmin}$, the incidence at which locally the blade pressure distributions signalled a loss of the leading edge pressure peak, which for the 8 bladed rotor configuration was noted to be of the same order.

The swirl angle was experimentally measured for all tested rotor configurations by the method described above. Figure (2.46) gives a comparison of the measured swirl velocities at different radial stations for the 8, 4 and 2 bladed rotor configurations with the smaller of the two tested nose cone diameters for which $h = 0.560$.

The curves reveal a strong solidity dependency of the swirl effect. The data recorded at $(c/r) = 0.350$ and $(c/r) = 0.380$ shows that the swirl velocity rapidly decreases when these blade sections have stalled locally and for large incidences is nominally zero. This indicates a dramatic change of the rotor wake structure at high flow rates i.e. low tip speed ratios.

At large local blade incidences the swirl data measured at the more inboard radial stations $(c/r) = 0.410$ for the 8 and 4 bladed rotors and $(c/r) = 0.470$ for the 2 bladed rotor at which the local blade force data discussed earlier showed delayed stall, interestingly, suggests that for all three rotors there is still a sig-

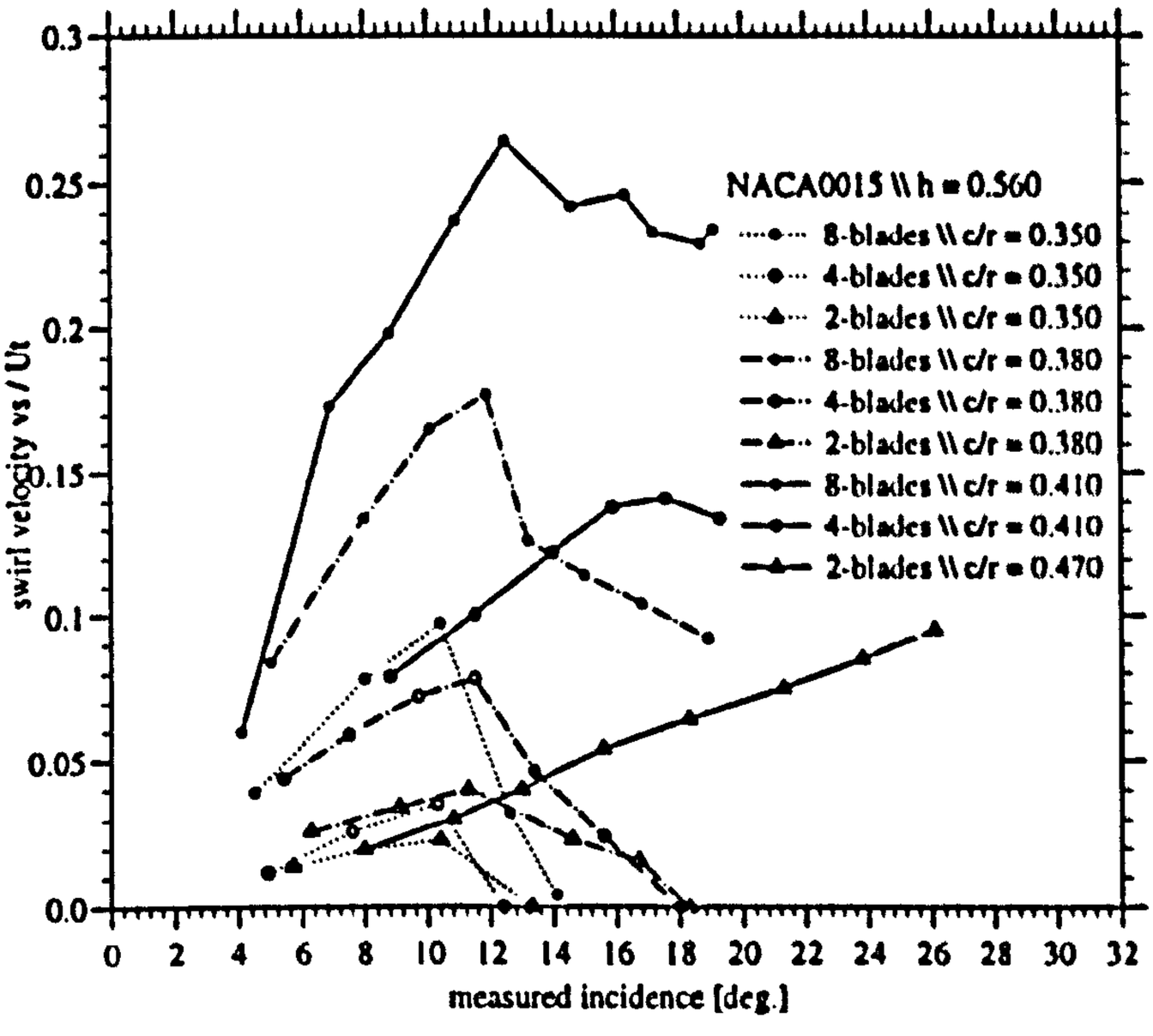

Figure 2.46: Variation of The Swirl Velocities v_s

nificant swirl effect. An apparent interpretation of this may be that close to the hub at large flow rates which cause post stall angles of attack there is still a considerable amount of blade circulation that sheds into the rotor wake and to which the swirl effect relates.

Induced Axial Velocity

A theory was also given earlier in the report which relates u_x to the normal force coefficient C_N acting on the rotor blades. From this theory it was apparent that u_x may be expected to vary with the rotor solidity and of the rotor configurations tested is highest for the 8 bladed rotor.

Equations(1.6) and (1.8) were used in conjunction with the C_N force data presented earlier in the report for the 8 bladed rotor with $h = 0.650$ to estimate u_x and hence V_{xe}, the effective axial velocity in the plane of blade rotation. The values of V_{xe} deduced at radial positions at which the Cp distributions were measured are shown as a fraction of $U_t(tip)$ in figure (2.47) for a nominal tip speed ratio of 5.7 . Qualitatively the depicted increase of V_{xe} of 28% compared to the mean close to the blade tip and decrease of 22% near the blade root are in good agreement with the data presented by Ragunathan (1995) for a high solidity

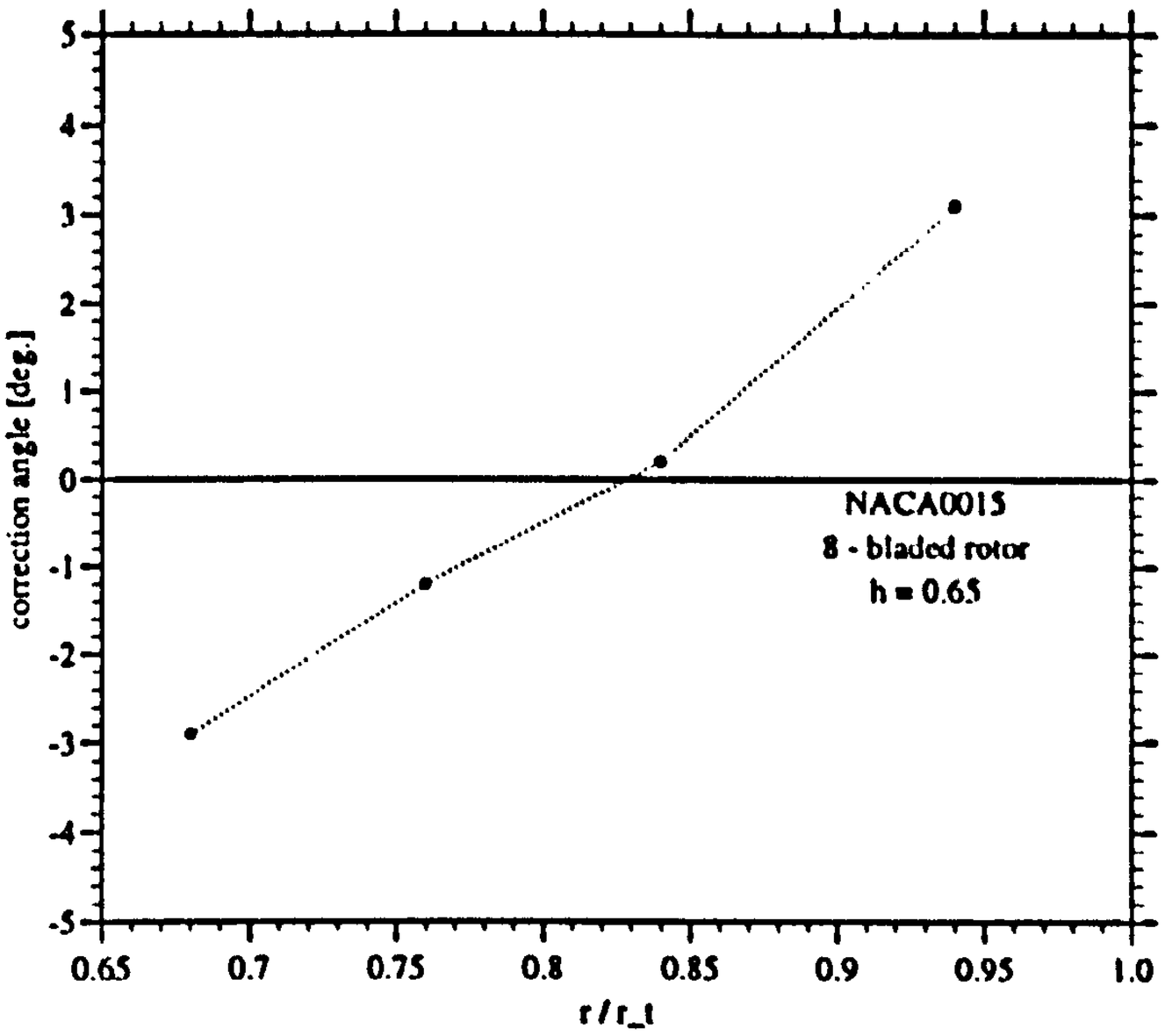

Figure 2.48: Incremental Incidence $\Delta\alpha$

2.4 Concluding Remarks

The experimental work reported on in this chapter was intended to provide a fundamental study of the aerodynamic characteristics of a rotating Wells turbine blade that define the rotor performance characteristics in steady, unidirectional ducted flow. A model scale wind tunnel experiment was purposely designed and constructed, which allowed the steady chord wise static surface pressure distributions to be measured reliably at a number of radial positions on a rotating NACA0015 sectioned turbine blade over a range of flow rates, rotor solidities and for two different hub/tip ratios.

It was shown in the course of these measurements that in steady, unidirectional flow the Wells turbine stall is largely steady and free of hysteresis effects.

The characteristics of the experimentally recorded chord wise Cp distributions, which in the text were presented for an 8 bladed rotor, at pre-stall blade incidences (i.e. at high tip speed ratios) resembled those measured separately for the static blade. They could be qualitatively well explained by the theoretical and experimental analysis provided by other researchers for an aerofoil operating in a 2D static cascade, which forms the basis for conventional performance prediction methods applied to the Wells turbine in ducted flow and which has been

discussed in the introduction.

At higher measured blade incidences the Cp distributions differed radically from those of the static blade at equivalent angles of attack in that they revealed a considerable extent of remarkably high upper surface suction particularly at the inboard sections of the rotating blade. These Cp distributions could not be explained from the conventional 2D linear cascade theory, which does not account for effects due to the blade rotation. However, due to the strong qualitative resemblance noted between the Cp distributions measured on the Wells turbine blade and those which have been published by other researchers for rotating wind turbine blades, the stall delay phenomenon which is comparatively well understood for wind turbine rotors could be inferred as an explanation.

The local C_L values derived from the measured Cp distributions confirmed that for high tip speed ratios there are linear cascade effects, which are strong for high solidity turbines such as the 8 bladed rotor tested. These were qualitatively and quantitatively well described by the conventional 2D cascade theory. Further, the measurements showed that for high tip speed ratios cascade effects on C_D are negligible.

For lower tip speed ratios for which a significant portion of the blade operates at post-stall angles of attack, the delayed stall, which was confirmed to depend on (c/r) and was found to be particularly strong for (c/r) values greater than 0.340, causes local C_L values to be considerably higher than those derived for the static blade section. A comparison of the data recorded for the 2, 4, and 8 bladed rotors revealed that on high solidity Wells turbine rotors operating at low tip speed ratio there are strong post-stall cascade effects on C_L and C_D. This comparison also gave a clear indication that the stall delay effects which occur at low tip speed ratios strongly interact with cascade effects.

It was found by comparing the data recorded in the experimental work for two different sized nose cones that by reducing the hub/tip ratio the extent of radial flow that occurs at low tip speed ratios over the inboard part of the rotating blade is increased, while the tip flow is relatively unaffected.

The experimental and theoretical investigations of the axial and swirl velocities induced by the rotor wake in the rotor plane showed that for a high solidity Wells turbine appreciable corrections need to be applied to the local geometric blade incidence, which is conventionally derived using the radial equilibrium approach and neglecting wake effects, to obtain the local effective blade incidences. In particular it was found that for all flow rates and rotor solidities tested the swirl velocities at the blade tips are small compared with those at the blade root, which for the highest solidity were considerable.

Chapter 3

The Wells Turbine Performance in Unducted Oscillatory Flow

The research work reported on in the following chapters has investigated an unconventional arrangement of the Wells turbine in which it was used to convert energy directly from oscillatory water flow (waves) in an unducted configuration. Previous to the current work no published numerical or experimental analysis of the hydrodynamic performance of the Wells turbine in this type of application was available. In order to enable potential future applications of this type of turbine arrangement as a wave power device to be assessed some fundamental research of the hydrodynamic characteristics of a mono plane unducted Wells turbine rotor in axial oscillatory water flow was therefore required.

From preliminary considerations it seemed likely that in this type of application the Wells turbine will operate in small to moderate KC flows. In analogy with the flow structures that are known to occur for flat disks in oscillatory flow it seemed apparent that in this case the vortex wake of the rotor would have a great influence on the turbine performance. Since no relevant data for the turbine performance in this arrangement was available it was important as a first step in obtaining a basic physical understanding of the hydrodynamic behaviour of the turbine in unducted oscillatory flow to experimentally measure, at model scale, the rotor shaft power over a range of flow regimes and geometric configurations.

It was in principle considered possible to apply more sophisticated numerical models such as e.g. vortex lattice codes to study the basic flow physics that governs the rotor/wake interactions in this type of Wells turbine arrangement. However, as a first step in gaining an understanding of the ideal fluid dynamic performance of the unducted Wells turbine in small to moderate KC flows it seemed desirable to develop a more simple computationally less expensive numerical model which could be validated against the experimentally measured data.

Both, numerical and model scale experimental work was carried out to promote a first physical understanding of the performance of unducted Wells turbines in oscillatory water flows. This work is reported on the following chapter of this thesis.

3.1 Research Objectives

The main aim of the work reported on in the following chapter was to provide a physical understanding of the fluid dynamic phenomena that govern the performance of an unducted Wells turbine in sinusoidal flow over a range of low to moderate KC flows through experimental and numerical work.

For that purpose the shaft power of a Wells turbine was to be experimentally measured at model scale over a range of rotor tip speed ratios and small to moderate KC flows. Further, flow visualisation experiments were to be carried out to provide an insight into the flow structures that affect the hydrodynamic behaviour of the rotor.

The experimental data was to be used to develop and verify a computationally inexpensive numerical model similar to the actuator disc theory or BET for unidirectional flow.

3.2 Theory

3.2.1 The Actuator Disc Theory

An in depth theoretical study of the fluid dynamic performance of an unducted axial flow turbine in oscillatory flow using a full Navier-Stokes numerical simulation requires fairly complex analysis, would be computationally very expensive and is beyond the scope of the current work objectives. In the absence of any published numerical treatment so far of this kind of flow problem it seemed desirable to develop initially a conceptually simple analytical scheme to model the performance of unducted Wells turbine configurations.

As a first step, therefore, a theoretical model was developed for the turbine performance for small to moderate amplitude oscillating flows which in analytical complexity is at the level of the actuator disc theory developed for unidirectional steady flow by Glauert (1947). In analogy with this performance model for unidirectional flow a number of simplifying assumptions were made to develop the

theory: the rotor itself is assumed to have a large number n of high aspect ratio blades so that it resembles an actuator disc. For the flow through the disc the axial velocity is considered to be uniform over the whole disc area and continuous. The fluid is treated as incompressible, inviscid and irrotational.

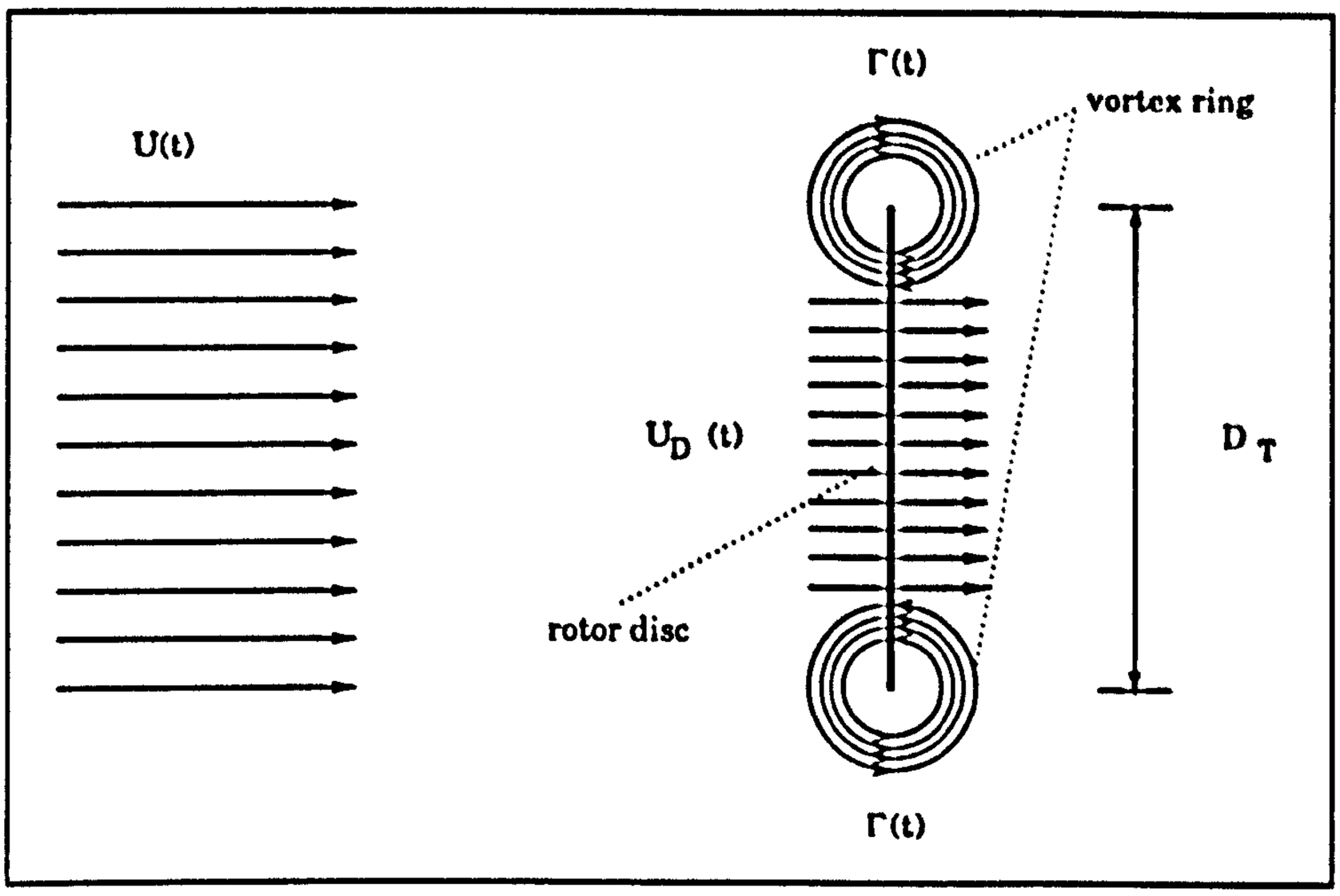

Figure 3.1: The Actuator Disc Model For Oscillatory Flow

Figure (3.1) schematically shows the incident free stream velocity $U(t)$, and the axial velocity $U_D(t)$ at the rotor disc, which has a diameter D_T. The free stream varies sinusoidally with time with a constant velocity amplitude U_0 and constant period $T = 2\pi/\omega$:

$$U(t) = U_0 sin(\omega t)$$

As a first step in developing the theory we can consider an elemental section dr of a constant chord, untwisted rotor blade, located at a distance r from the axis of rotation. If the rotor blades are rotating at a constant angular velocity Ω then the components of the resultant velocity $W(r,t)$ incident to a blade element are as shown in figure (3.2). It needs to be observed at this point that effects of wake rotation and induced swirl, which for unidirectional flow past horizontal axis wind turbines are usually found to be small, are not included in the model. In accordance with the conventional blade element approach which assumes radial stream tube independence the section is treated as an aerofoil which produces lift force $dL(r,t)$ and drag force $dD(r,t)$. As also illustrated in figure (3.2) these are resolved into axial and tangential force components, denominated $dF_X(r,t)$ and $dF_T(r,t)$. If for attached flow (i.e. high tip speed ratio operation) the drag

of the acrofoil is neglected then

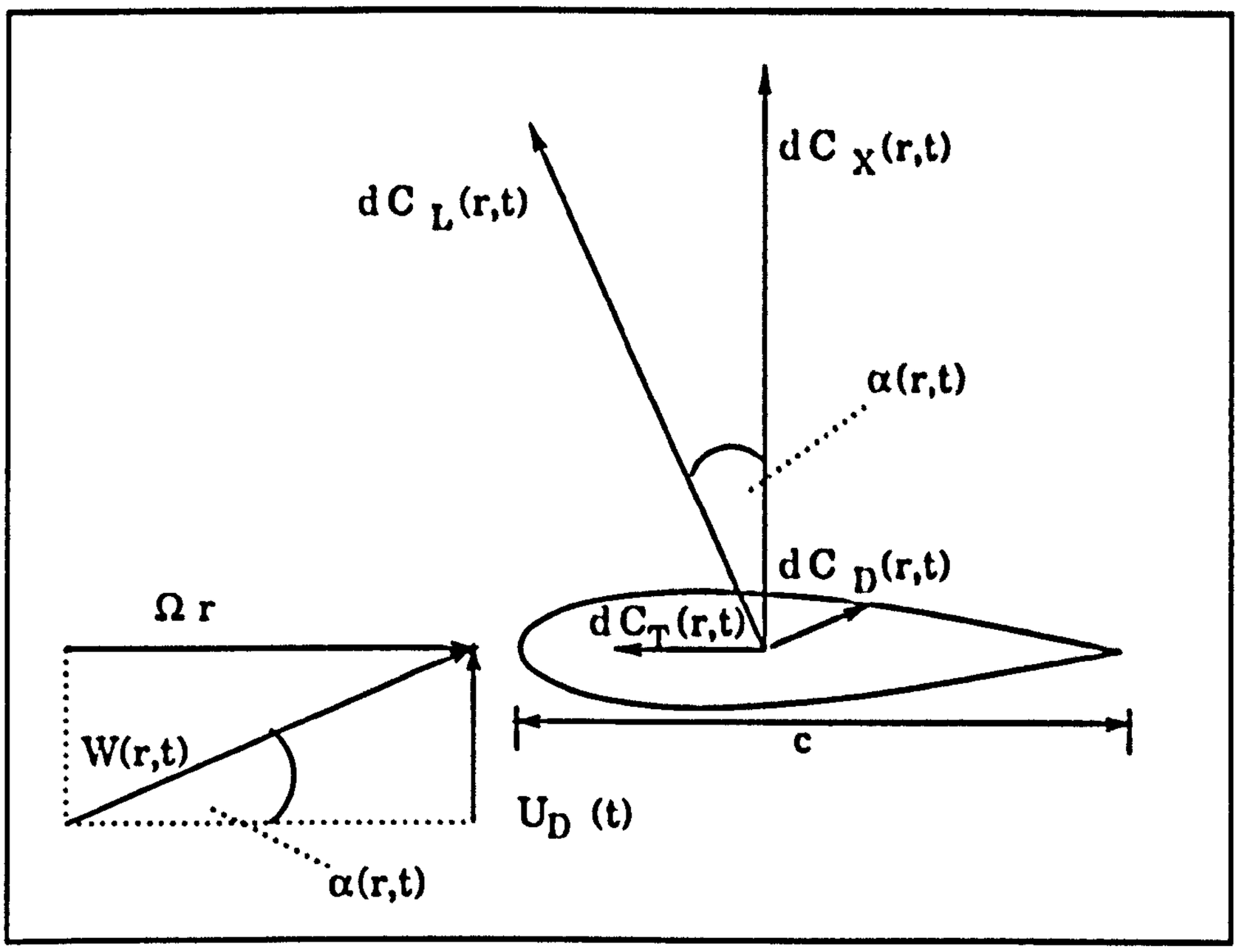

Figure 3.2: Blade Forces

$$(3.1) \qquad dF_T(r,t) = dL(r,t)sin\alpha(r,t) = 0.5\rho W(r,t)^2 c\frac{U_D(t)}{W(r,t)}dC_L(r,t)$$

$$(3.2) \qquad dF_X(r,t) = dL(r,t)cos\alpha(r,t) = 0.5\rho W(r,t)^2 c\frac{\Omega r}{W(r,t)}dC_L(r,t)$$

where

$\alpha(r,t)$:	local blade incidence
ρ :	fluid density
c :	blade chord
$dCL(r,t)$:	$dL(r/t)/(0.5\rho W(r,t)^2 c)$

The power produced by this blade element is then

$$(3.3) \qquad dP(r,t) = \Omega r dF_T(r,t) = U_D(t)dF_X(r,t)$$

As schematised in figure (3.3) the rotor blades have a bound circulation $\Delta\Gamma(r,t)$. For the purpose of this simple model we now assume the blade circulation Γ to be constant along the blade span so that the total circulation Γ is

thus shed at the tip of each blade and at the root $r = 0$ but nowhere else. The shed vorticity of from the tip of each blade forms an approximately helical vortex wake of strength $\Delta\Gamma$. If, as assumed, the rotor has a large number of blades then the helical vortices of strength $\Delta\Gamma$ may be approximated by a uniform cylindrical vortex sheet. Further, if now the amplitude of the oscillatory free stream flow is small enough , this vortex sheet can be idealised as a single vortex ring. This idealisation is justified since the cylindrical vortex sheet would develop very small stream wise extent before flow reversal convected it back towards the rotor plane. The amplitude A of the incident oscillatory flow will be defined as for oscillatory flows about fixed bodies by the Keulegan-Carpenter number as $KC = \pi A/D_T$ and for sinusoidal flow $KC = U_0 T/2R_T$. Since for low KC flows the vortex wake is expected to convect only a small distance away from the plane of rotation, in the following theoretical analysis, therefore, as schematised in figure (3.1) it will be assumed that the vortex ring is fixed in the rotor plane and has a constant radius equal to that of the blade tips.

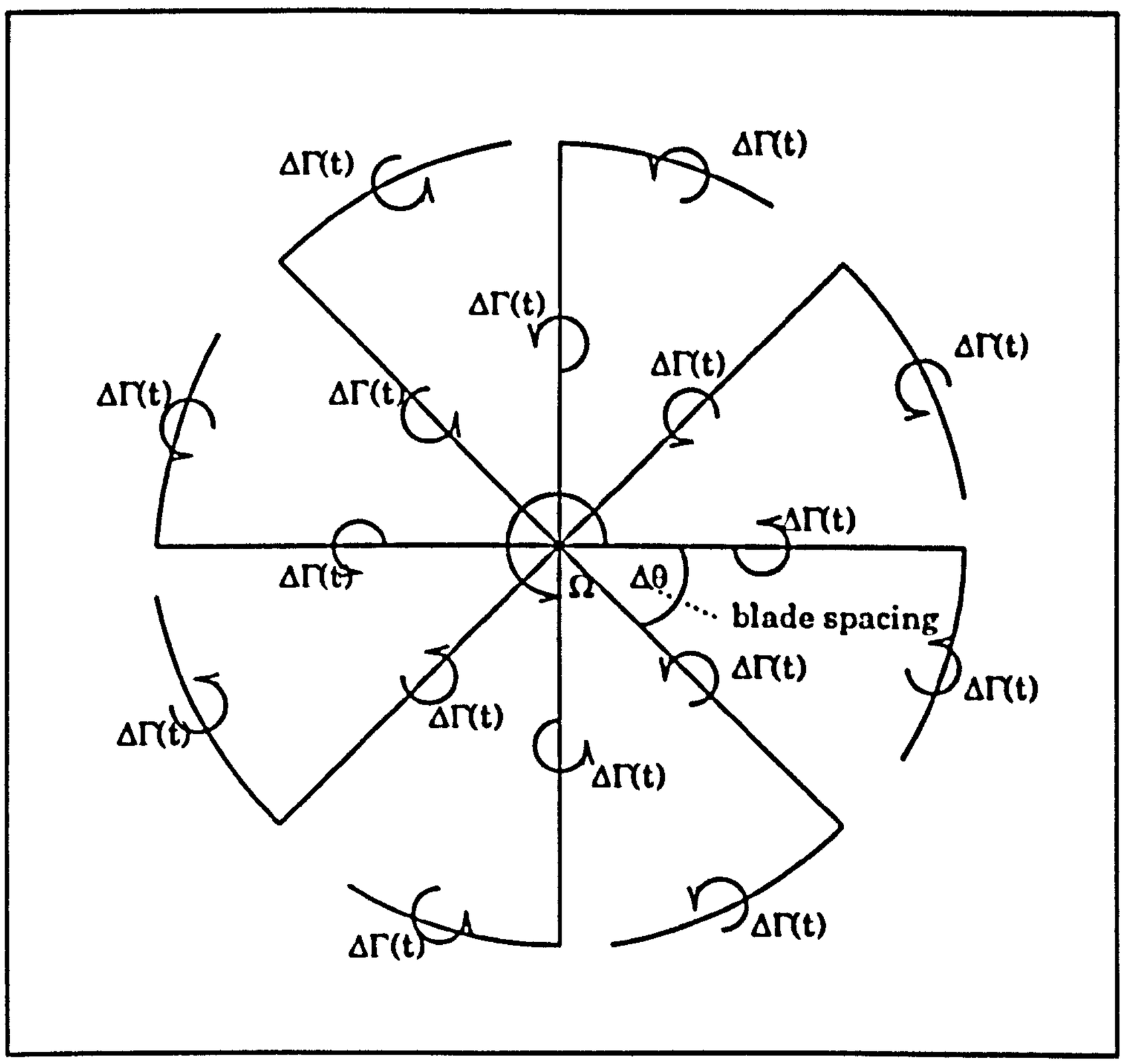

Figure 3.3: Blade Circulation

Therefore, the model of the rotor is an actuator disc with its wake (on both sides) combined into a vortex ring of time varying strength around the perimeter of the disc. The vorticity shed from the blade roots forms axial vorticity (on $r = 0$). This is of small extent (for low KC) and only generates a small swirl ignored in this part of the analysis. Finally, the model is completed by span wise vorticity shed from the blades as there circulation changes with time. For a rotor with large numbers of blades the velocity induced by these is again mainly swirl.

In order to calculate the power produced by each blade element from equation (3.3) the flow velocity through the rotor disc $U_D(t)$ must be determined. Due to the action of the vortex ring the net flow is

$$U_D(t) = U(t) - U_\Gamma(r,t) \tag{3.4}$$

$U_\Gamma(r,t)$ is the axial component of velocity induced by the vortex ring. $U_\Gamma(r,t)$ does not vary greatly along the blade span but it will be assumed that the value induced on the axis $r = 0$ is fairly representative of values over the whole rotor disc. This assumption means that in the numerical model there is no radial variation of $U_D(t)$. Using the Biot-Savart law it can easily be shown that the velocity a vortex ring of strength Γ and radius R_T induces on its centreline is equal to $\Gamma/2R_T$. The flow velocity through the rotor disc can according to this argument be approximated by

$$U_D(t) = U(t) - \frac{\Gamma}{2R_T} \tag{3.5}$$

where R_T is the tip radius.

Neglecting unsteady aerodynamic effects the lift of the blade element $dL(r,t)$ may be related to its bound circulation $\Delta\Gamma(t)$ through the Joukowski theorem for steady flow

$$dL(r,t) = \rho\, W(r,t)\, \Delta\Gamma(t) \tag{3.6}$$

The lift coefficient C_L is defined as $C_L = L/(1/2\rho W^2 c)$ and according to 2D steady thin aerofoil theory is equal to $2\pi sin\alpha$ for inviscid, attached flow. Also from figure (3.2) it can be seen that $W = U_D sin\alpha$ so that using equation (3.6) it can be shown that if unsteady effects and cascade effects are neglected and it is assumed that the blades are of high aspect ratio :

$$\Delta\Gamma(t) = \pi\, U_D(t)\, c \tag{3.7}$$

This means that since $U_D(t)$ is taken to be constant along the blade span the assumption that the blade circulation does also not vary radially is not a bad one for a rectangular blade with constant chord c.

For the whole blade the total lift $L(t)$ is given by

$$L(t) = \rho \int_0^{R_T} W(r,t)\, \Delta\Gamma(t)\, dr \tag{3.8}$$

The total axial force acting on all of the n blades $F_X(t)$ using equation (3.2) is

$$F_X(t) = \frac{n}{2} \rho \Omega R_T^2 \Delta\Gamma(t) \tag{3.9}$$

From the geometrical definitions in figure (3.3) it is seen that

$$n = \frac{2\pi}{\Delta\theta} \tag{3.10}$$

where $\Delta\theta$ is the angular spacing of the blades. If Δt is the time during which the rotor blades move through $\Delta\theta$ so that the geometry of the flow is reproduced then:

$$\Omega = \frac{\Delta\theta}{\Delta t} \tag{3.11}$$

and it follows that

$$F_X(t) = \pi \rho R_T^2 \frac{\Delta\Gamma(t)}{\Delta t} \tag{3.12}$$

The axial force of all blades can be considered as equivalent to a pressure difference across the actuator disc it can be seen that the pressure drop across the rotor disc is proportional to the shedding rate $\Delta\Gamma(t)/\Delta t$. After every time increment Δt during which the rotor blades rotate through $\Delta\theta = \Omega\Delta t$, it can be seen from figure (3.3) that the circulation Γ in the wake is increased by $\Delta\Gamma$. This circulation is absorbed in the single vortex ring the total strength of which as a result oscillates with time. Therefore $\Gamma = \int \Delta\Gamma$ or in the limit as $n \to \infty$, $(\Delta\Gamma/\Delta t) \to (d\Gamma/dt)$.

The mean power produced by the rotor over a full flow cycle of period T is, therefore, given by

$$\overline{P} = \overline{U_D(t) F_X(t)} = \frac{1}{T} \int_0^T \left(U(t) - \frac{\Gamma(t)}{2R_T} \right) \pi \rho R_T^2 \frac{d\Gamma(t)}{dt}\, dt \tag{3.13}$$

However, for a sinusoidal variation of $\Gamma(t)$, over a full cycle

$$\begin{aligned} \overline{\Gamma \frac{d\Gamma}{dt}} &= \frac{1}{mT} \int_0^{mT} \Gamma \frac{d\Gamma}{dt}\, dt \\ &= \frac{1}{2m\,\Delta T} \left[\Gamma^2(mT) - \Gamma^2(0) \right] \\ &= 0 \end{aligned} \tag{3.14}$$

where $m = 1, 2, 3, ...$

As a result the expression for the mean power reduces to

$$\overline{P} = \frac{\rho \pi R^2}{T} \int_0^T U \frac{d\Gamma}{dt} dt \tag{3.15}$$

A power coefficient $\overline{C_P}$ may be defined as the mean power of the rotor $\overline{P(t)}$ divided by the maximum energy flux passing through the swept area of the turbine rotor πR_T^2 in its absence:

$$C_P(t) = \frac{P(t)}{1/2\, \rho\, U_0^3\, \pi\, R_T^2} \tag{3.16}$$

Substituting the expression of equation (3.15)

$$\overline{C_P} = \frac{2}{U_0^3\, T} \int_0^T U(t)\, \frac{d\Gamma(t)}{dt}\, dt \tag{3.17}$$

Using equation (3.7) $d\Gamma/dt$ is given by:

$$\frac{d\Gamma(t)}{dt} = \frac{\Delta\Gamma(t)}{\Delta t} = \pi\, U_D(t)\, \sigma\ (\Omega\, R_T) \tag{3.18}$$

where

$$\sigma = \frac{nc}{2\pi R_T}$$

is the blade solidity. Substituting into equation (3.17) the expression for $\overline{C_P}$ becomes

$$\overline{C_P} = \frac{2\pi}{U_0^3}\, \sigma\, \Omega\, R_T\, \overline{U(t)^2} - \frac{2\pi}{U_0^3\, T}\, \sigma\, \Omega\, R_T\, \frac{1}{2R_T} \int_0^T U(t)\, \Gamma(t)\, dt \tag{3.19}$$

The tip speed ratio Λ is defined as $\Lambda = (\Omega R_T / U_0)$ and is a minimum for constant RPM rotation since Λ varies with time. This definition can be introduced into equation (3.18) to give

$$\frac{d\Gamma(t)}{dt} = \pi\, \sigma\, \Lambda\, U_0 \left(U(t) - \frac{\Gamma}{2R_T} \right) \tag{3.20}$$

This differential equation has the solution:

$$\Gamma = a\, sin(\omega t) + b\, cos(\omega t) \tag{3.21}$$

where

$$a = \frac{2\, R_T\, \sigma^2\, \Lambda^2\, U_0\, KC^2}{4 + \sigma^2\, \Lambda^2\, KC^2}$$

$$b = -\frac{4\,R_T\,\sigma\,\Lambda\,U_0\,KC}{4 + \sigma^2\,\Lambda^2\,KC^2}$$

(3.22)

Substitution of this solution in equation (3.19) results in :

$$\overline{C_P} = \frac{4\,\pi\,\sigma\,\Lambda}{4 + \sigma^2\,\Lambda^2\,KC^2} \tag{3.23}$$

This gives the variation of the mean power coefficient as a function of the non-dimensional parameter $\sigma\Lambda$. From equation (3.23) the mean rotor power coefficient has a maximum when

$$\sigma\Lambda = \frac{2}{KC} \tag{3.24}$$

for which

$$C_{Pmax} = \frac{\pi}{KC} \tag{3.25}$$

This shows that the power coefficient and therefore the apparent fluid dynamic efficiency tends to ∞ as KC tends towards zero. If however, KC is increased to large values the peak cyclic efficiency of the unducted turbine measured by $\overline{C_{Pmax}}$ would be expected to tends towards the value for the ideal turbine efficiency achievable in unidirectional steady flow which is 0.59. It must therefore be concluded not surprisingly from the assumptions made that the above theory does not hold for large values of KC.

Clearly, for small values of KC, C_{Pmax} can be greater than unity. This can only be due to the action of the rotor wake, represented here by a concentrated vortex ring. An apparent physical interpretation of the above result is that on the return cycle of the oscillatory incident flow the back flow induced by the vortex ring augments the flow through the rotor disc by bringing in momentum from a larger region acting rather like the wind energy concentrators proposed for wind turbines. However, as the present result depends on a number of major simplifying assumptions it will be very important to test it.

In the above definition the mean (cyclic) power coefficient is based on the cube of the peak incident velocity U_0 and, therefore, underestimates the efficiency. The real fluid dynamic efficiency over a full flow cycle should be based on $\overline{U^3}$ and is higher than that derived in the above analysis.

3.2.2 The Improved Theory

General

The derivation of the actuator disc theory given in the previous section has produced an analytical expression for the turbine power coefficient as a function of various flow parameters and the rotor geometry by making a number of simplifying assumptions about the rotor wake structure and its influence on the flow through the plane of rotation.

In order to assess the validity of these assumptions and gain further insight into the wake behaviour a more sophisticated numerical model was developed (as well as the experimental tests described in a later section). This model allows a more detailed analysis of the span wise variation of the flow through the rotor and to some extent models the convection of the rotor wake. In the following text this model is referred to as 'the (improved) numerical model' as opposed to 'the (actuator disc) theory', which denominates the basic theory described above. It is described in the following in concept and numerical implementation.

Wake Representation

A more complete theoretical description of the rotor wake structure would need to model the approximately helical shape formed by the shear layers shed from each turbine blade as they are convected away from the rotor as well as their roll up further downstream.

Pesmajoglou and Graham (1994) have successfully performed an inviscid numerical simulation of a wind turbine rotor wake in unsteady unidirectional flow using a vortex lattice method, which modelled the rotor blades by a lattice of vortex panels placed on the camber line of the individual blade sections. This method in its original implementation allowed for time dependent turbulent fluctuations of the unidirectional incident flow and modelled the wake downstream of the rotor by shedding vortex panels after each computational time step along the entire trailing edge of each rotor blade. The initial orientation of each shed wake panel was determined by enforcing a Kutta condition at the trailing edge of each modelled blade section, which for attached flow forces the wake panel to be aligned with the camber line of the section. For the sake of computational efficiency an amalgamation scheme was implemented for the force free wake, which consisted of the shed vortex panels that were iteratively aligned with the local flow so that there was no pressure jump across the them.

An adaption to the more complicated oscillating flow situation where the wake reverses direction and is swept back through the rotor was initially considered

feasible. The existing FORTRAN77 code was changed to allow for sinusoidal variation of the free stream velocity. It was soon realised, however, from some trial computations carried out that as the flow reversed direction the motion of the wake panels became increasingly chaotic and unstable. The numerical manipulation required to stabilise the behaviour of the wake panels and force more controlled wake roll-up using this method was not attempted since, within the project objectives and time scale, it was decided that a more stable intermediate model would be a less risky alternative.

A simpler, computationally cheaper approach which represents a more direct extension of the basic theory was, therefore, chosen to describe the rotor wake. In this more detailed model the bound circulation of the blade is allowed to vary in the span wise direction and vorticity is thus shed not only at the blade tip but from the trailing edge along the entire blade span. In order to maintain computational efficiency and numerical stability it was decided that all shed circulation from each radial station as in the basic actuator disc analysis, should be absorbed into and represented by a single concentrated circular vortex ring whose axis is concentric with the rotational axis of the rotor. Using a separate vortex ring for each span wise station was considered but flow visualisation -discussed in the following report chapter- indicated a strong roll up of the wake in a single vortex ring. Hence this model which also assumes a large number of blades (azimuthal averaging) was adopted. This simplification is considered legitimate for small KC flows. In contrast to the simpler theory in the improved model the vortex ring is not fixed in the rotor plane but is allowed to convect away from the rotor as it grows in strength, under the influence of the incident flow and its own induced velocity.

A similar approach was used by Montgomerie (1985) to model the wake induced back flow for a horizontal axis wind turbine rotor operating in unidirectional, unsteady flow. In his approach a time stepping routine was implemented in which a sequence of vortex rings whose strength was related to the blade circulation were released at fixed time intervals and were convected away from the rotor at the free stream velocity.

In the current numerical study the vortex ring formation is performed according to the model originally developed by Brown and Michael to analyse vortex shedding from the sharp leading edge of a slender delta wing (1955). However, since then the model has been further developed and applied by a number of researchers for a variety of different unsteady vortex flows: Lowson (1973) used an extension of the model for separated flows on slender wings in unsteady motion. Graham (1980) used the method to calculate the forces on sharp edged cylinders in oscillatory flow at low KC numbers. More recently, roll damping due to vortex shedding from slender ship hulls was calculated by Al-Hukail (1993) utilising the same equations as Brown and Michael. The main features of the

model are discussed in some detail by Graham (1977) for vortex shedding from sharp edges for which, in the model, the vorticity is concentrated into a single line (or ring) but the convection speed is modified to take account of growth in the circulation of the vortex due to the shedding from the sharp edge of a body.

In the physical starting flow around a sharp edged body the field is dominated by a growing spiral vortex sheet emanating from the sharp edge. The Brown and Michael model represents this spiral by a concentrated line vortex and a so called 'cut' which constitutes the feeding sheet. For two dimensional flow the model idealisation of the real flow becomes a point vortex and a line cut. By imposing a zero total force condition on the point vortex itself and the feeding sheet analytical expressions for the growth and movement of the point vortex can be derived. These expressions become equivalent to the usual convection of a free vortex by the locally induced flow when its circulation is constant but are modified in general to account for the effects of changing circulation.

In analogy to this model the current model is set up to study the vortex wake behaviour by concentrated growing vortex rings. As suggested by Graham (1977), each vortex ring grows until it is shed ('released' from the rotor and a new vortex ring started) when the time rate of change of the vortex ring circulation is zero. The strength of the vortex ring is fixed and in principle should not change from then on. Subsequent to shedding the vortex ring moves due only to convection. This is dependent on the velocity imposed by the free stream as well as velocities induced by other vortex rings present. In the case of a ring vortex unlike a straight line vortex there is also an additional convection velocity induced by the shed vortex ring on itself. The velocity induced by vortex rings which have been shed on each other is calculated according to the Biot-Savart law. Lamb (1932) has studied the speed at which thin cored vortex rings travel. This tends to ∞ as the vortex ring core tends to zero and he gives an equation for it which is used in the present numerical model to calculate the self-induced component of the vortex ring convection.

The computational efficiency of the numerical model over a large number of flow cycles is enhanced by imposing a limit on the number of vortex rings in the calculation. For long run times this is achieved as follows. On shedding each vortex ring is artificially decayed exponentially once it has moved away from the rotor so that it can be removed from the computation without causing instabilities in the numerical solution. For an infinite Reynolds number flow, strictly, there is no physical reason for the vortex rings to decay. However, in other discrete vortex calculations it is not unusual for the sake of convenience to introduce artificial decay. In reality reduction of circulation is only possible due to diffusion at $r = 0$ or with other rings.

As far as the current numerical model is concerned the convected vortex rings only directly affect the computation of the rotor power by the velocities they induce in the plane of rotation. However, they also have an indirect effect on the computation even when they have convected far away from the rotor because they affect the position of other shed vortex rings closer to the rotor which induce larger velocities at the rotor disc. If, therefore, a vortex ring which has convected far away from the rotor is removed from the computation the system of vortex rings which form the far field of the flow may become destabilised. The extent of this destabilisation is in proportion to the strength of the vortex rings in the far field. For this reason the numerical decay was introduced, which reduces the strength of the far field vortex rings which can, as a result, be more 'smoothly' removed from the numerical model. The vortex ring decay was initiated when the radial convection of the vortex ring core had reached nominally three times the rotor radius.

The basic actuator disc theory given earlier assumes that the back flow due to the presence of the vortex ring has no span wise variation and is in fact approximated by the induced velocity on the centre line of the rotor. In contrast to this, the improved model calculates the radial variation of the induced axial velocity U_Γ due to all vortex rings. Consequently, in this model, there is also a span wise variation of $U_D = U_D(r,t)$ and the blade circulation $\Gamma = \Gamma(r,t)$. The turbine power in this improved numerical model is as in the simpler analysis inferred from blade element theory.

3.2.3 Mathematical Description And Numerical Implementation

The Vortex Ring Formation

Due to the assumed axisymmetric nature of the flow field it is possible to reduce the calculation of the vortex ring formation to two dimensions. In this case the vortex ring is represented by a point vortex in a sectional plane of the flow. Figure (3.4) shows the idealisation of the time dependent inviscid flow past the turbine rotor used to apply the Brown and Michael model which controls the vortex motion. The idealisation consists of the intersection of the vortex ring with the plane ($\theta = 0, \pi$) which appears as two point vortices of strength $\Gamma(t)$ and their feeding sheets originating from the centres of the m elements into which the blade has been divided. According to the analysis of Brown and Michael (1955) a zero-force boundary condition is applied to the cut and the point vortex. Al-Hukail (1993) from this derived the following time dependent analogue formula for a single point vortex being fed from a feeding sheet which extends between the vortex position and the starting point of the feeding sheet

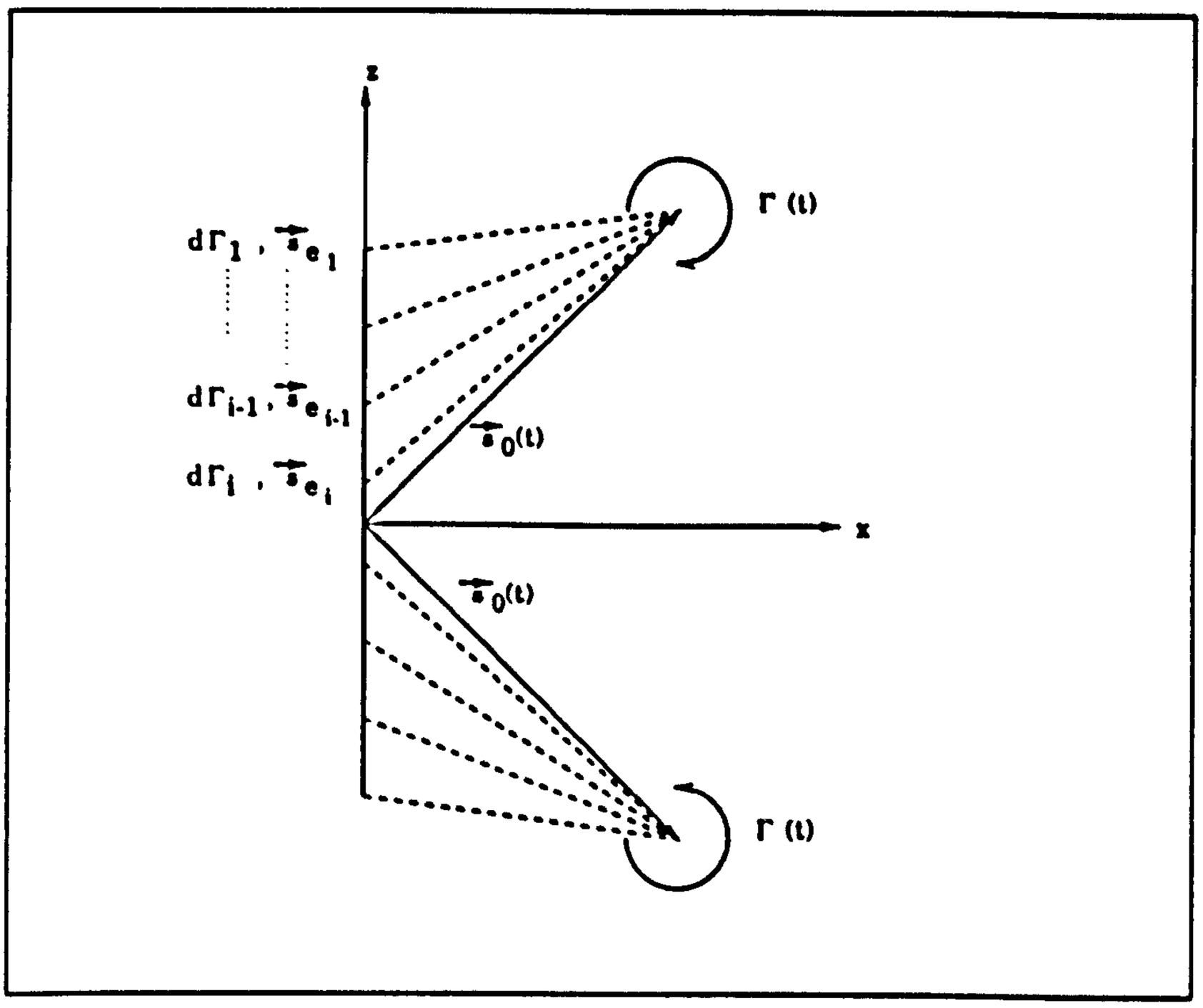

Figure 3.4: The Brown And Michael Model For The Wells Turbine Rotor

$$\frac{d\Gamma(t)}{dt}(\vec{s_0} - \vec{s_e}) + \Gamma(t)\left(\frac{d\vec{s_0}}{dt} - \vec{V_0}\right) = 0 \tag{3.26}$$

where $\vec{V_0}$ is the value of the velocity field at the point vortex and $(\vec{s_0} - \vec{s_e})$ is the length of the feeding sheet. The first term of equation (3.26) represents the force acting on the feeding sheet while the second is the force on the vortex. Strictly this equation which is for planar flow should be modified for the effect of axisymmetry on the forces. However, the modification is small if the length of the feeding sheet is not very large compared with its mean radius.

Equation(3.26) may be rearranged:

$$d\,\vec{s_0} = \vec{V_0}dt - (\vec{s_0} - \vec{s_e})\frac{d\Gamma(t)}{\Gamma(t)} \tag{3.27}$$

Adapting equation (3.27) to incorporate shedding from all m blade elements which each feed $d\Gamma(r,t) = (\partial\Gamma_{bound}/\partial r)\delta r$ into the point vortex this equation becomes

$$d\,\vec{s_0} = \vec{V_0}dt - \sum_{j=1}^{m}\left(\vec{s_0} - \vec{s_{e_j}}\right)\frac{d\Gamma(t)_j}{\Gamma(t)} \tag{3.28}$$

where $d\Gamma(t)_j = d\Gamma(r_j, t)$

Equation (3.28) may be numerically discretised for use in a time stepping routine which for given values of Γ at time step k calculates the new point vortex position $\vec{s_0}$ from

$$\vec{s_0}^{k+1} = \vec{s_0}^{k} + \Delta t \vec{V_0}^{k} + \sum_{j=1}^{m} \left(\vec{s_{e_j}} - \vec{s_0}\right) \frac{d\Gamma_j^{k+1}}{\Gamma^k} \tag{3.29}$$

and the strength at the new time step $k+1$ from

$$\Gamma^{k+1} = \Gamma^k + \sum_{j=1}^{m} d\Gamma_j^{k+1} \tag{3.30}$$

The value of $\vec{V_0}(t)$ at a given time is defined by

$$\vec{V_0}(t) = U(t) + \vec{V}_{0ind}(t) \tag{3.31}$$

where $\vec{V}_{0ind}(t)$ is the total induced velocity at $\vec{s_0}(t)$. It is composed of the contribution of all vortex rings in the flow field $\vec{V_i}(t)$ and the velocity component which the vortex ring induces on itself $\vec{V_S}(t)$:

$$\vec{V_0}(t) = U(t) + \sum_{i=1}^{nrings} \vec{V_{i_i}}(t) + \vec{V_S}(t) \tag{3.32}$$

Motion and growth of the vortex ring are computed in a time stepping algorithm according to these equations until the shedding criterion $(d\Gamma(t)/dt)=0$ is reached, whereupon growth is terminated, the ring is shed and a new vortex ring of opposite sign is formed on the other side of the rotor. Since for shed vortex rings $(d\Gamma(t)/dt)=0$, equation (3.28) reduces to

$$d\,\vec{s_0} = \vec{V_0}(t)dt \tag{3.33}$$

which is the usual convection equation for point vortices.

It should at this point be noted that the shedding criterion enforced above in analogy to calculations for shedding phenomena with only one feeding sheet allows the vortex ring just prior to being shed to absorb some circulation of the opposite sign from from some stations while the total rate of change of vorticity has still not yet reversed sign. This is due to the span wise variation of $U_D(r,t)$ which as the free stream velocity becomes small towards the end of one half of a flow cycle has a sign change with respect to radius as shown in figure (3.5). In contrast to this model which enforces an exclusive downstream orientation of the feeding sheets irrespective of the sign of their vorticity until the total of the

feeding vorticity changes sign an alternative model is also suggested in figure (3.5) and has been numerically explored. This essentially differs from the previous set up in that a new vortex ring is formed as soon as the vorticity in any of the feeding sheets changes sign. Towards the end of the each half of a flow cycle this model actually maintains two simultaneously growing vortex rings.

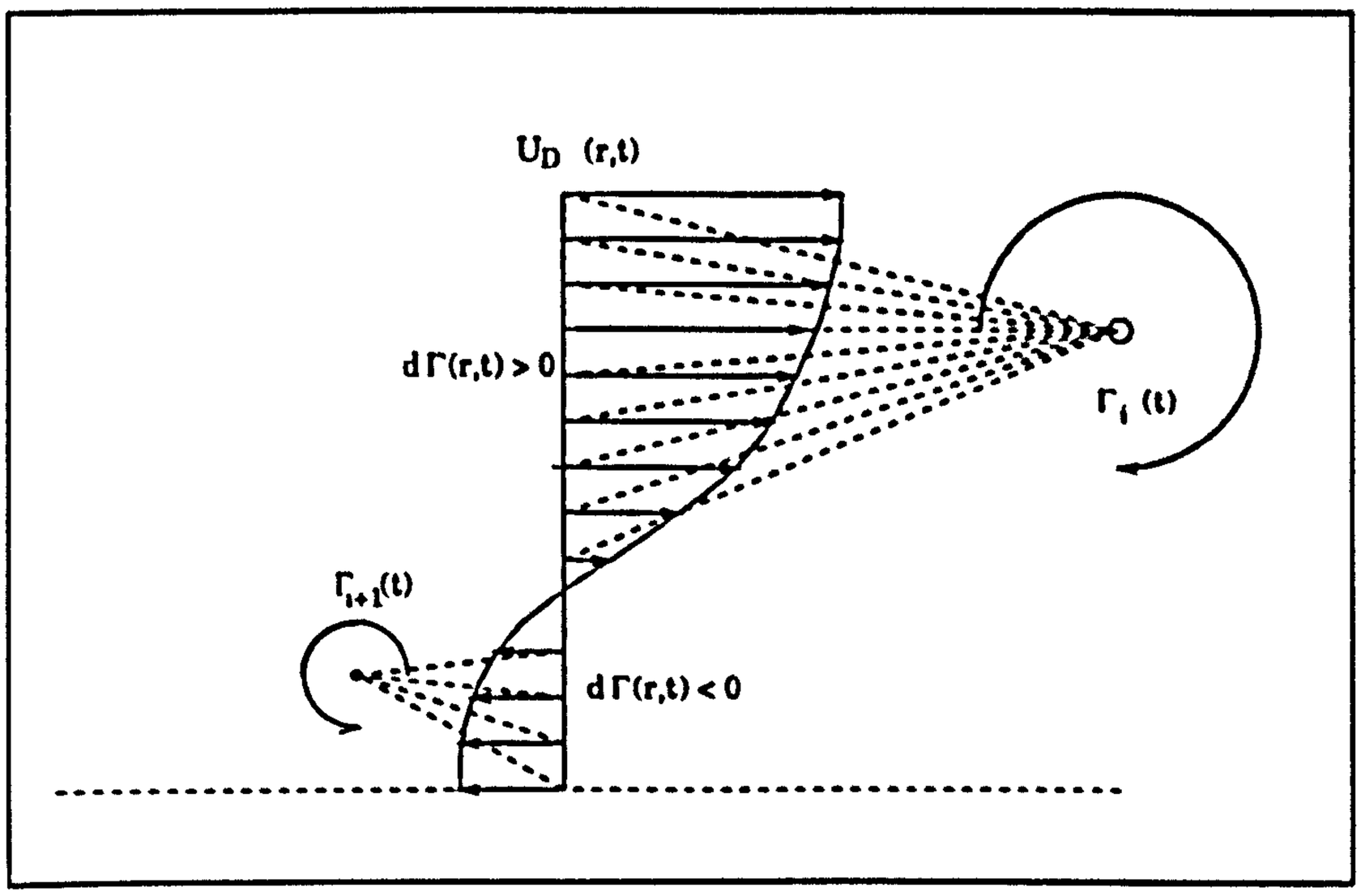

Figure 3.5: Alternative Vortex Shedding Model For Wells Turbine Rotor

The Induced Velocities Due to an Axisymmetric Vortex Ring

The vortex rings used in the numerical method represent axisymmetric circular vortex filaments of constant strength Γ and are assumed to have an infinitesimally small core. The velocity field due to a vortex filament in inviscid incompressible flow is given by the Biot-Savart law. Formulated for a vortex segment of length $\vec{dl}$ the velocity $d\vec{V}$ induced by at a point P which is at a radial distance $\vec{r}$ is:

$$d\vec{V} = \frac{\Gamma}{4\pi}\frac{\vec{dl} \times \vec{r}}{|\vec{r}|^3} \tag{3.34}$$

where by definition $d\vec{V}$ is perpendicular to $\vec{dl}$ and $\vec{r}$.

Applying this the velocity induced by the whole vortex ring at a general point is

$$d\vec{V} = \frac{\Gamma}{4\pi}\int_0^{2\pi}\frac{\vec{dl} \times \vec{r}}{|\vec{r}|^3} \tag{3.35}$$

De Bernardinis (1980) who studied oscillatory past flat discs developed this equation for an arbitrary point in 3 dimensional space and obtained fairly complicated expressions for the velocity components comprising elliptic integrals. For the current study an analytically simpler approach outlined by Katz and Plotkin (1991) and applied for planar rectangular vortex rings by Pesmajoglou was chosen. In this solution to the problem the vortex ring is geometrically approximated by a finite number of straight line segments of length $\vec{dl}$ and circulation Γ. For each of these segments the induced velocity at some point P may be calculated using equation (3.35), which is easily implemented for a straight line segment:

Consider the vortex line segment $\vec{dl}$ schematised in figure(3.6). If the position

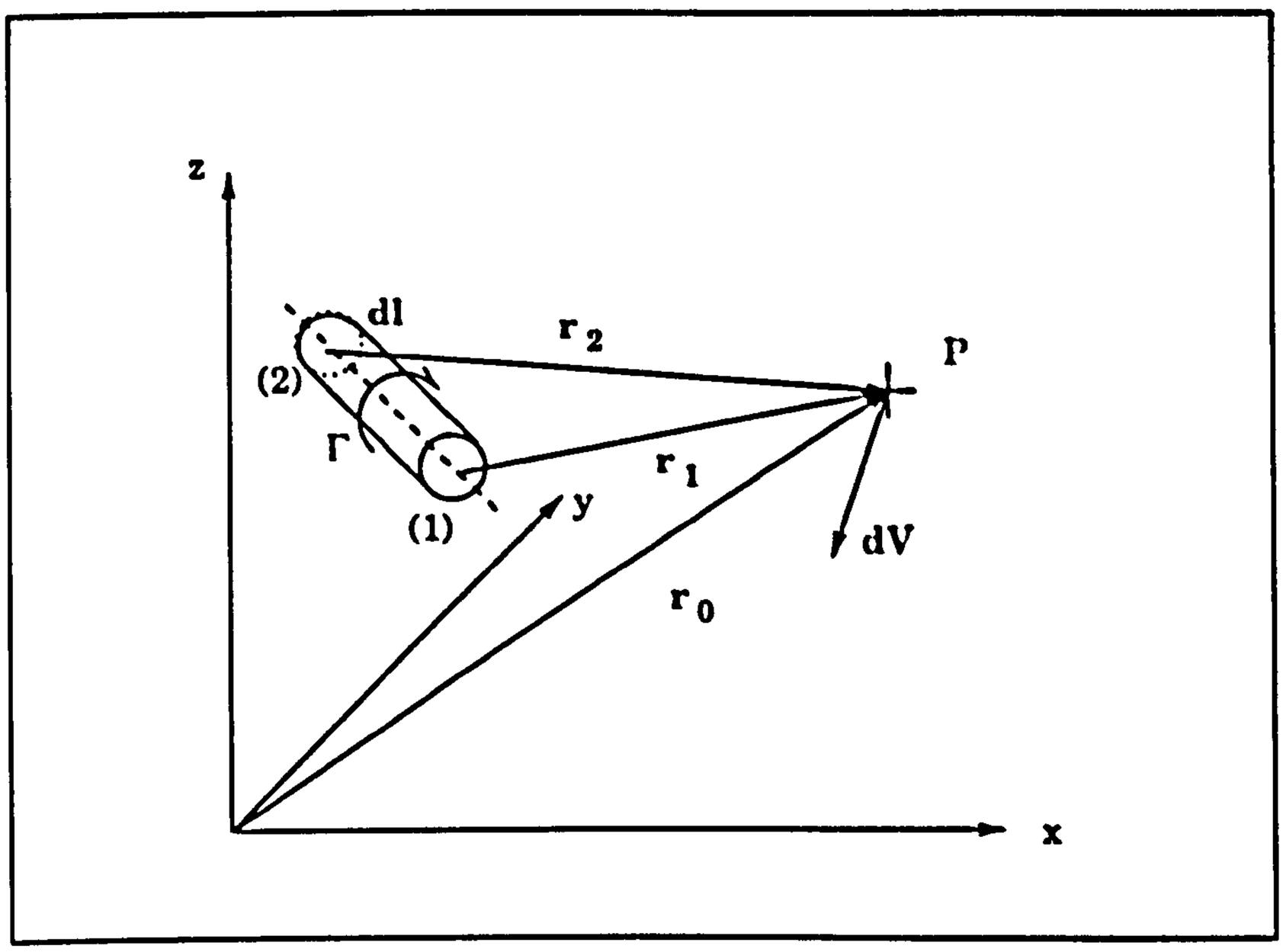

Figure 3.6: Straight Line Vortex Model

of point P is given by $\vec{r_0}$ and the distances to the ends of the line segment are $\vec{r_1}$ and $\vec{r_2}$ then the induced velocity, by equation (3.35), is:

$$d\vec{V} = \frac{\Gamma}{4\pi} \frac{\vec{r_1} \times \vec{r_2}}{|\vec{r_1} \times \vec{r_2}|} \vec{r_0} \left(\frac{\vec{r_1}}{r_1} - \frac{\vec{r_2}}{r_2} \right) \tag{3.36}$$

It is clear that equation (3.36) has a singularity if P lies on the vortex segment. This case is given special treatment when the method is computationally executed by setting the value of the induced velocity to zero if $\vec{r_1}$ or $\vec{r_2}$ are very small or zero. If the vortex ring consists of $nseg$ straight line segments then the induced velocity $\vec{V}$ due to the whole vortex ring is

(3.37) $$\vec{V} = \sum_{j=1}^{nseg} d\vec{V}_j$$

where $d\bar{V}_j$ is the contribution of the j^{th} segment which is calculated from equation (3.36). Since the vortex rings are defined to be planar their coordinates for a given stream wise location x is given by $\vec{r}_j = \vec{r}_j(y_j(\theta_j), z_j(\theta_j))$. As illustrated in figure (3.7)

(3.38) $$y_j = a\cos\theta_j$$

(3.39) $$z_j = a\sin\theta_j$$

(3.40) $$\theta_{j+1} = \theta_j + d\theta$$

where a is the radius of the vortex ring and $d\theta = 2\pi/nseg$

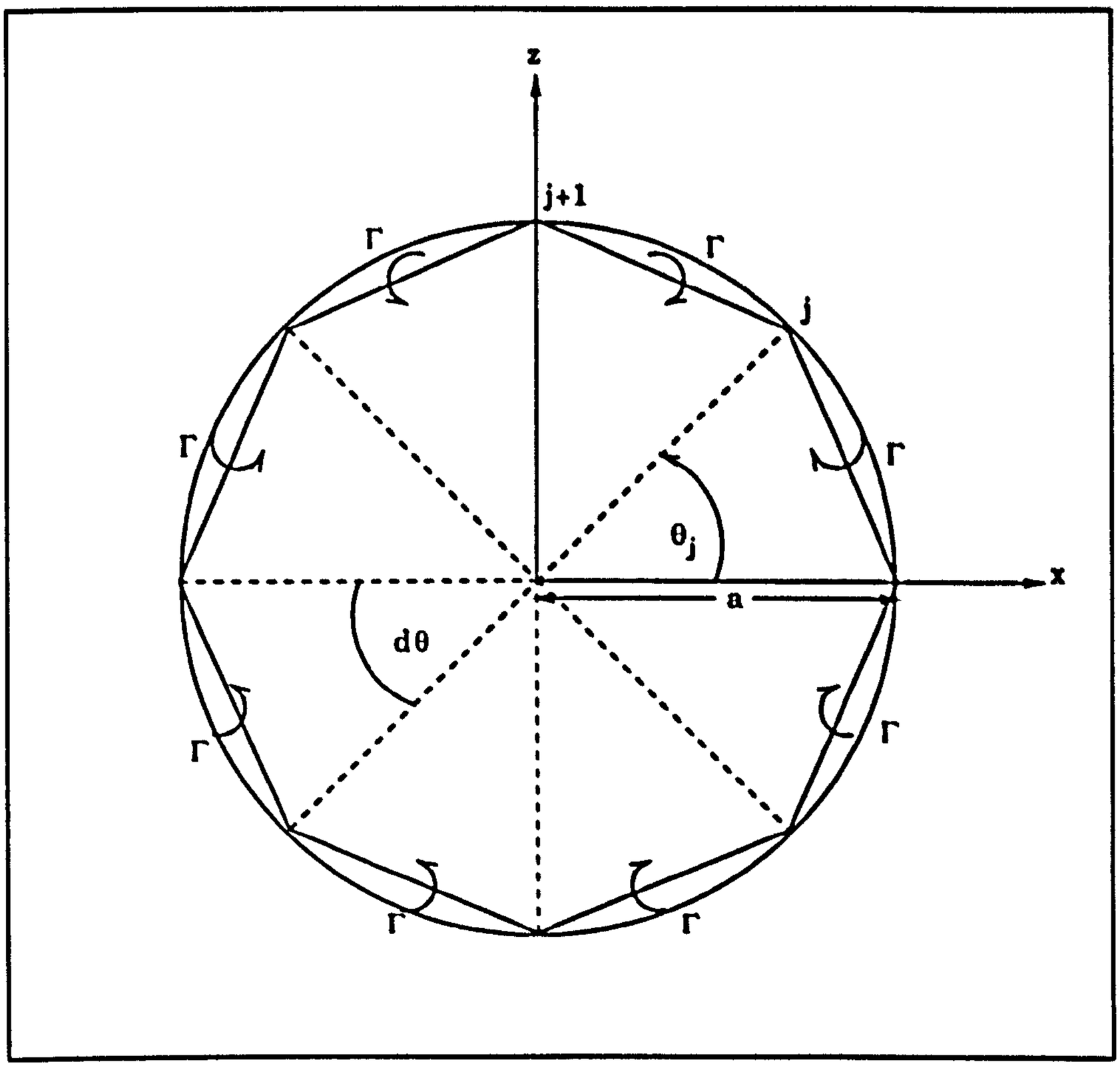

Figure 3.7: Straight Line Vortex Ring Model

The analytical result for the induced velocity u by a vortex ring at a point which lies on its axis of symmetry is derived by Duncan, Thom and Young (1960)

as:

$$u = \frac{\Gamma a^2}{2(a^2 + x^2)^{3/2}} \tag{3.41}$$

where x is the distance along the axis.

In figure (3.8) a comparison between the above approximate method for a vortex ring comprising of 30 line segments and the exact result for a ring of unit radius is shown.

When the arbitrary point moves onto the ring the induced velocity becomes

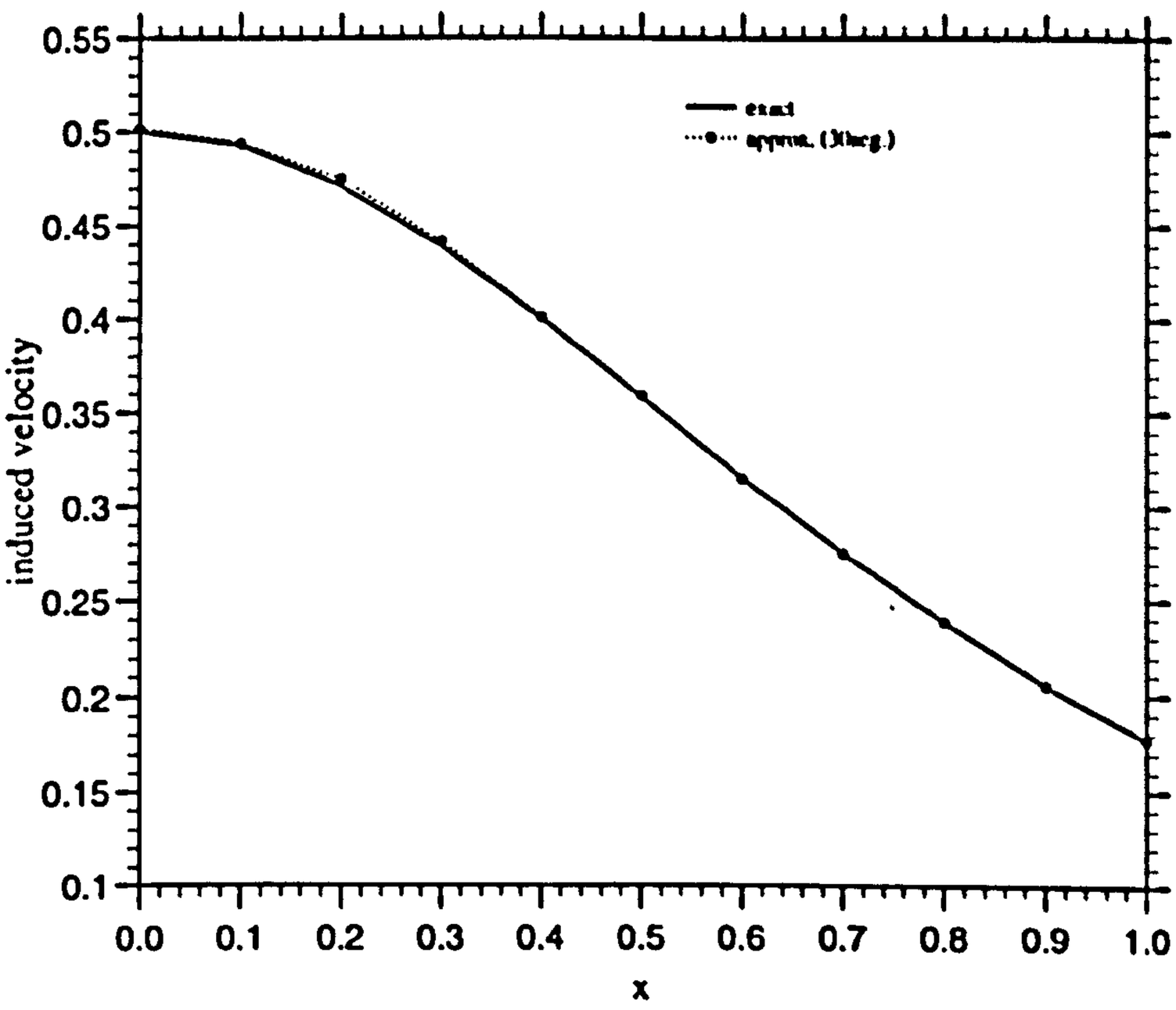

Figure 3.8: Centerline Induced Velocities

infinite and must be carefully considered. Lamb has shown that the vortex ring induces an axial velocity on itself which for a thin cored vortex is:

$$V_{self} = \frac{\Gamma}{4\pi R}\left(log\frac{8R}{c_0} - 0.25\right) \tag{3.42}$$

where R is the radius of the vortex ring and c_0 is the vortex core radius.

In the present case the vortex ring is representing a rolling up spiral vortex sheet. From empirical observation the size of this rolled up region of the vortex

core is related to the distance from the shedding point. In the numerical model is taken to be equal to half the distance from the shedding point, which is a fairly arbitrary definition. The maximum core size is specified to be limited by the radius of the vortex ring. When the vortex ring has been shed the size of the core stays constant. Inside the defined core area the velocity field is treated as that of a 2 dimensional vortex with solid rotation in the core:

$u = u(r)$ for $r > c_0$

$u = u(r) * r/c_0$ for r, c_0

Others (eg. De Bernardinis (1980)) have used a similar 'cut-off' to represent this effect.

The Flow Through The Rotor

The general methodology of the turbine performance computation is as for the actuator disk type theory given earlier based on a blade element approach. In the numerical implementation the rotor blades are represented by a number of span wise elements which are treated as isolated aerofoils and at which the velocity field is computed. Figure (3.2) shows the defined components of velocity locally incident to the blades. The net axial velocity at the rotor $U_D(r,t)$ is taken to be:

$$U_D(r,t) = U(t) - U_\Gamma(r,t) \tag{3.43}$$

$U(t)$ is the free stream and $U_\Gamma(r,t)$ is calculated as the net induced axial velocity at the blade element due to all the vortex rings present in the flow field:

$$U_\Gamma(r,t) = \sum_{i=1}^{nrings} q_i(t) \tag{3.44}$$

where $q_i(t)$ is determined for each vortex ring from equation.

Applying the steady flow Kutta-Joukowski theorem for attached flow the span wise variation of the bound circulation on each blade is given by the thin aerofoil theory as:

$$\Gamma(r,t) = \pi\, c(r)\, U_D(r,t) \tag{3.45}$$

This distribution is used to compute in finite difference form the value of circulation shed from each blade element $\Delta\Gamma(r,t)$ to retain continuity of circulation everywhere. It is schematised in figure (3.9) in its numerical discretisation.

The whole of $\Delta\Gamma(r,t)$ is shed when a blade has moved through an angle $\Delta\theta = 2\pi/n$, where n is the number of rotor blades. For a constant angular velocity Ω, $\Delta\Gamma(r,t)/\Delta t$, the rate at which the bound circulation is shed into the concentrated vortex ring, is therefore:

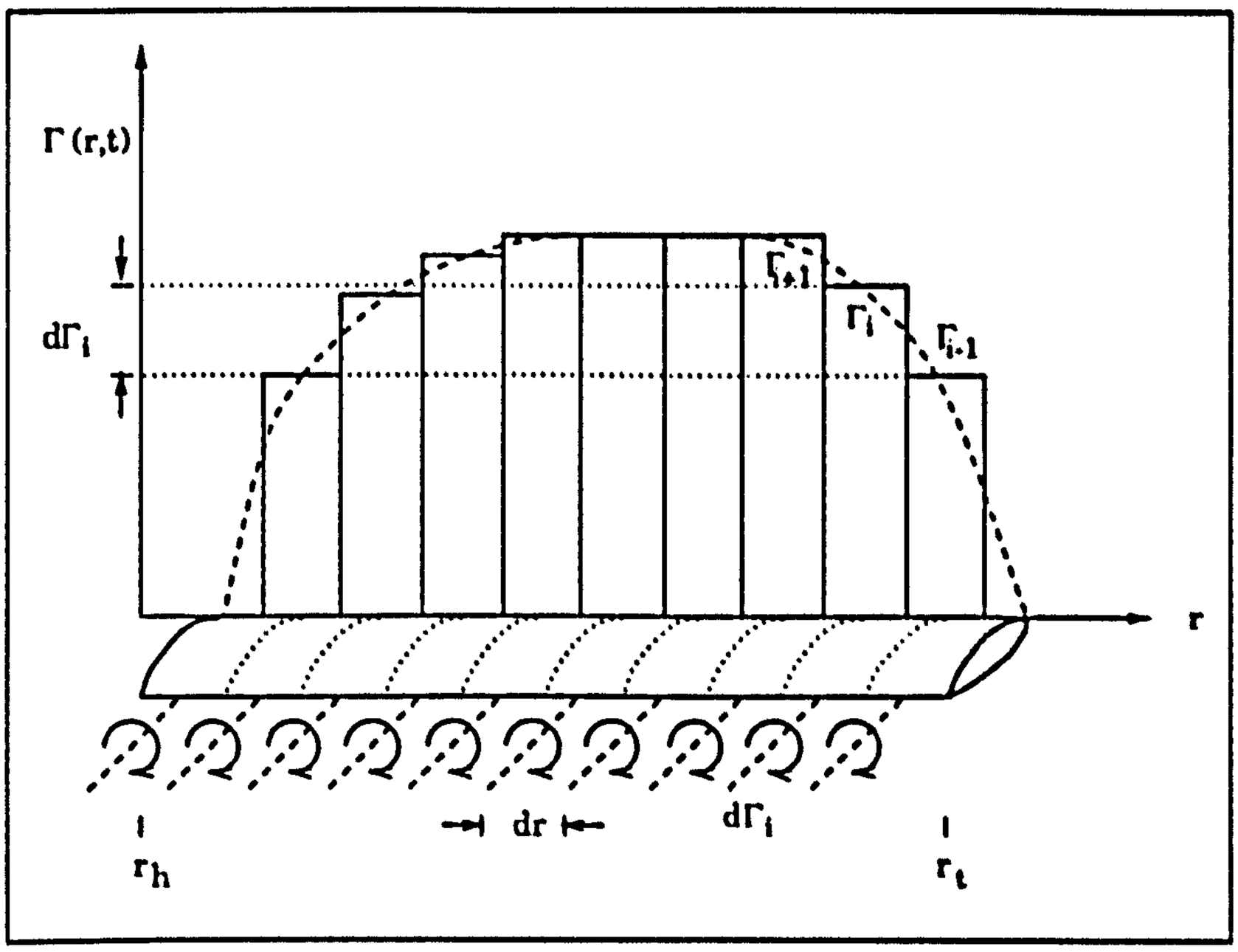

Figure 3.9: Blade Circulation

$$\frac{\Delta\Gamma(r,t)_{shed}}{\Delta t} = \Delta\Gamma(r,t)_{bound}\frac{n\Omega}{2\pi} \tag{3.46}$$

The Turbine Performance

Equation (3.3) states the power produced by a blade element in terms of its radial position r, the rotor angular velocity Ω and the tangential thrust $F_T(r,t)$. By inspection of the defined incident velocities and acting blade forces shown in figure (3.2) the following expression for the power contribution of the element is derived:

$$dP(r,t) = 1/2\,\rho\,c(r)\,C_L(r,t)\,U_D(r,t)\,U_t(r,t)\,W(r,t) \tag{3.47}$$

where $U_t(r,t) = \Omega r$. The hub vortex which only generates swirl has been neglected.

For the entire blade, therefore, the power produced is

$$P = 1/2\,\rho\int_{r_h}^{r_t} c(r)\,C_L(r,t)\,U_D(r,t)\,U_t(r,t)\,W(r,t)\,dr \tag{3.48}$$

The turbine efficiency is defined in terms of the power coefficient $C_P(t)$, which as stated in equation (3.48) gives:

$$C_P(t) = \frac{n}{U_0^3 \pi} r_t^2 \int_{r_h}^{r_t} c(r)\, C_L(r,t)\, U_D(r,t)\, U_t(r,t)\, W(r,t)\, dr \tag{3.49}$$

and a cyclic mean is formulated as:

$$\overline{C_P(t)} = \frac{1}{T} \int_0^T C_P(t) dt \tag{3.50}$$

By analogy with the above analysis for the turbine shaft power, the axial force produced by a blade element is :

$$dF_X(r,t) = 1/2\, \rho c(r)\, C_L(r,t)\, U_t(r,t)\, W(r,t) \tag{3.51}$$

Accordingly, the axial force produced by a blade is

$$F_X(t) = 1/2\, \rho \int_{r_h}^{r_t} c(r)\, C_L(r,t)\, U_t(r,t)\, W(r,t)\, dr \tag{3.52}$$

and if an axial force coefficient is defined as

$$C_X(t) = \frac{F_X(t)}{1/2\, \rho\, U_0^2\, \pi\, R_t^2} \tag{3.53}$$

then for the total axial force of the rotor:

$$C_X(t) = \frac{n}{U_0^2\, \pi\, R_t^2} \int_{r_h}^{r_t} c(r)\, C_L(r,t)\, U_t(r,t)\, W(r,t)\, dr \tag{3.54}$$

3.3 Results

3.3.1 The Actuator Disc Theory

The theory derived in the preceding section for an unducted Wells turbine operating in sinusoidal small KC number flow gives an analytical expression for the mean cyclic power coefficient $\overline{C_P}$ which is given in equation (3.23) and is a measure of the turbine fluid dynamic efficiency. A graphical illustration of the dependency of $\overline{C_P}$ on the dimensionless quantities $\sigma\Lambda$ and KC is given in figure (3.10), which presents $\overline{C_P}$ as a function of $\sigma\Lambda$ for a number of KC values. At

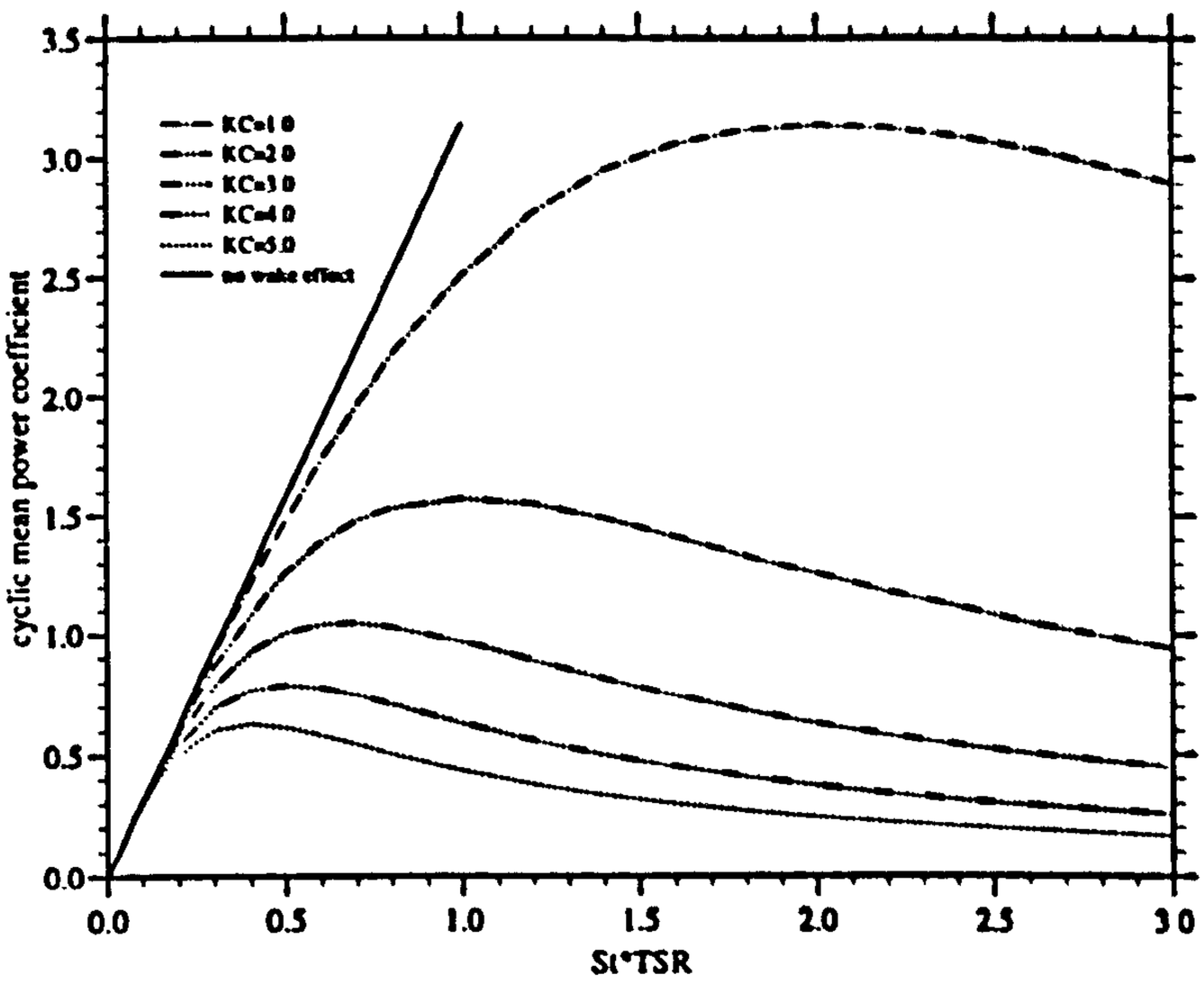

Figure 3.10: Mean Power Coefficient $\overline{C_P}$ vs $\sigma\Lambda$

all values of KC the gradient $\partial\overline{C_P}/\partial(\sigma\Lambda)$ of the curve is fairly large for values of $\sigma\Lambda$ which are significantly smaller than the value for optimum rotor efficiency given by $(\sigma\Lambda)_{opt} = 2/KC$ according to equation (3.24). For values of $\sigma\Lambda$ greater than this it is evident that $\overline{C_P}$ is not as strong a function of $\sigma\Lambda$. As formulated in equation (3.25) the curves reveal a strong non-linear KC dependency of the maximum turbine efficiency $\overline{C_{Pmax}}$ which is illustrated in figure (3.11) below. This shows that especially at small amplitude to rotor diameter ratios large gains in fluid dynamic efficiency of the turbine may be achieved by small changes in KC.

Moreover, it is clear that the theory predicts that maximum power coefficients greater than unity are possible. This was discussed earlier in the derivation of the theory and was attributed to the induced back flows of the rotor wake.

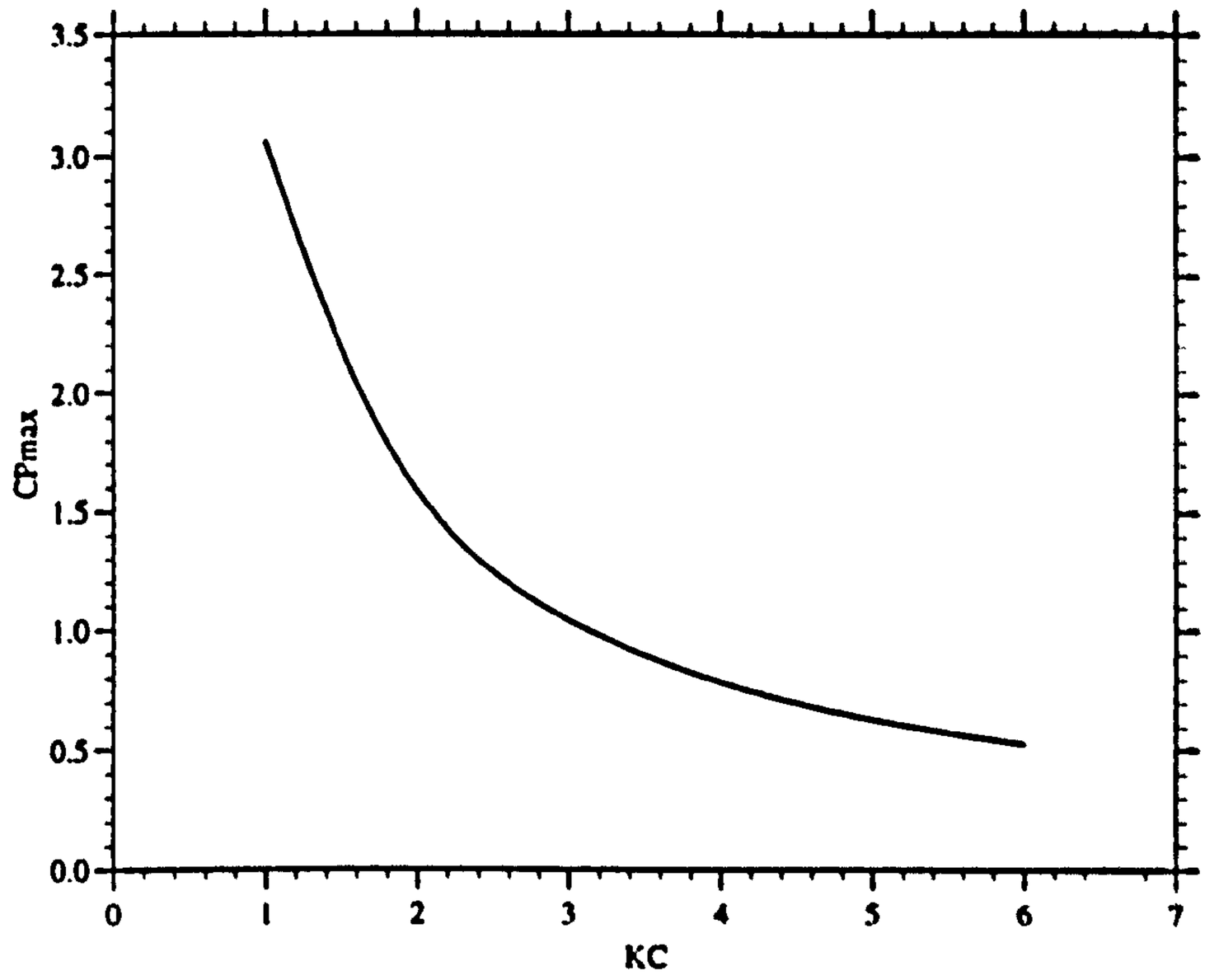

Figure 3.11: $\overline{C_{Pmax}}$ vs KC

A better understanding of the vortex wake action causing the above $\overline{C_P}$ characteristics are obtained in the following:

If the effect of the rotor wake is neglected, then the velocity through the rotor disc, $U_D(t)$ is equal to the free stream velocity $U(t)$. It can be shown using equations (3.17) and (3.18) that in this case

$$\overline{C_{Pnowake}} = \pi\sigma\Lambda \tag{3.55}$$

This equation gives the ideal cyclic turbine efficiency in sinusoidal flow in the absence of any wake losses and is included above in figure (3.10) as a solid line. An equivalent expression may be derived for steady unidirectional flow for which $C_{Pnowake} = 4\pi\sigma\Lambda$. In steady unidirectional flow the turbine efficiency is rather strongly reduced from this ideal value due to the axial back flow induced by the rotor wake, which always acts in opposition to the free stream velocity.

It is further clear from figure (3.10) that in unducted oscillatory flow the cyclic rotor efficiency is also reduced from the ideal value which the rotor would achieve in the absence of wake losses. However, particularly for small values of KC, it can be seen that over a range of $\sigma\Lambda$ values the efficiency calculated according to equation (3.23) reduces by a comparatively small extent from that given by equation (3.55). This indicates that the wake in oscillatory flow acts so that the

mean flow velocity through the rotor is much less reduced from the free stream value than in unidirectional flow. As suggested earlier this must mean that for a part of a flow cycle the induced back flow from the rotor wake is in the same direction as the free stream. This is studied in more detail in the following.

By comparing equation (3.55) with equation (3.23) a wake loss factor μ may be defined as

(3.56)
$$\mu = \frac{\overline{C_{Pwake}}}{\overline{C_{Pnowake}}} = \frac{1}{1 + 0.25(\sigma\Lambda)^2 KC^2}$$

and, therefore, $\overline{C_P} = \mu\pi\sigma\Lambda$.

Figure (3.12) below shows μ as a function of $\sigma\Lambda$ at different values of KC.

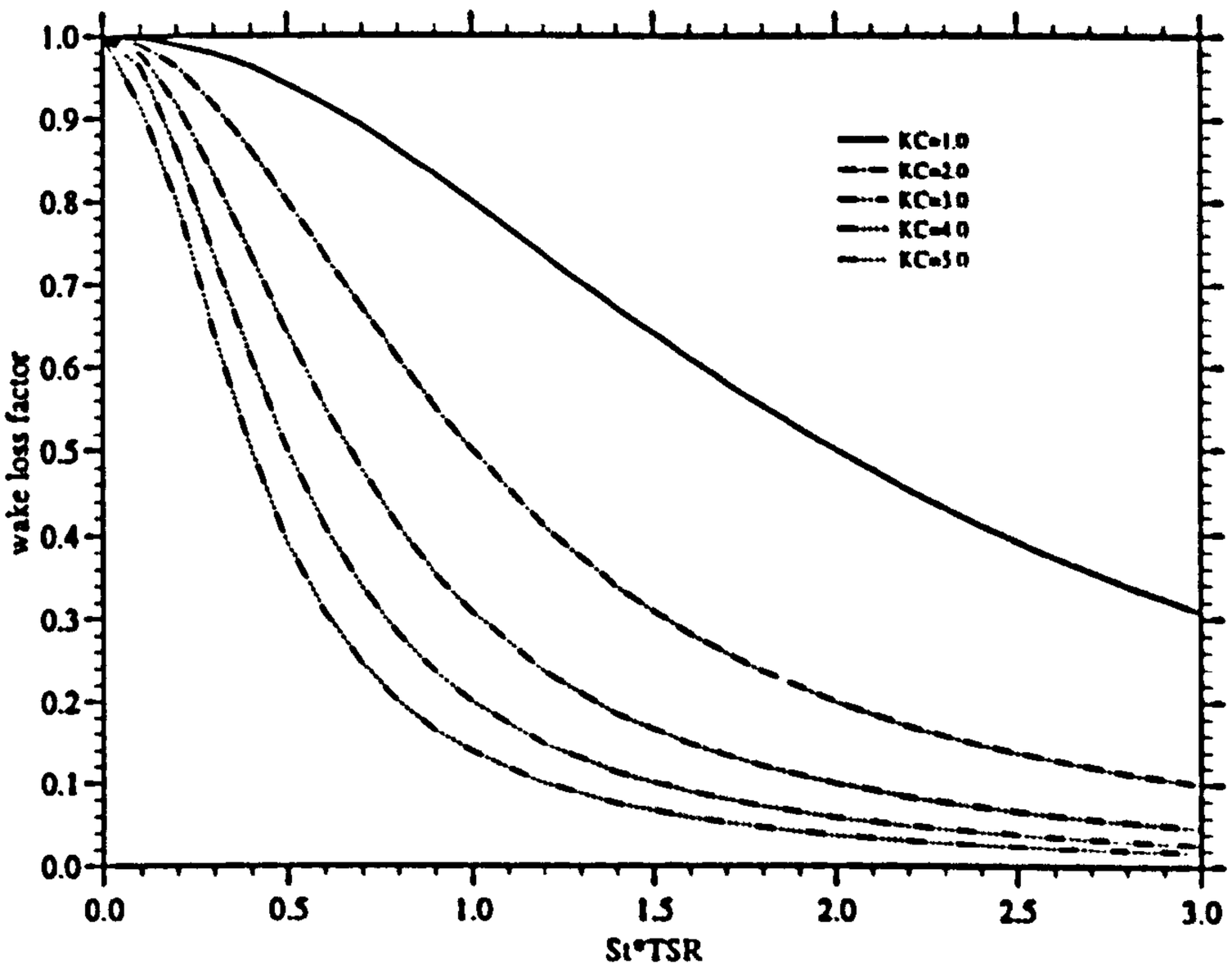

Figure 3.12: μ vs $\sigma\Lambda$

It can be seen in the above figure that at higher values of KC the wake losses initially increase rapidly with $\sigma\Lambda$ i.e. as the rotor wake increases in strength. However, the curves shown for a number of higher KC values flatten off as the values of $\sigma\Lambda$ becomes quite large. This shows that beyond a certain level at large KC the wake losses are relatively insensitive to the strength of the wake. In contrast, for small values of KC the curves shown suggest a much more gradual increase in wake losses as the the rotor wake increases in strength.

It is clear that the sensitivity of μ to KC and $\sigma\Lambda$ given by $\partial\mu/\partial KC$ and $\partial\mu/\partial(\sigma\Lambda)$ varies. From equation (3.56) it is found that

$$\frac{\partial\mu/\partial KC}{\partial\mu/\partial(\sigma\Lambda)} = \frac{\sigma\Lambda}{KC} \tag{3.57}$$

This means that the relative sensitivity of the wake losses to KC increases linearly with $\sigma\Lambda$.

The effect of the rotor wake can be studied in more detail by rewriting equation (3.18) as

$$\frac{\Delta\Gamma}{\Delta t} = \pi\,\sigma\,\Lambda\,U_0\,U_D(t) \tag{3.58}$$

where U_0 is the peak velocity of the sinusoidal free stream. This equation shows that the strength of the wake is directly proportional to $\sigma\Lambda$. Substitution into equation (3.17) gives

$$\overline{C_P} = \frac{2\pi}{D_T}\int_0^T \frac{\sigma\Lambda}{KC}\,U(t)\,\frac{U_D(t)}{U_0}\,dt \tag{3.59}$$

where D_T is the rotor diameter and T is the period of the flow.

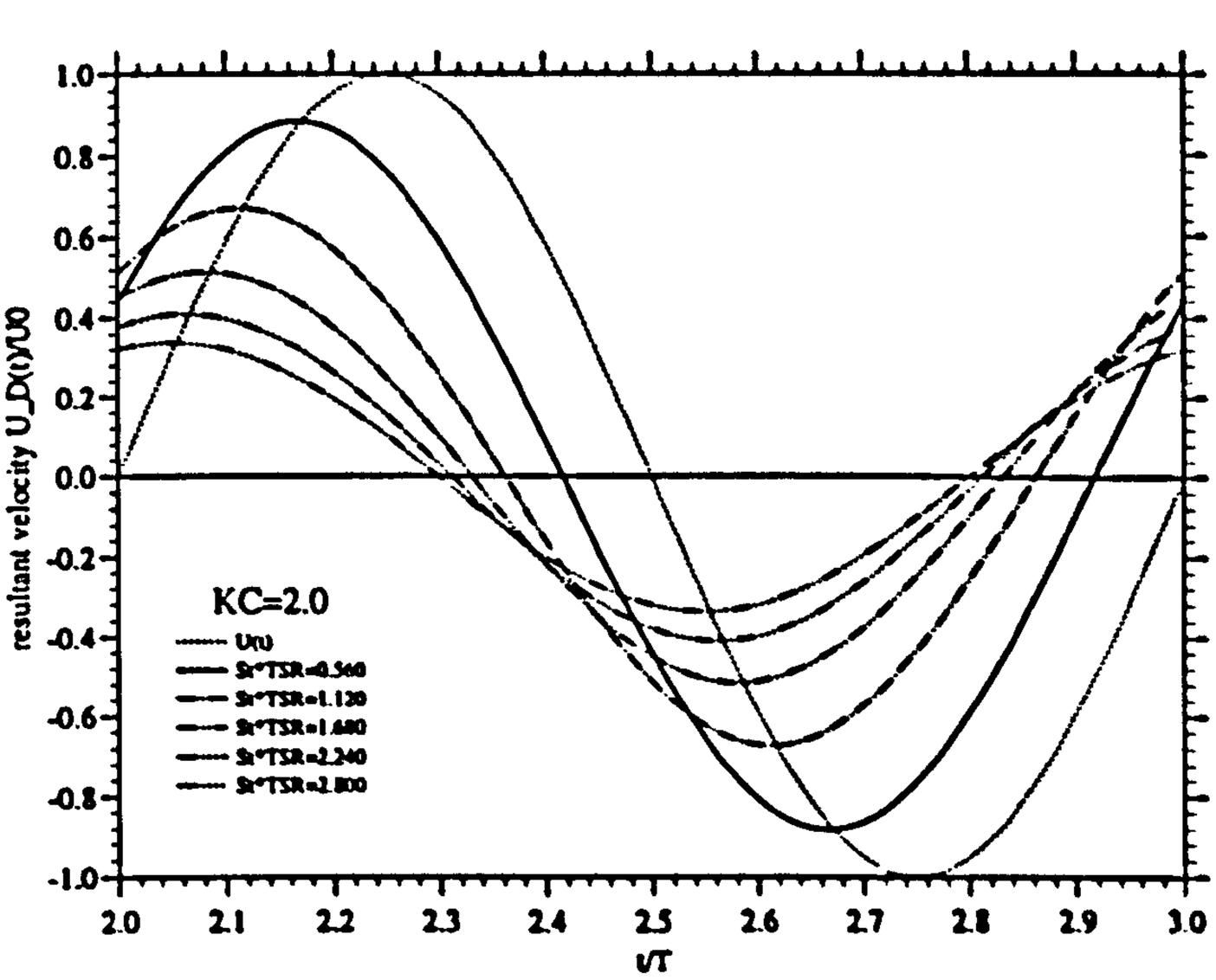

Figure 3.13: $U_D(t)$ vs t/T

The equations of the actuator disc theory given in the previous section were programmed as a time stepping routine in FORTRAN77, which was used to compute the cyclic variation of $U_D(t)$. Results obtained for KC of 2.0 at a number of $\sigma\Lambda$ values greater and smaller than that for optimum rotor efficiency are presented in figure (3.13). The graph shows the variation of $U_D(t)$ and $U(t)$ normalised by U_0 over a full cycle.

It is apparent that $U_D(t)$ has a sinusoidal behaviour and is shifted relative to $U(t)$ by some phase angle τ. This phase shift is obviously due to the back flow induced by the vortex ring which causes $U_D(t)$ to change sign ahead of free stream flow reversal. $U_D(t)$ may now be written as $U_D(t) = \hat{U}_D sin(\omega t + \tau)$, where $\hat{U}_D$ is the peak velocity through the rotor and $\omega = 2\pi/T$. Substitution in equation (3.59) leads to

$$\overline{C_P} = \frac{2\pi}{T} \kappa \int_0^T sin(\omega t)\, sin(\omega t + \tau)\, dt \tag{3.60}$$

where $\kappa = \sigma\, \Lambda\, (\hat{U}_D/U_0)$.

For a given flow period, therefore, $\overline{C_P}$ depends only on κ and the phase angle. The variation of κ and τ with $\sigma\Lambda$ is quantified for KC=2 in figures (3.14) and (3.15) below.

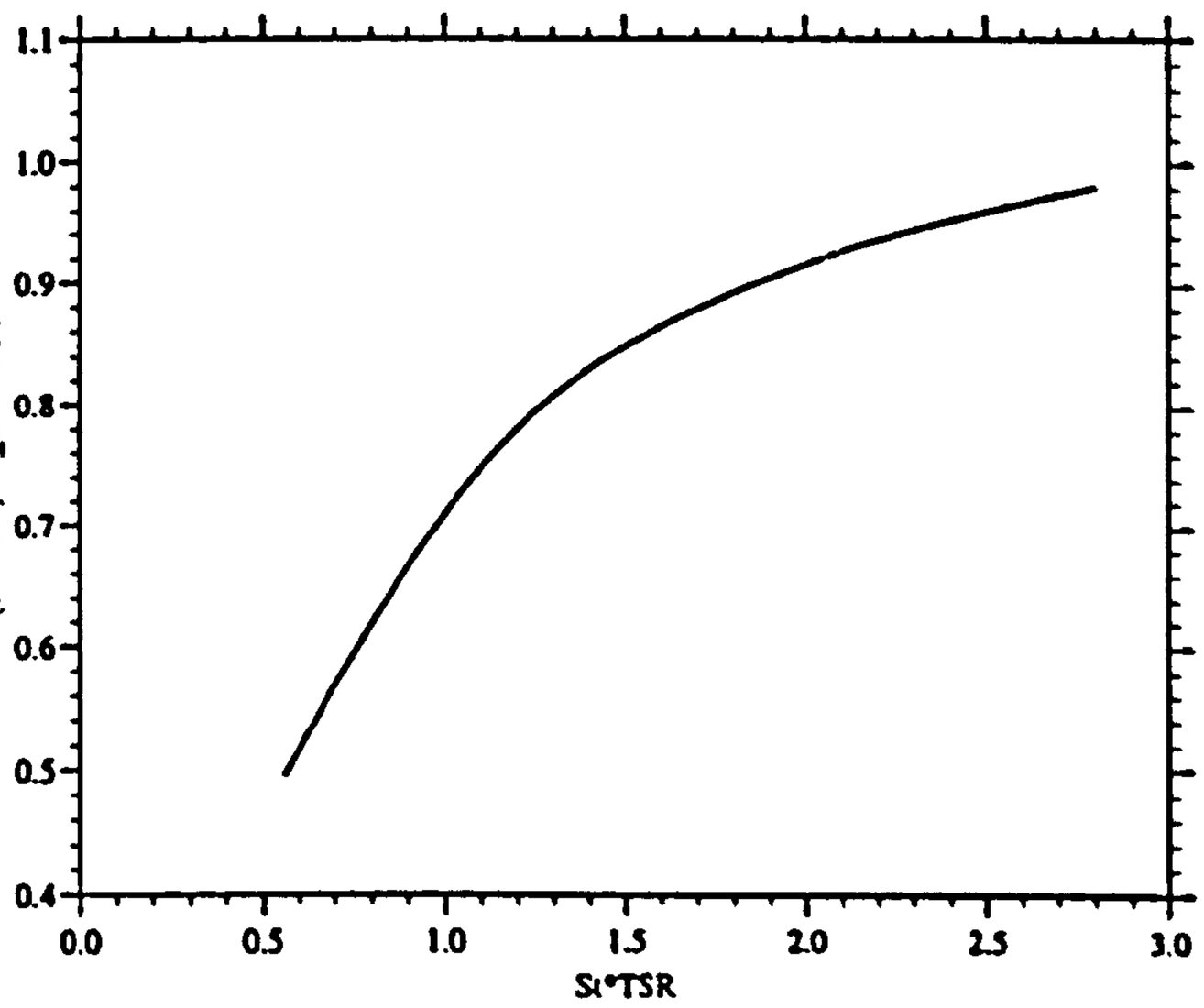

Figure 3.14: KC=2.0 - κ vs $\sigma\Lambda$

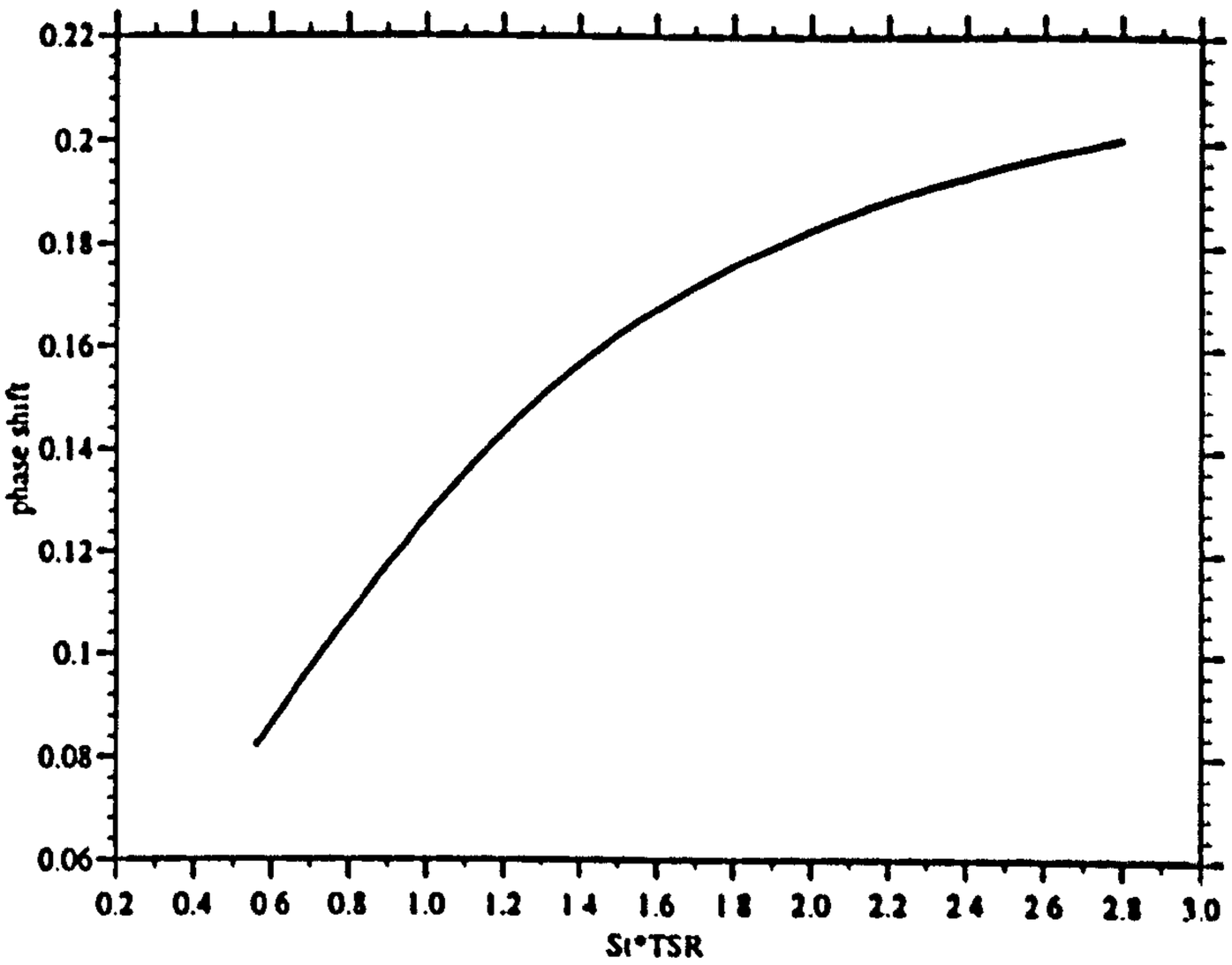

Figure 3.15: KC=2.0 - τ vs $\sigma\Lambda$

It can be seen that the gradient of both curves decreases at high values of $\sigma\Lambda$, which explains the comparative insensitivity of the wake losses to $\sigma\Lambda$ shown in figure (3.12) and expressed in equation (3.57) for turbine operation in this regime.

An interesting result of the theory is presented below in figure (3.16), which shows the computed variation of $U_D(t)/U_0$ in time for different KC at respective values of $(\sigma\Lambda)_{opt}$. It appears that when the turbine is operating at $\overline{C_P}_{max}$ the variation of $U_D(t)/U_0$ is independent of KC with $(\hat{U}_D/U_0)_{opt} = 0.72$ and $\tau_{opt} = 0.064/\pi$. This result may be verified from equation (3.59) which after substitution of $\sigma\Lambda = 2/KC$ by comparison with equation (3.25) gives

$$\frac{T}{4} = \int_0^T sin(\omega t)\frac{\hat{U}_D}{U_0} sin(\omega t + \tau)\, dt \tag{3.61}$$

which is satisfied by the derived values of$(\hat{U}_D/U_0)_{opt}$ and τ_{opt}.

Also shown in figure (3.16) is the corresponding axial back flow velocity $U_\Gamma(t)$ induced by the vortex ring. This velocity is presented in normalised form as the axial back flow factor $a_0(t)$ which is defined as $a_0(t) = U_\Gamma(t)/U_0$. From the figure it is evident that $a_0(t)$ varies sinusoidally with time so that $a_0(t) = \hat{a}_0 sin(\omega t + \tau_a)$. In fact, as is also illustrated in figure (3.16), it is found that when the turbine is operating at maximum efficiency $(\hat{a}_0)_{opt} = (\hat{U}_D)_{opt}$ and $(\tau_a)_{opt} = (\tau)_{opt} + \pi/2$. This condition for achieving the optimum efficiency is the oscillating flow equiv-

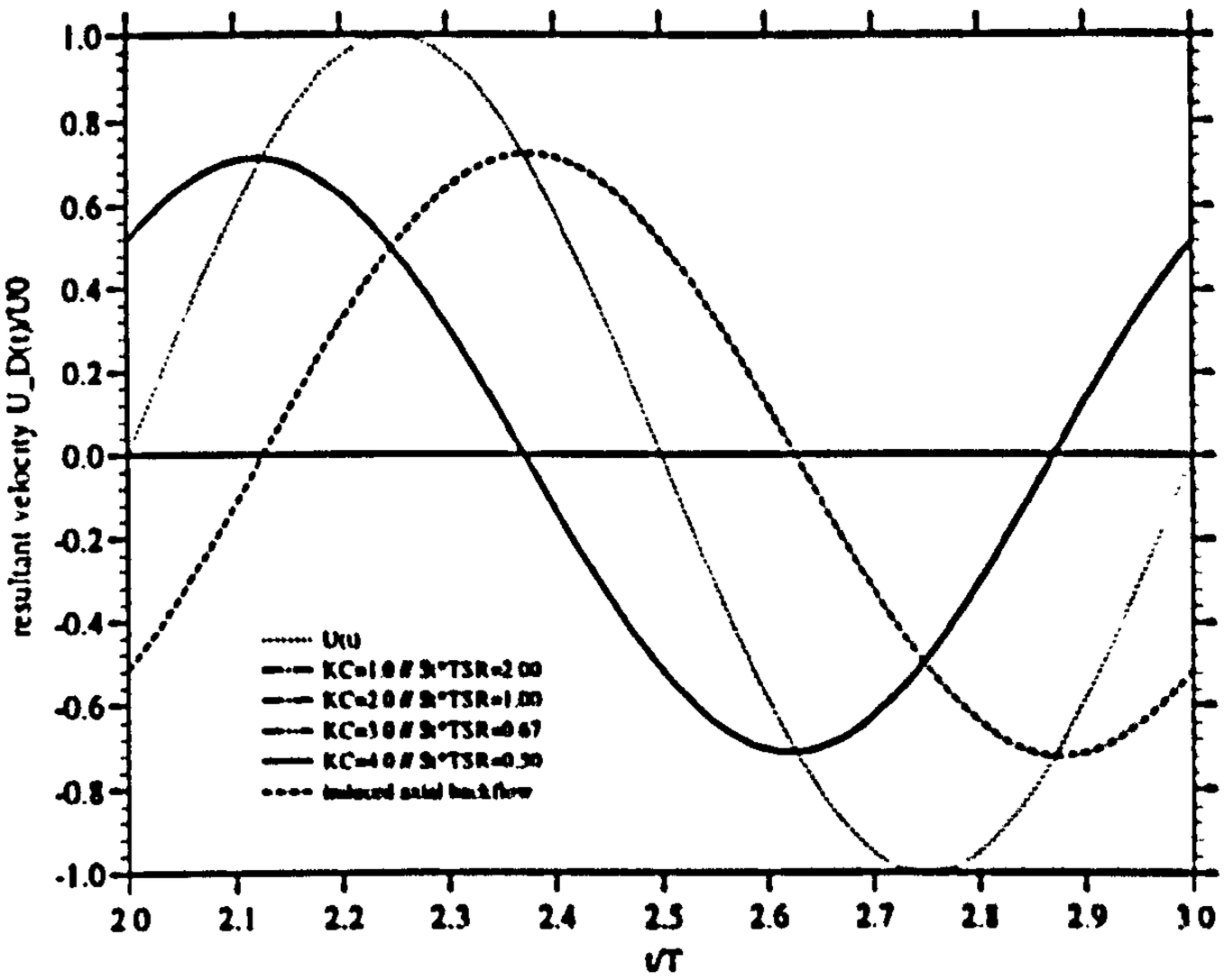

Figure 3.16: $U_D(t)_{opt}$ And $a_0(t)_{opt}$ vs t/T

alent to the well known steady flow result which states that the maximum ideal turbine efficiency of 0.59 (16/27) in inviscid flow occurs for an axial back flow coefficient of 1/3.

3.3.2 The Improved Numerical Model - Small KC Flow

Vortex Ring Formation And Convection

In the following, the rotor wake behaviour in small amplitude oscillatory flow is numerically studied for a KC number of 1.0 using the improved numerical model outlined in the previous report section. The results of the computations shown below were produced for a tip speed ratio Λ of 10.0 and $\sigma\Lambda$=0.570.

Figures (3.17) - (3.22) show a sectional presentation (noting the defined symmetry of the flow field) of the motion in discretised time steps of 1/10 of the flow cycle period T of the most recently formed vortex rings after 14 completed flow cycles. The vortex rings are depicted by circles the radius of which is proportional to their respective strength $\Gamma(t)$.

A notable flow feature is the strong unidirectional bias of the stream wise convection of the shed rings, which is initially stronger in the radial direction than in line with the flow.

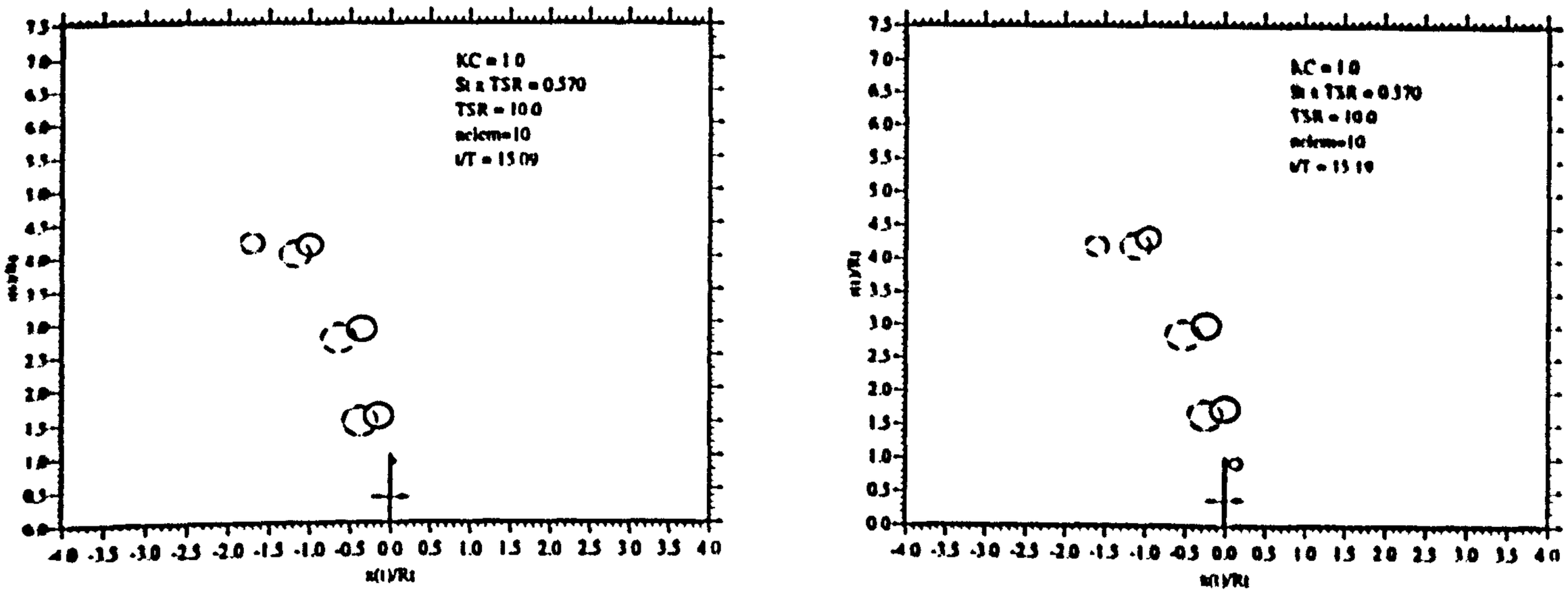

Figure 3.17: Vortex Ring Motion $KC = 1.0$; $\sigma\Lambda = 0.570$

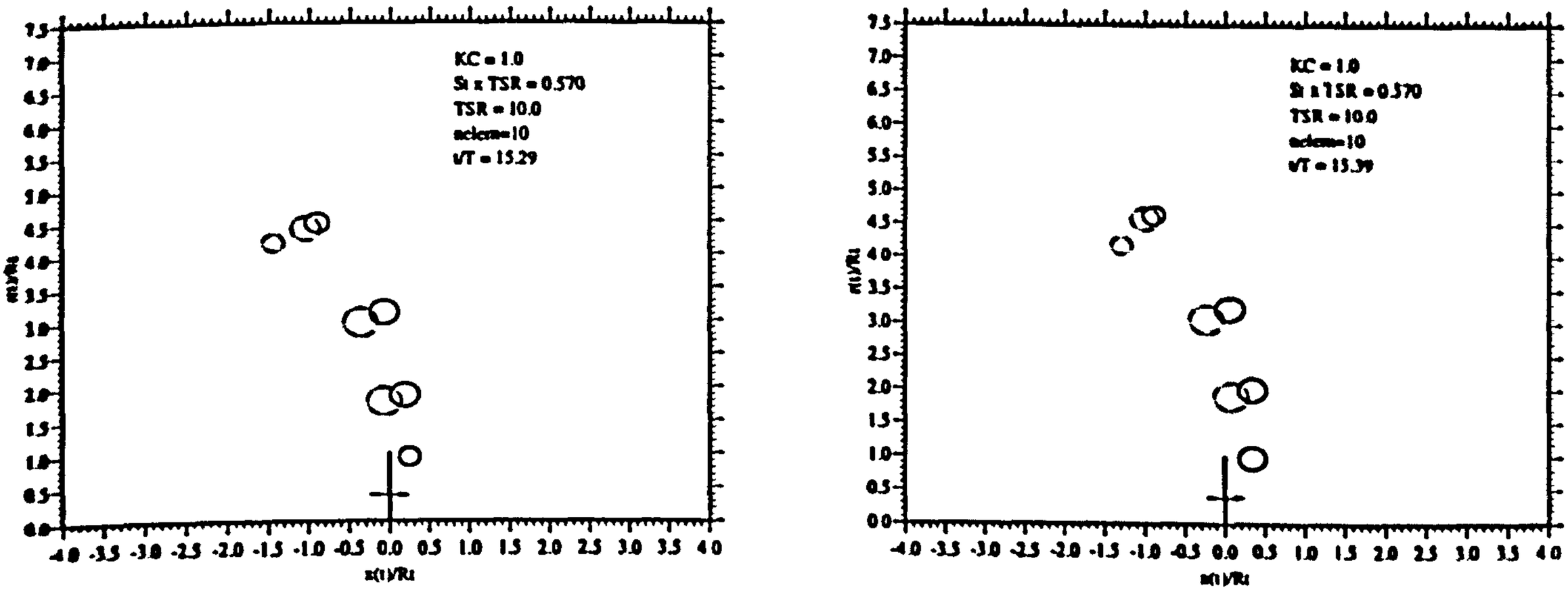

Figure 3.18: Vortex Ring Motion $KC = 1.0$; $\sigma\Lambda = 0.570$

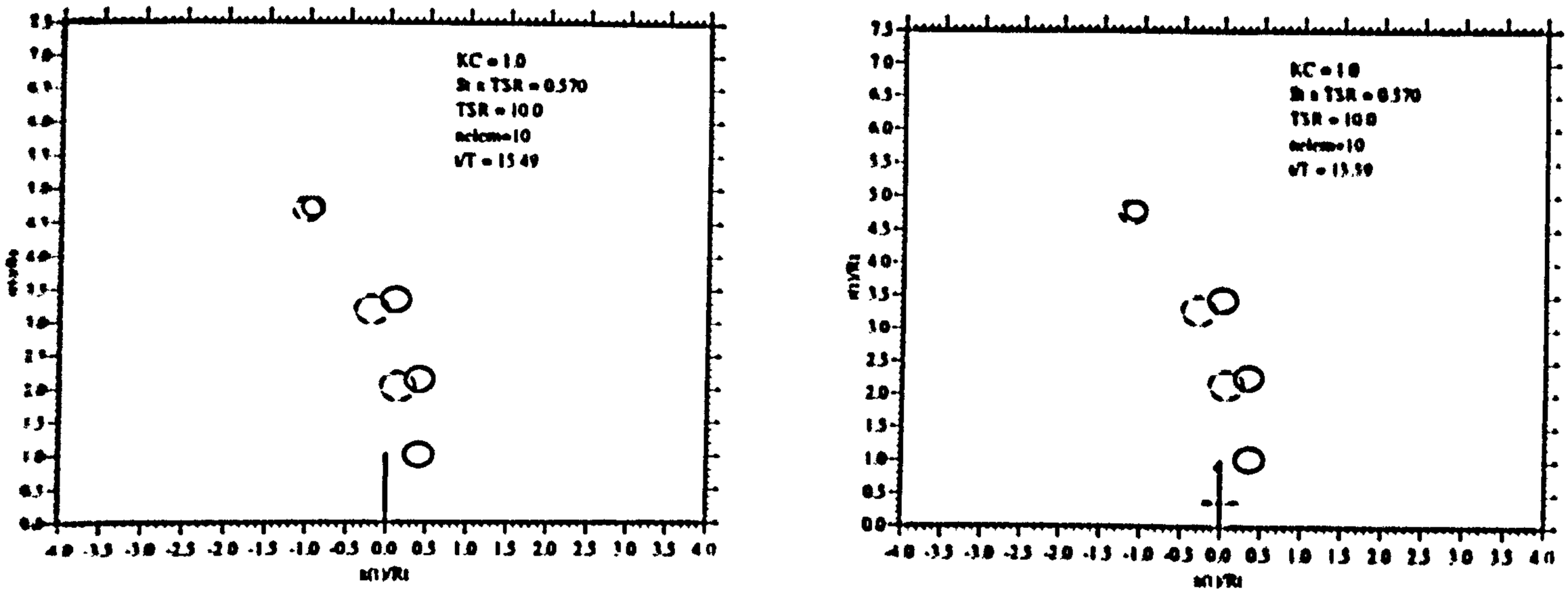

Figure 3.19: Vortex Ring Motion $KC = 1.0$; $\sigma\Lambda = 0.570$

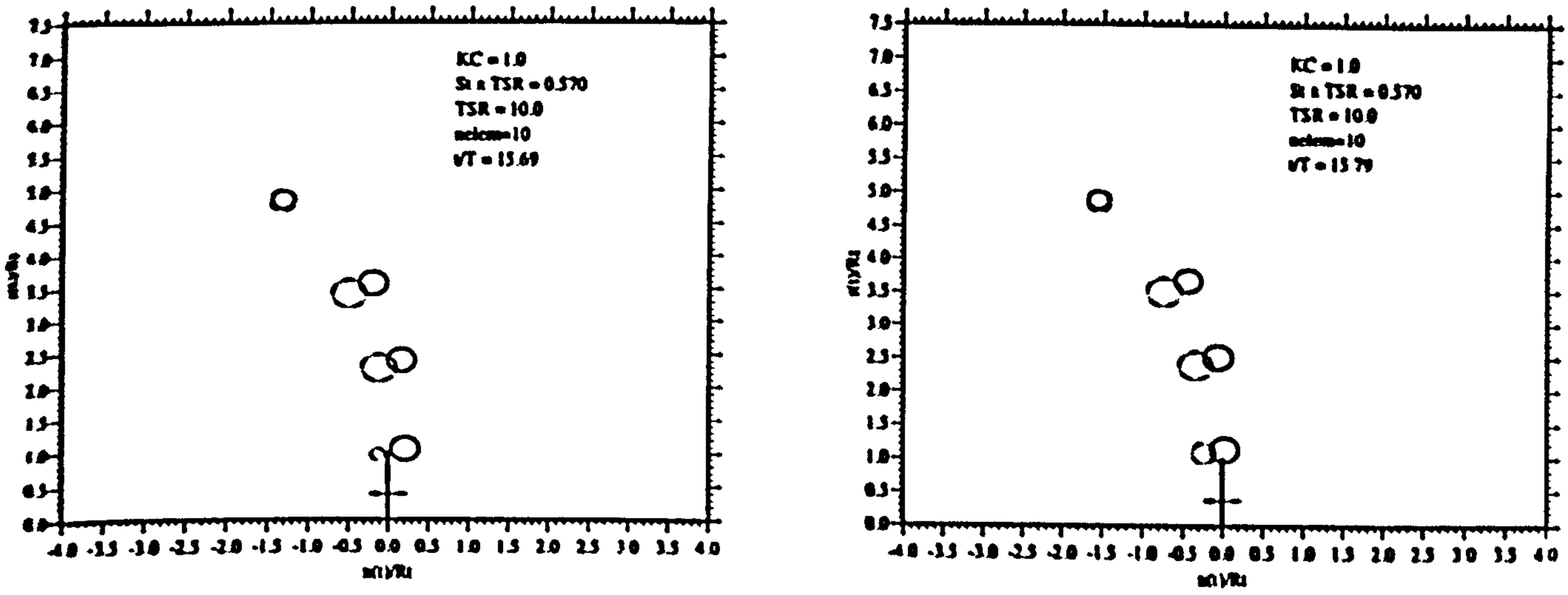

Figure 3.20: Vortex Ring Motion $KC = 1.0$; $\sigma\Lambda = 0.570$

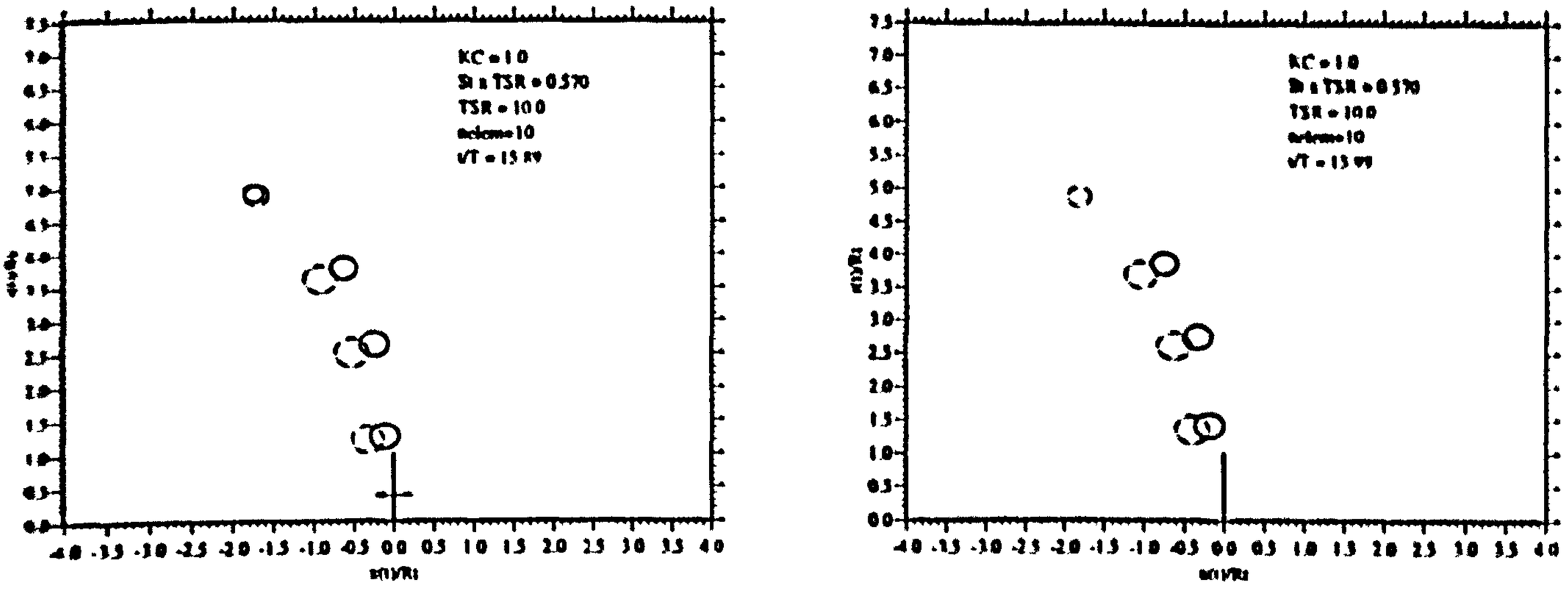

Figure 3.21: Vortex Ring Motion $KC = 1.0$; $\sigma\Lambda = 0.570$

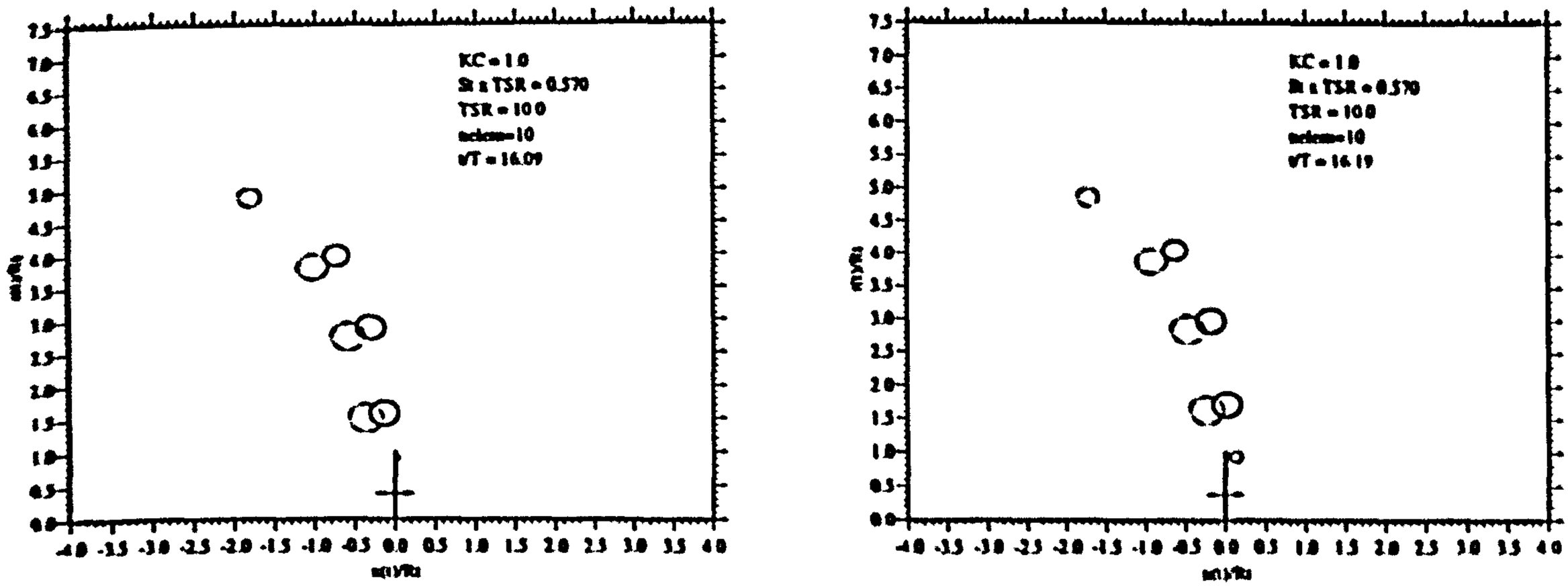

Figure 3.22: Vortex Ring Motion $KC = 1.0$; $\sigma\Lambda = 0.570$

Further, it is apparent that the vortex ring growing during the first half of the flow cycle stays close to the rotor tip during its formation. The depicted stream wise convection of the nascent vortex ring is around 40% R_T. This suggests that for small KC flows the assumption made in the actuator disc theory that the stream wise convection is small is not a bad one for this part of the flow cycle. In contrast, the convection of the nascent second vortex ring is somewhat greater since it evidently is forced to radially expand as the vortex ring formed on the first half of the cycle is swept back over the rotor.

In fact, the two rings subsequently pair up and convect away from the rotor under mutual influence. Clearly, this behaviour is somewhat different from the assumptions made in the actuator disc theory which proposes an entirely symmetrical wake structure over the the two sequential half flow cycles. The implications of this for the fluid dynamic performance of the rotor is discussed later in the report.

Evident in this illustration is also an imbalance of the vortex ring strength of the two rings formed during a flow cycle. Given that the vortex rings pair up it actually is this imbalance that causes the unidirectional stream wise convection and the apparent curved path of motion of the vortex pair. The extent of stream wise convection of the vortex ring pairs is therefore a direct indication of the imbalance of the paired rings. This imbalance is quantified in figure (3.23) which shows the normalised strength $\Gamma_0(t)/(U_0 R_t)$ of a number of the most recently formed vortex rings as a function of time.

Figure (3.24) shows the axial velocity induced on the centre line of the rotor due to individual vortex rings and the net induced velocity calculated as the sum of all contributions. It can be seen that due to the pairing of the vortex rings their effect in the plane of rotation almost cancels. Because, however, the paired vortex rings are not exactly equal and opposite in strength there is a residual component of induced velocity in the rotor plane. Overall, however, it is apparent that as a result of this pairing process the flow field in the rotor plane during a given flow cycle is dominated by the two vortex rings formed during that cycle.

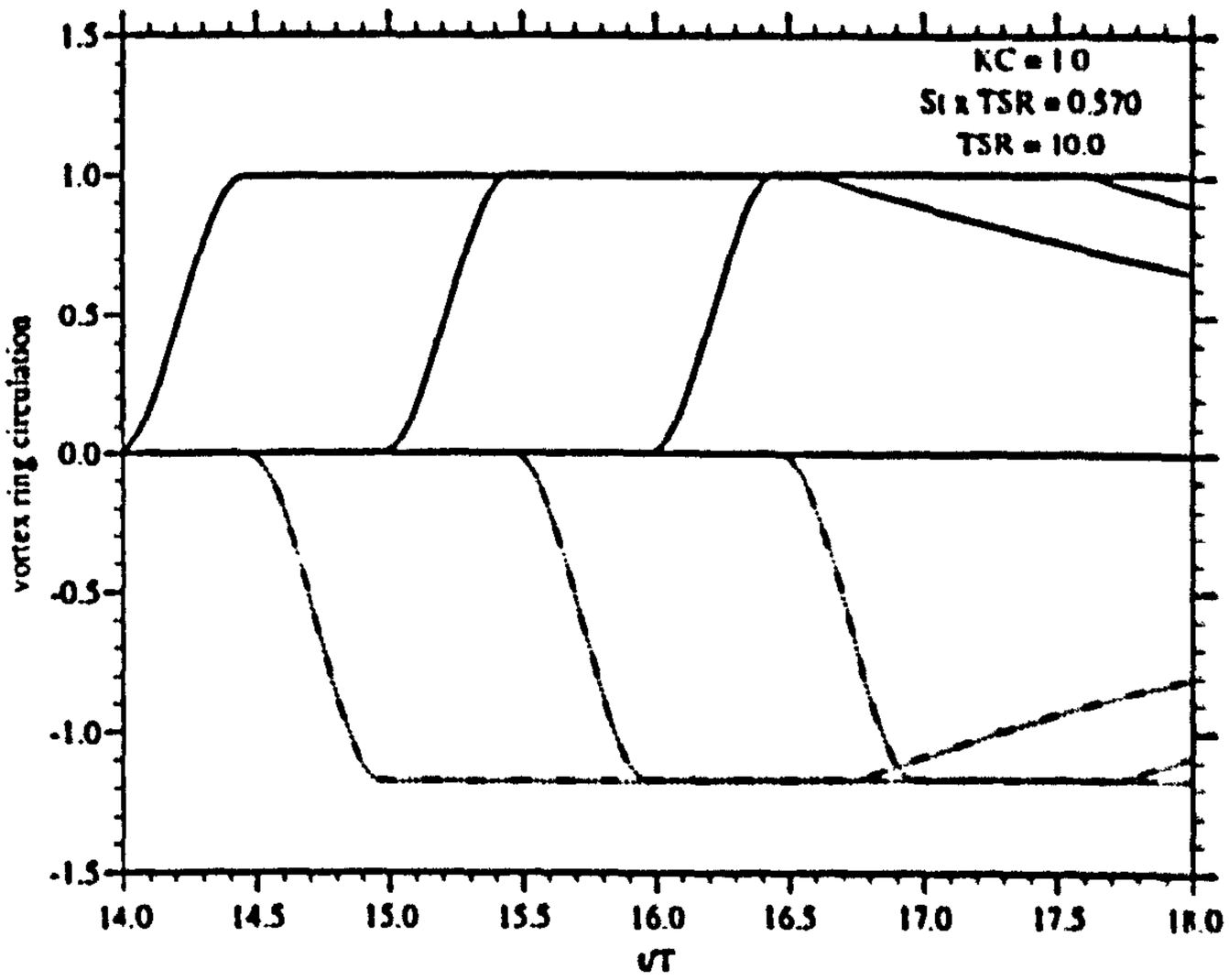

Figure 3.23: Vortex Ring Circulation

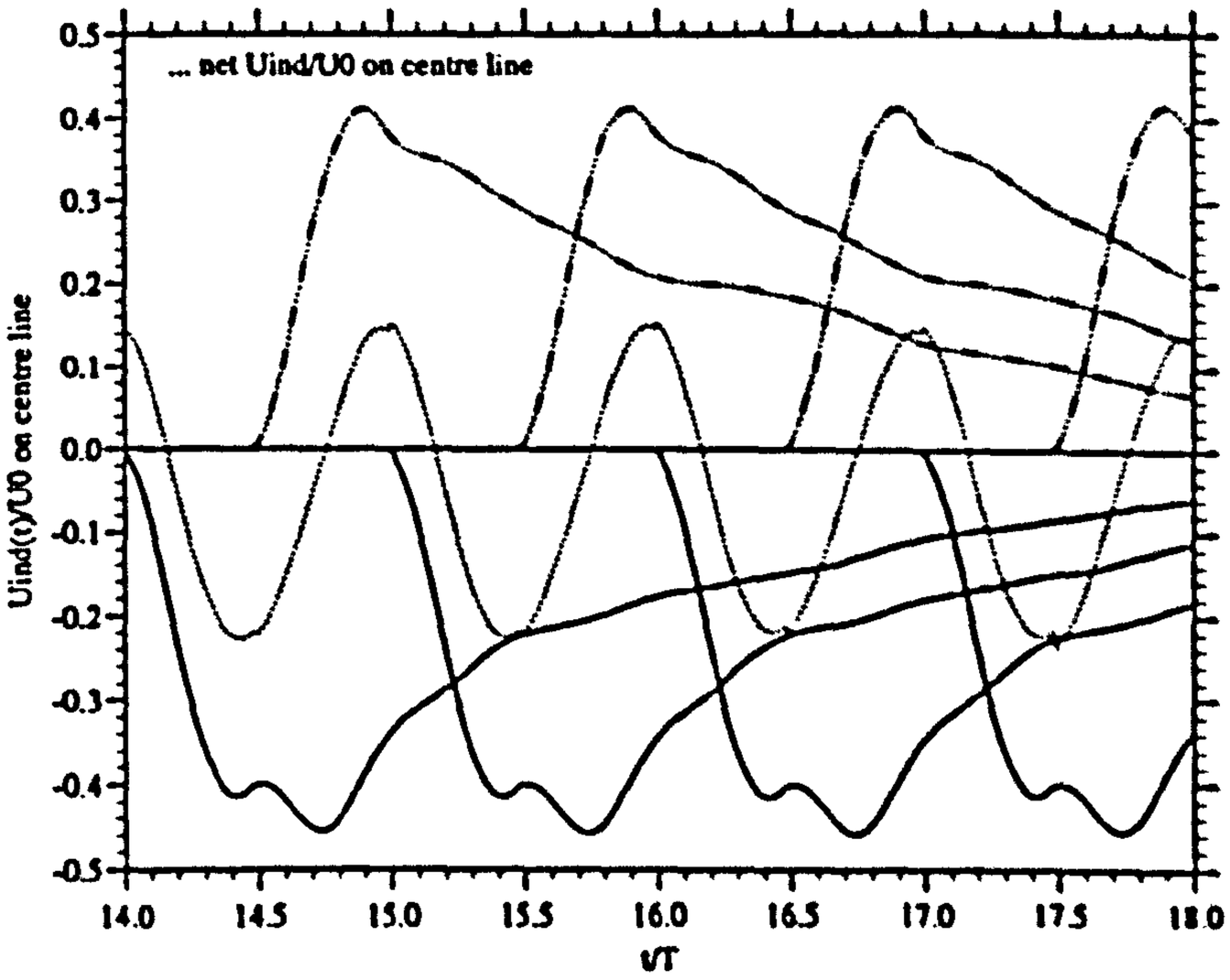

Figure 3.24: Vortex Ring Induced Velocities on Rotor Centreline

Noteworthy also is the asymmetrical time variation of the net induced velocity on the centre line producing a non zero mean. This is due to the described difference in vortex ring convection during the formation period on the two halves of the flow cycle as well as the imbalance of paired vortex rings.

Figure (3.25) tracks the variation of the core radius $a(t)$ to the vortex ring radius $r(t)$ with time for a number of vortex rings. It can be seen that the ring grows rapidly on both halves of the flow cycle until it is shed slightly ahead of flow reversal when $a(t)/r(t)$ reaches a maximum and the core growth is terminated. After the rings have been shed $a(t)/r(t)$ decreases in a $1/t$ fashion because r increases while $a(t)$ remains constant.

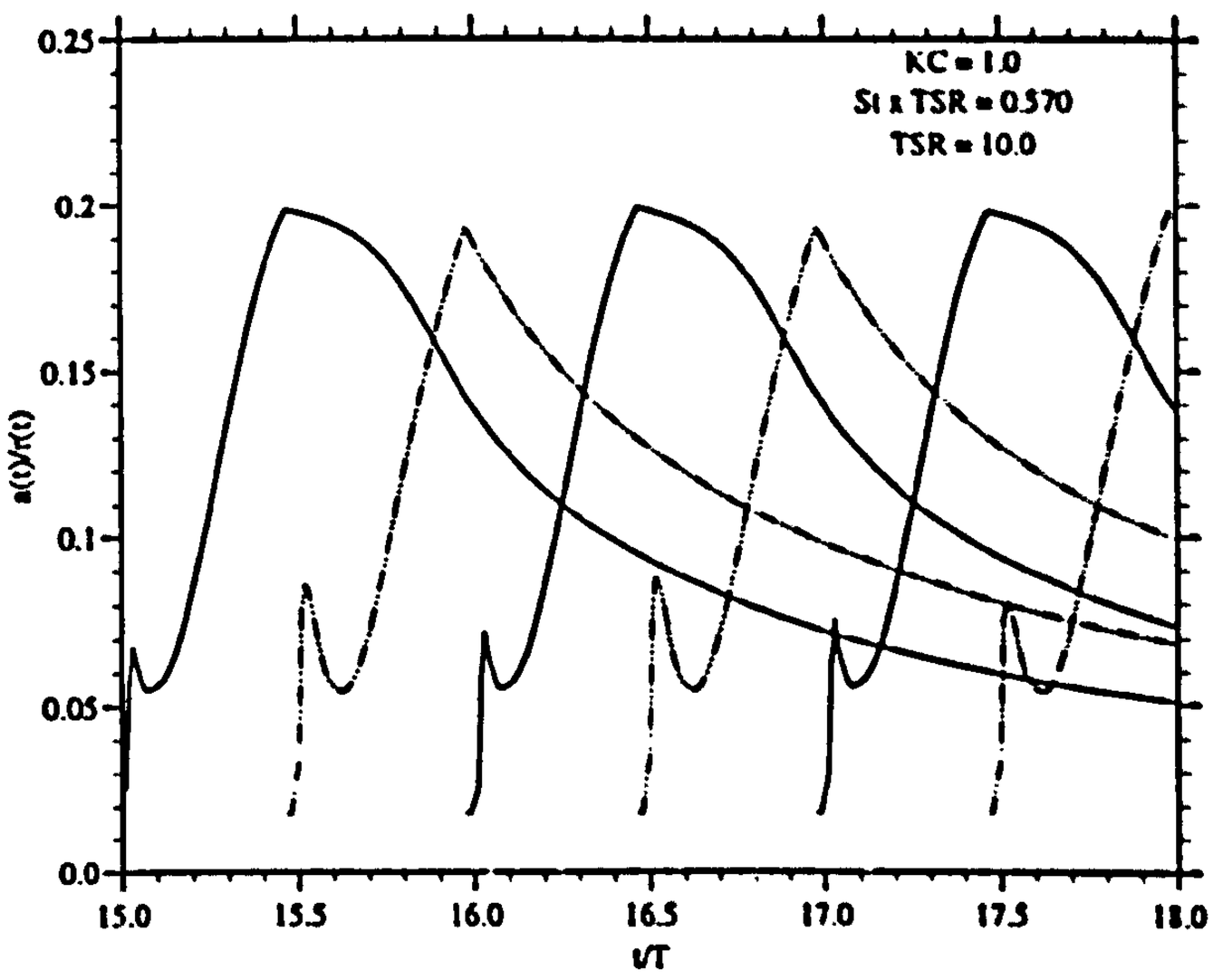

Figure 3.25: Vortex Ring Radius $a(t)$

It is apparent that in the first few computational time steps the newly formed vortex rings see a rapid increase in $a(t)/r(t)$. An explanation of this is offered in figure (3.26) below which shows the development of the radial and stream wise coordinates r(t)and x(t) of the vortex core position as well as the core radius a(t). It can be seen that the dramatic increase in $a(t)/r(t)$ is due to a rapid reduction in r(t) which results from the Brown and Michael model according to which the radial motion of the vortex ring is proportional to the ratio of the newly shed circulation to the current strength of the absorbing vortex ring, $d\Gamma/\Gamma$. As is discussed in more detail in the following it is found that for the cases under consideration the vortex ring growth commences at a point in the flow cycle when the resultant flow velocity $U_D(t)$ through the rotor and consequently the shedding

rate is high. It is due to this that the ratio of $d\Gamma/\Gamma$ is initially high causing rapid radial motion of the vortex ring core. A more in depth understanding of the vortex

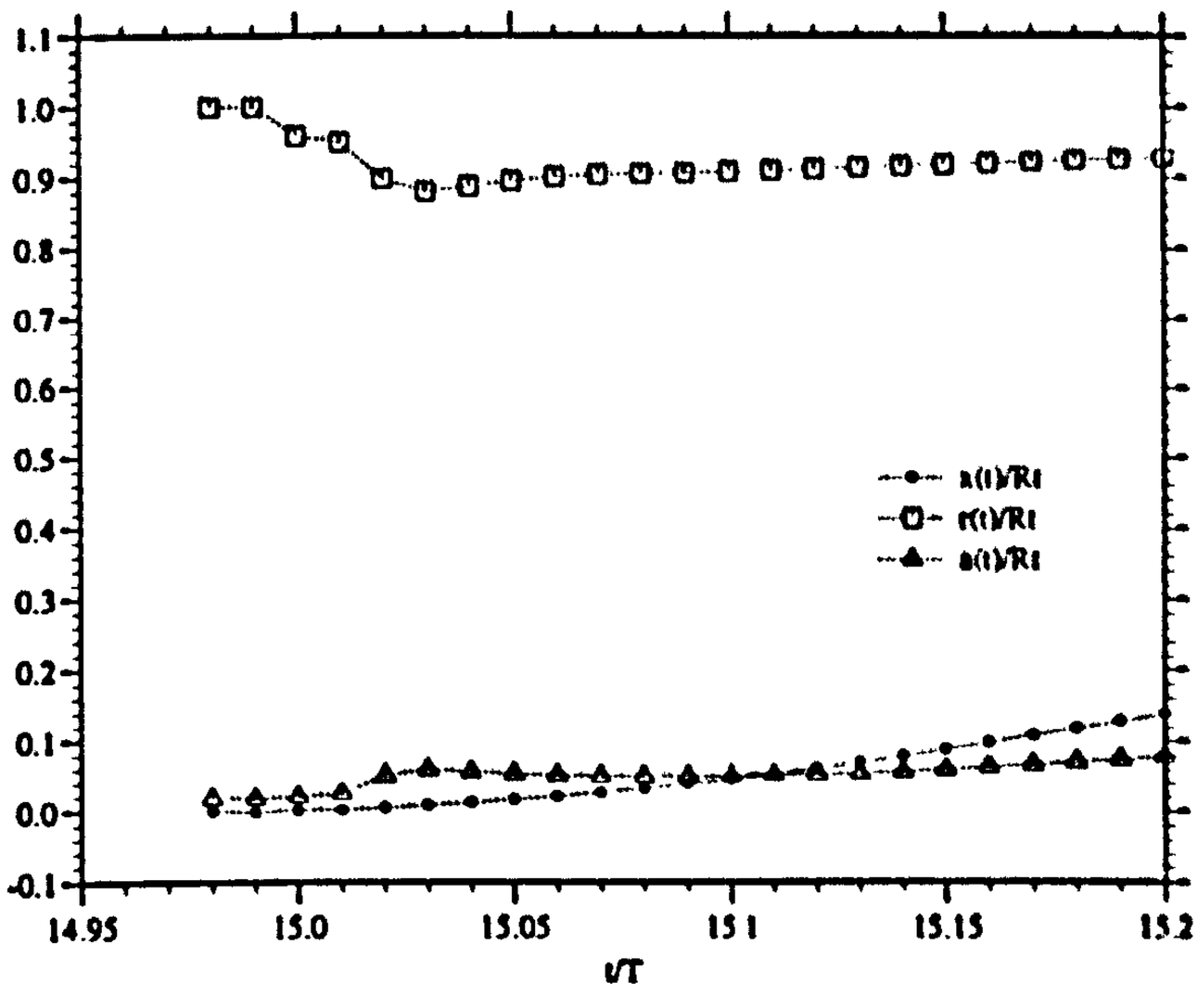

Figure 3.26: Initial Vortex Ring Growth And Convection

ring development may be obtained by considering the net induced axial and radial velocities as well as the self induced velocity, in the following denoted $U_{rind}(t)$, $U_{zind}(t)$ and $U_{self}(t)$ respectively, which the vortex rings experience at the centre of their cores and according to which they are convected. These velocities are presented in figure (3.27) for the two vortex rings formed on the 6th flow cycle.

It is apparent, that for the vortex ring formed on the first half of the cycle induced radial and axial velocities are initially small and of comparative magnitude. This is due to the fact all previous shed rings have paired up and their effect on the growing ring almost cancels. $U_{self}(t)$ increases steadily until the strength of the vortex ring has reached a maximum, at which point it almost equals $U_{zind}(t)$ in magnitude. Because, during the phase of formation the sign of $U_{self}(t)$ is in opposition to the free stream it acts so as to retard the stream wise convection away from the rotor. When the vortex ring is shed and the flow reverses direction $U_{self}(t)$ actually aides the motion back through the rotor.

As the new vortex ring on the other side of the rotor gains in strength and the two rings approach each other in space there is a dramatic increase in $U_{zind}(t)$ for the first ring. From the start of its formation the second ring itself experiences a fairly large $U_{zind}(t)$ due to the presence of the first ring. As is the case for the first

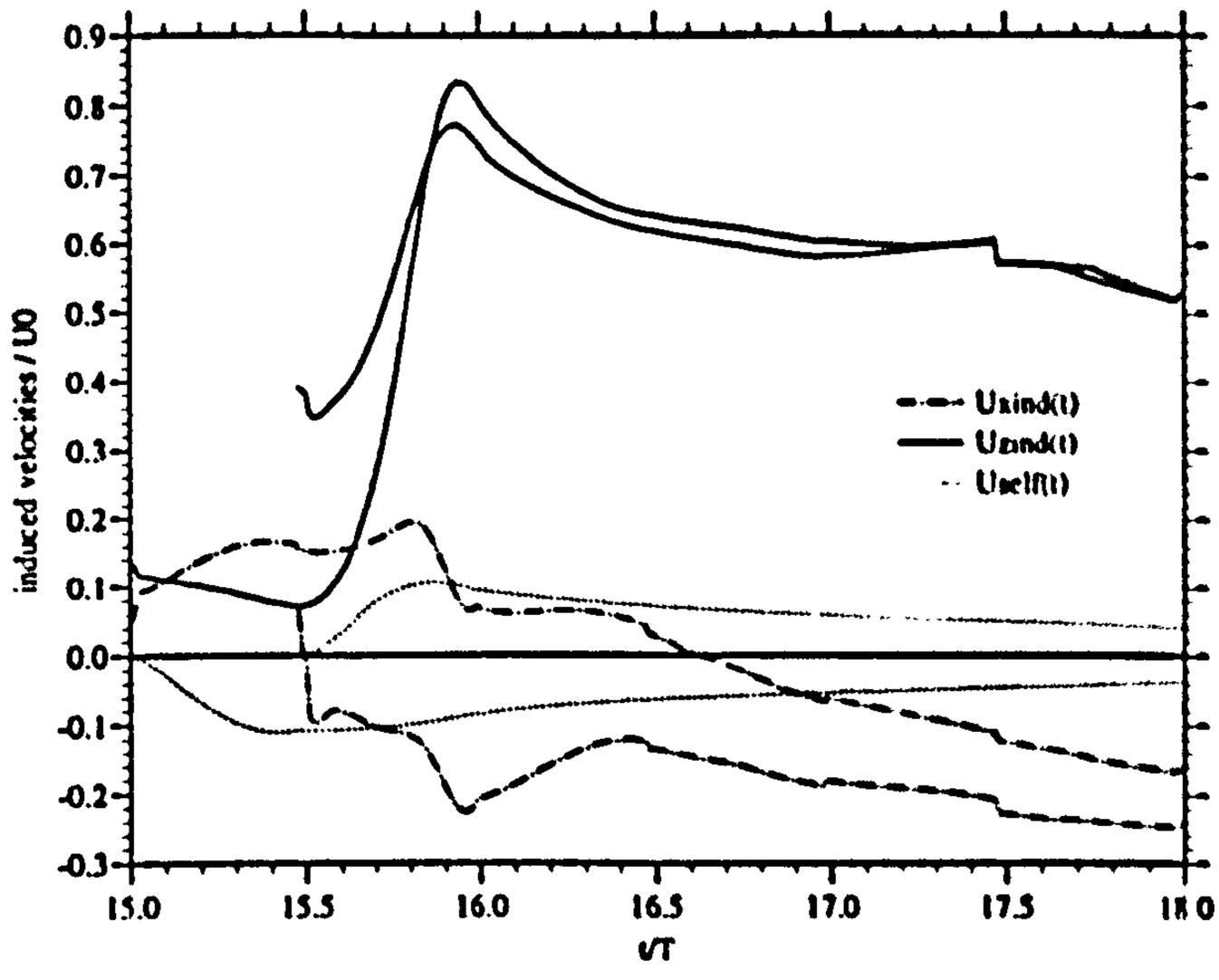

Figure 3.27: Velocities Induced on Vortex Rings

ring $U_{xind}(t)$ increases equally as rapid as the proximity between the two rings grows. This explains the initially strong radial expansion and coalescence of the two rings. However, when the two rings have paired up and move further away from the rotor their expansion becomes more strongly affected by the presence of the vortex rings shed on previous flow cycles. As far as $U_{xind}(t)$ is concerned, it can be seen that until the vortex rings are very close together they do not appear to greatly affect each other. The pairing process gains emphasis in the presentation through the notable coalescence of $U_{xind}(t)$ and $U_{xind}(t)$ shown for the two vortex rings. Once they have paired up each mutually dominates the other's stream wise component of convection over the influence of other previously formed rings until they have moved further away from the rotor and other vortex pairs have been formed.

Though, the wake structure described above was initially stable computations carried out over a larger number of flow cycles showed that a different mode of vortex ring motion can evolve as shown in figures (3.28) - (3.33) below.

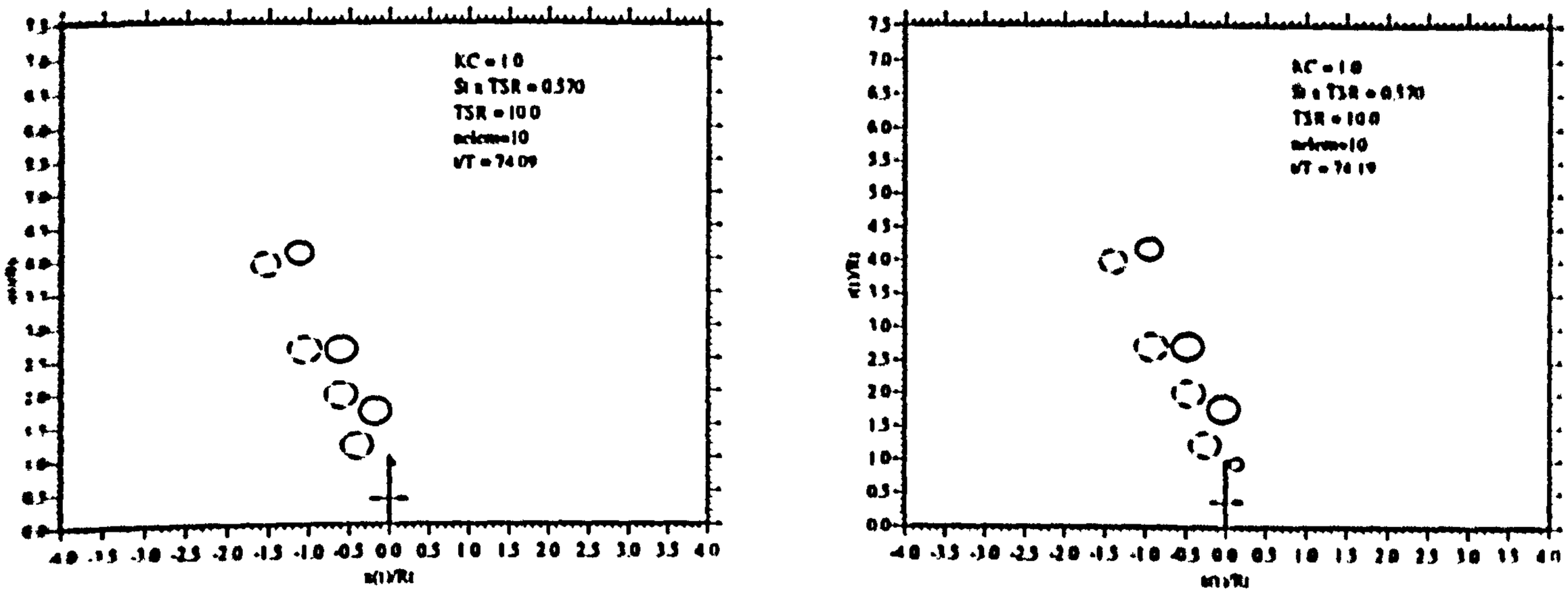

Figure 3.28: Vortex Ring Motion $KC = 1.0$; $\sigma\Lambda = 0.570$

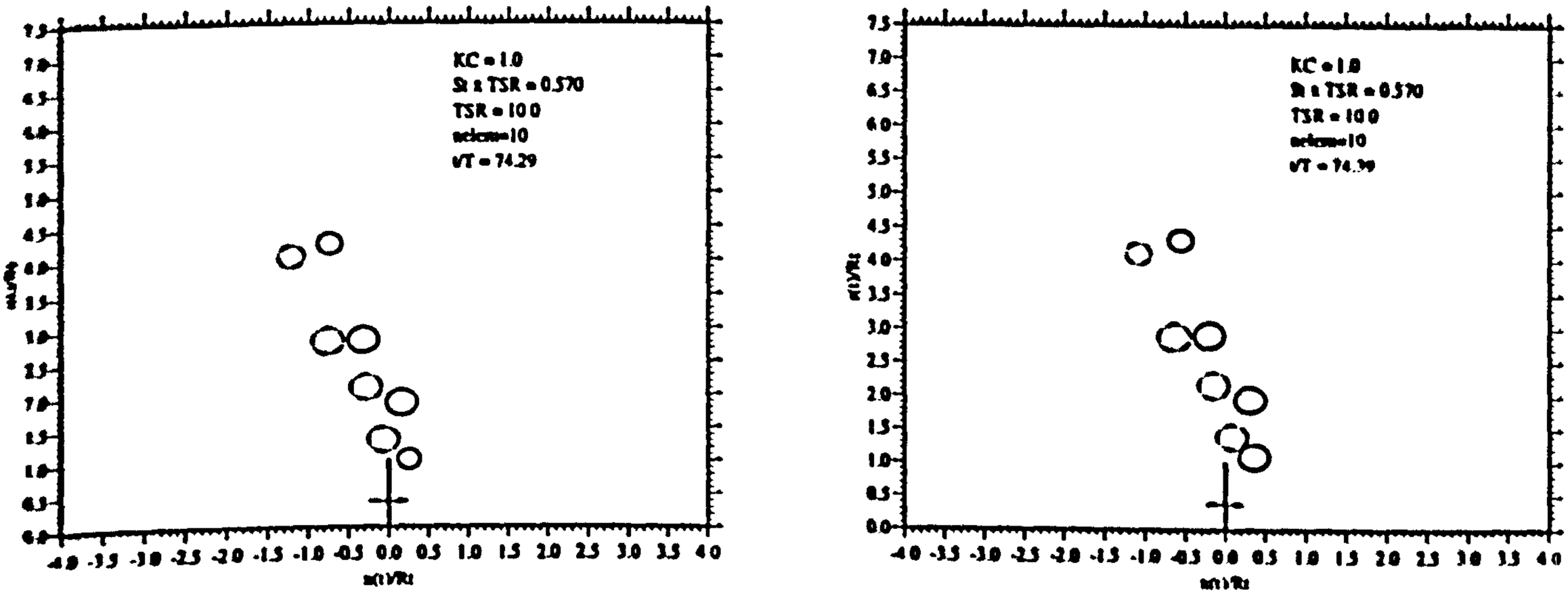

Figure 3.29: Vortex Ring Motion $KC = 1.0$; $\sigma\Lambda = 0.570$

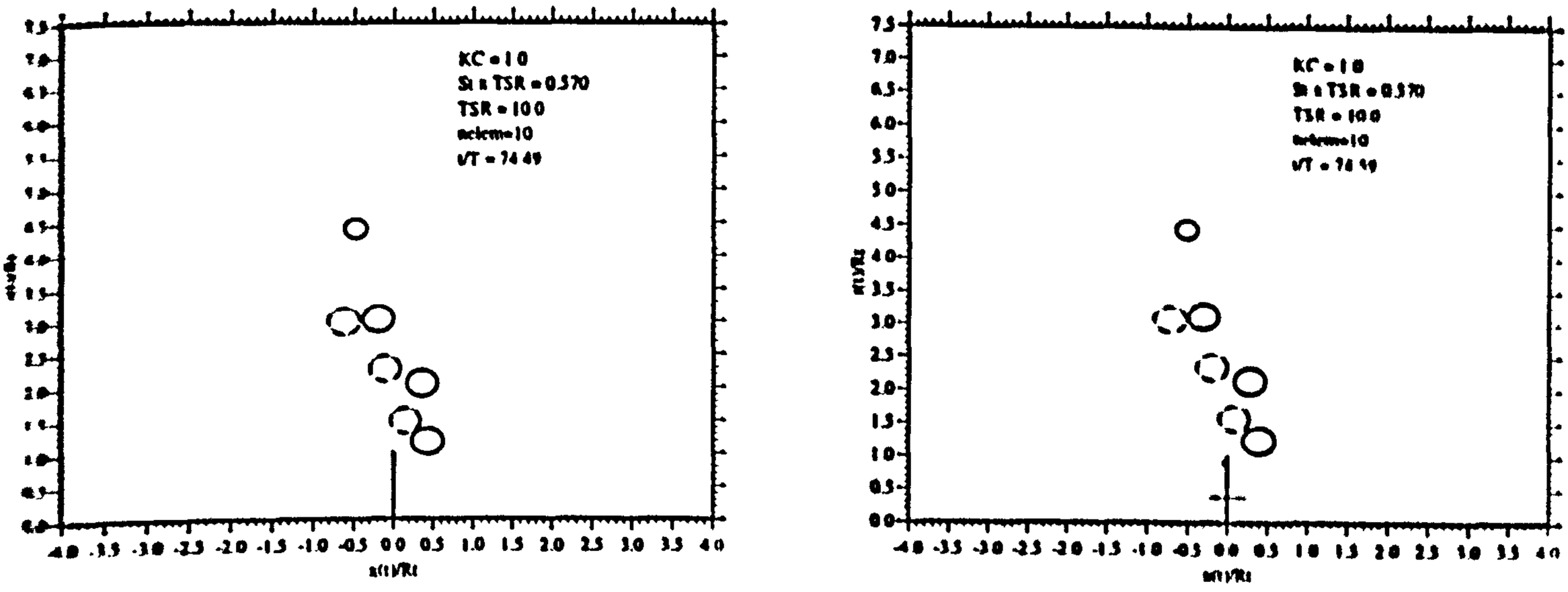

Figure 3.30: Vortex Ring Motion $KC = 1.0$; $\sigma\Lambda = 0.570$

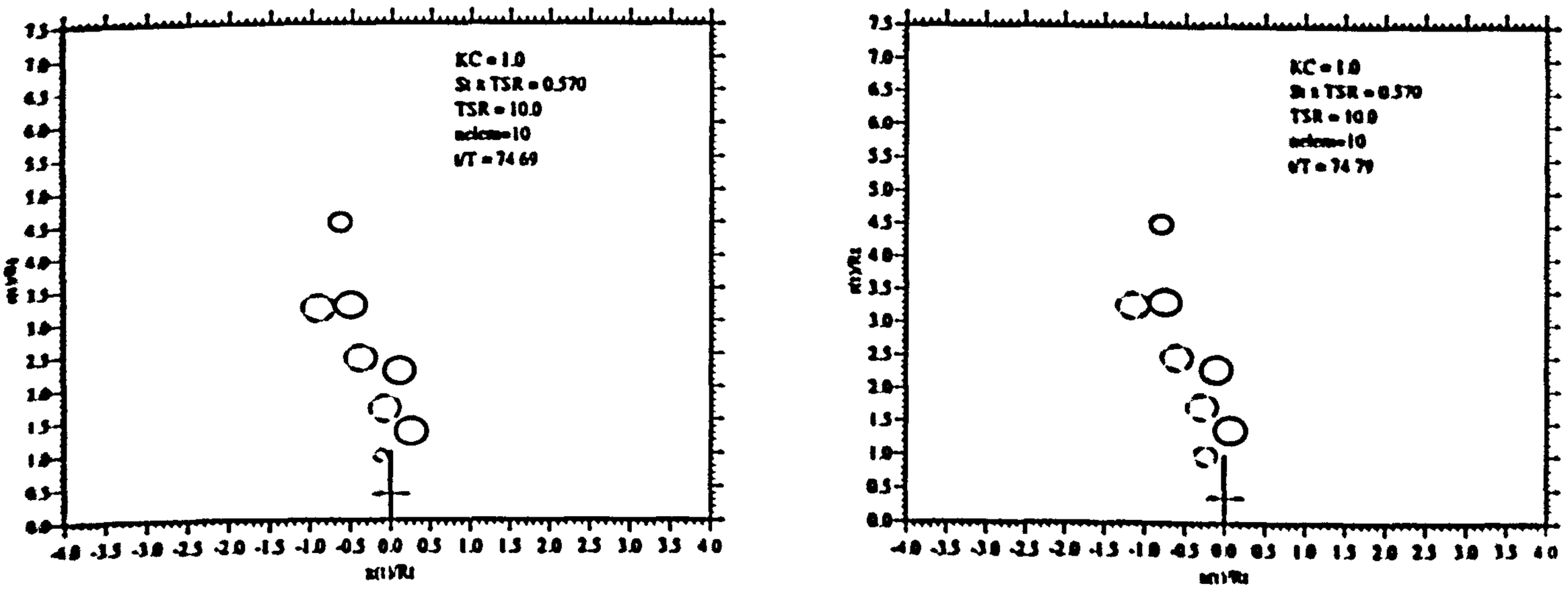

Figure 3.31: Vortex Ring Motion $KC = 1.0$; $\sigma\Lambda = 0.570$

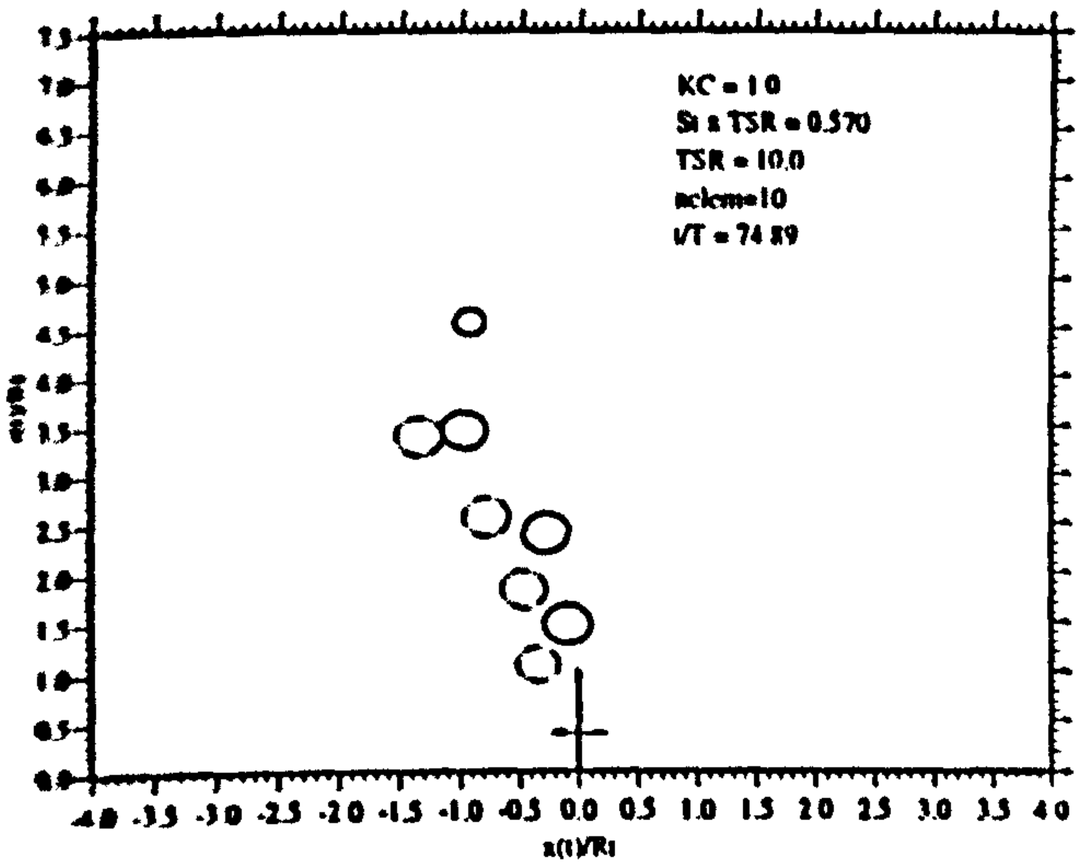

Figure 3.32: Vortex Ring Motion $KC = 1.0$; $\sigma\Lambda = 0.570$

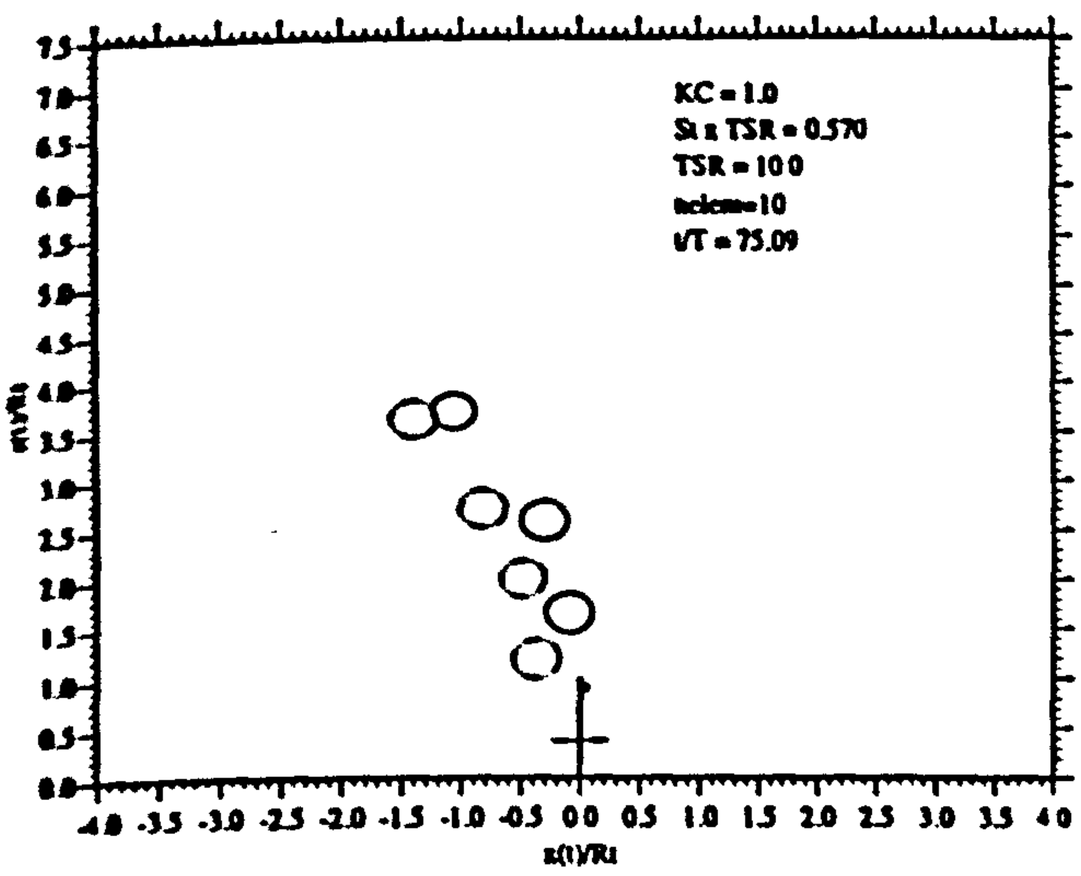

Figure 3.33: Vortex Ring Motion $KC = 1.0$; $\sigma\Lambda = 0.570$

In the sequence shown which occurred after 73 complete flow cycles the vortex ring convection is as was shown for previous flow cycles strongly dictated by radial expansion, but now shows a more balanced convection process on the sequential halves of the flow cycle. It can be seen that the rings no longer pair up and move off together with the vortex ring formed first dominating the motion of the second from its point of formation. A further notable difference to the flow development discussed above is that in this mode both vortex rings shed on opposing sides of the rotor during one flow cycle are swept back over the rotor subsequent to being shed.

This flow development shows greater resemblance to that assumed for the actuator disc theory given earlier. It will be shown later that for this transient wake mode there is better agreement between the performance predictions made from the two numerical models, as may be expected.

Figures (3.34) and (3.35) further quantify the symmetry of the flow field showing that vortex rings shed on both halves of a flow cycle have near equal strength and, therefore, produce a more symmetrical variation of net induced velocity on the rotor centreline.

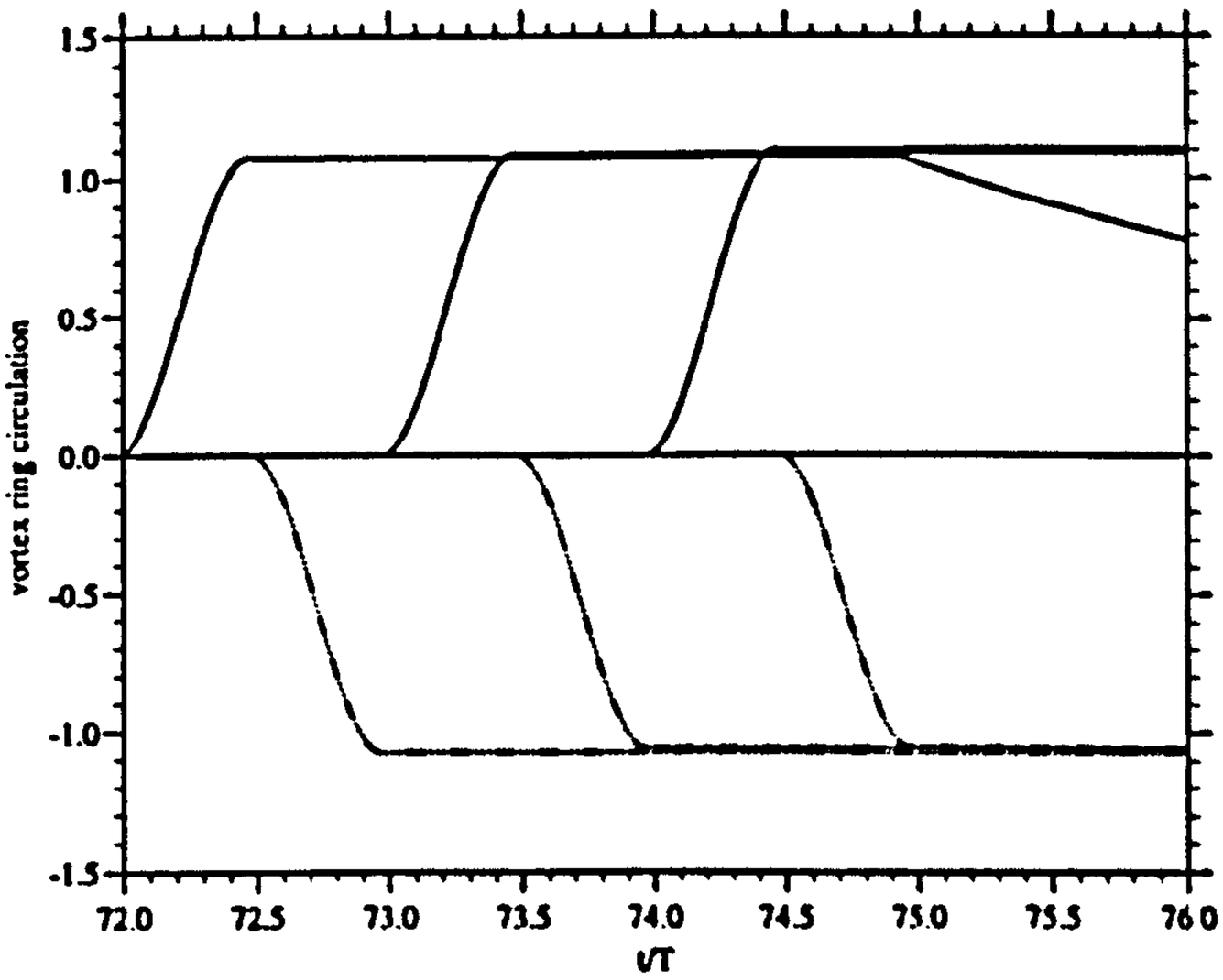

Figure 3.34: Vortex Ring Circulation

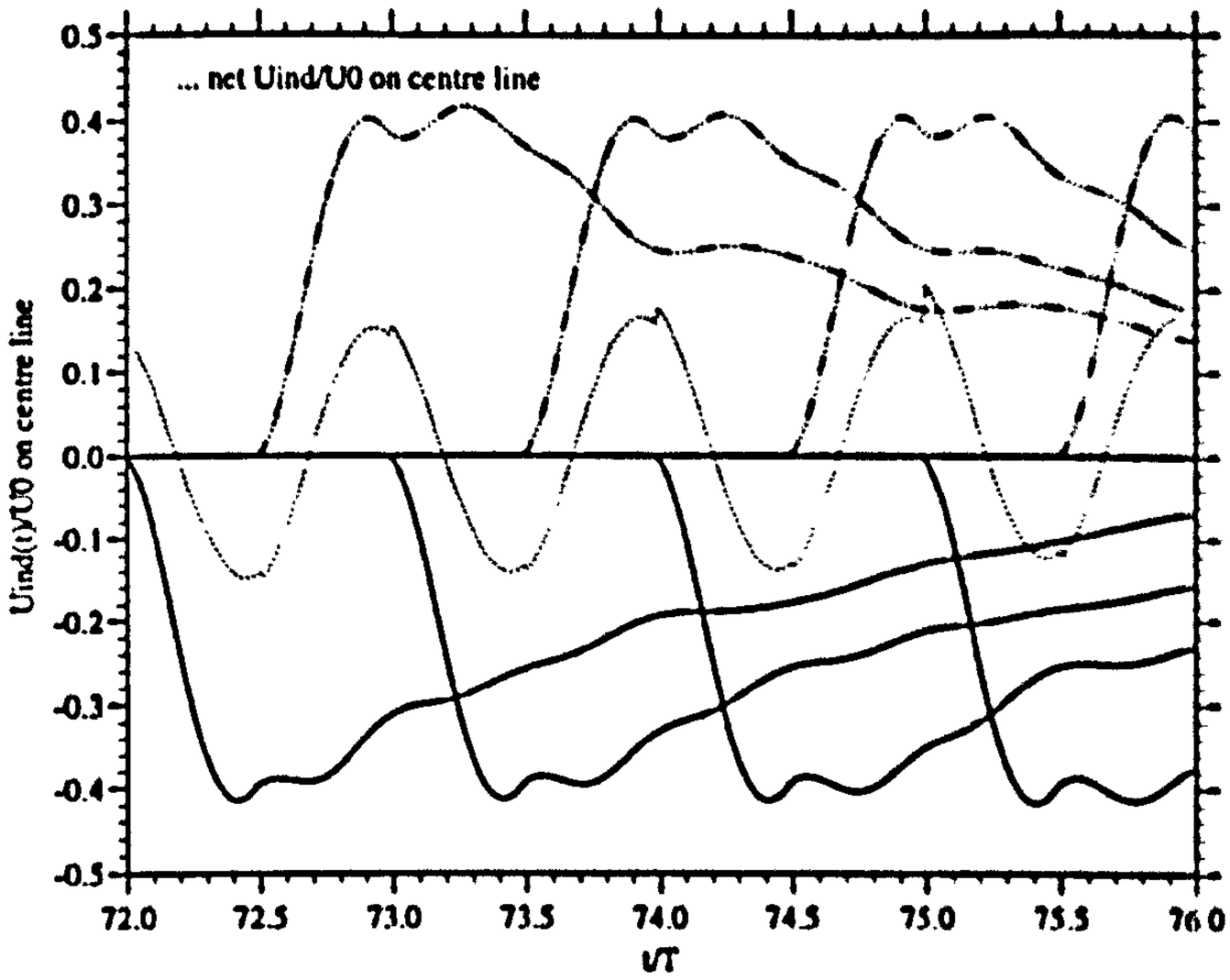

Figure 3.35: Vortex Ring Induced Velocities on Rotor Centreline

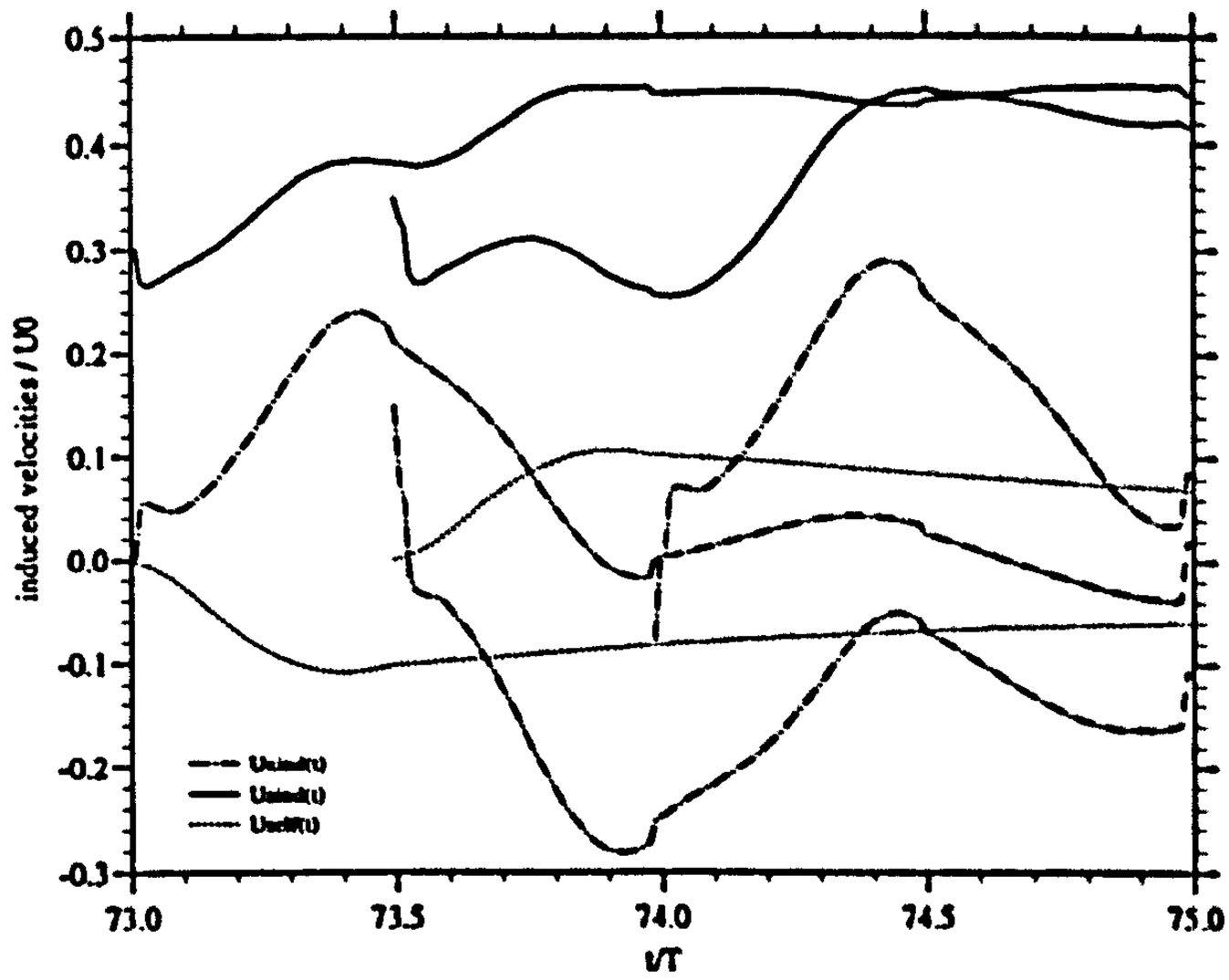

Figure 3.36: Velocities Induced on Vortex Rings

From figure (3.36) it can be seen that in this range of wake development all vortex rings experience a significant radial velocity from the start of their formation which does not increase as rapidly as in the earlier wake mode while a vortex ring is growing. In contrast to the characteristics of the earlier flow structure, it is the axial velocity experienced by the nascent ring that sees a rapid increase up to a maximum value which is reached just prior to the point of shedding. On both halves of the cycle the induced velocity $U_{ind}(t)$ exceeds $U_{self}(t)$ which is in opposition to it so that in this case the net effect of all induced axial velocities is to promote a greater rate of convection away from the rotor.

Flow Through The Rotor And Turbine Performance

In the derivation of the numerical performance analysis it was shown that the rotor performance is strongly dependent on the net axial back flow $U_r(t)$ induced by the rotor wake. Figure (3.37) shows the time dependent variation of the axial back flow factor $U_r(t)/U_0$ computed by the numerical model for KC=1.0 and $\sigma\Lambda = 0.570$ at radial stations $r/R_T = 0.00$ / 0.15 / 0.51 / 0.96 (n.b. $r/R_T = 0$ is the centreline of the rotor) over two flow cycles which correspond to the vortex ring motion after 14 flow cycles shown in figures (3.17) - (3.22).

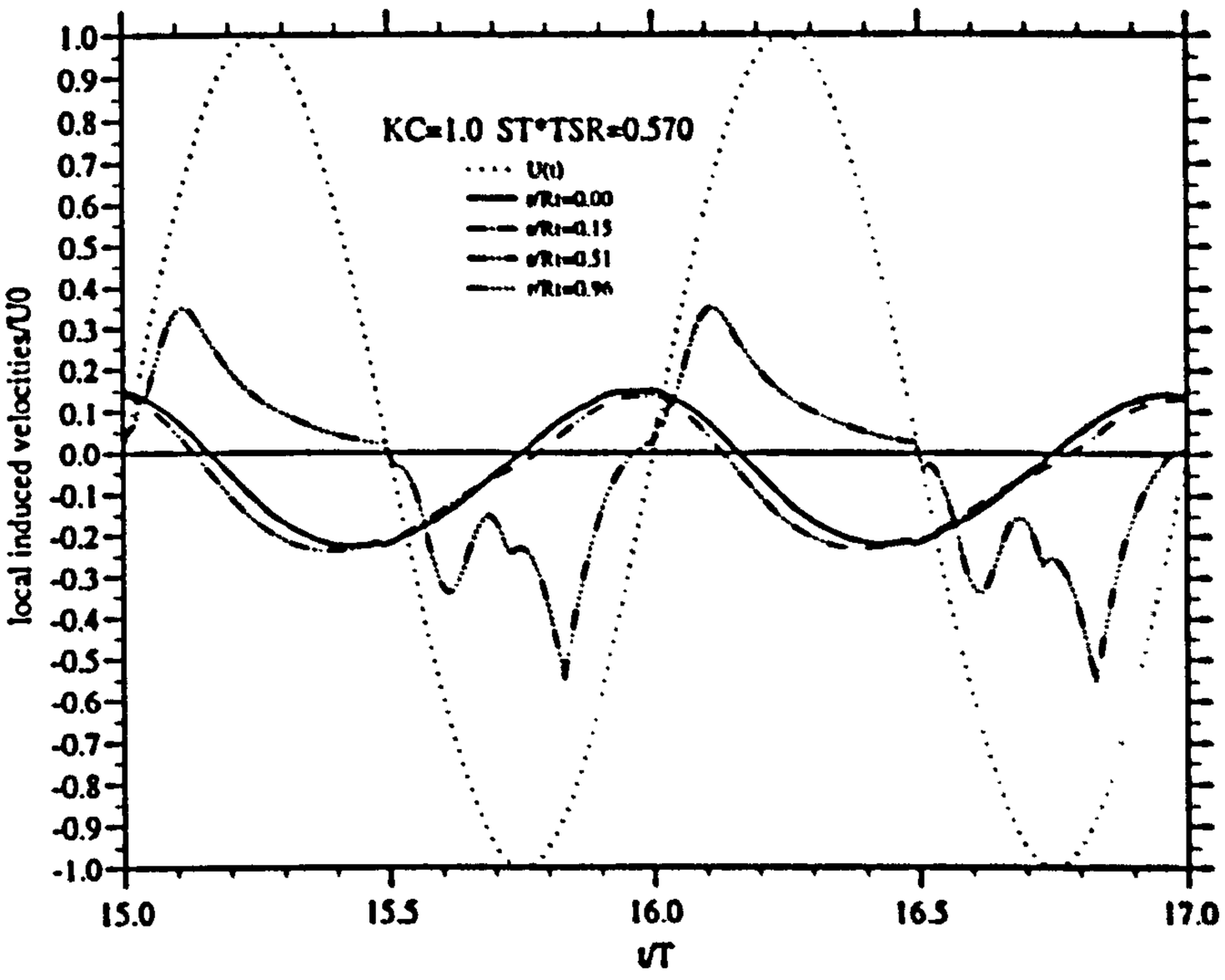

Figure 3.37: $U_r(t)/U_0$ vs. (t/T)

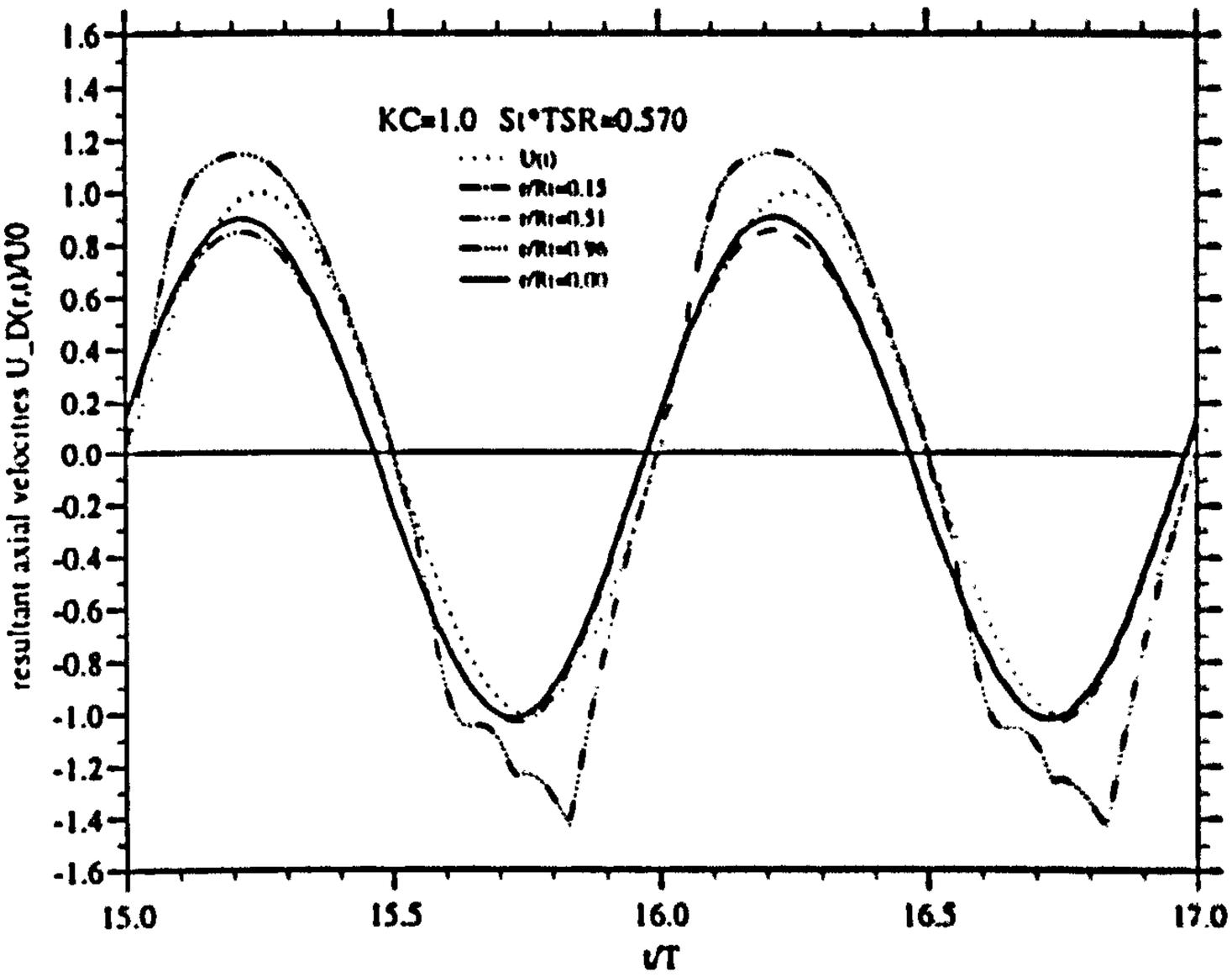

Figure 3.38: $U_D(t)/U_0$ vs. (t/T)

While there is little difference in the variation of $U_T(t)$ at $r/R_T = 0.00$ / 0.15 and 0.051, which is almost $\pi/2$ out of phase with the free stream $U(t)$, it is evident that the tip flow at $r/R_T = 0.96$ is significantly different from that further inboard. In fact, it is seen that the sign changes of $U_T(t)$ at $r/R_T = 0.96$ are almost perfectly in phase with $U(t)$. Considering the corresponding vortex ring motion it is clear that the flow at stations far outboard at this small KC is dominated by the proximity of the growing vortex ring cores which throughout the whole flow cycle always stay close to the tip. Most notable evidence of this are discrete peaks in $U_T(t)/U_0$ which occur at $r/R_T = 0.96$ when recently shed vortex rings move back through the rotor. More generally, it may be seen that $U_T(t)$ at all radial stations along the blade shown reflect the asymmetry of the vortex wake development on sequential half cycles at this stage in the computation.

These results find emphasis in figure (3.38) which shows the variation of the resultant velocity $U_D(t)$ at the same radial blade stations as considered above. The figure demonstrates clearly that over the inboard stations of the blade shown the net flow velocity $U_D(t)$ deviates only insignificantly from its value on the centerline of the rotor and has a phase shift relative to $U(t)$, which is due to the wake action. This result gives some confidence in the assumption made in the simpler actuator disc theory that $U_D(t)$ does not vary radially. Obviously this

is untrue for the tip regions and the implications for the rotor performance are discussed in the following.

For the inboard radial stations the wake asymmetry described above manifests itself as a 10% difference in peak values of $U_D(t)$ occurring on the two sequential halves of a flow cycle. Since the sign of $U_T(t)$ at the tip was shown to be in phase with $U(t)$ it is seen that $U_D(t)$ at $r/R_T = 0.96$ exceeds $U(t)$ at all times.

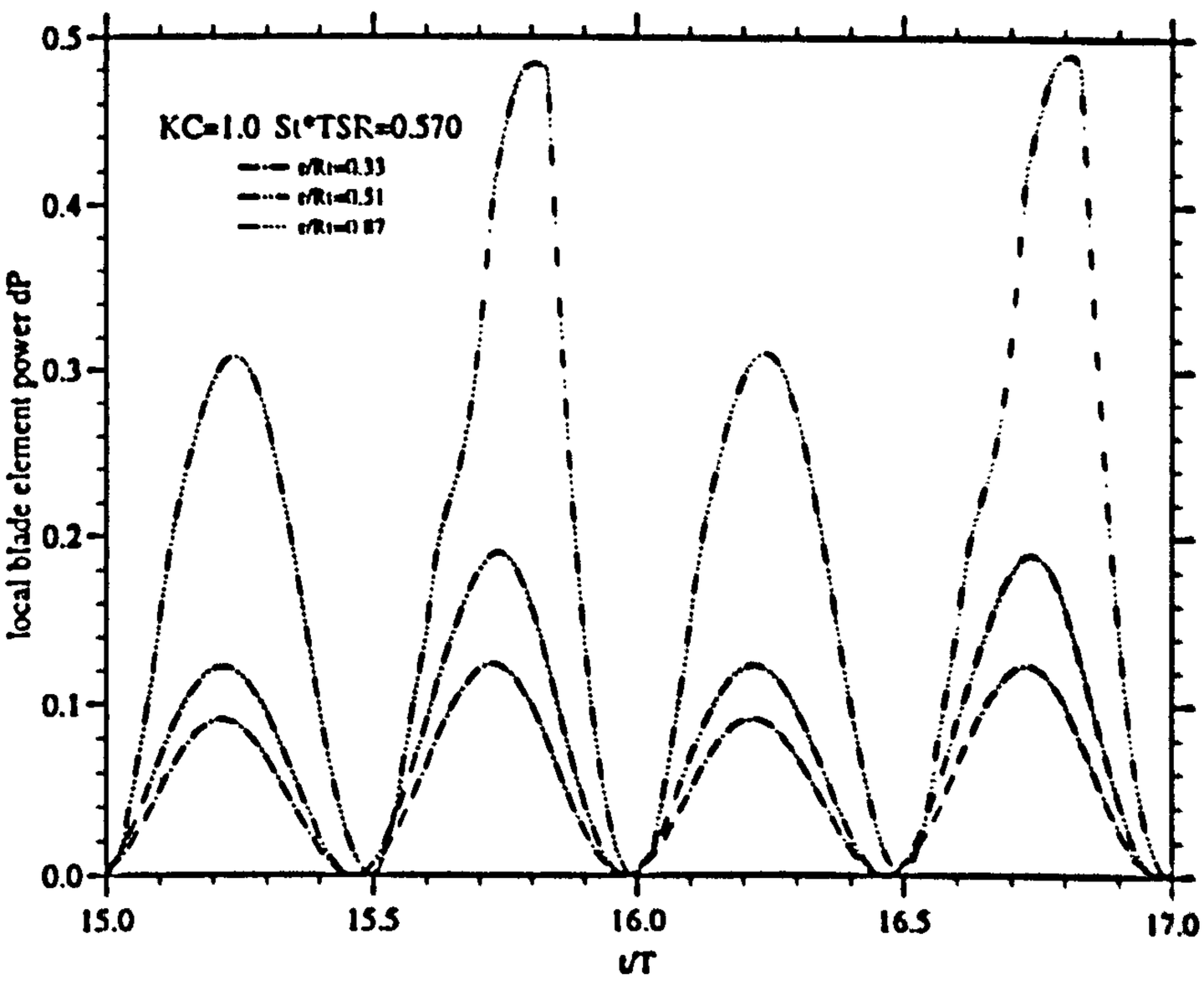

Figure 3.39: dP vs. (t/T)

Illustrated in figure (3.39) is the radial variation of the incremental blade element contributions at $r/R_T = 0.33/0.51/0.87$ to the instantaneous rotor power coefficient $C_P(t)$. As can be expected from the behaviour of $U_D(t)$ presented the data shows asymmetrical variation on sequential halves of a flow cycle and a phase shift between the more inboard stations and the blade tip. It is notable that the blade elements at the tip are predicted to have higher contributions to the overall rotor power than those nearer the blade mid span and root.

Figure (3.40) shows the resulting variation $C_P(t)$ defined in equation(3.49) and calculated as the sum of the incremental blade element contributions. It is of interest to note that the variation of $C_P(t)$ is thus on average in phase with $U(t)$. As a result of the asymmetrical variation of $U_D(t)$ the cyclic variation of $C_P(t)$ is clearly split into sequential 'high power' and 'low power' halves. It is interesting to note that the peak instantaneous power coefficients shown in this figure are extraordinarily high.

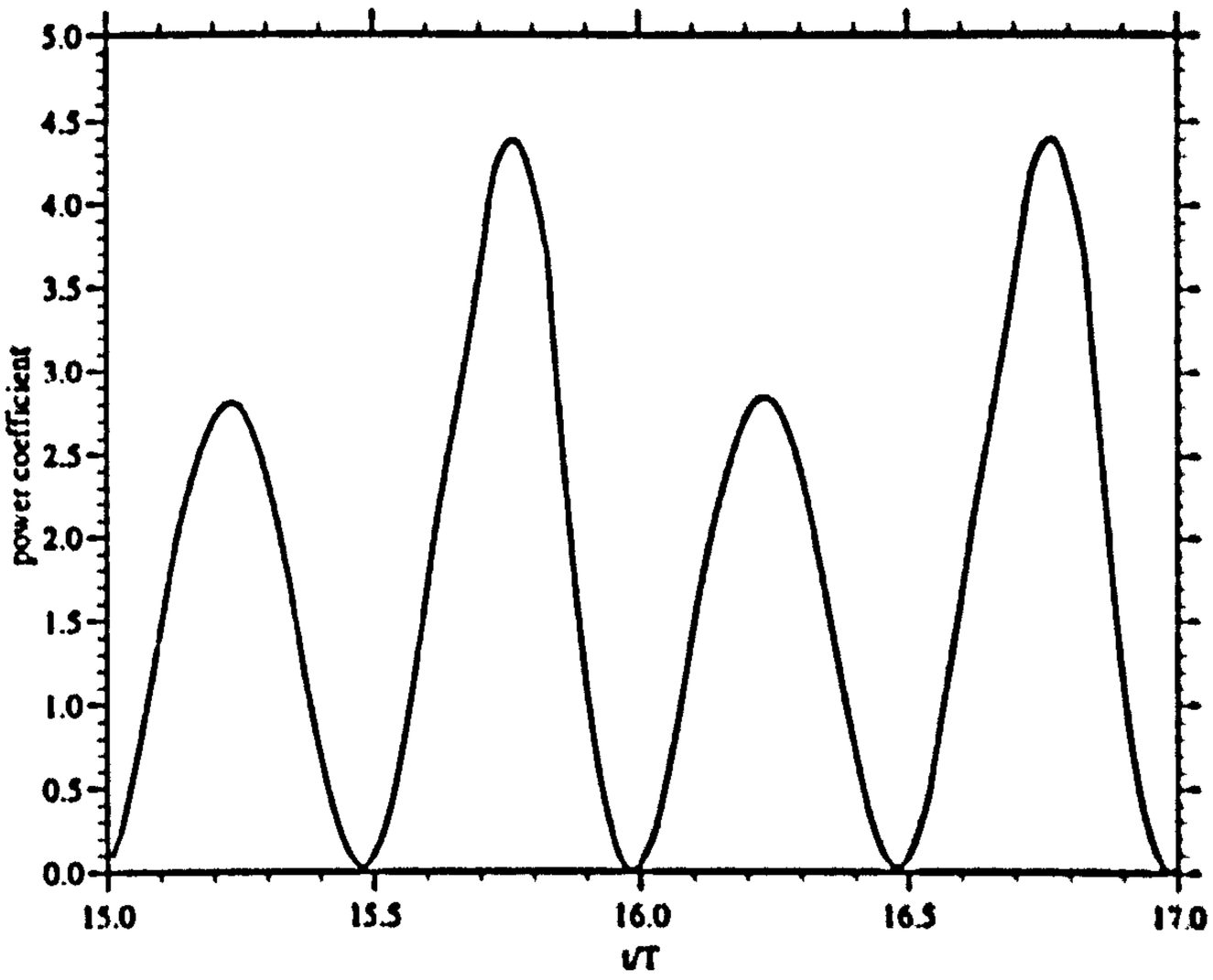

Figure 3.40: $C_P(t)$ vs. (t/T)

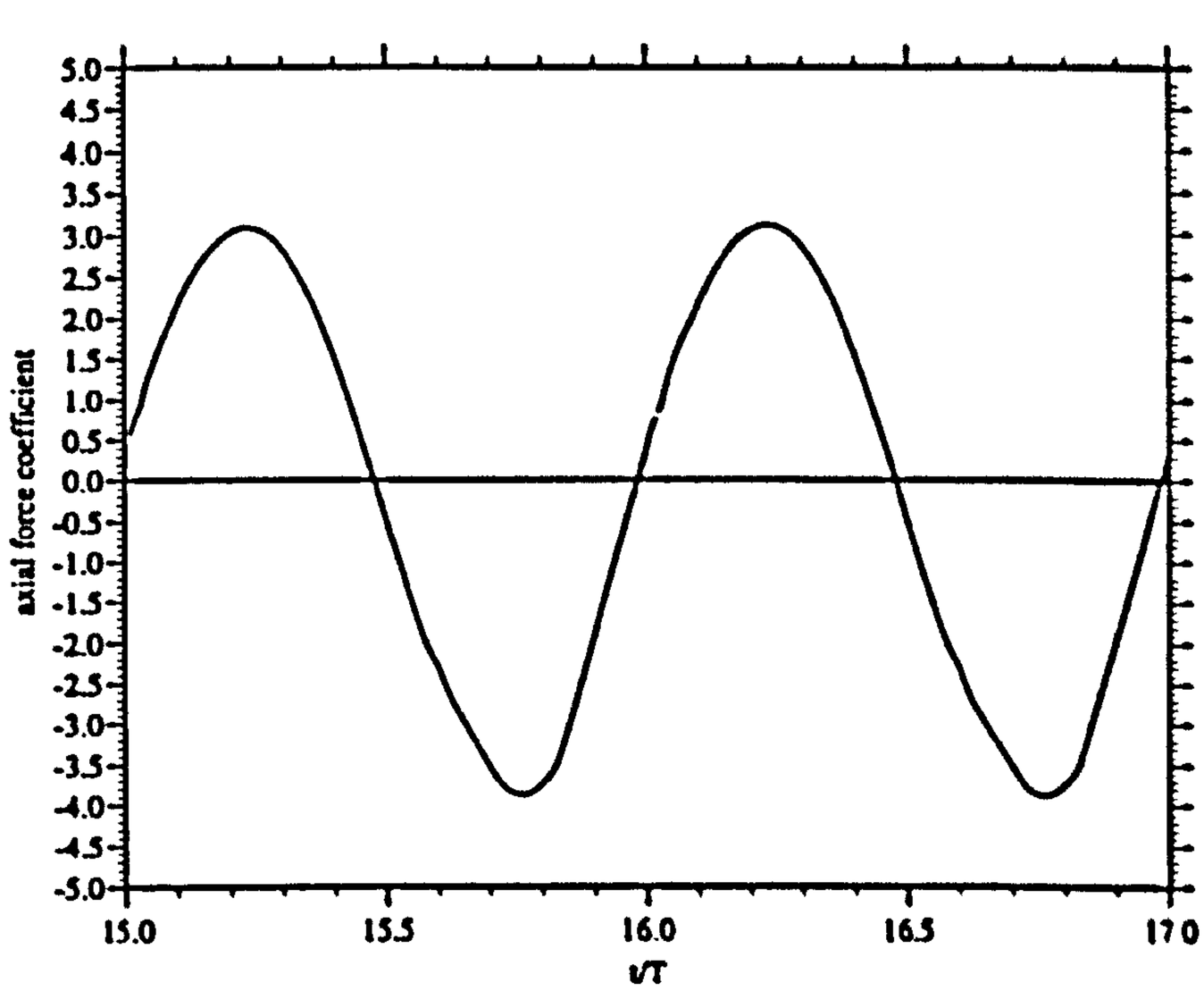

Figure 3.41: $C_X(t)$ vs. (t/T)

The variation of the rotor axial force coefficient $C_X(t)$, shown in figure (3.41), is obviously not sinusoidal and as a result of the flow asymmetry clearly has a non-zero cyclic mean value. This result would be expected from the motion of

the vortex rings described earlier and is compatible with the unidirectional bias of the stream wise convection of the paired vortex rings.

However, de Bernardinis (1981) showed through numerical simulation that sharp edged, flat plates can produce a unidirectional mean cyclic axial force in small and moderate amplitude sinusoidal oscillatory flows. Interestingly, the numerical technique employed by de Bernardinis was similar to the current numerical model in that it used concentrated point vortex elements which were shed from the sharp edge of the plates according to a formulation of the Brown and Michael model. Further, de Bernardinis observed a strong tendency for the vortex rings shed from the plates on sequential half cycles to pair up, in a manner not dissimilar to that noted above for the case of an unducted Wells turbine operating in small KC flow.

It is clear however, that the wake development that causes this mean axial force is strongly affected by the idealisation of the spiral vortex wake as a concentrated vortex ring. The interactions that occur in the numerical model between these idealised concentrated vortex rings may be expected to be more 'violent' than in the real physical flow where the wake vorticity may not be quite as discretely concentrated as in the computation. Nevertheless, for small amplitude oscillations the wake roll up is expected to be a defining feature of the wake flow and it is not entirely obvious, therefore, that this biased wake structure occurs only because of possible inadequacies in the idealisation of the physical flow used in the numerical model.

In the previous section it was shown that a more symmetrical flow structure can evolve after long enough a time in the numerical computations. As will be illustrated later these symmetrical flow structures don't numerically stabilise for a large number of cycles and are therefore only transient states in the computation. The variation of $U_D(t)/U_0$ which was calculated for blade elements positioned at $r/R_T = 0.15$ / 0.51 / 0.96 shown in figure (3.42) corresponds to the convective behaviour of the vortex rings after 72 flow cycles which has been earlier illustrated in figure (3.28) - (3.33). At this stage in the computation $U_D(t)$ is near perfectly sinusoidal for $r/R_T = 0.15$ / 0.51 with cyclic peak values of $U_D(t)$ at these positions deviating by less than 1%. Apparent at these stations is also a decrease of phase shift relative to $U(t)$ compared to the asymmetrical wake mode. This is due to reduced stream wise convection of the vortex rings. At $r/R_T = 0.96$ $U_D(t)$ is still strongly influenced by the closeness of the vortex ring cores but also shows a less biased oscillation with cyclic peak values remaining constant to a similar extent to those at stations further inboard.

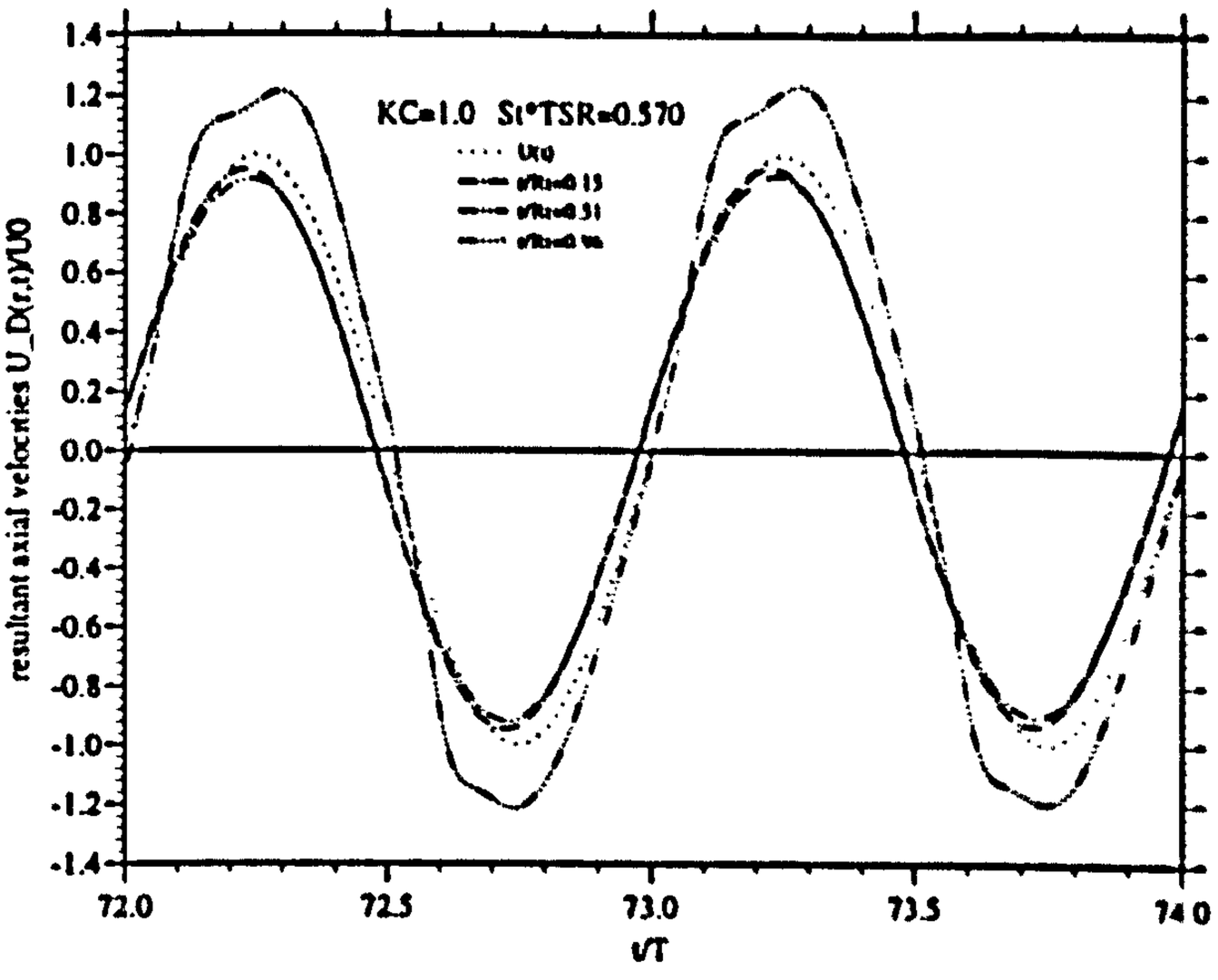

Figure 3.42: $U_D(t)/U_0$ vs. (t/T)

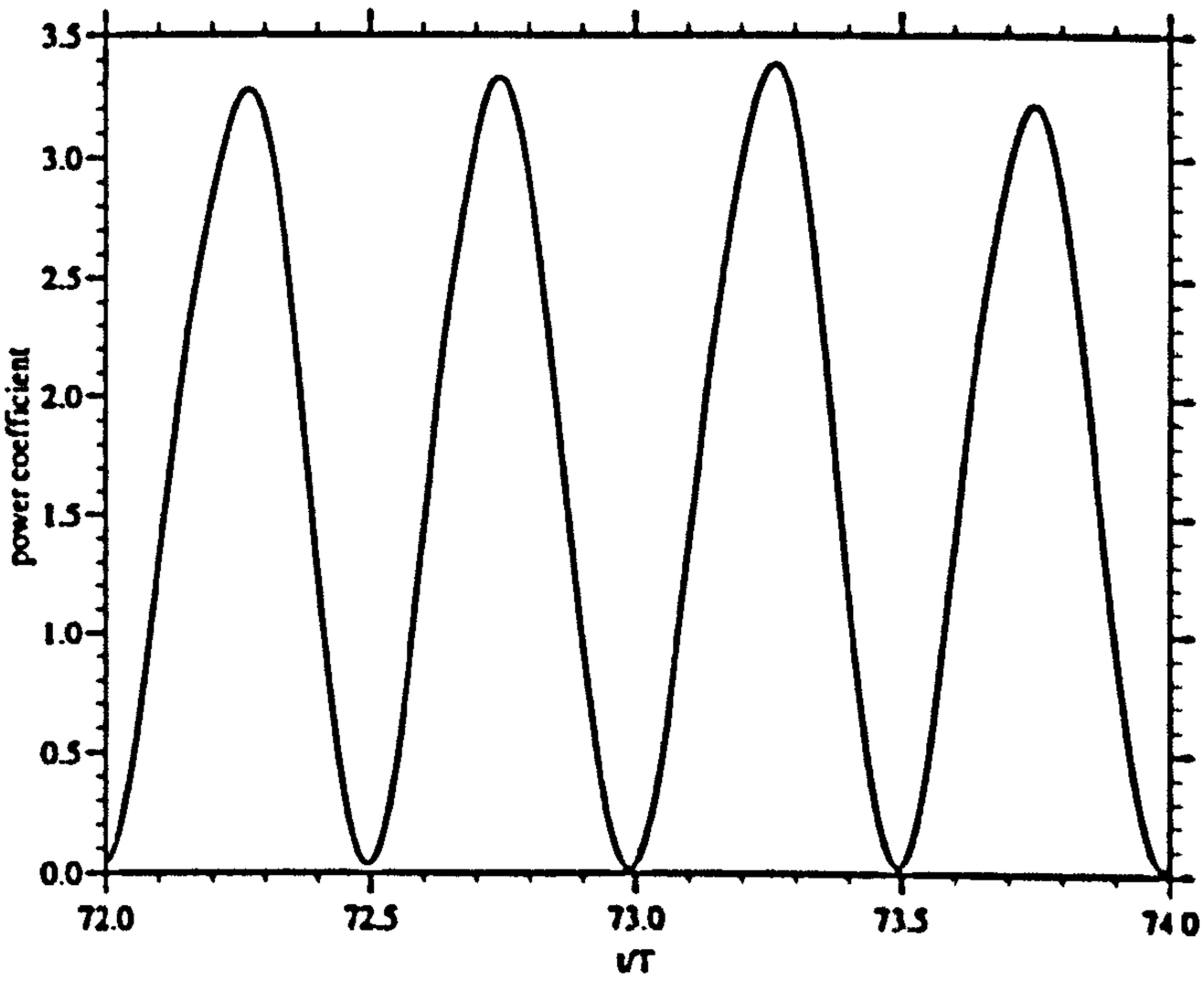

Figure 3.43: $C_P(t)$ vs. (t/T)

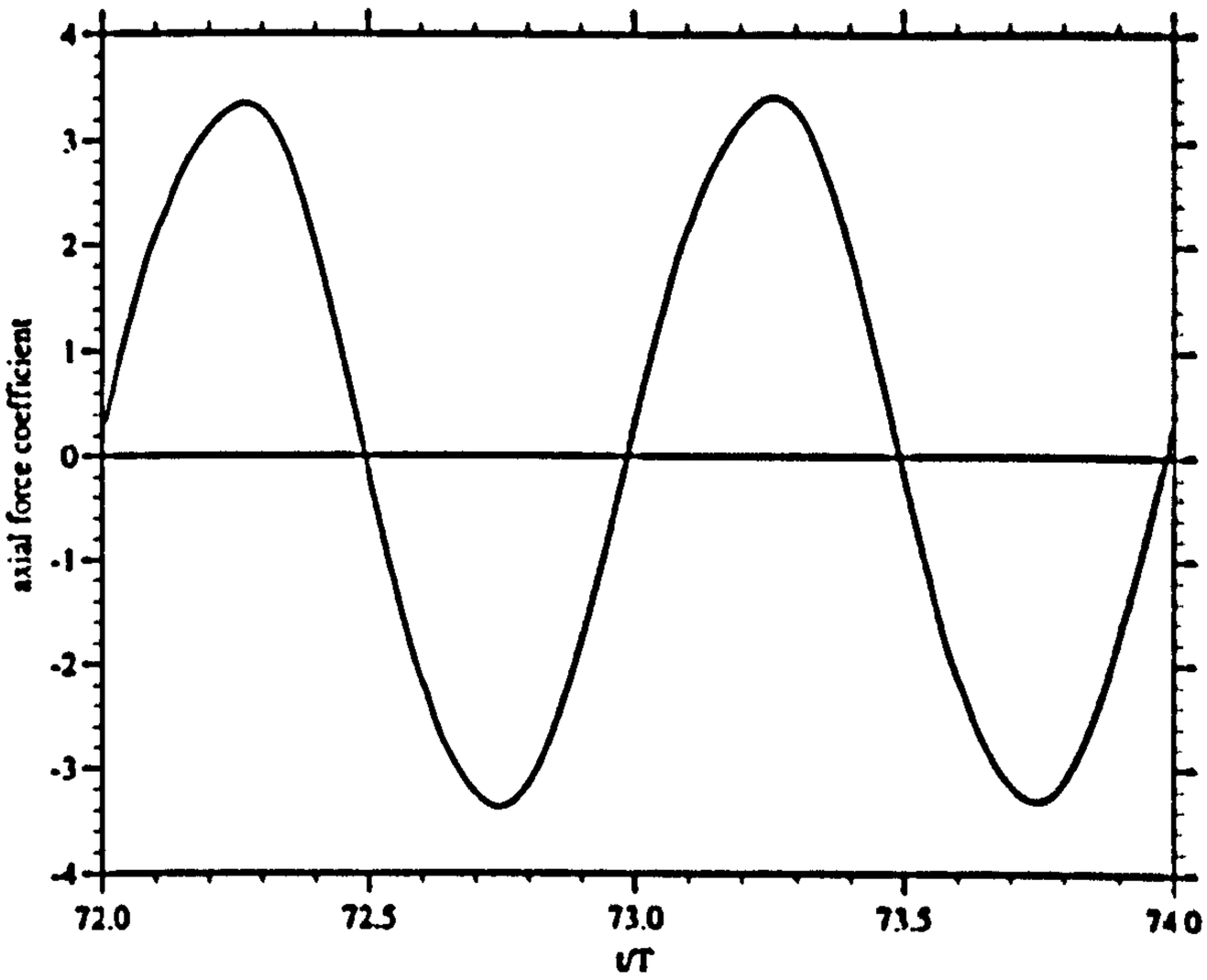

Figure 3.44: $C_X(t)$ vs. (t/T)

As a result of the more balanced behaviour of $U_D(t)$, the time history of $C_P(t)$ and $C_X(t)$ have less variable peak amplitudes over the two halves of the flow cycle as shown in figures (3.43) and (3.44) above. In this mode of vortex ring convection there is also virtually no cyclic mean axial force.

Comparison With The Actuator Disc Theory

Since it was a main objective of developing the more sophisticated numerical model to assess the validity of the assumptions made in the derivation of the actuator disc theory about the wake structure and flow through the rotor itself a direct comparison of the predictions made from the two theoretical models for the rotor performance is shown for small KC number flow.

Figure (3.45) shows the comparison of the cyclic variation of $U_D(t)$ on the rotor centreline after 72 completed flow cycles as calculated by the computational formulation of the basic actuator disc theory and the improved numerical model for KC=1 and $\sigma\Lambda$=0.570. At this stage in the computation the numerical model has established a vortex wake structure which sheds more symmetrically in time about the plane of rotation than in earlier flow cycles and is thus more suitable for direct comparison with the actuator disc theory.

It can be seen that while agreement in the magnitude of peak values is very good, the actuator disc theory evidently predicts a greater phase shift between

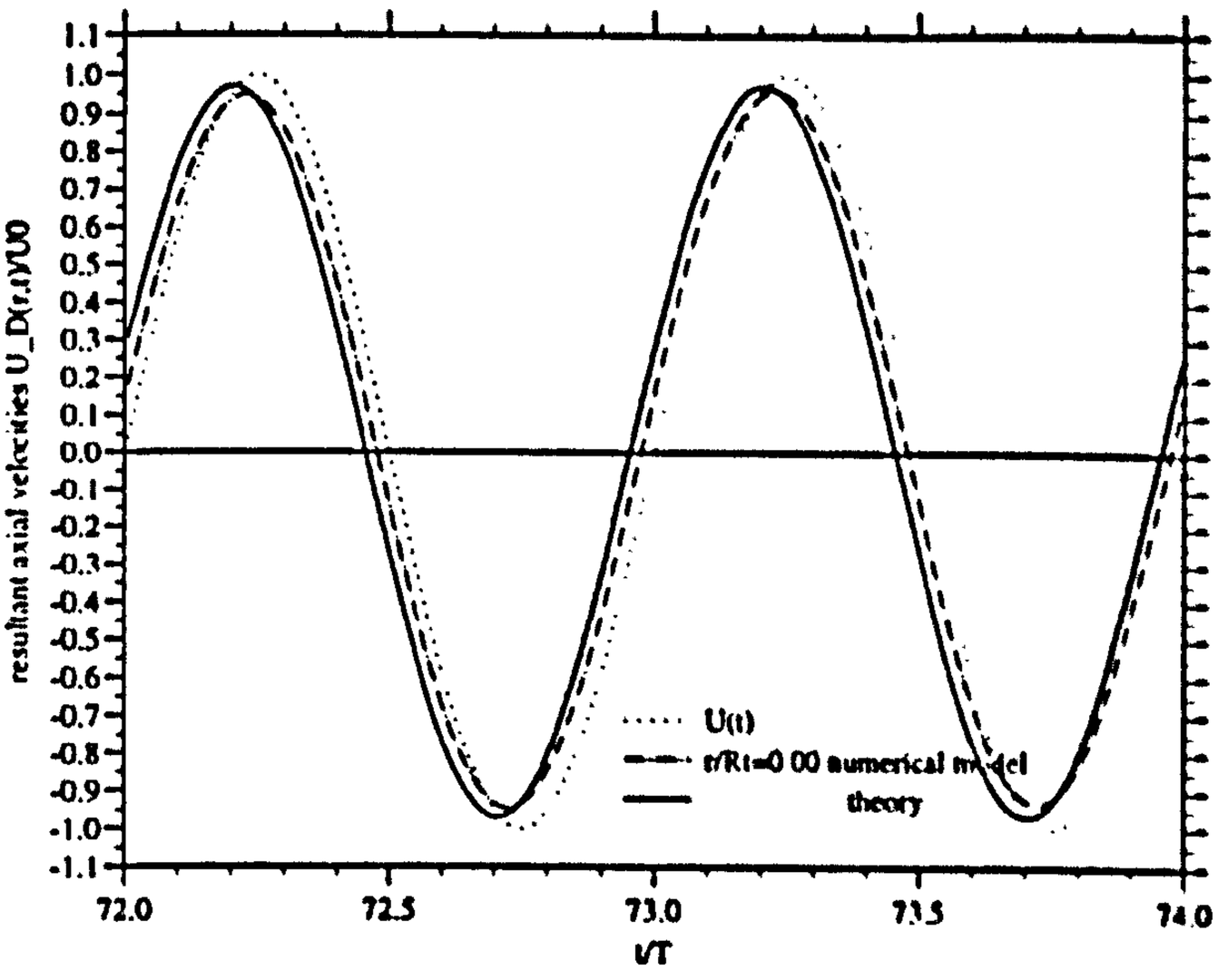

Figure 3.45: $U_D(t)$ vs. (t/T)

$U_D(t)$ and $U(t)$ than the numerical model. This is due to the fact that in the analysis of the actuator disc theory the vortex ring representing all the wake vorticity stays in the plane of the rotor while the improved numerical model allows the rings to move away from the rotor. Hence the difference in phase shift is an indication of the stream wise convection of the vortex ring occurring for the numerical model. Generally, the correlation of the $U_D(t)$ behaviour on the centre line of the rotor predicted by the two models for the computed test case may be considered quite good.

Figure (3.46) below shows the cyclic variation of the incremental blade element contribution, $dC_P(t)$ for radial stations r/R_T= 0.33 / 0.51 / 0.87 compared with the equivalent contributions from the actuator disc model. It appears that the main differences between the two models occur near the blade tip where , on the one hand in the improved numerical model the values of the induced velocity are reversed relative to those further inboard, while the actuator disc theory on the other hand does not allow for the radial variation of $U_D(t)$.

It can be seen from this presentation that agreement for predicted local peak values of $dC_P(t)$ is reasonable for blade elements at r/R_T=0.33 and 0.51 with deviation between predictions being around 4.5% and 9.0% respectively. Due to the higher velocities predicted to occur in the tip regions of the rotor blades by the numerical model, as previously shown in figure(uxres0b.ps)), the peak value

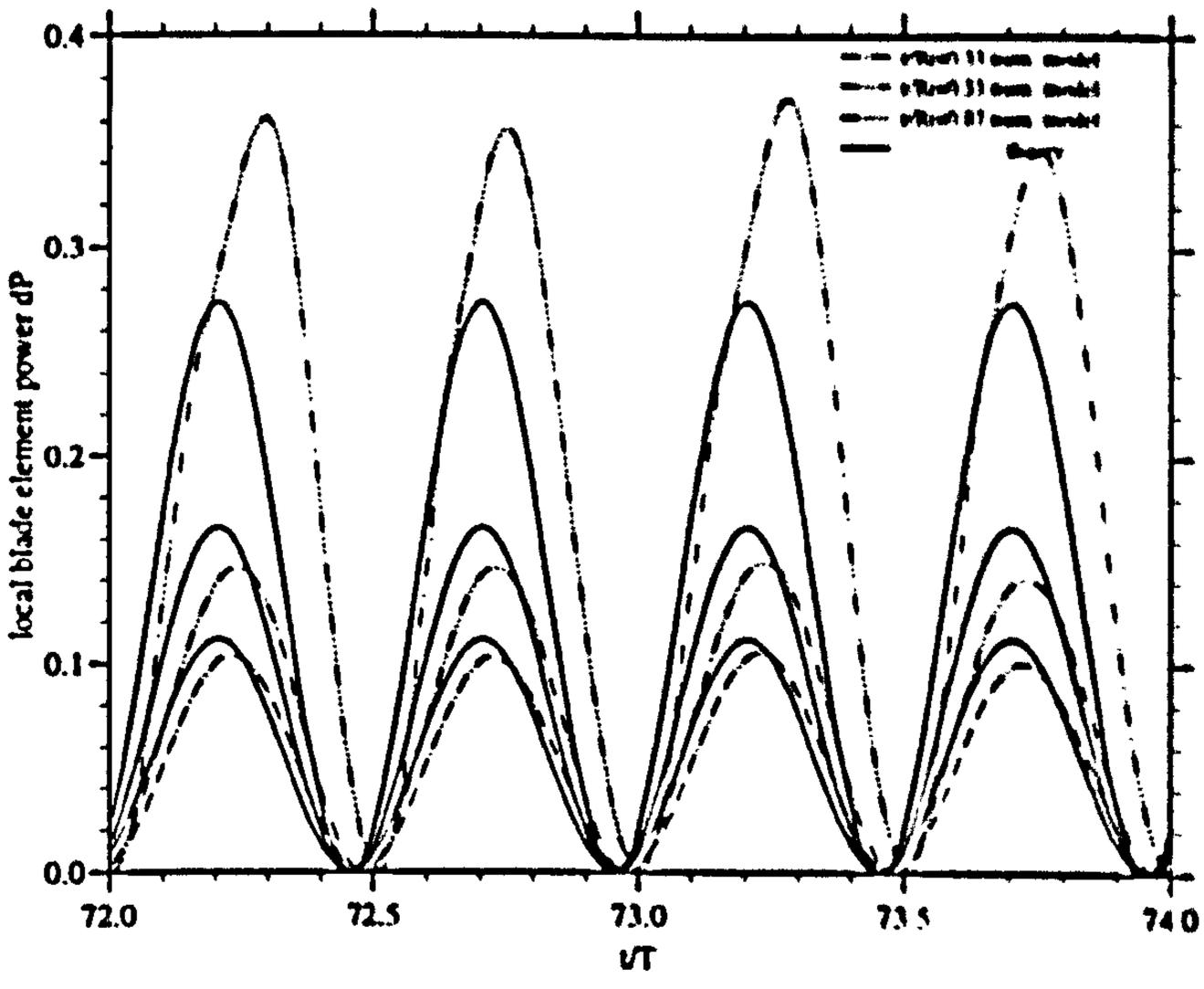

Figure 3.46: $dP(t)$ vs. (t/T)

of $dC_P(t)$ at r/R_T=0.87 is approximately 20% higher than that computed using the simpler momentum theory. Also the apparent span wise phase shift in $dC_P(t)$ shown by the numerical model data is not present in the actuator disc theory.

Figure (3.47) traces the resultant variation of the instantaneous rotor power coefficient $C_P(t)$ as predicted by the two models. The agreement of the cyclic peak values shown is remarkably good and suggests that the effect of relative lower and higher predicted values of $dC_P(t)$ in the root and tip regions respectively made by the improved numerical model approximately balance each other. The curves show that due to the tip contributions the phase shift in $C_P(t)$ between the two predictions has increased from that shown in figure (3.45) for $U_D(t)$ on the centre line of the rotor. In fact, $C_P(t)$ as computed by the improved numerical model varies almost exactly in phase with the free stream $U^{\cdot}(t)$.

Figure(3.48) shows that the comparison of axial force coefficient $C_X(t)$ is equally as good between the two models when in the improved numerical model a more symmetrical wake structure has evolved.

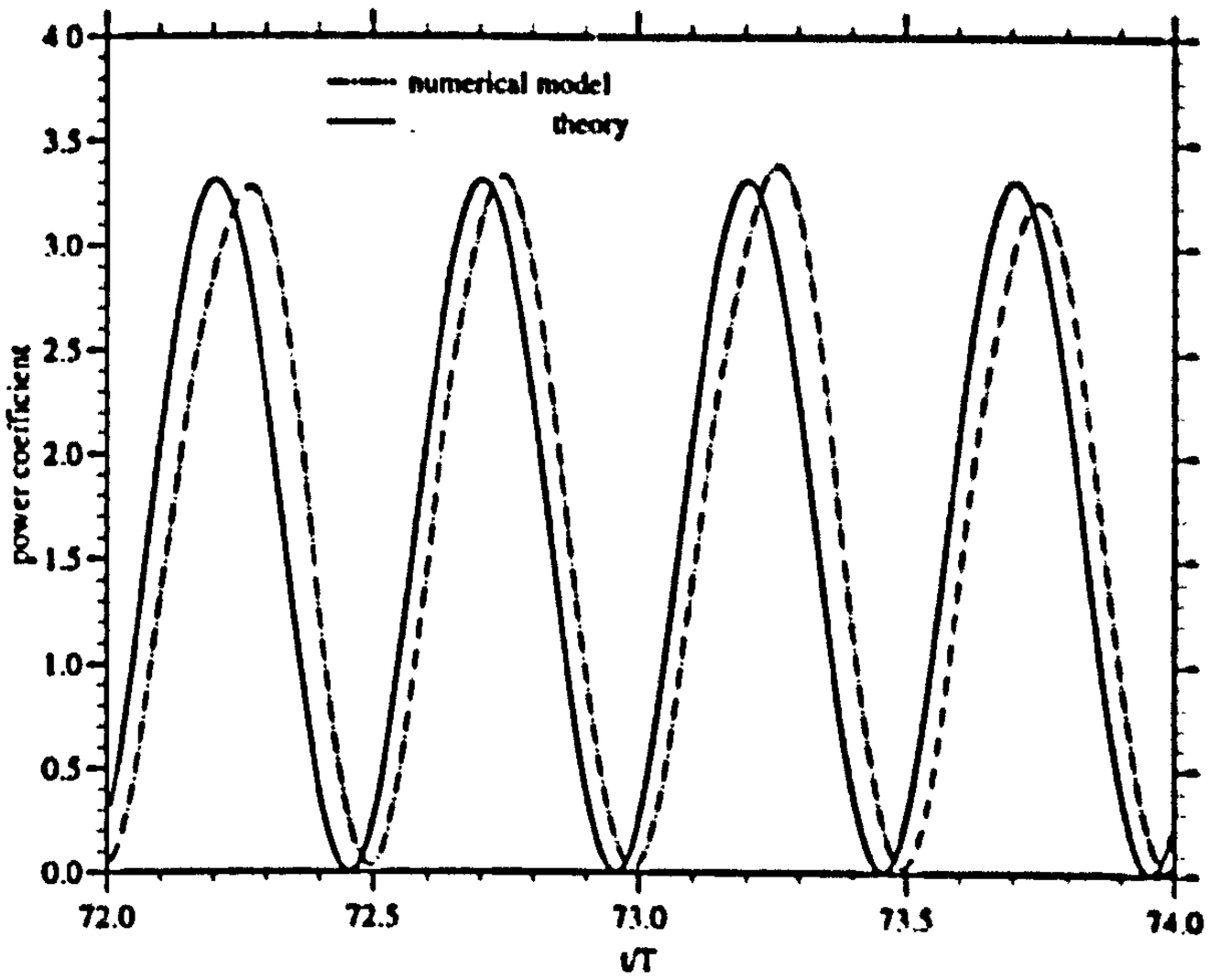

Figure 3.47: $C_P(t)$ vs. (t/T)

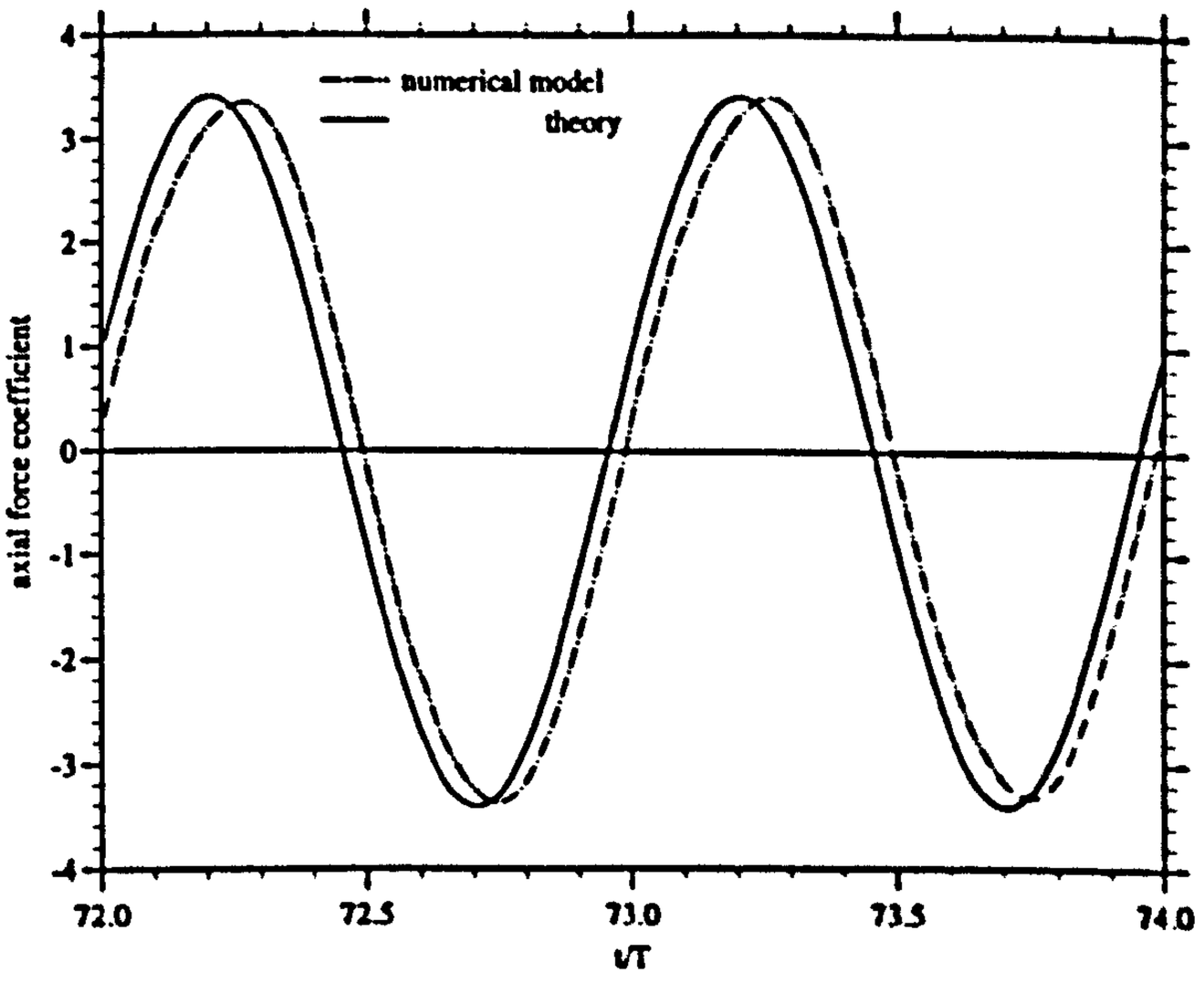

Figure 3.48: $C_X(t)$ vs. (t/T)

Presented in figures (3.49) and (3.50) below are the instantaneous variation of $C_P(t)$ and $C_X(t)$ as well as cyclic mean values as calculated by the numerical model for KC=1.0 and $\sigma\Lambda$=0.570 over 80 flow cycles. Also included for comparison are mean values predicted from the actuator disc theory. Clearly, for the numerical model the asymmetric mode (- a higher power half cycle followed by a lower power half cycle -) seems to persist over the initial 50-60 flow cycles producing a non zero value of $\overline{C_X}$, which, however, is small compared to the peak values of C_X achieved. Over this computational period $\overline{C_P}$ seems constant and deviates from the mean cyclic power coefficient predicted by the momentum theory by approximately 5%. However, after approximately 65 completed cycles the more symmetrical flow structure establishes itself intermittently and shows better comparison between the two calculations of $\overline{C_P}$ and has a zero cyclic mean axial force coefficient.

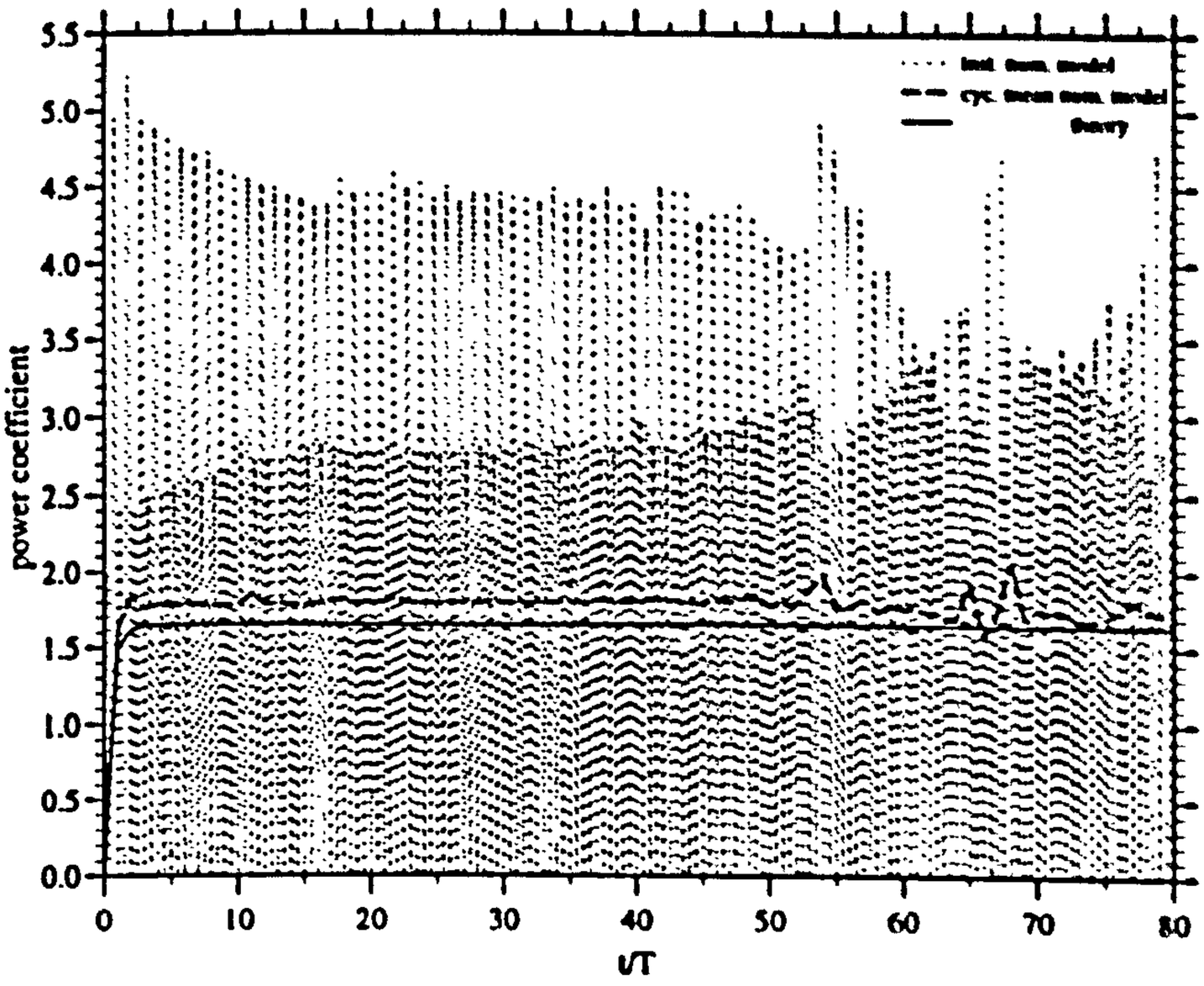

Figure 3.49: $C_P(t)$ & $\bar{C}_P$ vs. (t/T)

It was found that if the computation is continued for an even larger number of flow cycles neither of the two wake modes prevail consistently. Calculations carried out at lower values of $\sigma\Lambda$ for which the wake vortex rings are weaker than the above case of 0.570 at $KC = 1.0$ showed that the symmetrical mode evolves more frequently while at higher values of $\sigma\Lambda$ the symmetrical mode occurs less frequently and eventually does not occur at all. The implications of this are summarised in figures (3.51) and (3.52) which respectively show the variation of $\overline{C_P}$

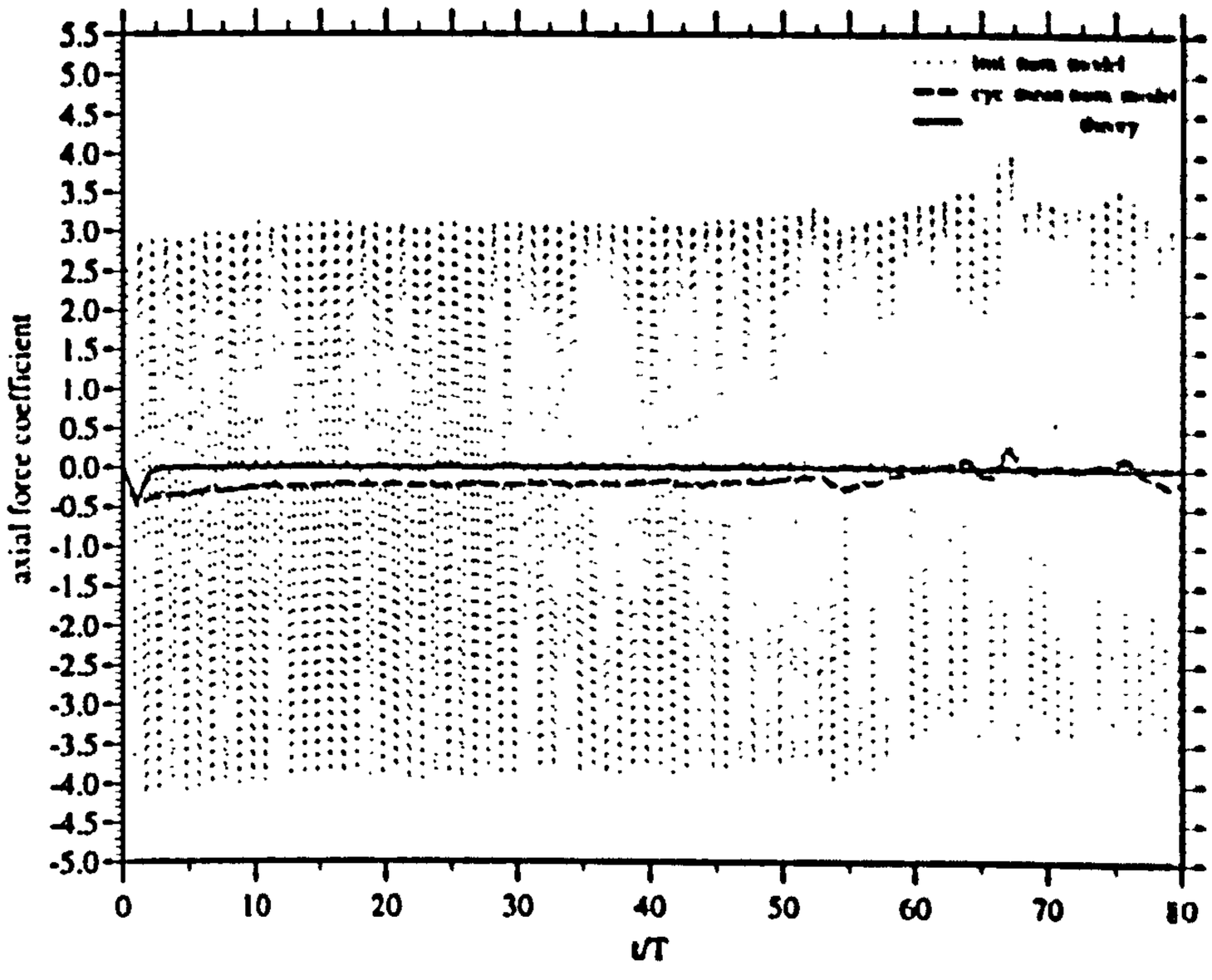

Figure 3.50: $C_X(t)$ & $\bar{C}_X$ vs. (t/T)

and $\overline{C_X}$ with $\sigma\Lambda$ averaged over the 20 first flow cycle of computations using both theoretical models. It is clear from the figure(3.50) that the imbalance of shed vorticity of the two sequential half flow cycles increases with $\sigma\Lambda$. Further it may be concluded from the comparative study of $\overline{C_P}$ presented in figure (3.51) that disagreement between the two models increases as the extent of wake asymmetry does.

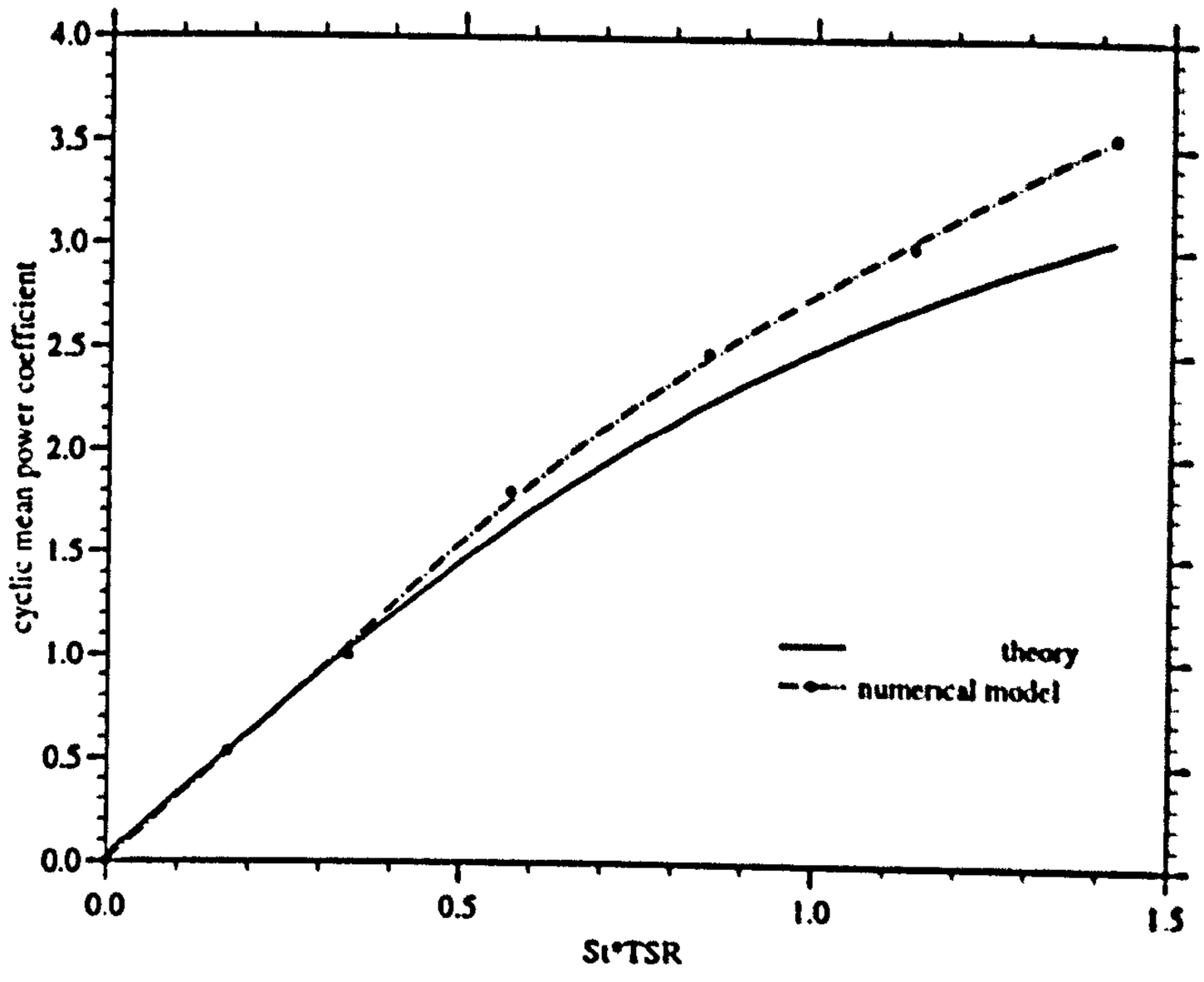

Figure 3.51: $\bar{C}_P$ vs. $\sigma\Lambda$

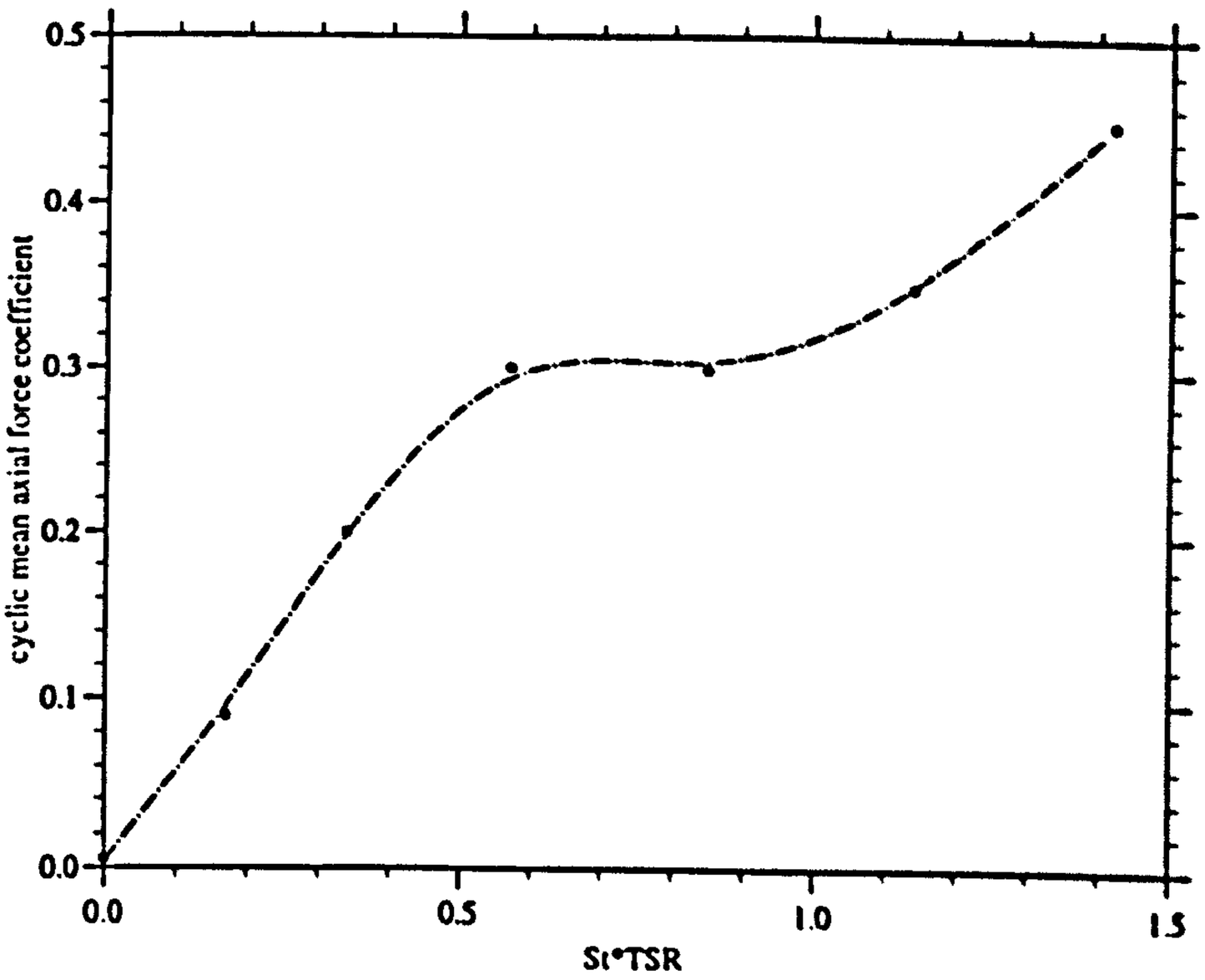

Figure 3.52: $\bar{C}_X$ vs. $\sigma\Lambda$

3.3.3 The Improved Numerical Model - Moderate KC Flow

In the previous section the improved numerical model was used to investigate the applicability of the actuator disc theory for oscillatory flow of small KC number. This report section aims to provide a similar study for moderate KC flows in which the importance of the stream wise motion of the vortex rings forming the wake is more significant.

Vortex Ring Formation And Convection

Figures (3.53) - (3.58) below show results of computations carried out for a KC of 3.0 and $\sigma\Lambda$=0.170. The vortex ring motion is presented as previously in a schematised form after 11 computational cycles have been completed. The depicted radii of the vortex rings are proportional to their non-dimensional strength $\Gamma/(U_0 R_T)$.

Qualitatively the main features of the vortex ring formation and convection show a strong similarity to those presented in earlier for a KC=1.0. As was seen in the latter case the convection is driven by initially strong radial expansion experienced by two vortex rings formed on sequential half flow cycles as they approach each other. Most notable is again the tendency for the two rings formed during a full cycle to move away from the rotor as a pair. As noted earlier for the small KC case, the stream wise convection is strongly biased due to the apparent strength imbalance of the paired vortex rings. While for the smaller KC case, however, the vortex rings stayed close to the rotor during its formation in the present case of $KC = 3.0$ the stream wise convection is significant and of the order of the rotor radius R_T. It was found that the extent of flow asymmetry depicted varied for later flow cycles but unlike in the small KC case, presented the more symmetrical mode in which the vortex rings do not pair up never occurred.

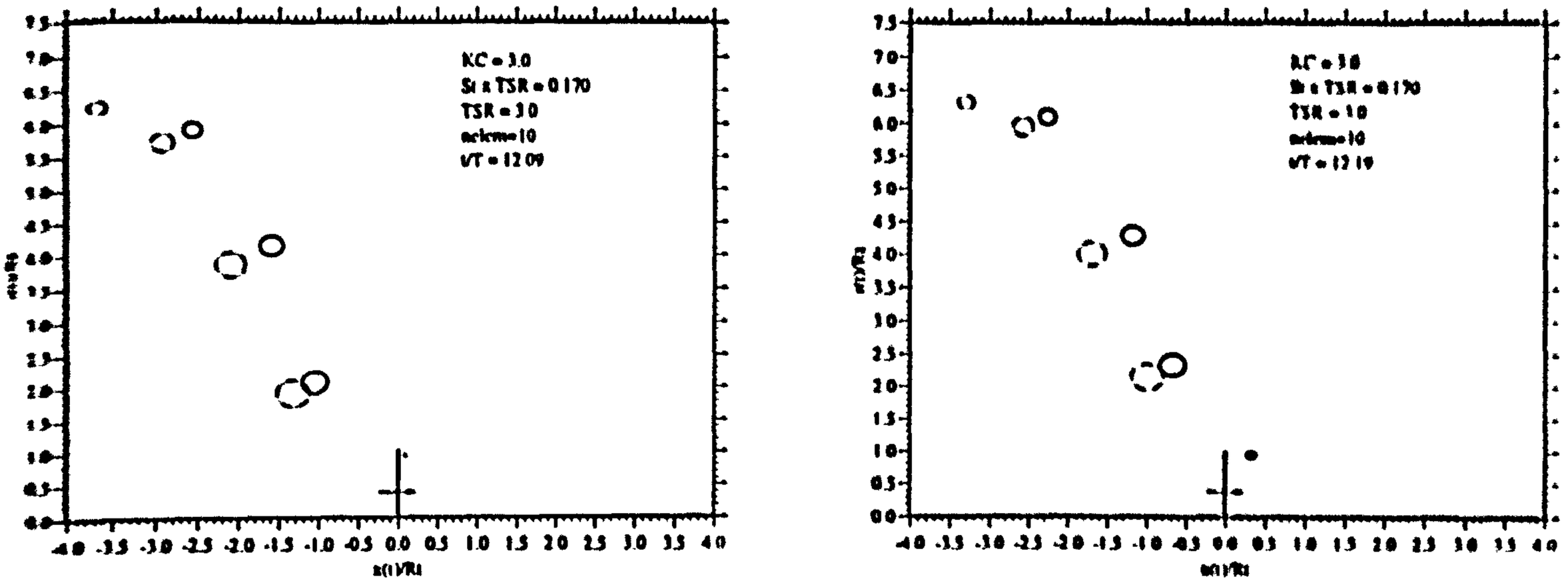

Figure 3.53: Vortex Ring Motion $KC = 3.0$; $\sigma\Lambda = 0.170$

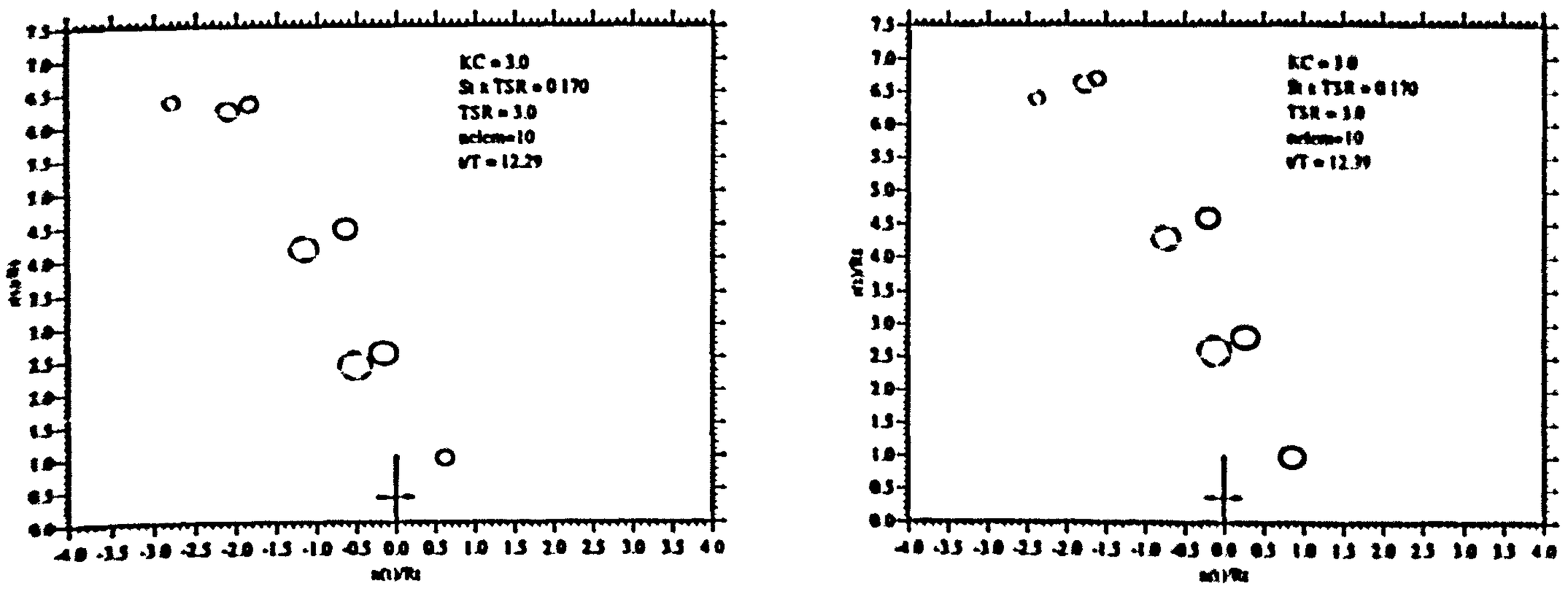

Figure 3.54: Vortex Ring Motion $KC = 3.0$; $\sigma\Lambda = 0.170$

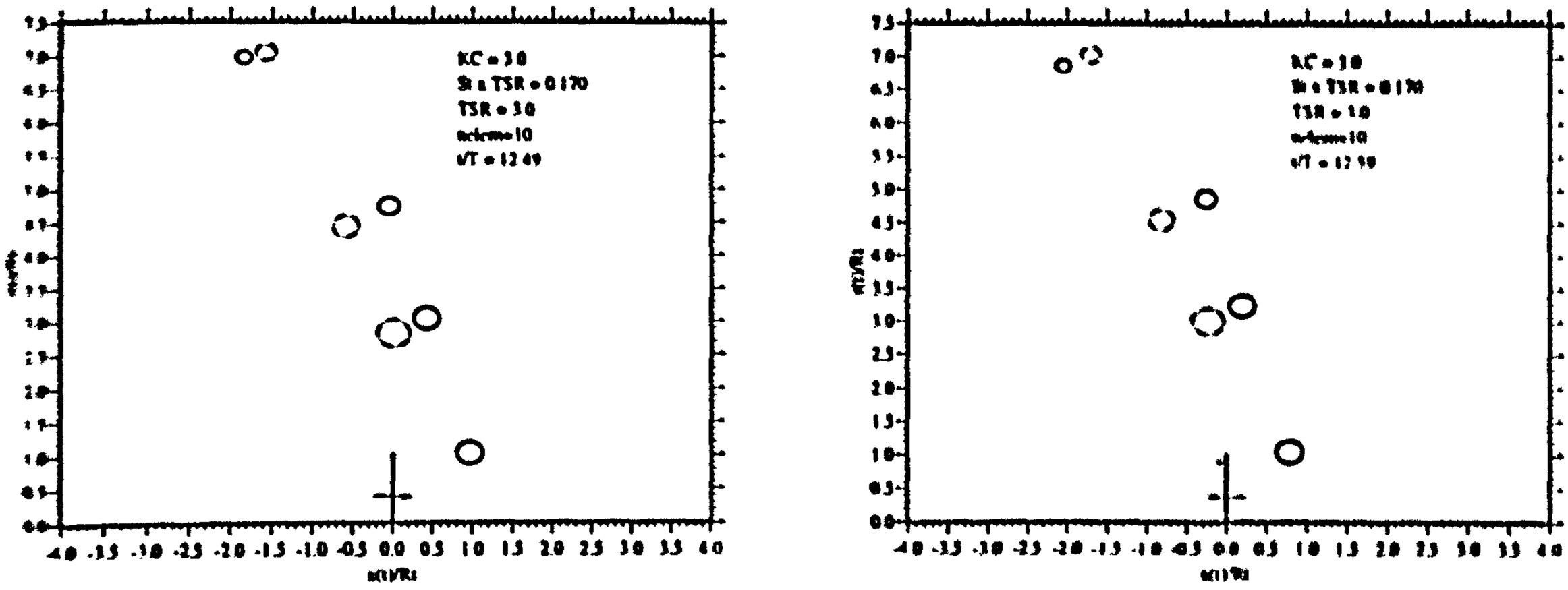

Figure 3.55: Vortex Ring Motion $KC = 3.0$; $\sigma\Lambda = 0.170$

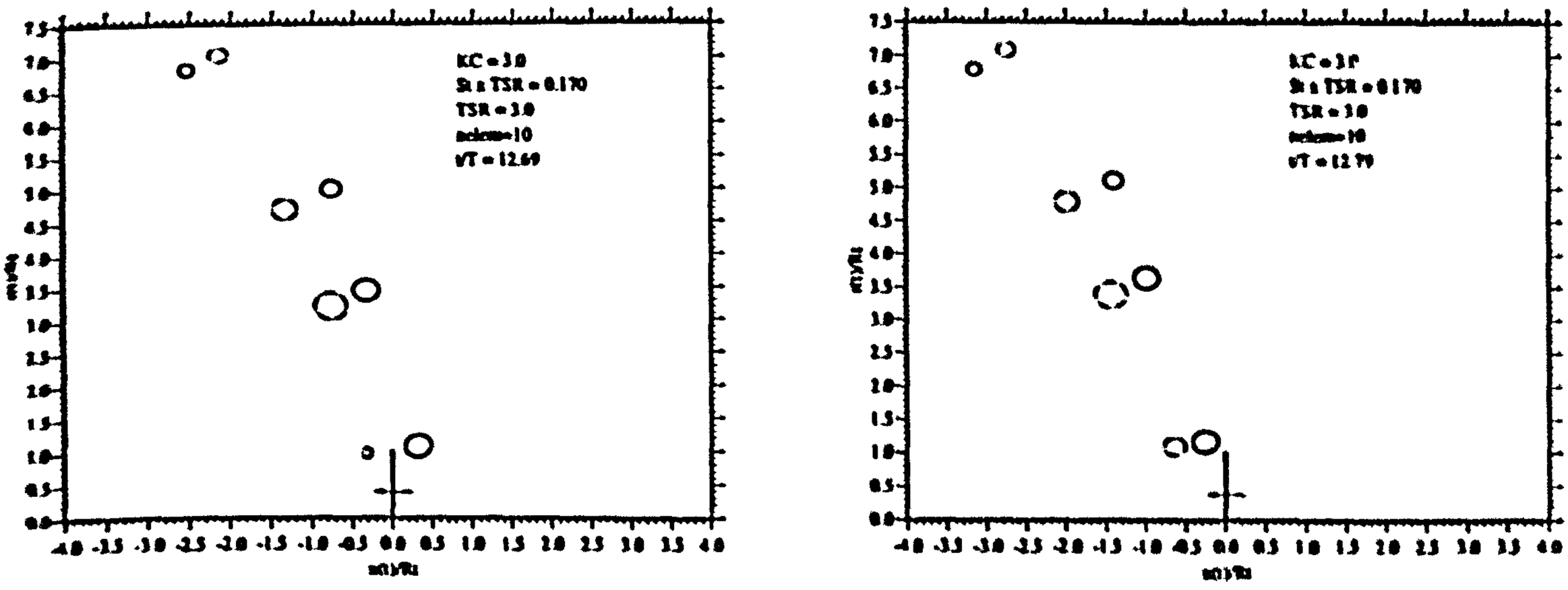

Figure 3.56: Vortex Ring Motion $KC = 3.0$; $\sigma\Lambda = 0.170$

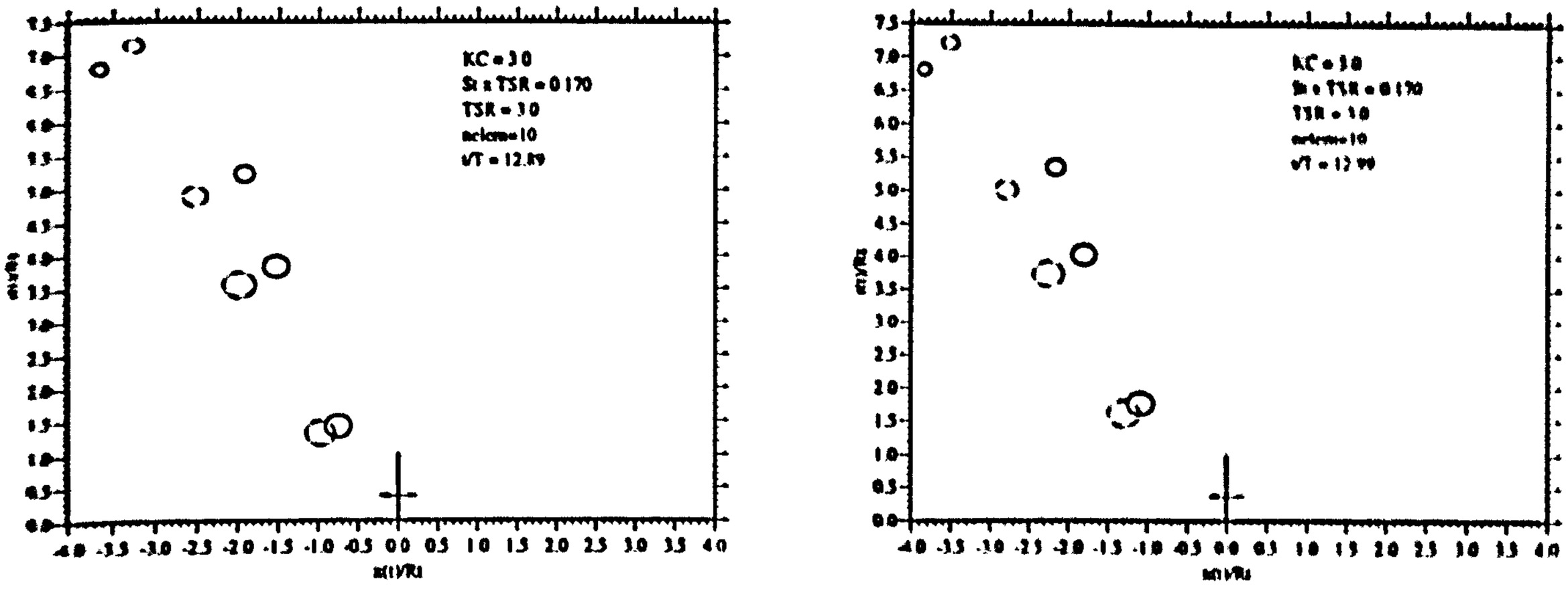

Figure 3.57: Vortex Ring Motion $KC = 3.0$; $\sigma\Lambda = 0.170$

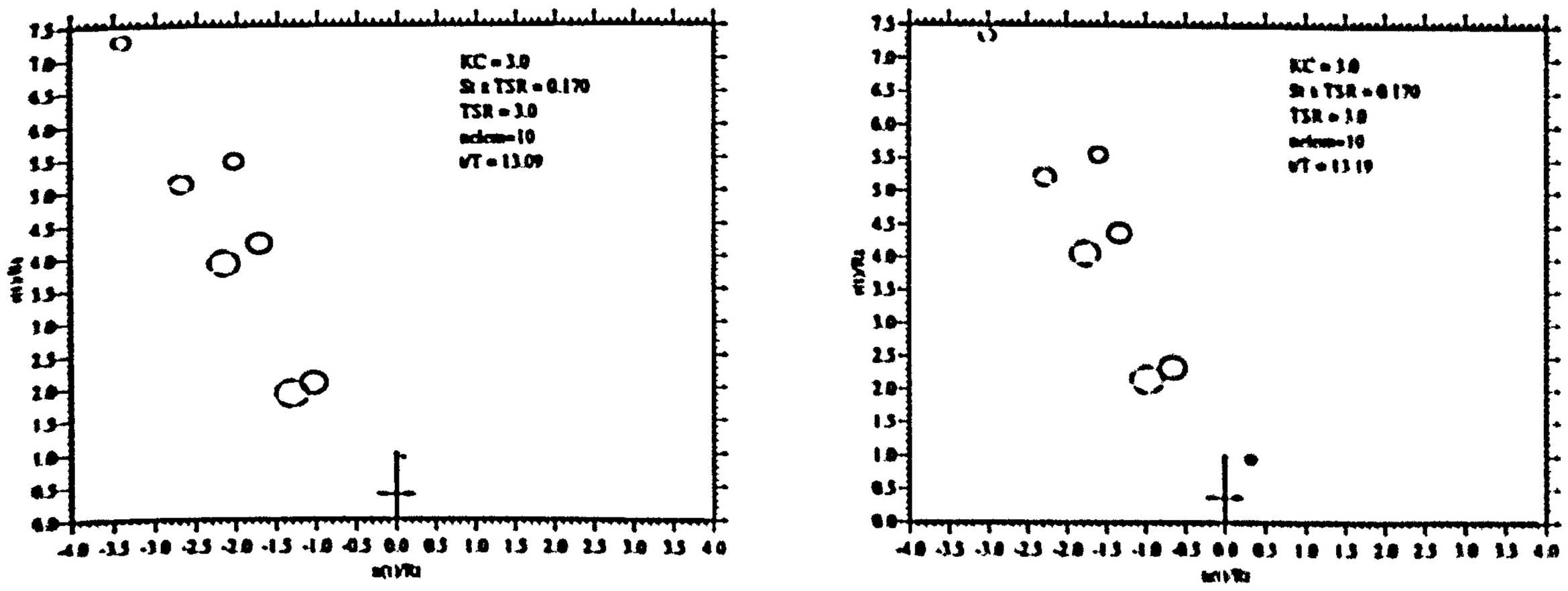

Figure 3.58: Vortex Ring Motion $KC = 3.0$; $\sigma\Lambda = 0.170$

Flow Through The Rotor And Turbine Performance

In the following the effects of the apparent higher (- compared to the small KC case -) vortex ring convection for the test case of KC=3.0 and $\sigma\Lambda$=0.170 on the flow through the plane of rotation and the rotor power are studied using the improved numerical model and contrasted to predictions made from the simpler actuator disc theory.

Figure (3.59) shows the computed variation of $U_D(t)$ which in the illustration is normalised by the peak free stream flow velocity U_0 at span wise positions along the rotor blades given by r/R_T = 0.00 / 0.33 / 0.51 / 0.87, where as previously r/R_T = 0.00 corresponds to the rotational axis of the rotor. The most striking difference compared to the small KC case presented earlier is that there is significant radial variation of $U_D(t)$ even over the inboard blade regions as well as the fact that the flow through the rotor is almost exactly in phase with $U(t)$ across the entire blade span. It is interesting to observe that on the reverse half of the flow cycle the peak values of $\hat{U}_D$ occurring as the vortex ring moves through the plane of rotation are highest around midspan, where the net induced velocities are evidently of the same sign as $U(t)$.

Figure (3.60) presenting the variation of $U_D(t)$ on the centreline of the rotor shows that for the computed case the actuator disc theory would predict a phase shift of approximately 0.09 π relative to the sinusoidal free stream velocity $U(t)$ whereas the numerical model which allows the vortex rings to move predicts virtually no phase difference. As may be expected from the variation of $U_D(t)$ the related plot of instantaneous power coefficient $C_P(t)$ presented in figure (3.61) shows the sensitivity to the asymmetric wake geometry. As a result, it is evident in the plot that peak values of $C_P(t)$ occurring on the reverse half cycles exceed those predicted by the actuator disc theory by approximately 28% and the computed mean cyclic power coefficients $\overline{C_P}$ for the two models differ by 9%.

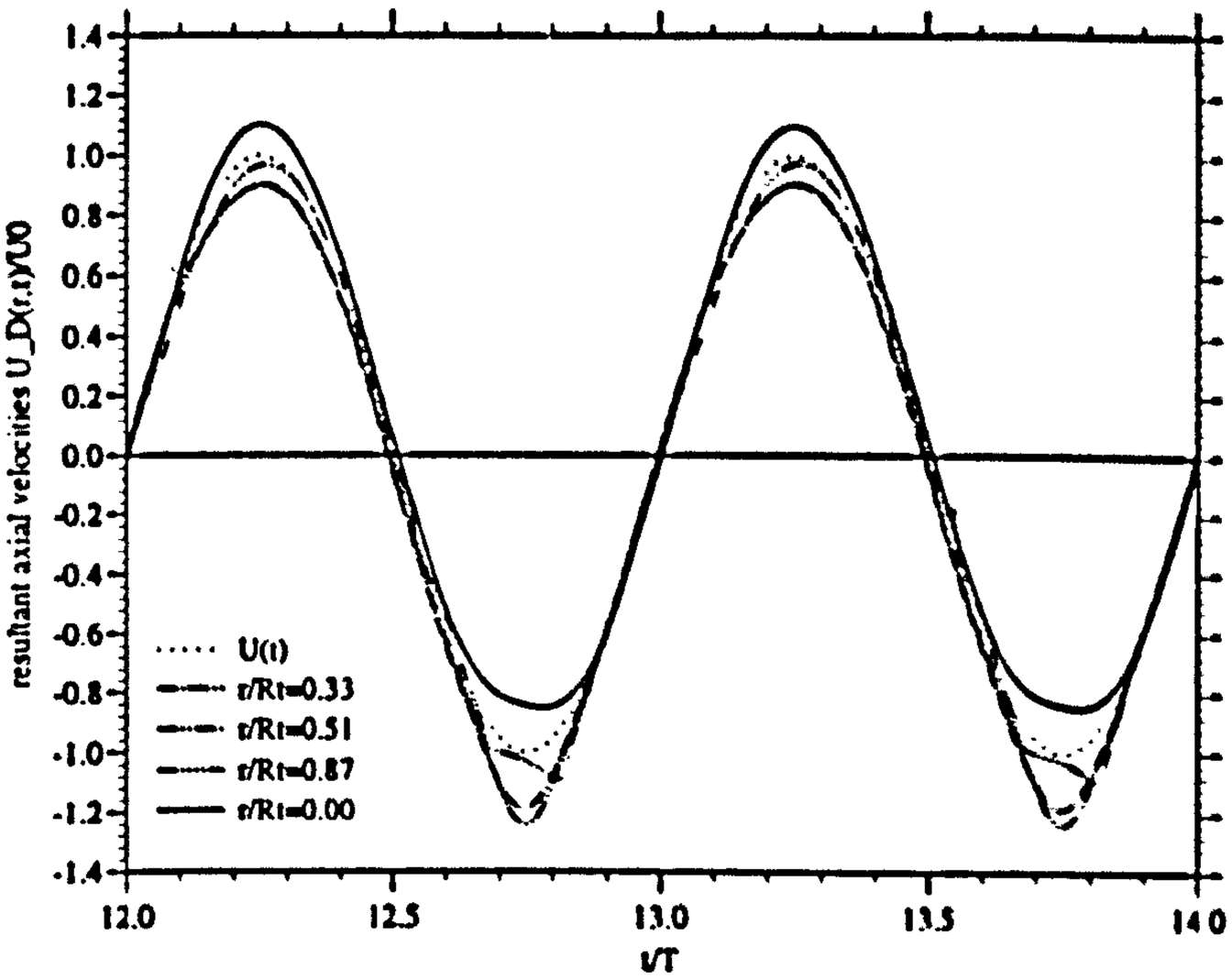

Figure 3.59: $U_D(t)$ vs. t/T

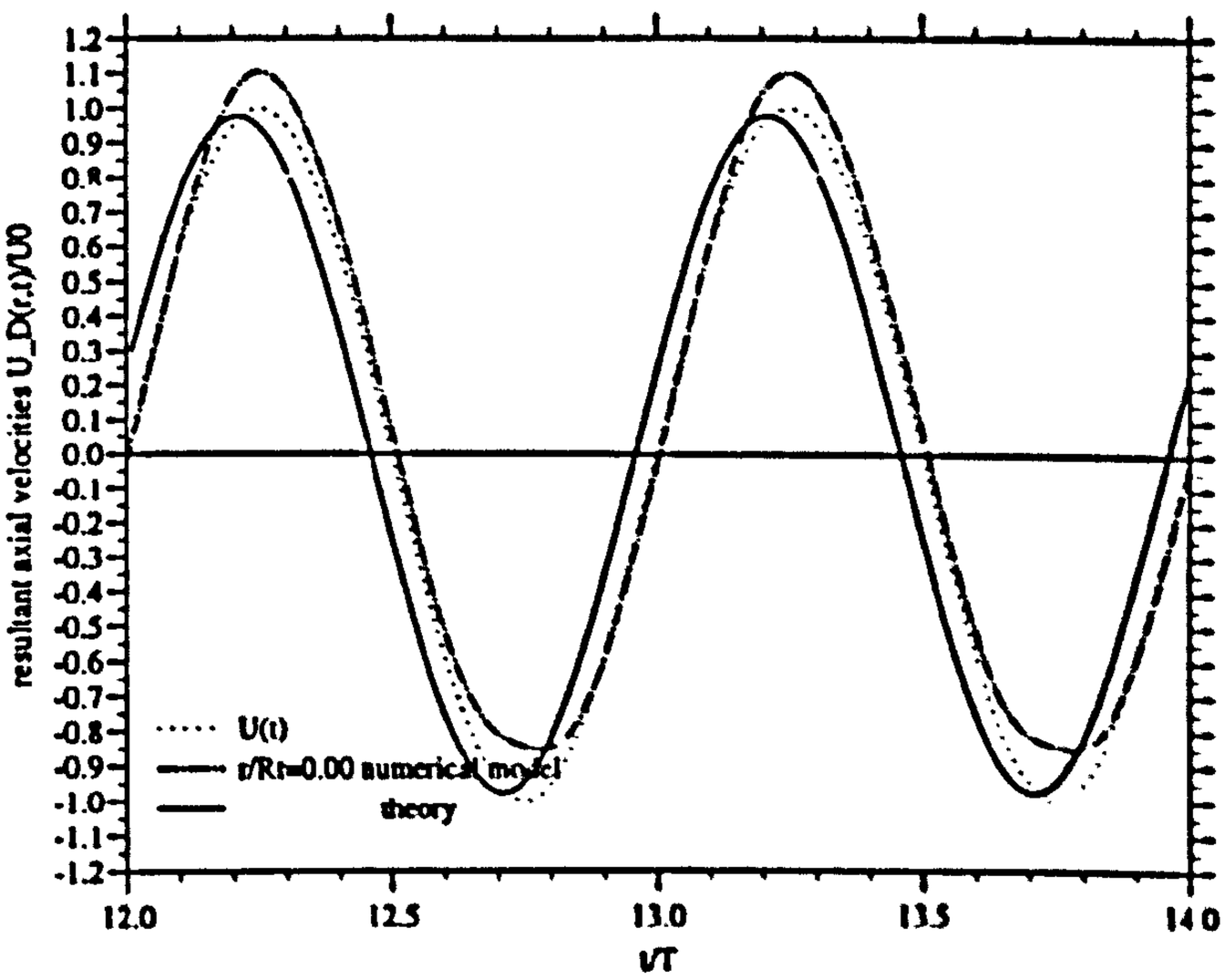

Figure 3.60: $U_D(t)|_{centreline}$ vs. t/T

Figure (3.60) presenting the variation of $U_D(t)$ on the centreline of the rotor shows that for the computed case the actuator disc theory would predict a phase shift of approximately 0.09 π relative to the sinusoidal free stream velocity $U(t)$ whereas the numerical model which allows the vortex rings to move predicts virtually no phase difference. As may be expected from the variation of $U_D(t)$ the related plot of instantaneous power coefficient $C_P(t)$ presented in figure (3.61) shows the sensitivity to the asymmetric wake geometry. As a result, it is evident in the plot that peak values of $C_P(t)$ occurring on the reverse half cycles exceed those predicted by the actuator disc theory by approximately 28% and the computed mean cyclic power coefficients $\overline{C_P}$ for the two models differ by 9%.

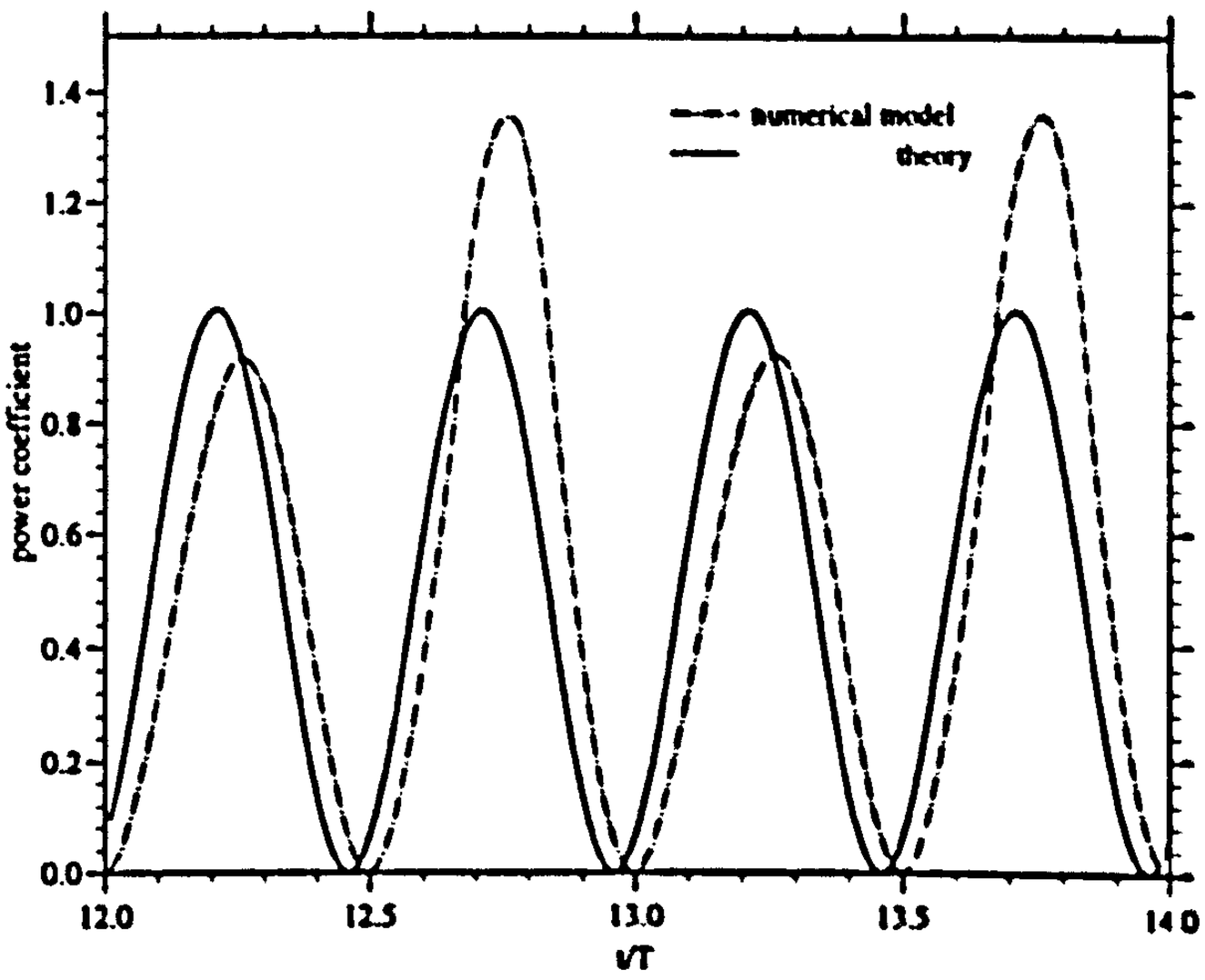

Figure 3.61: $C_P(t)$ vs. t/T

Figures (3.62) and (3.63) show the computed development of $C_P(t)$ and $C_X(t)$ which are produced by the rotor over 40 flow cycles according to the numerical model at KC=3.0 and $\sigma\Lambda$=0.170. Also included are the cyclic mean values $\overline{C_P}$ and $\overline{C_X}$ predicted by the numerical model and the actuator disc theory. Evident in both figures is the tendency of the model to show a gradual reduction in the extent of flow asymmetry. However, a symmetrical mode of vortex ring convection as described for the small KC case was not achieved as computations for a larger number of flow cycles proved numerically unstable.

As was found in the computations for small KC oscillations and is visualised in figures (3.64) and (3.65) showing $\overline{C_P}$ and $\overline{C_X}$ as functions of $\sigma\Lambda$ the flow asymmetry of which $\overline{C_X}$ is a direct measure strongly affects the degree of agreement

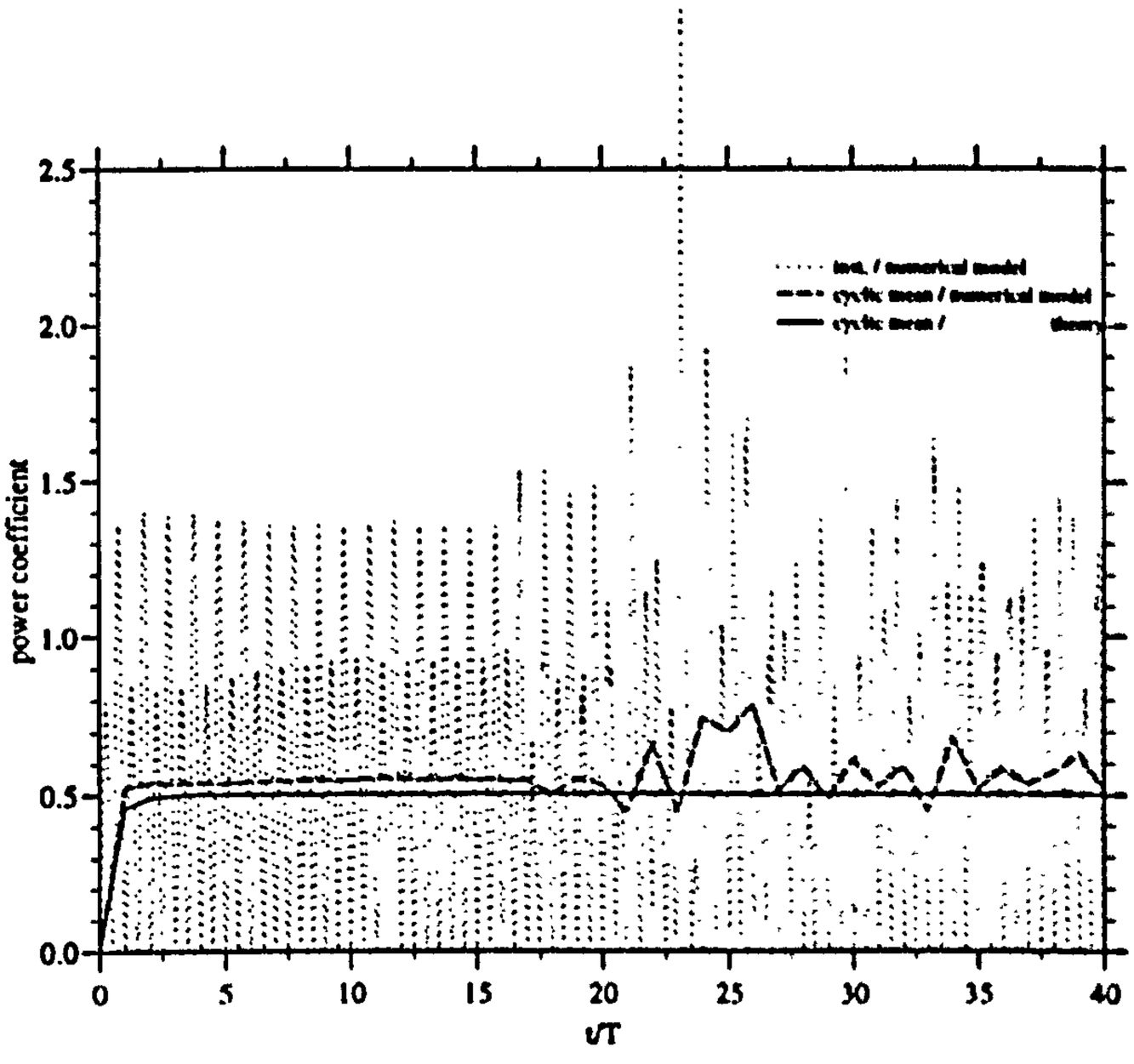

Figure 3.62: $C_P(t)$ & $\bar{C}_P$ vs. t/T

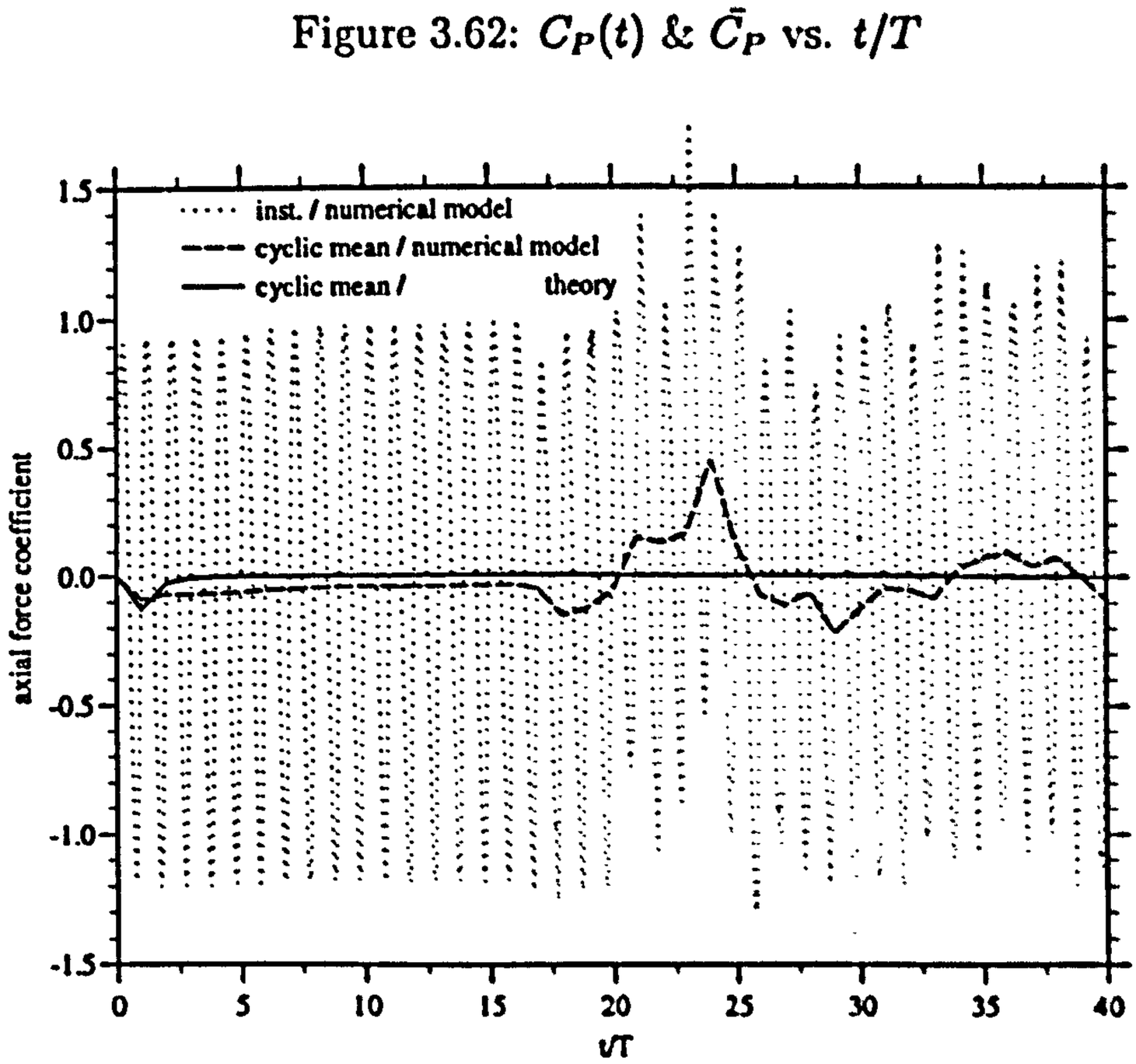

Figure 3.63: $C_X(t)$ & $\bar{C}_X$ vs. t/T

of $\overline{C_P}$ of the two theoretical approaches at all values of $\sigma\Lambda$.

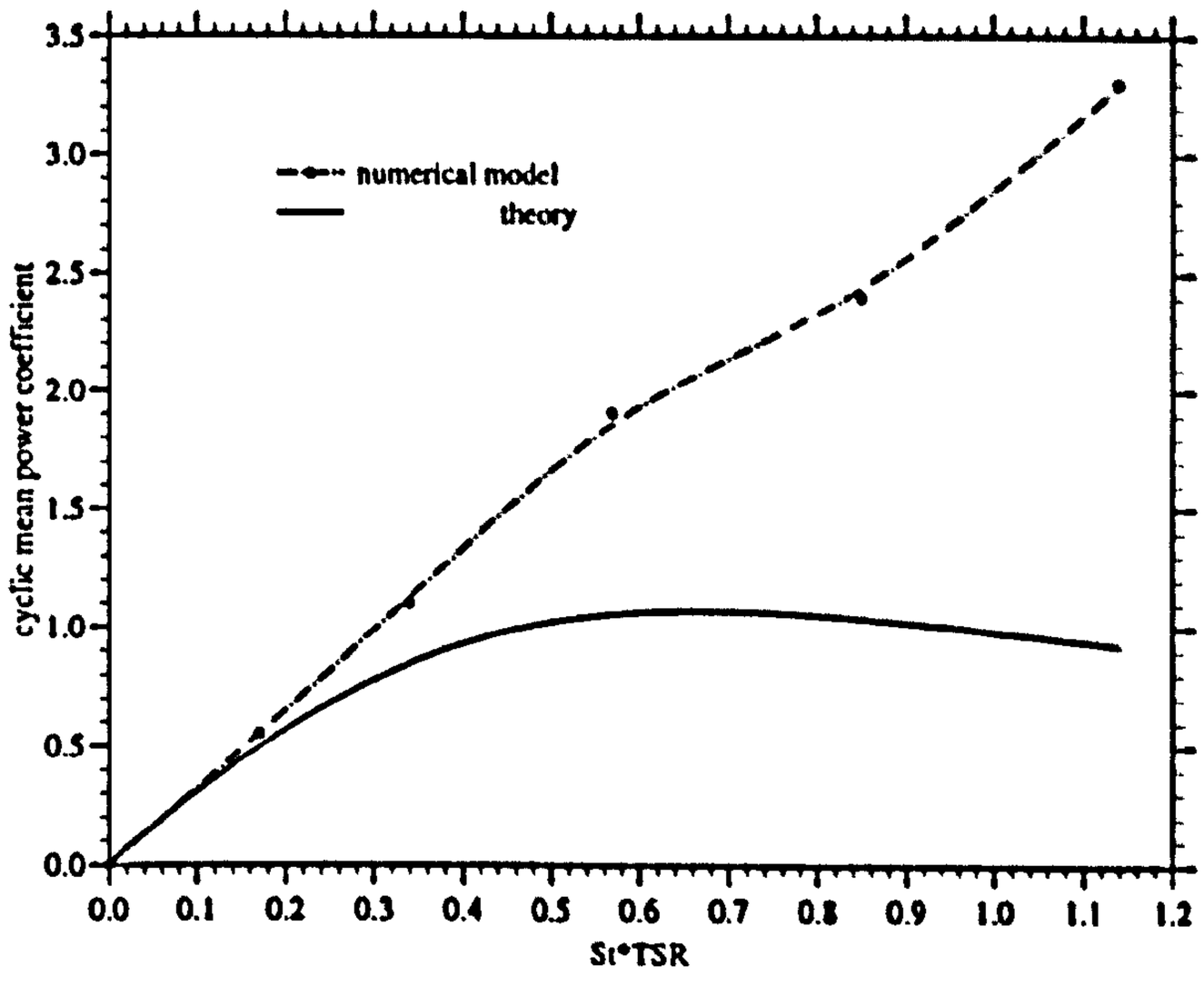

Figure 3.64: $\bar{C}_P$ vs. $\sigma\Lambda$

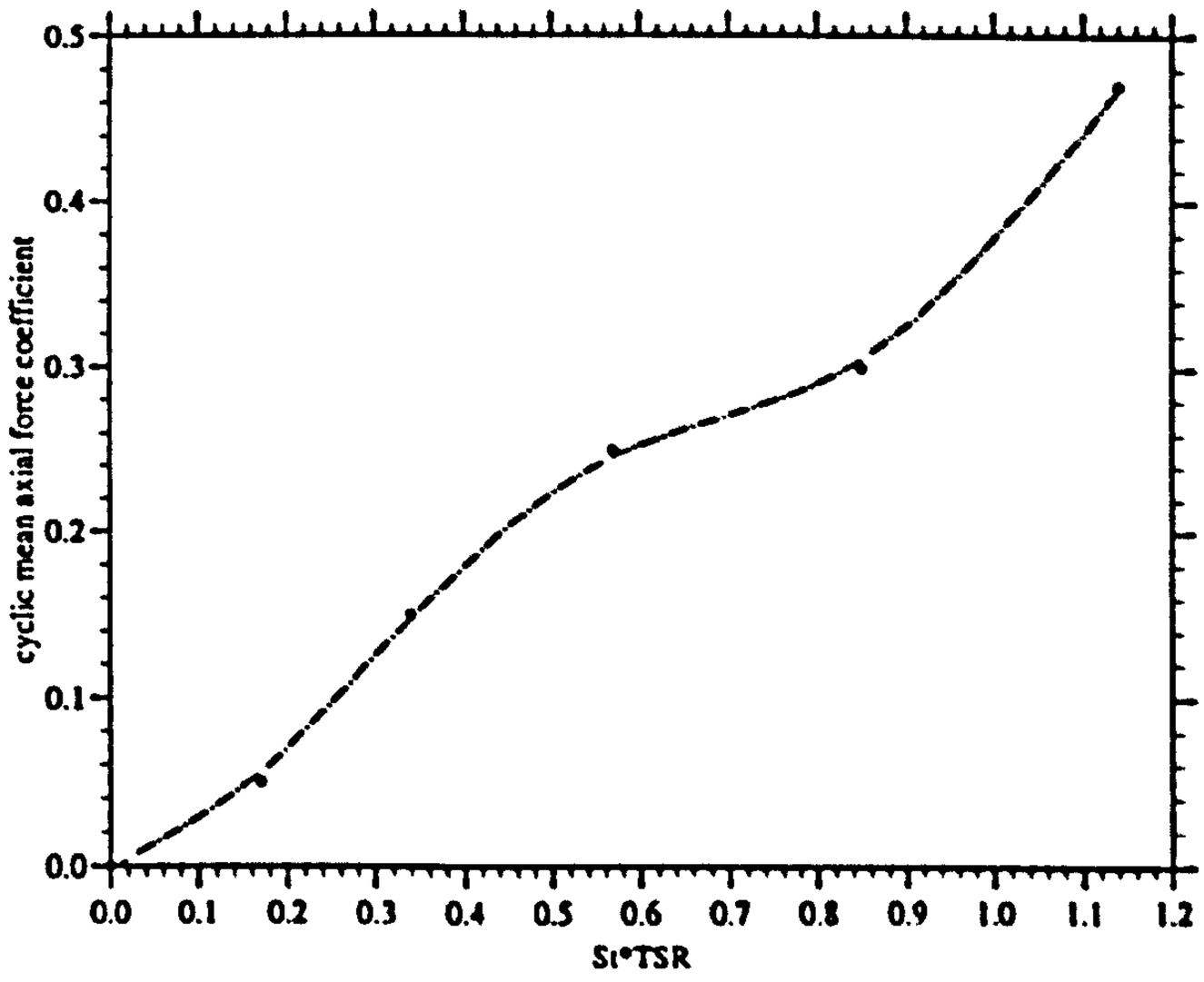

Figure 3.65: $\bar{C}_X$ vs. $\sigma\Lambda$

3.4 Concluding Remarks

A simple numerical model was developed to assess the ideal hydrodynamic efficiency of the Wells turbine in unducted small to moderate KC oscillatory flow, for which previously no method of performance analysis has existed. This theory is similar to the actuator disc theory developed by Glauert for unidirectional steady flow and takes account of the back flow velocity induced by the rotor wake, which is assumed to be uniform across the rotor disc. The wake is simplistically modelled as a vortex ring which for small amplitude flow oscillations was assumed to lie in the plane of rotation. This approximation was made on the assumption that the extent of stream wise convection of wake vorticity is small.

The model showed that the cyclic mean ideal fluid dynamic efficiency of an unducted Wells turbine in oscillatory flow depends on the non-dimensional quantities $\sigma\Lambda$ and KC. Further, the theory revealed that the peak cyclic efficiency of the rotor is inversely proportional to KC and can take values greater than unity. It was also shown that the axial back flow factor based on the peak induced back flow and the maximum incident flow velocity for which the peak cyclic efficiency is achieved is equal to 0.72 and is independent of KC.

It was concluded that the values of peak efficiencies greater than unity are related to the back flow induced by the rotor wake, which over part of the flow cycle augments the flow through the rotor disc.

Further, the preceding discussion of the model showed that the derived actuator disc model is not useful for performance analysis of the unducted Wells turbine in larger KC flows for which the convection of wake vorticity is significant and the chosen idealisations of the flow model are no longer applicable.

As an extension of the simple actuator disc theory a second more sophisticated model was developed and numerically implemented in a FORTRAN77 code. This model to some extent allowed the effects of the rotor wake convection to be studied. The rotor wake was modelled by concentrated vortex rings which were shed on sequential half cycles according to the Brown and Michael model.

The improved numerical model revealed that two different transient wake structures can evolve for small KC flows at lower values of $\sigma\Lambda$. In one wake mode the concentrated vortex rings shed on sequential half cycles showed a strong tendency to form a vortex pair. For this mode a unidirectionally biased stream wise wake convection was noted, which produced a non-zero mean axial force on the rotor disc. The second transient wake structure showed that sequentially shed vortex rings convect independently in an unbiased manner producing a zero mean axial force.

For moderate KC number flows, on the other hand, the strong interactions between the concentrated wake vortex rings only promoted the biased wake structure which was caused by the tendency of sequentially shed rings to pair up. The extent of the stream wise convection of the nascent vortex rings was found to be of the order of the rotor tip radius and is, therefore, considered to be non-negligible.

The improved numerical model showed that for small KC flows the stream wise convection of the nascent vortex rings is small and, therefore, justifies the approximation in the actuator disc theory that the wake vortex rings remain in the plane of rotation. It was shown by comparison of computations using the two models that the wake convection causes mainly a small difference in the phase lag between the velocity of the flow through the rotor disc and that of the sinusoidal free stream flow.

Further, it was demonstrated using the improved numerical model that the induced velocity in the plane of the rotor disc is comparatively uniform at small values of KC, as assumed in the derivation of the simpler actuator disc theory. However, near the tip the induced velocities were shown to deviate considerably from those over the rest of the rotor disc. For the moderate KC case presented it was found that the radial variation of the velocity in the rotor plane is more significant.

Comparison of the mean cyclic power coefficients predicted by the two numerical models for small KC flow showed that there is good quantitative agreement between the models when the wake structure of the improved model establishes the more symmetrical variation in time.

Due to the considerable discrepancies of the flow fields assumed in the actuator disc theory and computed by the improved numerical model the agreement between the power predictions made from the two models at moderate KC was unsatisfactory.

3.5 Experimental Work

3.5.1 General

It was decided to carry out model scale experimental investigations in order to provide some verification of the theoretical and numerical fluid dynamic performance analysis of the Wells turbine in unducted oscillatory flow. These experimental studies consisted mainly of shaft power measurements over a range of small to moderate KC flows. In addition, flow visualisation studies were performed in water tank flows to develop a qualitative appreciation of the physical nature of the wake structure of unducted Wells turbine rotors in small amplitude oscillatory flows. The experimental implementation and the results of these studies are discussed in the following.

3.5.2 Experimental Programme and Apparatus

Initial experimental studies of the hydrodynamic performance of an unducted Wells turbine in low to moderate KC flows were carried out in the Departmental U-tube water tank described below. In these tests the water was caused to oscillate past a turbine whose axial position was fixed. The U-tube tests were supplemented by power measurements which were made in a large (- still water -) water tank in which the turbine was oscillated axially. These tests were also aimed at establishing the importance of constraint effects to which the turbine in the U-tube testing may be subject. However, experimental studies on cylinders in oscillatory flow in the same U-tube water tank carried out by Kuehtz (1996) have shown in agreement with findings of Sarpkaya (1975) that in oscillating flows the effect of blockage is small so that in the present study a similar result was anticipated. In the experiments carried out in the large water tank the turbine was oscillated in the otherwise still fluid using an electrically driven carriage. Since the frequency of oscillations was controllable in this set-up, measurements could be made at smaller amplitudes than those achieved in the U-tube tests because for a given amplitude of oscillation the amount of energy in the fluid flow available for conversion by the turbine rotor increases with the cube of the flow frequency. Hence the energy capture of the rotor in absolute terms can be made high enough to overcome losses to enable accurate measurements to be made for small amplitude motions.

The U-tube Water Tank Arrangement

The U-tube water tank consists of a horizontal working section attached to two vertical limbs. The cross section of the U-tube is 610 [mm] square and each vertical limb has a typical height of 650 [mm] from the top of the curved joining

section to the mean free surface. Sinusoidally oscillating flow of a fixed period of approximately 3.3 [sec] is generated by a blower, which is placed at the top of one of the limbs and exerts pressure on the water column as it moves downwards. Using a conductive wave probe the water motion is monitored in the second limb and feedback is provided to the blower which acts so that the amplitude of the motion remains constant. Singh (1979) gives a more in-depth description of the U-tube water tank and its operation. In the U-tube power measurement tests a model Wells turbine was suspended from the top of the U-tube and placed into the vertically oscillating water motion of this limb. Figure (3.66) shows the experimental arrangement in schematised form. The turbine is suspended so that the plane of blade rotation is nominally 400 [mm] below the mean water level (MWL) and approximately 250 [mm] above the curved section connecting the horizontal and vertical sections of the U-tube water tank, in the centre of the cross-section.

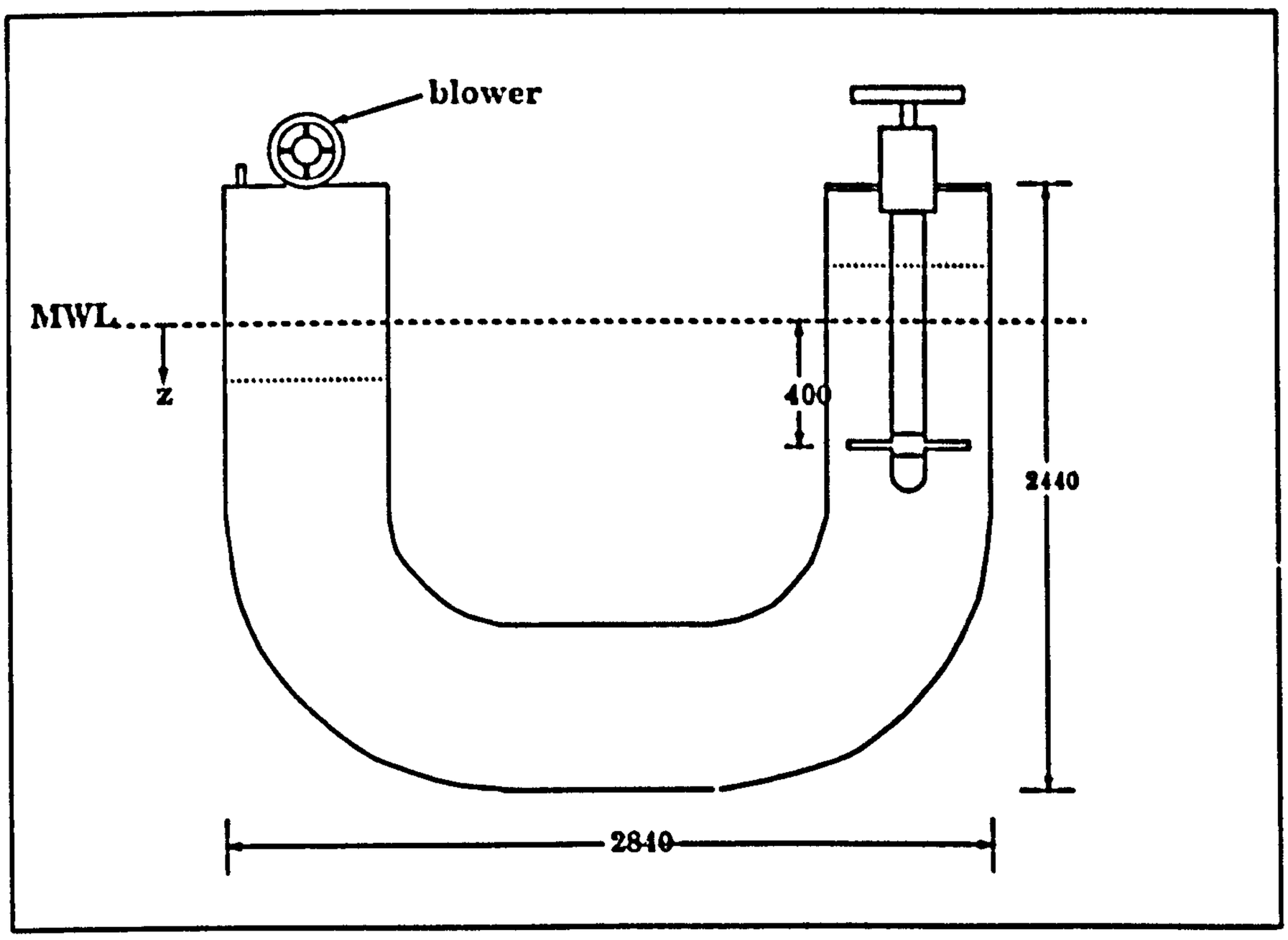

Figure 3.66: The U-tube Water Tank Arrangement

The Large Water Tank Arrangement

The Departmental large water tank has a cross section of 2.40 [m] square and is 2.30 [m] deep. It has a working platform above the free water surface providing a support frame from which test objects may be suspended. In the power measure-

ment tests carried out a SEASIM CONTROLS Ltd. driving carriage was fixed to the support frame. The carriage was arranged to vertically oscillate a Wells turbine model via a specially manufactured horizontal transmission link. The mass of the turbine apparatus, which was approximately 13 [kg], was counter balanced through a pulley system to ensure that the workload required to oscillate the turbine apparatus did not exceed the capacity of the driving carriage. Figure (3.67) shows the water tank itself and figure (3.68) shows the turbine model operating in the water tank. In this set-up the zero displacement position of the rotor plane was approximately 340 [mm] below the free surface in the centre of the tank (plan form).

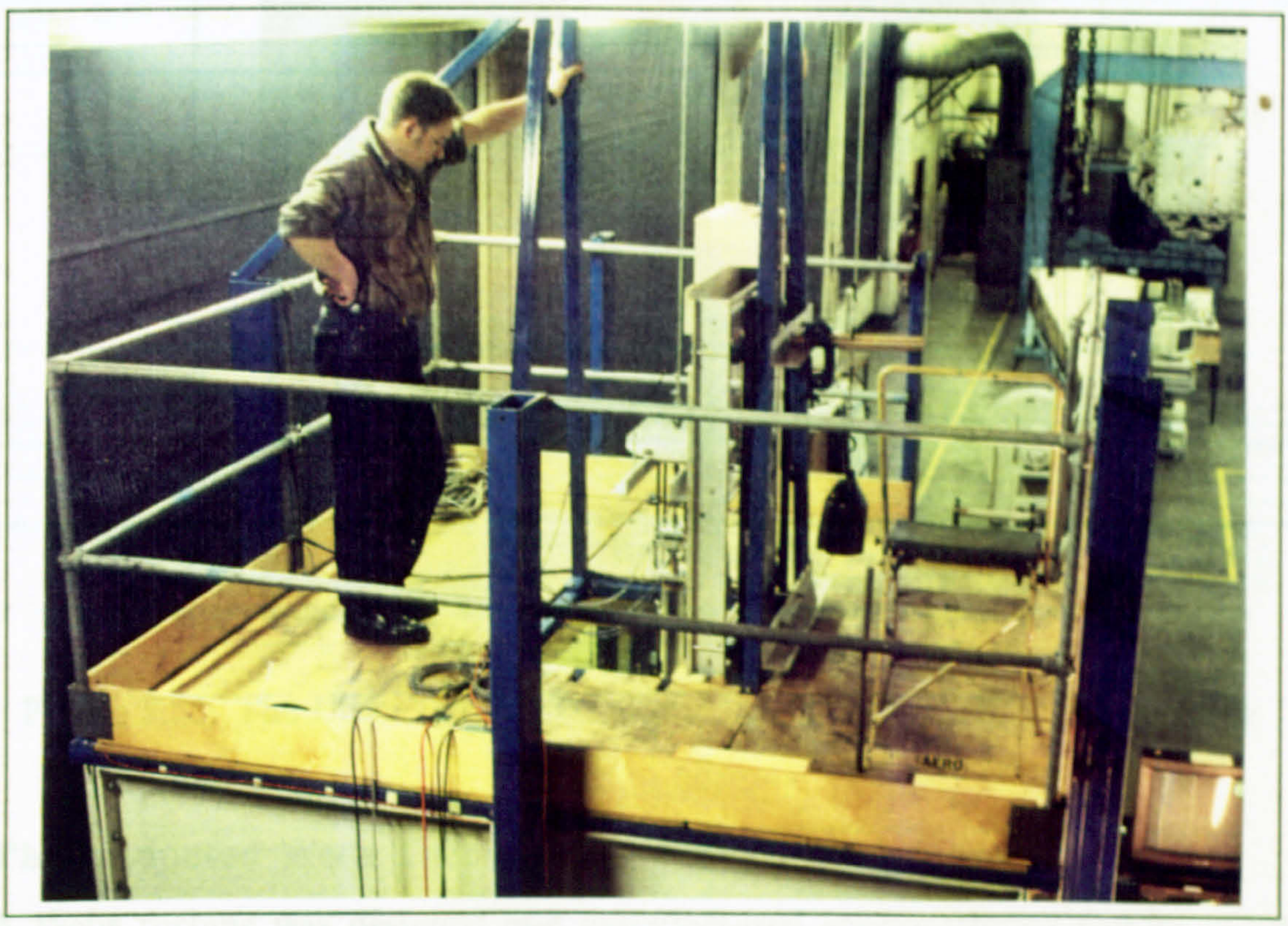

Figure 3.67: The Large Still Water Tank Arrangement

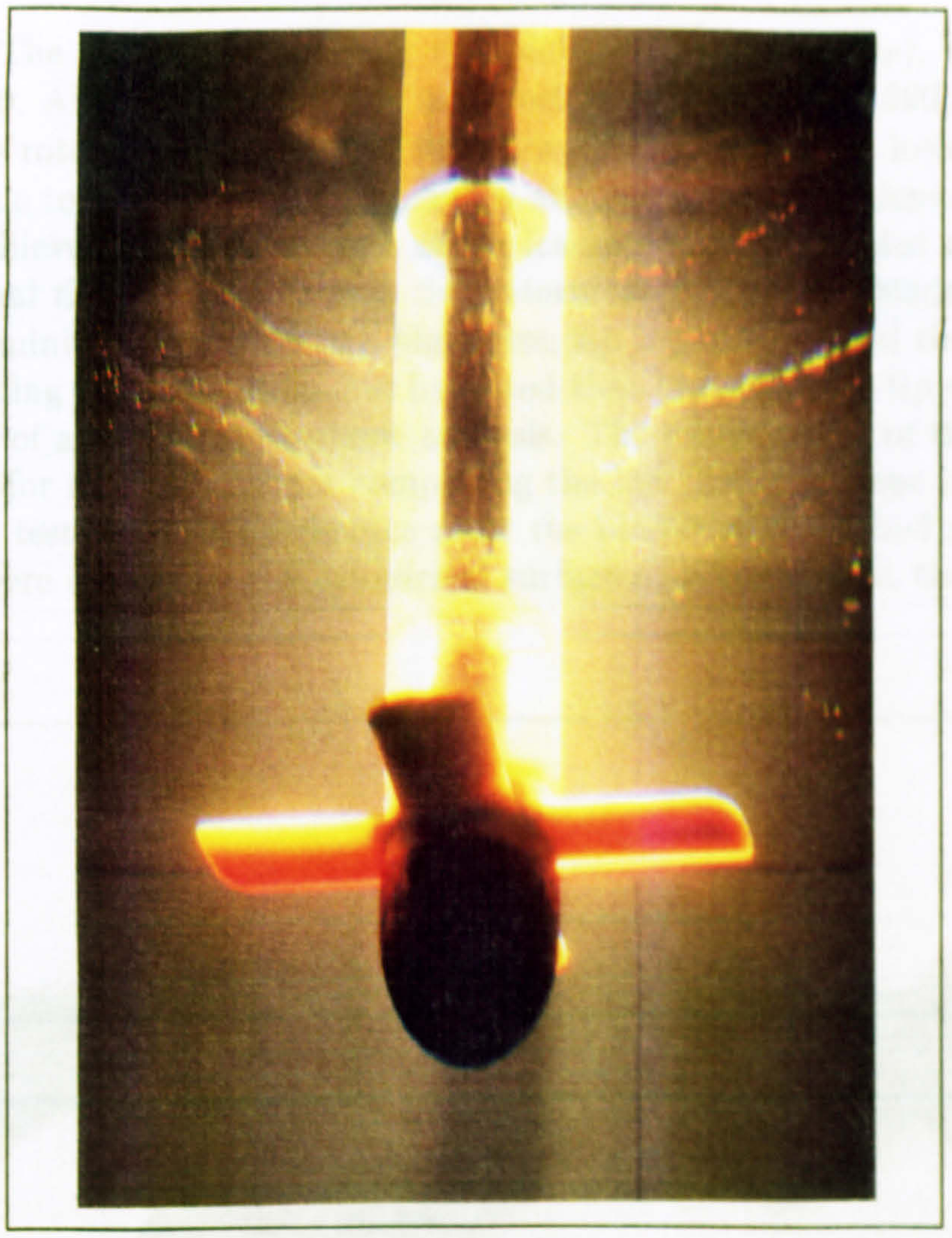

Figure 3.68: The Unducted Wells Turbine Model in The Large Water Tank

The Unducted Wells Turbine Model

A Wells turbine was designed and manufactured specifically for testing in the water tank described above, though the turbine rotor diameter was constrained by the cross sectional dimensions of the U-tube. It was constructed to allow the shaft power to be measured over a number of rotational speeds and amplitudes of oscillatory flow.

The turbine hub was laid out so that the rotor was interchangeable. Turbine rotors were assembled with a diameter of 235 [mm] comprising two, three, and four constant 50 [mm] chord NACA0018 sectioned blades cast from poly-urofane resin. These rotors were formed by bonding the individually cast blades to specially manufactured mounting rings that had an external diameter equal to that of the rotor hub. The mounting rings allowed the rotors to be fastened to the

rotor hub. The corresponding rotor tip solidities, $\sigma = (nc/\pi D_T)$, were 0.135 / 0.200 / 0.270. All the rotors had the same hub to tip ratio h of 0.320 . In order to optimise the rotor performance, the blades were shaped to have lower tip losses, which are due to the profile drag generated at the tip and are independent of lift. This was achieved by introducing a swept leading edge, a rounded trailing edge and a gradual thickness taper over the outermost 10% of the blade span. The aim was to minimise the blade tip bluntness, tip separations and the amount of drag generating tip area. It should be noted that the resulting tip shape is not the product of any rigorous tip flow analysis. The effectiveness of the tip shape was verified for a 2-bladed rotor comprising the low drag tip shape in still water deceleration tests against a reference rotor the blades of which had no thickness taper and were cut off by the cylindrical surface of revolution at their outer diameter.

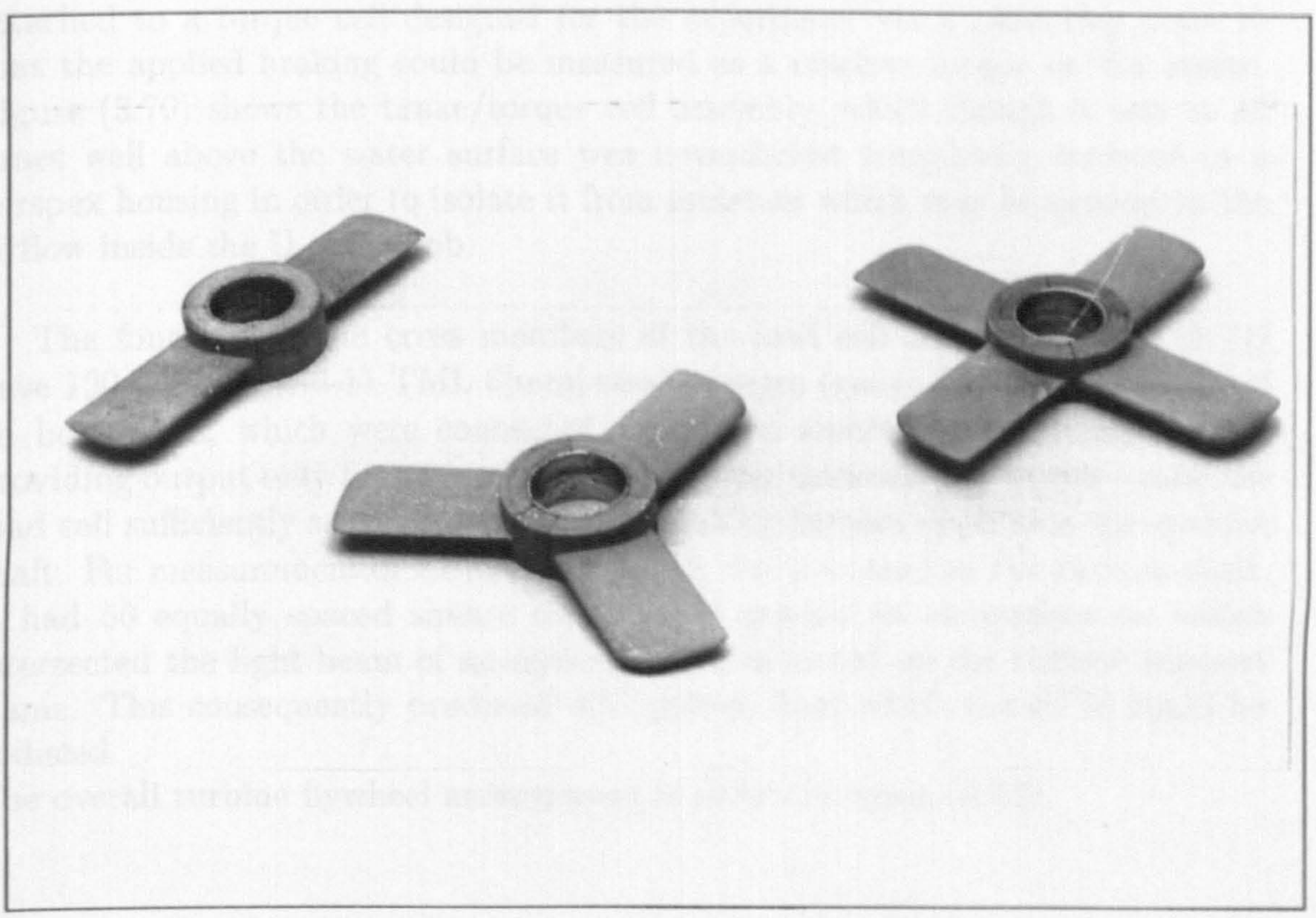

Figure 3.69: Test Rotors For The Unducted Wells Turbine

Shown in figure (3.69) are the different turbine rotors comprising the low drag tip shape for which power measurements were carried out. The rotor was fitted with a wooden nose cone of elliptical cross section and a length to diameter ratio of approximately 1.27. The turbine shaft and bearings were housed in a metal casing of 750.0 [mm] length. In order to ensure disturbance free flow immediately up-/downstream of the rotor, a cylindrical perspex tube equal in diameter to that

of the rotor hub was fitted around the metal casing.

The RPM of the turbine rotor was controlled using a Clark Electric Clutch BM175 electro magnetically operated friction brake, which exerts a maximum braking torque of 1[Nm] at 24 [V] d.c. supply voltage. Initial testing of the turbine in oscillatory flow showed that the torque produced by the rotor over a short period at either half of a flow cycle was insufficient to overcome even small amounts of applied braking and the rotor, therefore, slowed down and tended to stall . This problem was overcome by attaching a separately supported perspex flywheel, 300 [mm] in diameter, through flexible couplings to the main drive shaft of the turbine. By adding steel masses at discrete radial locations the flywheel inertia was adjustable up to a maximum of 10.0e-3 $[kgm^2]$.

While the brake rotor was fixed to the turbine shaft, the brake stator was attached to a torque cell designed for the experiment via a mounting plate so that the applied braking could be measured as a reactive torque on the stator. Figure (3.70) shows the brake/torque cell assembly, which though it was at all times well above the water surface was nevertheless completely enclosed in a perspex housing in order to isolate it from moisture which may be present in the airflow inside the U-tube limb.

The four aluminium cross members of the load cell shown in figure (3.71) have 120 Ohm FLK-6-11 TML 6[mm] strain gauges (gauge factor 2.13) attached on both sides, which were connected up in two separate Wheatstone bridges providing output only for torque. A cross member thickness of 0.8[mm] made the load cell sufficiently sensitive to the small braking torques applied to the turbine shaft. For measurement of RPM a rotary disc was mounted on the turbine shaft. It had 50 equally spaced square slots placed around its circumference, which intersected the light beam of an optical device mounted on the turbine support frame. This consequently produced 4[V] pulses, from which the RPM could be deduced.
The overall turbine flywheel arrangement is shown in figure (3.72).

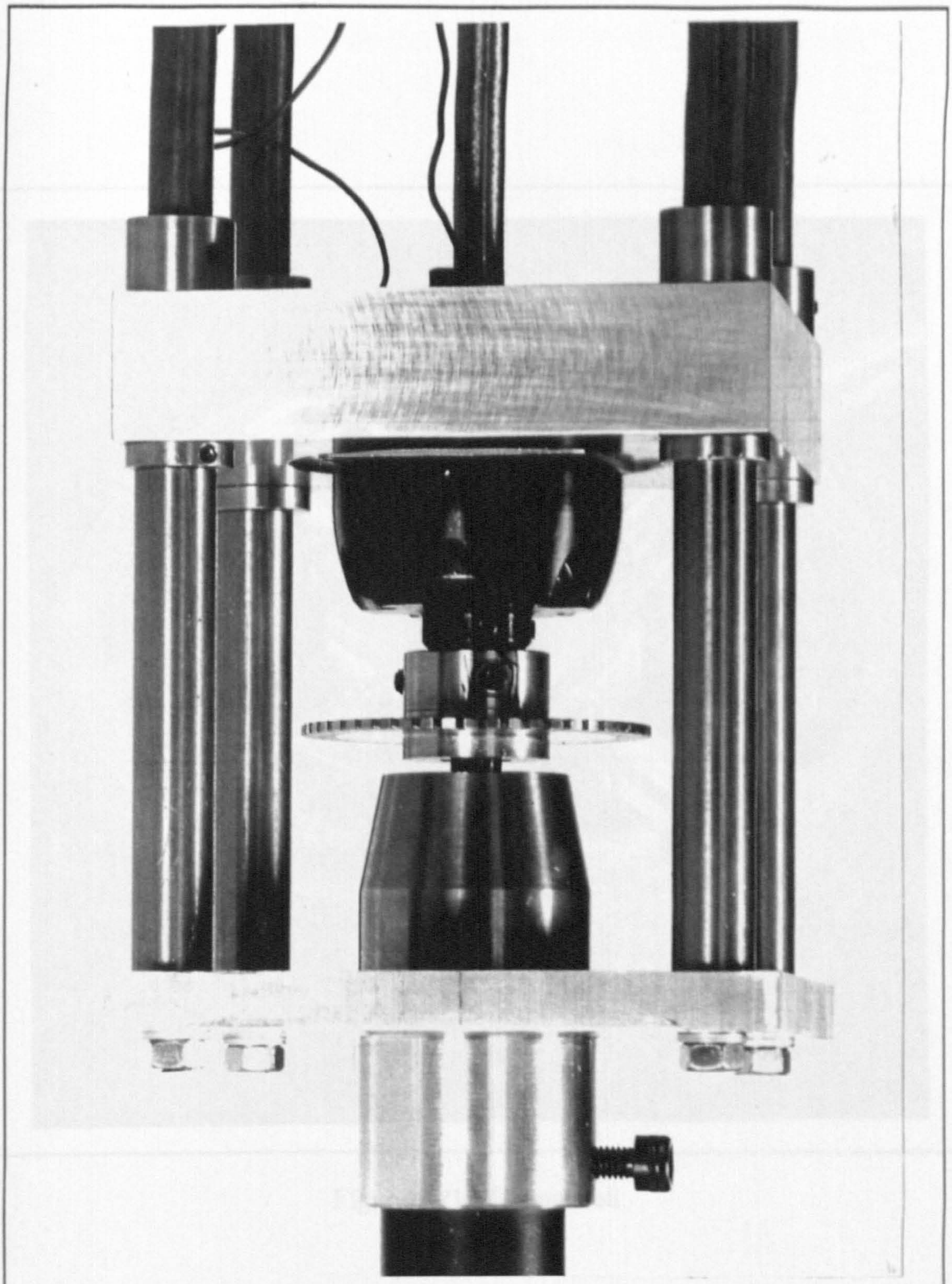

Figure 3.70: Brake / Tacho / Torque Cell Assembly

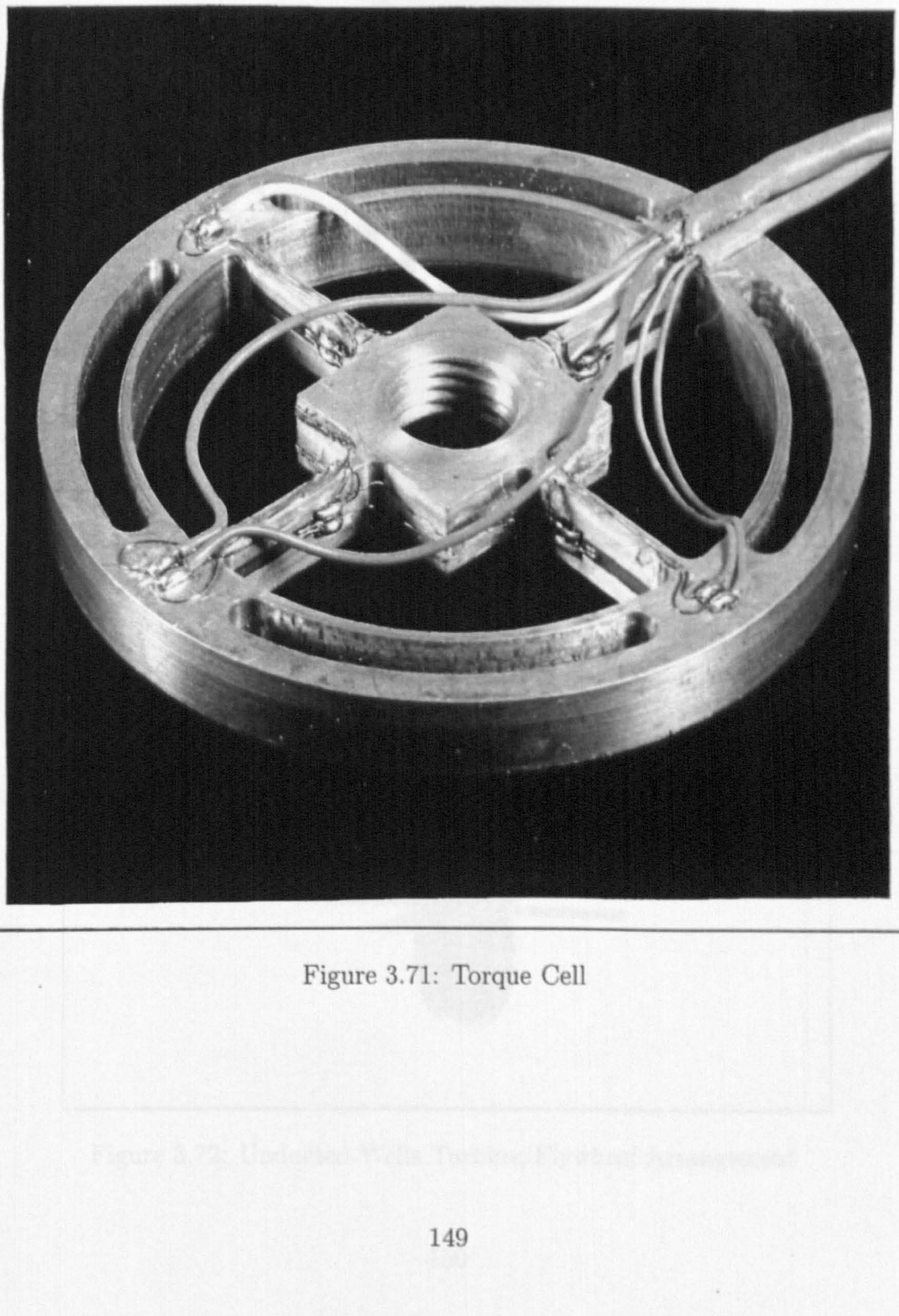

Figure 3.71: Torque Cell

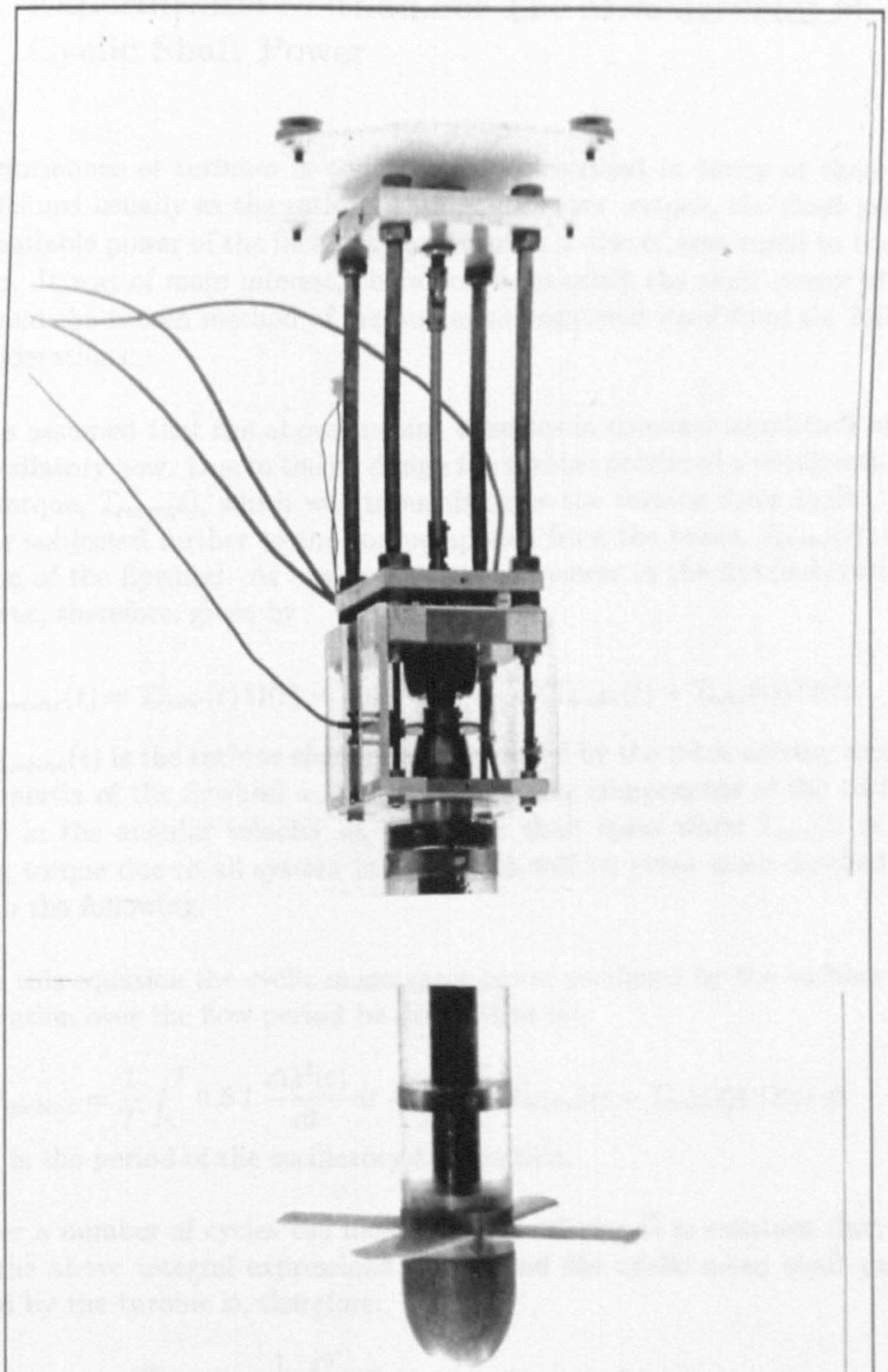

Figure 3.72: Unducted Wells Turbine/Flywheel Arrangement

3.5.3 Experimental Method For The Measurement of The Cyclic Shaft Power

General

The performance of turbines is conventionally described in terms of their efficiency defined usually as the ratio of the useful power output, the shaft power, to the available power of the incident flow through a disc of area equal to that of the rotor. It was of main interest, therefore, to quantify the shaft power of the turbine and the chosen method of measurement suggested itself from the following considerations:

It was assumed that the above turbine operates in constant amplitude sinusoidal oscillatory flow. Due to the its design the turbine produced a unidirectional driving torque, $T_{rotor}(t)$, which was transmitted to the turbine drive shaft. The shaft was subjected further to the torque applied from the brake, $T_{brake}(t)$, and the action of the flywheel. At any given time the power in the flywheel/turbine system was, therefore, given by

$$(3.62)\ P_{turbine}(t) = T_{rotor}(t)\,\Omega(t) = 0.5\,I\,\frac{d\Omega^2(t)}{dt} + (T_{brake}(t) + T_{loss}(t))\,\Omega(t)$$

where $P_{turbine}(t)$ is the turbine shaft power produced by the rotor driving torque, I is the inertia of the flywheel and all other rotating components of the turbine and $\Omega(t)$ in the angular velocity at which the shaft spins while $T_{loss}(t)$ is the retarding torque due to all system losses, which will be given more detailed attention in the following.

From this equation the cyclic mean shaft power produced by the turbine can by integration over the flow period be deduced to be:

$$(3.63)\ \overline{P}_{turbine} = \frac{1}{T}\int_0^T 0.5\,I\,\frac{d\Omega^2(t)}{dt}dt + \frac{1}{T}\int_0^T (T_{brake}(t) + T_{loss}(t))\ \Omega(t)\,dt$$

where T is the period of the oscillatory fluid motion.

If over a number of cycles the mean angular velocity $\overline{\Omega}$ is constant then the first of the above integral expressions is zero and the cyclic mean shaft power produced by the turbine is, therefore:

$$(3.64)\qquad \overline{P}_{turbine} = \frac{1}{T}\int_0^T (T_{brake}(t) + T_{loss}(t))\ \Omega(t)\,dt$$

So, the mean cyclic shaft power the turbine produces in an oscillatory flow according to this expression could be quantified by measuring the braking torque, the turbine losses and the angular velocity over a full flow cycle.

Measurement of The Braking Torque

The braking torque was measured using the specially designed load cells described above. These were calibrated in static load tests after being attached to the brake on the fully assembled turbine. For the calibration, the turbine was placed horizontally with the brake applied and masses were hung from the rotor blade tips to exert a known torque. In the calibration the output voltages of the two strain gauge bridges were amplified using an in house built strain gauge amplifier (SGA) and a differential amplifier at a gain of 100, filtered for electrical noise from the mains and recorded on a PC after being converted to a digital signal. Figure (3.73) shows below the calibration curves produced by this method for the two torque cell bridge circuits, which were linear and showed a maximum of 2% hysteresis. The load cells were designed to be insensitive to axial loads. This was verified in static loading tests in which the turbine was vertically suspended. The torque cell response was monitored as axial weights up to a total of 1 [kg] were applied to the rotor and was found to be negligible compared to output for typical applied torques.

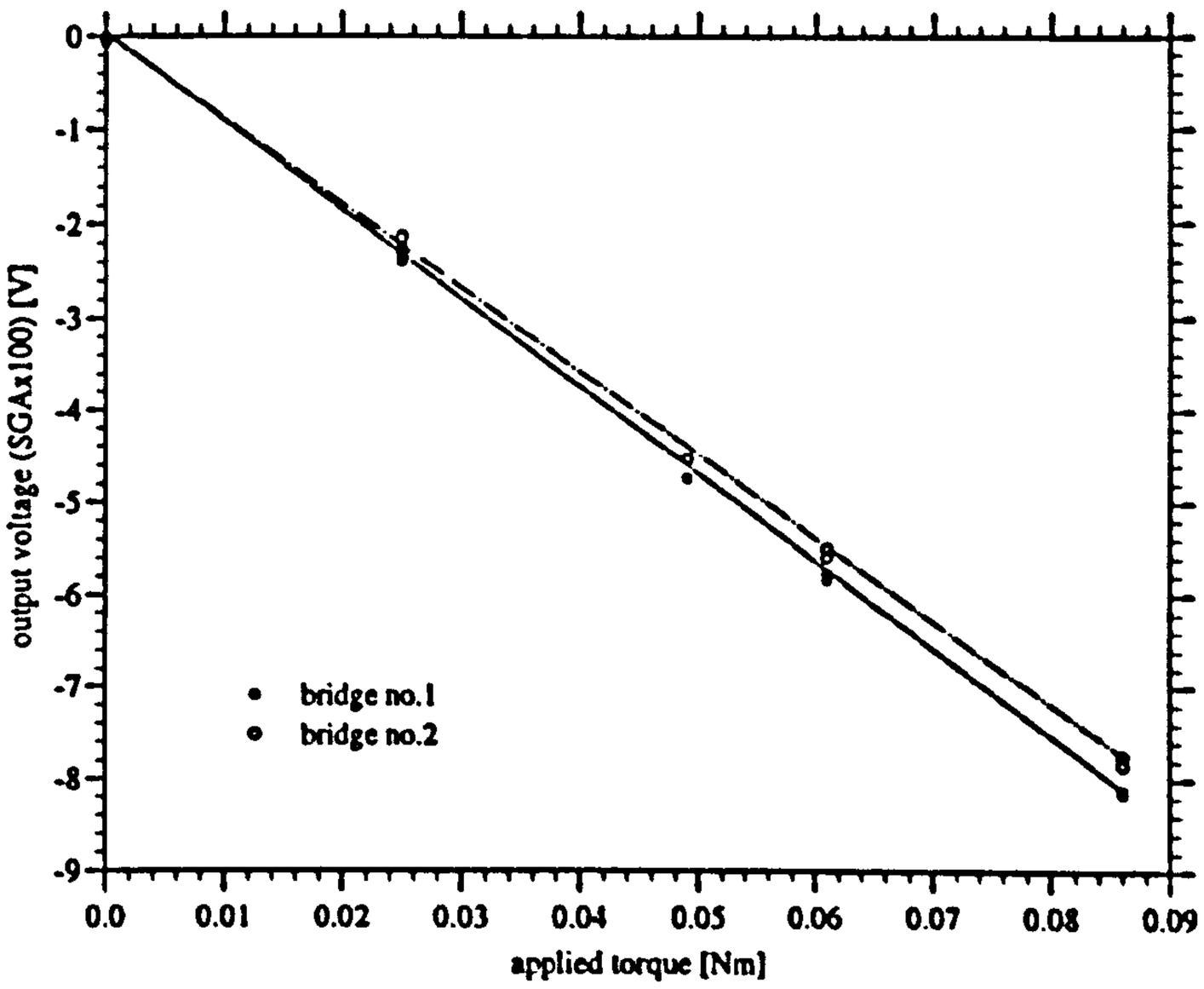

Figure 3.73: Torque Cell Calibration

Measurement of The Rotor RPM

As described above an optical tacho was installed on the turbine rig the output of which was recorded at a fixed sampling frequency, f. This produced a sequence of d.c. pulses consisting of data points with equal spacing dt in time. In the data reduction code the pulse length, T_{pulse}, was defined through the number of sampled data points counted between two consecutive voltage rises from 0[V] to 4[V]:

$$T_{pulse} = n \times dt = n \times f^{-1}$$

Since the rotary disc mounted on the turbine shaft has 50 holes which intersect the light beam of the optical device, a value of RPM can be calculated from each pulse length:

$$RPM = 60. \times (T_{pulse} \times 50.)$$

The value for the 'instantaneous' RPM calculated in this way is ascribed to a point in time which corresponds to mid pulse. Since average pulse lengths were typically of the order 10 to 20 [msec] phase errors incurred by assigning the deduced RPM values to times corresponding to mid pulse are small compared to the period of the fluid motion. The maximum error in determining a value of RPM by the outlined method is dt. For a pulse consisting of n sampled data points the maximum possible error is therefore $1/n$. Typically, for the highest rotor tip speeds achieved during testing the minimum number of samples in one pulse were around 7 so that the maximum possible error in this case is 14.3% . The magnitude of this possible maximum error was reduced by formulating a sliding average for each pulse which takes into account the pulse length of 5 pulses ahead and aft of this pulse. Further, the sampling frequency in the data acquisition process was chosen so that pulses are defined by a sufficiently large number of data points. For all measurements carried out sampling frequencies of either 0.50[kHz], in the case of values of rotor RPM up to approximately 180, or 1.0[kHz] for higher RPM values were used. Over the range of RPM covered in testing between approximately 50 to 100 pulses and, therefore, values of 'instantaneous' RPM could typically be recorded per second using this technique.

Measurement of The Oscillatory Motion

In the U-tube water tank tests the water displacement was measured directly in the limb of the U-tube in which the turbine was placed using the calibrated wave probe,which provides feedback to the controller of the U-tube blower mentioned previously.

In the experiments carried out in the large water tank the turbine vertical displacement was recorded using the calibrated dc-feedback signal provided by

the SEAWAVE SIMULATION LSC 24-48 servo control system which was used to operate the drive carriage.

Measurement of The Turbine Losses

In order to determine the turbine shaft power according to equation (3.64) it was necessary to define the variation of turbine losses with RPM. An easy method of measuring the mechanical losses due to bearing friction, the aerodynamic drag on the flywheel and the hydrodynamic drag on the rotor hub alone and the turbine shaft was to record the turbine shaft deceleration in stationary water from some initial RPM without any blades attached to the rotor and determine the corresponding loss torque from equation (3.64) above, noting that the turbine is not producing any power in this case. The inertia of all rotating components was estimated using their estimated respective radii of gyration and masses which was measured using accurate scales.

The turbine was fixed in the U-tube water tank with no rotor blades attached and was accelerated by hand. It was then left to decelerate in the stationary water. The deceleration was measured and found to be near linear and, therefore, a nominally constant torque of 0.0075 [Nm] due to the above mentioned losses was deduced from knowledge of the system inertia.

In addition to the mechanical losses the turbine suffers losses due to fluid dynamic drag acting on the rotor blades. These losses are a strong function of the Reynolds number. Typically, the Reynolds numbers achieved in the U-tube and large water tank tests were, based on the total flow velocity incident to the blade and the blade chord, of the order $10^3 - 10^4$. Figure (3.74) (Eastman (1937)) shows the experimentally measured profile drag of the NACA0018 airfoil section for a number of Reynolds numbers.

It is clear that at the low Reynolds numbers of the water tank tests carried out the profile drag losses of the blade are fairly large. As a result the rotor performance is significantly degraded from that predicted by the inviscid theory developed in the previous chapter. In order to provide a better basis for the comparison of experimentally measured and theoretically predicted rotor power coefficients it was decided to include these fluid losses as a torque in the total rotor loss torque T_{loss} which is used to calculate the cyclic mean power produced by the rotor. It may be argued that this approach which should provide an estimate of rotor power for inviscid flow allows more meaningful comments to be made about the performance of large scale rotors in wave flow to be made for which the anticipated Reynolds numbers are in the range of $10^6 - 10^7$, since for these Reynolds numbers the drag losses are significantly smaller.

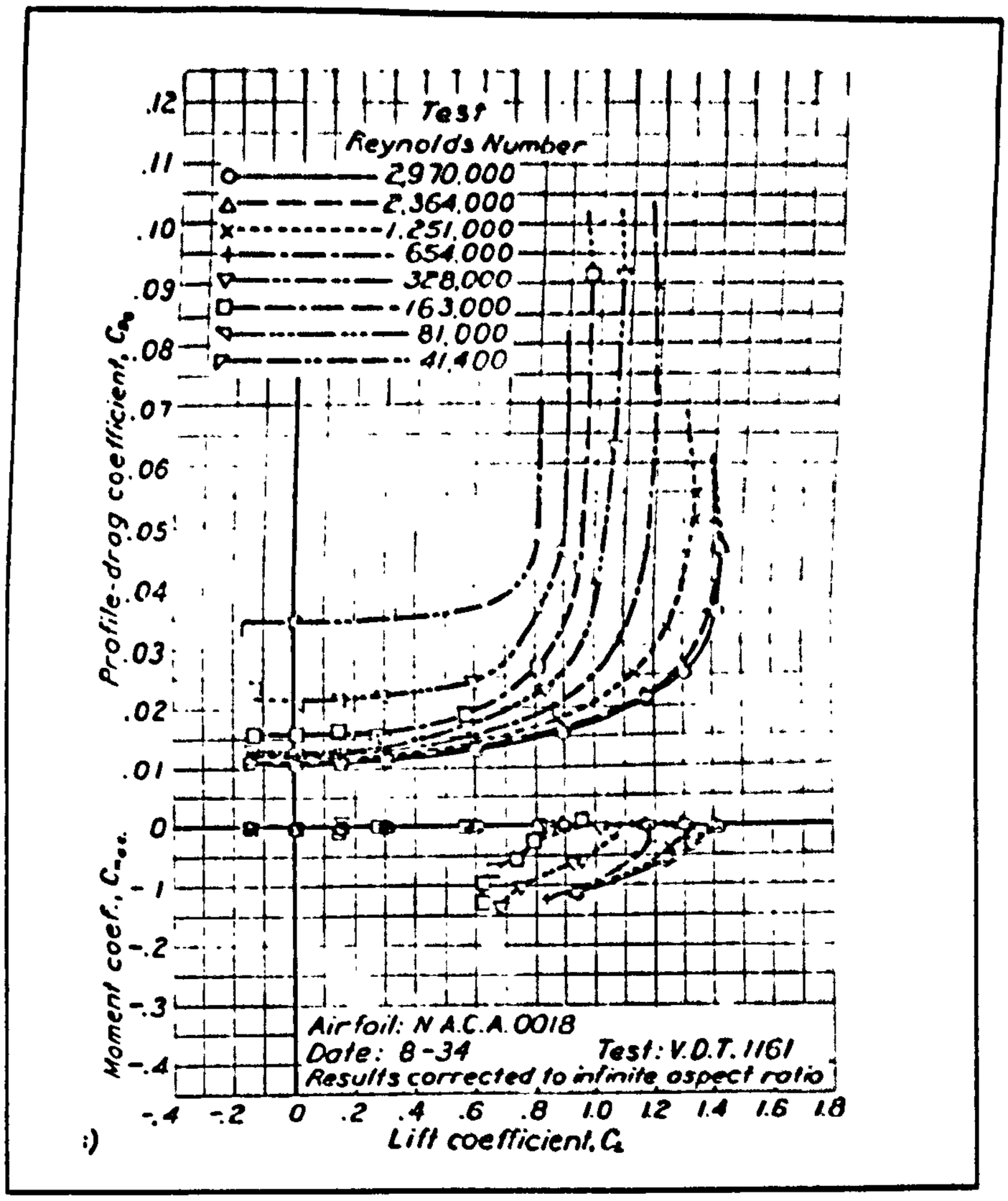

Figure 3.74: NACA0018 Profile Drag C_{D0} vs. Re

It was decided to experimentally determine the fluid losses and deceleration tests identical to those carried out to determine the mechanical losses in the system were carried out for all turbine rotors. Respective loss torques were deduced using equation (3.64) for different values of RPM. The torque values measured in these tests were, in fact, the net loss torque T_{loss} in equation (3.64), since the rotor deceleration was also due to the mechanical losses in the turbine bearings. The variation of T_{loss} with shaft angular velocity is presented in figure (3.75) for the three different rotor configurations for which power measurements were carried out.

Data Acquisition

Figure (3.76) schematically summarises the system set-up for all testing in the U-tube water tank.

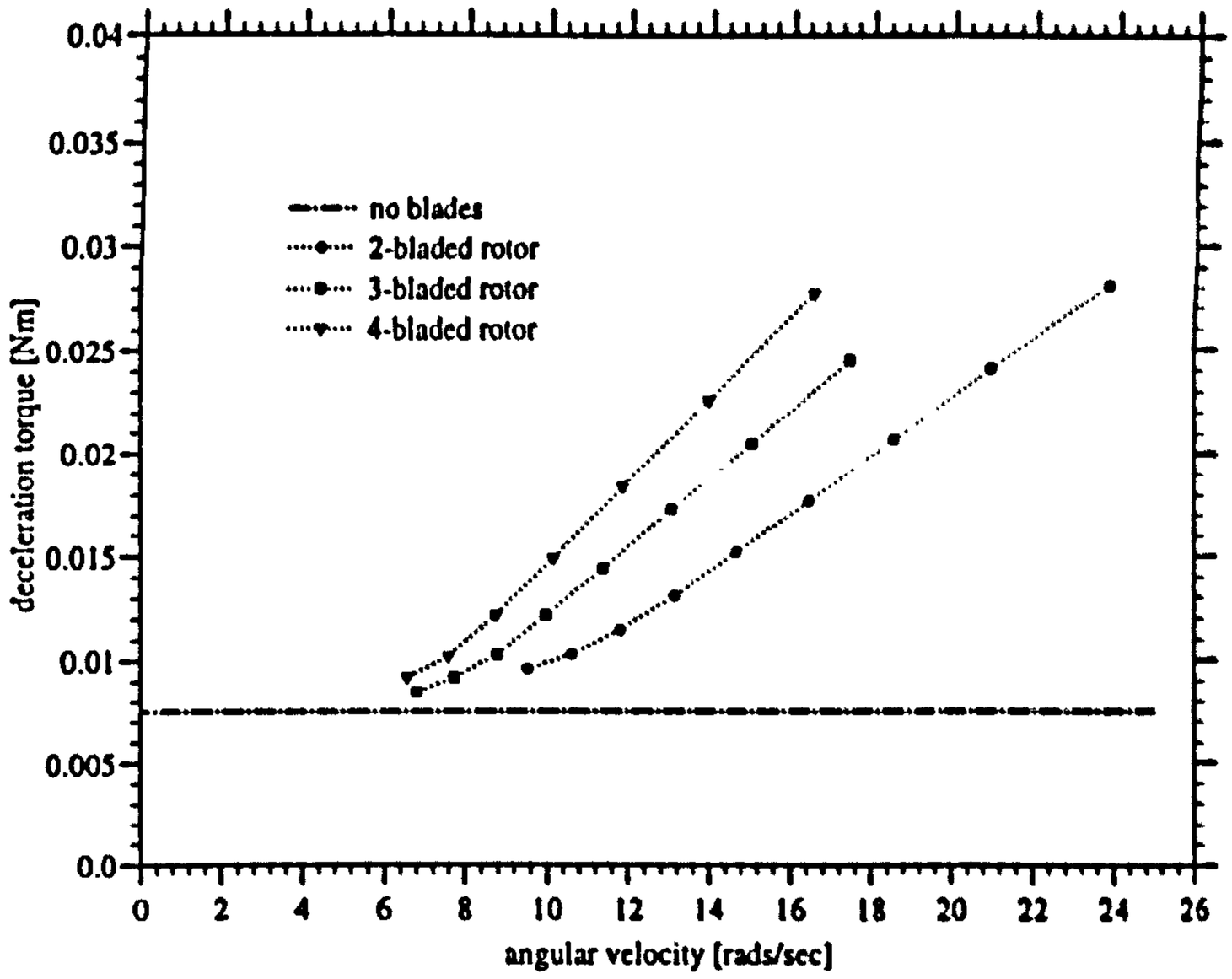

Figure 3.75: T_{decel} vs. Ω

The turbine braking was manually controlled by adjusting the supply voltage to the brake using the Clarke Electric Clutch P200 brake rheostat. Though, the brake produces its rated braking power of 1[Nm] at 24[V] d.c. supply voltage, the supply voltage for the experiment was set at 8[V] to allow for finer adjustment of the considerably smaller applied braking torques. In order to have two independent readings of braking torque from the load cell over which to average, the outputs of both strain gauge bridge circuits were fed into separate strain gauge amplifier units. The output of these was filtered for electrical noise and then further amplified by a factor of 100 using a differential amplifier to optimise the sensitivity of the load cell. In order to record any physically significant signals from the load cell which were at maximum likely to be at a frequency corresponding to the rotor RPM the bridge circuit output was filtered at 20[Hz]. This filtering frequency was low enough to remove any possible noise picked up from mains supply and other sources of electrical interference. No electrical noise significant in magnitude compared to mean load cell output signals was noted at this filtering frequency throughout the water tank testing.

The output of the optical tachometer,the optical sensor of which was supplied with 8 [V] d.c. from the same power supply as the turbine brake, required no further signal conditioning and was fed directly into the analogue to digital (A/D)

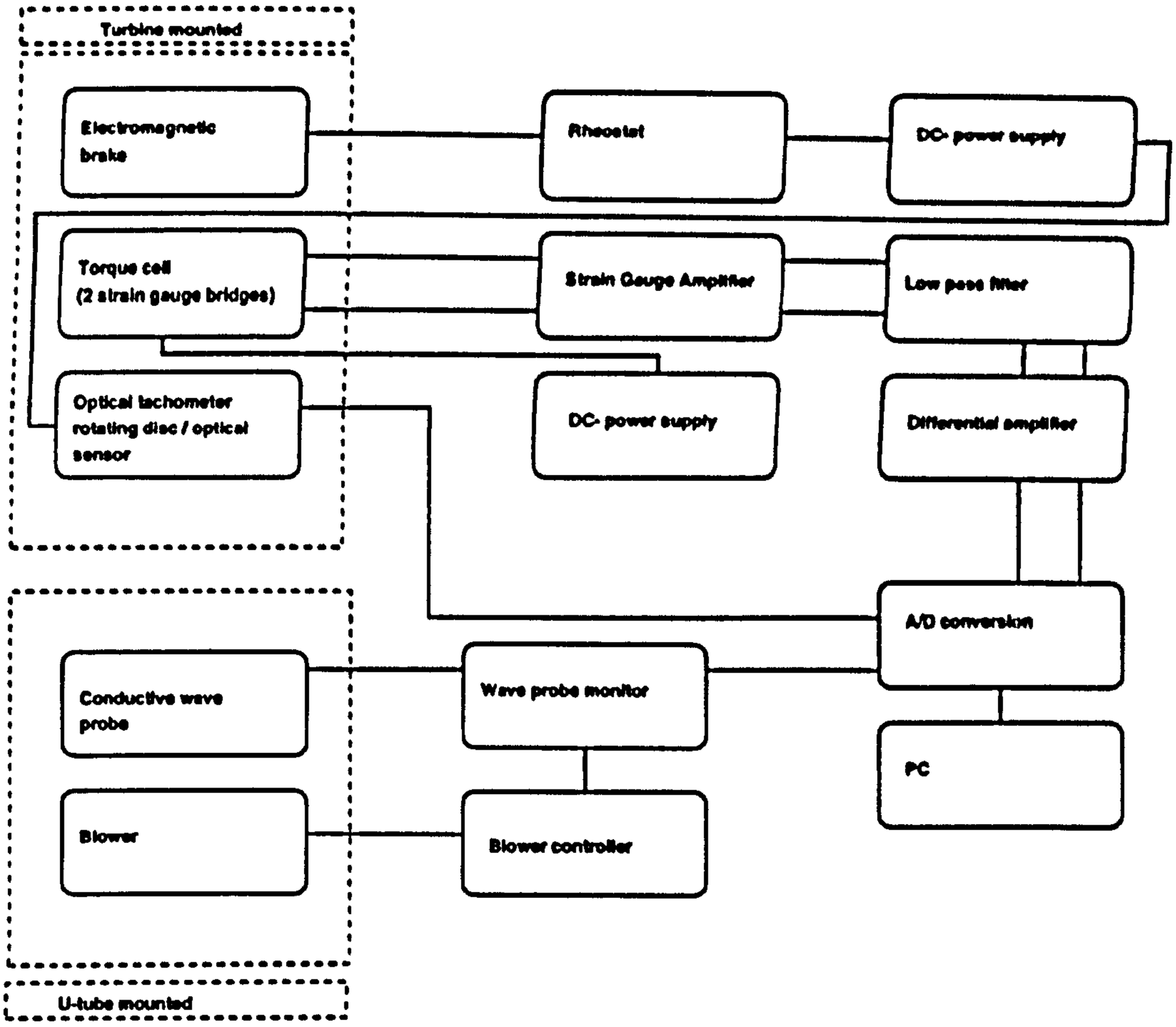

Figure 3.76: Data Acquisition System

conversion hardware. Similarly, the output of the wave probe monitor required no further processing and was connected up to the A/D conversion board.

All data was collected on a 386-Dell PC used in conjunction with Scientific Solutions Inc. 'Labmaster' hardware, which performed the A/D conversion of all signals recorded. An existing FORTRAN code, written and kindly provided for use by P.Mackwood (wind tunnel manager, Aeronautics Department, Imperial College, London) for data acquisition using the same A/D hardware, was adapted to allow sequential scanning of four A/D channels at sampling rates of 1.0[kHz]. In order to obtain information about the phase relation between the fluid oscillation and the variation of rotor RPM, which was important for the validation of the power measurement, all signals were sampled at the minimum frequency required for an accurate RPM measurement using the method outlined above. Since the sampling frequency required was at minimum 0.5 [khz] which is high compared to the frequency of the fluid motion of approximately 0.3 [Hz] relatively large data files were produced over relatively few cycles and the number of cycles captured in one measurement was limited by the working memory of the

computer. The number of cycles over which performance measurements were averaged in this experiment could therefore only be increased by repeating test runs.

The data-acquisition procedure employed in the large water tank testing was identical to that described above for the U-tube experiments and differed only in the measurement of the oscillatory motion as described earlier. However, since, in general, the period of the turbine oscillations was shorter in the large water tank tests the maximum number of data samples allowed a greater number of cycles to be covered in one measurement.

Sequence of Measurements

In the U-tube testing the amplitude of fluid motion and thereby the value of KC was adjusted by manually selecting a supply voltage on the blower controller which was kept constant during a particular test run. With the turbine fixed in the vertical U-tube limb and spinning freely without any applied braking the water motion was monitored until it had reached a constant amplitude. With no applied braking the turbine was self starting for all tested rotor configurations and at all values of KC covered in the water tank experiments. There was no evidence of the so called turbine crawling phenomenon noted by other researchers to occur for ducted Wells turbines in oscillatory flow (e.g Ragunathan (1982)) and the turbine was found to rapidly accelerate to a stable operating regime .

In order to account for any drift of electrical signals from the load cell during the experiment, which in general was noted to be no greater than approximately 1% of the mean load cell output, and to measure the zero torque output a reference reading of both bridge circuit outputs was taken when the turbine was spinning freely in this brake-off condition.

For a constant setting on the blower controller the mean turbine RPM and, therefore, the tip speed ratio (TSR) was then gradually reduced by applying increasing amounts of braking to the turbine shaft. After each increment in braking some settling time was allowed and measurements of water surface elevation, load cell outputs and optical sensor output of the tachometer were taken.

The braking was increased in sequential measurements until the turbine power was insufficient to sustain rotation at a constant mean cyclic RPM. When this point was reached the brake was released so that the turbine was left to rotate freely and a further reference measurement of the load cell output under brake-off conditions was taken.

The amplitude of the oscillating flow was progressively reduced and the above

testing sequence for measuring power at varying TSR repeated until any significant amounts of braking stalled the turbine.

The measurements in the large water tank were carried out analogous to the above procedure for the U-tube tests. A manually controllable signal generator which provided a sine-wave signal was used to operate the driving carriage controller and oscillatory flow relative to the turbine motion was produced at the desired amplitudes and frequencies. Though, in this set-up, there was no oscillating water column, some settling time was allowed for the flow and turbine operation to stabilise between changes in flow amplitude.

Data Analysis

The data acquisition program was mainly used to collect the output voltages of the experimental instrumentation. All data analysis was performed separately on a SUN UNIX workstation after the experiments had been carried out. A FORTRAN 77 code was written to handle all data reduction and analysis required.

The code applied calibration factors to the wave probe and load cell signals to obtain the water displacement in [m] and the brake torque in [Nm] respectively. On the assumption that electrical drift of the load cell signal varied linearly between the beginning and end of the experiment, a mean value was formulated from the time averaged output voltages before and after each test run and included as an offset voltage when applying the calibration to the load cell output. The code transformed the recorded voltage pulses from the optical tacho to 'instantaneous' rotor RPM values according to the method outlined above. For these RPM values the losses due to mechanical friction and fluid forces were calculated from regression curves fitted to the rotor loss data and added to the measured torque. From the variation of the water displacement the code identified the beginning and end of flow cycles. The turbine power was calculated by numerically integrating the product of net torque instantaneous angular velocity over each full cycle. Since time steps were sufficiently small, the integration was performed using the trapezium rule. For each flow cycle average values of Keulegan Carpenter number KC, tip speed ratio Λ and mean cyclic power coefficient $\overline{C_{Pturbine}}$ were calculated according to the following definitions and written to a data file:

$$KC = \frac{U_0 T}{D_t}$$

where, U_0 is the peak velocity of the incident sinusoidal flow, T is the the period of the oscillating fluid motion and D_t is the turbine diameter

$$\Lambda = \frac{U_0}{\hat{U}_t}$$

where Λ is the tip speed ration and $\hat{U}_t$ is the peak tangential velocity at the blade tip.

$$\overline{C_{Pturbine}} = \frac{\overline{P_{turbine}}}{1/2\rho U_0^3(\pi D_t^2/4)}$$

where the definition of $\overline{C_{Pturbine}}$ is consistent with that used in the theoretical performance analysis given earlier .

3.5.4 Experimental Method For Flow Visualisations in Oscillatory Flow

Flow visualisation studies were first carried out in order to gain a qualitative insight into the flow structures which dominate the performance of unducted Wells turbines in oscillating flow.

The turbine used for the tests was a 2-bladed design which had a rotor diameter of 200[mm], a blade chord of 50 [mm] and a spherical hub and is different from the turbine designed and built for the shaft power experiment. It is shown in figure (3.77) below and was rigged in the horizontal working section of the U-tube water tank and left to rotate free of any applied shaft loads.
A Spectra Physics 5W continuous wave argon ion laser was used together with a set of optical lenses to produce a planar sheet of light perpendicular to the plane of rotation. Figure (3.78) shows the schematised set-up. From this it can be seen that the flow images presented in the following show the turbine in side view with the light sheet illuminating the flow in vertical plane along the shaft axis of rotation.

Initially, no particles were added to the water since the laser was powerful enough to cause the light reflection of the microscopic impurities 'naturally' contained in the (industrial) water to be sufficiently strong for the purpose of flow visualisation. Provided that these particles were near neutrally buoyant in water they can be assumed to travel approximately in the direction of the local flow and at the local flow velocity. These particles produced surprisingly good flow images shown in figures (3.79) - (3.84), which were documented using a video camera operated at a recording rate of 1/50 [sec]. In subsequent testing polystyrene particles of sizes up to around 500 [μm] were added. These, though having high reflectivity did not produce as good results. Also, they were not found to be

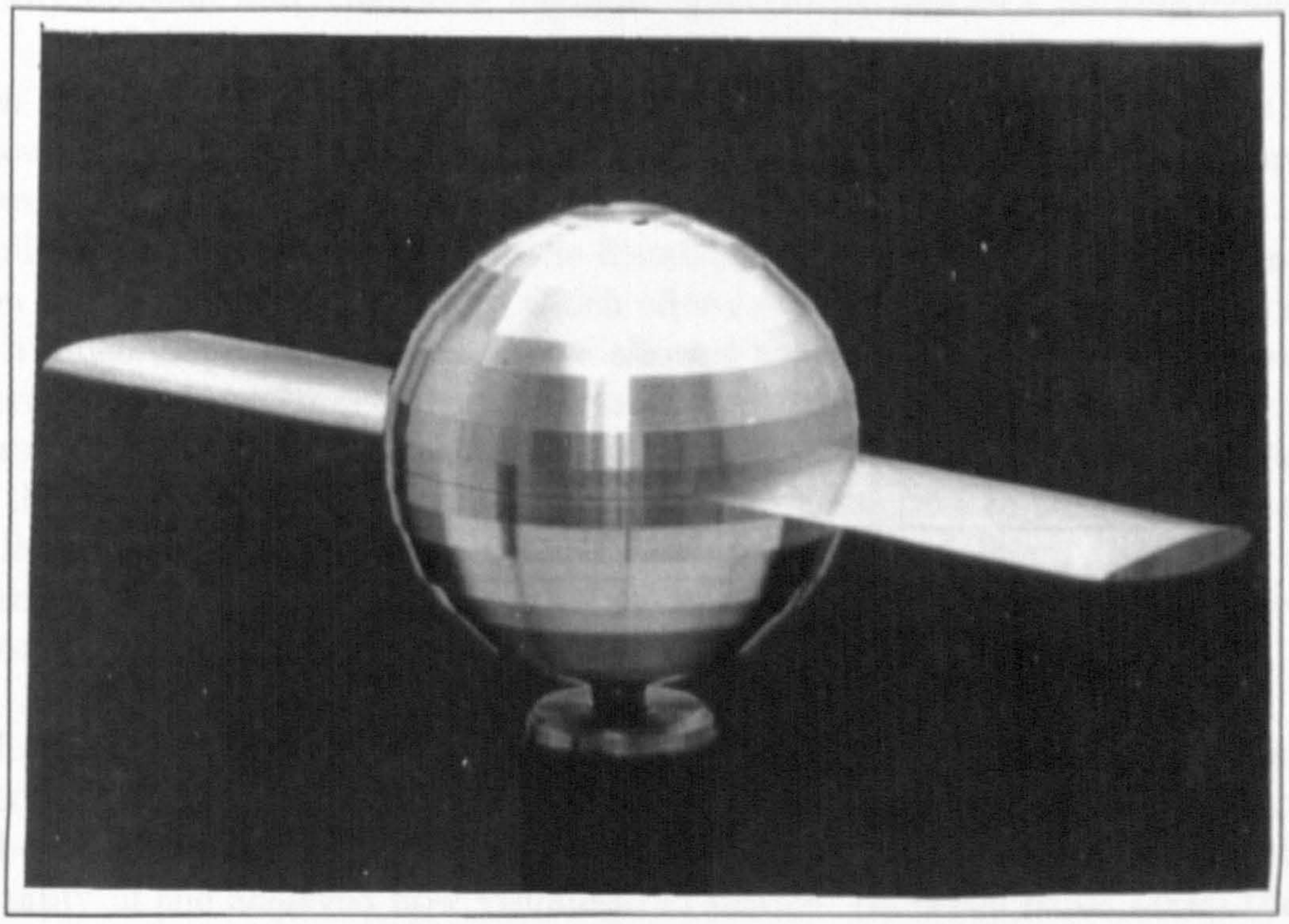

Figure 3.77: 2 Bladed Wells Turbine For Flow Visualisation Experiments

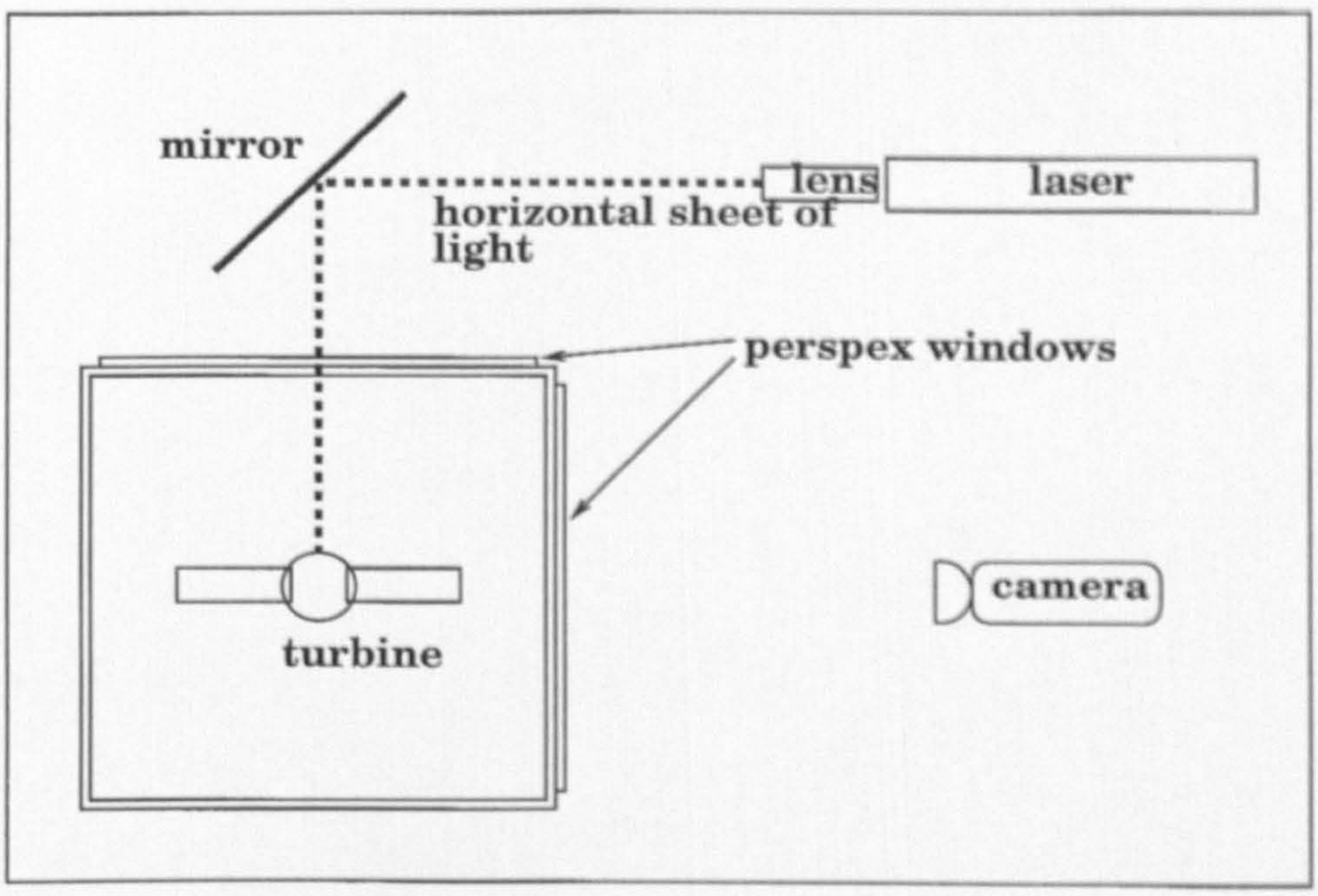

Figure 3.78: Experimental Set-Up For Flow Visualisation

neutrally buoyant and, therefore, distorted the flow pattern to a notable extent.

On the assumption of flow symmetry on two sequential flow half cycles of the flow the wake features were recorded only on one side of the rotor. Recordings were taken over a large number of flow cycles. The images presented in the following were produced using the frame-grabbing program 'VPANEL' on a Silicon Graphics Indy workstation which allows snapshot-images to be produced from a video recording. This software allowed the moving image to be paused and produced streak lines since the paused image was composed of a number of successive frames. As a result these streak lines illustrate the particle paths. Further, the streak lines are in proportion to particle velocities so that long streak lines indicate areas of high velocities. In the images shown below the length of the produced streak lines, therefore, allow -at least qualitatively- the relative velocities of free stream and wake flow to be judged.

The produced postscript files which are presented in the figures below were printed on a laser printer. There was a notable drop in the quality of the images between postscript files and hard copies which, unfortunately, do not do the quality of the achieved flow visualisation justice. (It needs to be noted that the circular dark mark in the plane of rotation is a sealing plug inserted in the perspex window)

Figure 3.79: Flow Visualisation

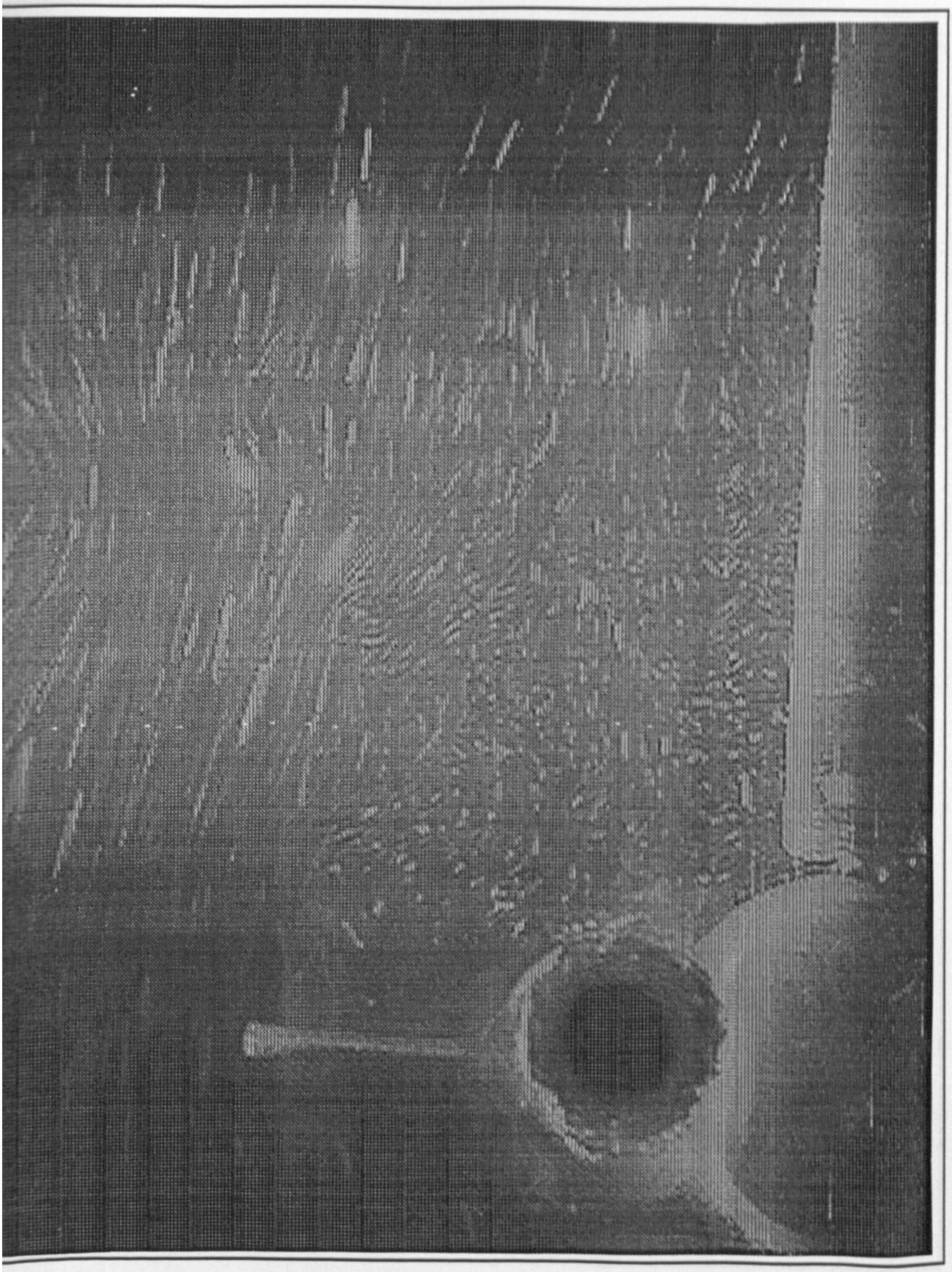

Figure 3.80: Flow Visualisation

Figure 3.81: Flow Visualisation

Figure 3.82: Flow Visualisation

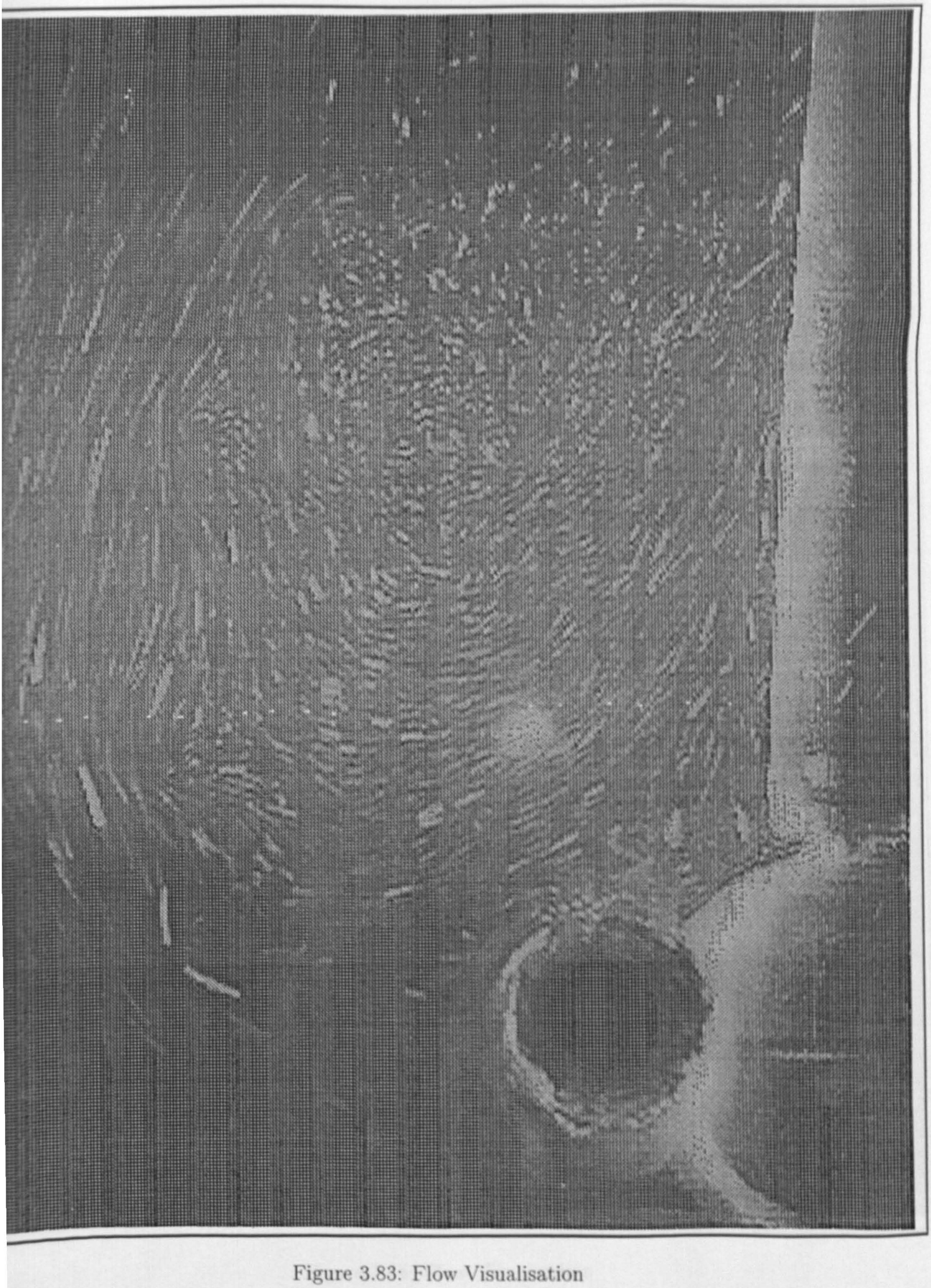

Figure 3.83: Flow Visualisation

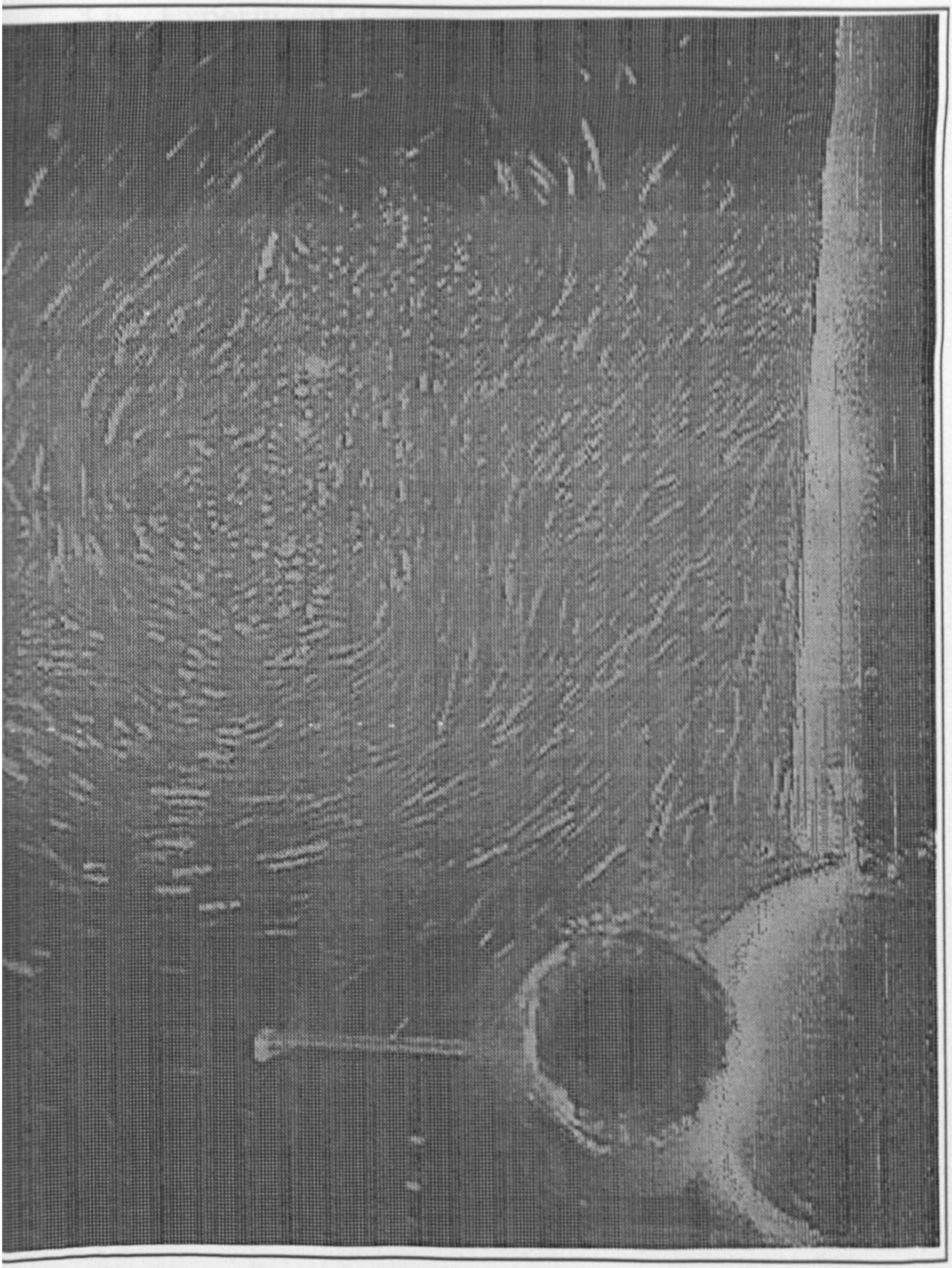

Figure 3.84: Flow Visualisation

3.6 Experimental Results

3.6.1 Flow Visualisation

Though, recordings were taken over a larger number of flow cycles, it was apparent that the turbine wake attained a fairly stable structure after a remarkably low number of flow cycles after the turbine was started. The results shown in figures (3.79) - (3.84) were achieved for an estimated KC of approximately 5.5. It was attempted to produce flow images at lower KC, but subsequent to previous power measurements using the turbine the bearings had become so corroded that they did not allow self-sustained rotation below KC=5.5 .

Notable in (3.79) - (3.82) is a strong concentrated vortex ring just above the blade tip. This has been carried over from the upstream side of the rotor and is convected with the mainstream outside the wake flow. It seems to significantly affect the convection of the helical vortex filaments formed from the vorticity which is shed at the blade tips on the downstream side of the rotor (see especially (3.81)&(3.82)). Apart from the concentrated vortex ring the most defining flow features visualised in the early stages of the documented flow half cycle are the tip vortex filaments which suggesting that the shed vorticity is highest in this region.

In figure (3.82) it can be noticed that the vortex spirals of the helix are not equally spaced. The stream wise distance between them is significantly less close to the rotor than further downstream. This is partly due to the varying RPM of the rotor but may also be an indication of the influence of the larger vortex ring which has now moved downstream. At this point the convection of the vorticity tied up in the wake vortex filaments has reached its maximum stream wise extent, which by inspection is estimated to be approximately 70% of the turbine diameter. The maximum stream wise distance that the newly shed vorticity convects away from the rotor before the free stream reverses flow direction $\hat{x}$ may be related to the KC number of the flow. In the illustrated case above the ratio of $\hat{x}$ to the flow amplitude is around 0.8 .

As the large vortex ring convects further downstream the helical wake structure close to the rotor becomes less affected (3.83). When towards the end of the first half of the flow cycle the free stream velocity decreases, locally induced velocities of the helix, which now has more uniformly spaced spirals, evidently become significant and it begins to roll up into a single vortex ring (3.84). This now becomes the dominant flow feature.

As the flow direction reverses this vortex ring radially expands and is swept back towards the rotor. Subsequently, the vortex ring becomes more concentrated

and is convected downstream on the opposing side of the rotor.

The results of the flow visualisation clearly show that over a significant period of the flow cycle the wake roll-up is a defining feature of the moderate KC oscillatory flow around an unducted Wells turbine. As such the flow visualisation carried out indicates that, in principle, approximation of the wake flow by a concentrated vortex ring chosen in the numerical analysis is not too far removed from the physical flow.

Further, the results indicate that the shed vorticity is significantly strongest at the blade tips. This suggests that, especially when the turbine is operating at high tip speeds, for small KC flows there may be a certain similarity to small KC oscillatory flows past discs as documented by de Bernardinis (1980) which have fairly distinct shedding sheets emanating from their edges.

The flow visualisation above showed that maximum stream wise convection of the shed vorticity on one half of a flow cycle is around 80 % of the flow amplitude. By comparison, the results of computations using the improved numerical model, which were carried out for a KC of 3.0 and are shown in figures (3.53) - (3.53) of the previous report section showed that the maximum stream wise distance the centre of the vortex rings convects is about 95 % of the flow amplitude which, qualitatively, is considered to be in fair agreement.

The above flow visualisation does not explicitly document the flow development on both sides of the rotor and thus does not really allow any conclusive comments about the extent of flow symmetry of two sequential half flow cycles. However, for the case illustrated it is evident that there is no pairing of the concentrated vortex rings formed on two successive halves of a flow cycle. In fact it is apparent that at moderate KC number flows when the concentrated vortex rings are swept over the rotor subsequent to flow reversal their rate of convection is such that they overtake the wake on the other side before it has entirely rolled up into a concentrated vortex ring. From the evidence of the flow visualisation, therefore, the unsymmetrical flow structure shown in the computations seem unrealistic.

For smaller KC number flows the roll-up process of the wake helical vortex filaments may be somewhat stronger than for the moderate KC number flows since the individual spiral vortex filaments are more closely spaced due to the comparatively reduced rate of convection. In this case the idealisation of the wake flow as a concentrated vortex ring used in the numerical model is considered to be quite good and the wake behaviour at small KC is thus more realistically modelled by the interaction of discrete vortex rings than at moderate KC. Unfortunately, the flow visualisation experiment was not carried out at smaller KC so that the

likelihood of sequentially formed vortex rings convecting away from the rotor as a pair which was indicated as a possible flow structure by the numerical model can only be speculated on. It may, however, be concluded that since the pairing up process shown in computations is evidently driven by the strong mutual influence of the concentrated vortex rings, which may be less dramatic when the shed vorticity is more spread out, the probability for a physical wake flow of this nature to occur is higher for small KC flows than for moderate KC flows.

3.6.2 Power Measurements

In the following some typical results of the basic quantities defining the turbine performance as measured in the U-tube water tank are presented to illustrate the experimental method and the turbine behaviour.

Figure (3.85) below shows the variation of the water column displacement $z(t)$ in [m], blade tip velocity $U_t(t)$ in [m/s] and turbine power $P(t)$ in [W] measured in the U-tube, for the 4-bladed rotor operating at a KC of 7.0 through 2 full flow cycles. The tip speed ratio which was achieved for a fairly low brake setting and was estimated from peak values of the measured rotor tip speed $\hat{U}_t$ and the peak incident flow velocity U_0 for the presented case is approximately 4.5 . Due to the action of the flywheel the oscillations of the tip speed $U_t(t)$ which can be seen to vary in near perfect phase with the flow velocity $U(t)$ of the oscillating water column, were limited to approximately 7% of the mean cyclic tip velocity which was measured to be constant. There is an indication of slightly asymmetric variation of $U_t(t)$ on the upward and downward strokes of a flow cycle which may be caused by the interference between the convected rotor wake and the free surface of the water column at the measurement point or by the effect of the rotor resistance on the oscillating water column.

The variation of $P(t)$ produced by the turbine/flywheel system is computed from the product of the measured instantaneous angular velocity $\Omega(t)$ and the corresponding total rotor torque $T_{rotor}(t)$, which is shown separately in figure (3.86) and consists of the braking torque measured by the two load cell bridges added to the rotor losses determined in the deceleration tests. The contribution of the fluid and friction losses cause a fluctuation of T_{rotor}, which is in phase with $U_t(t)$.

Notable in figure (3.86) are distinct peaks of T_{rotor} which occur at a frequency corresponding to the rotor RPM. These are due to a slight misalignment of the brake rotor and stator which during testing caused the applied braking torque to vary through a full cycle of shaft rotation. Unfortunately the type of friction braking used is very sensitive to alignment causing the non-uniform response

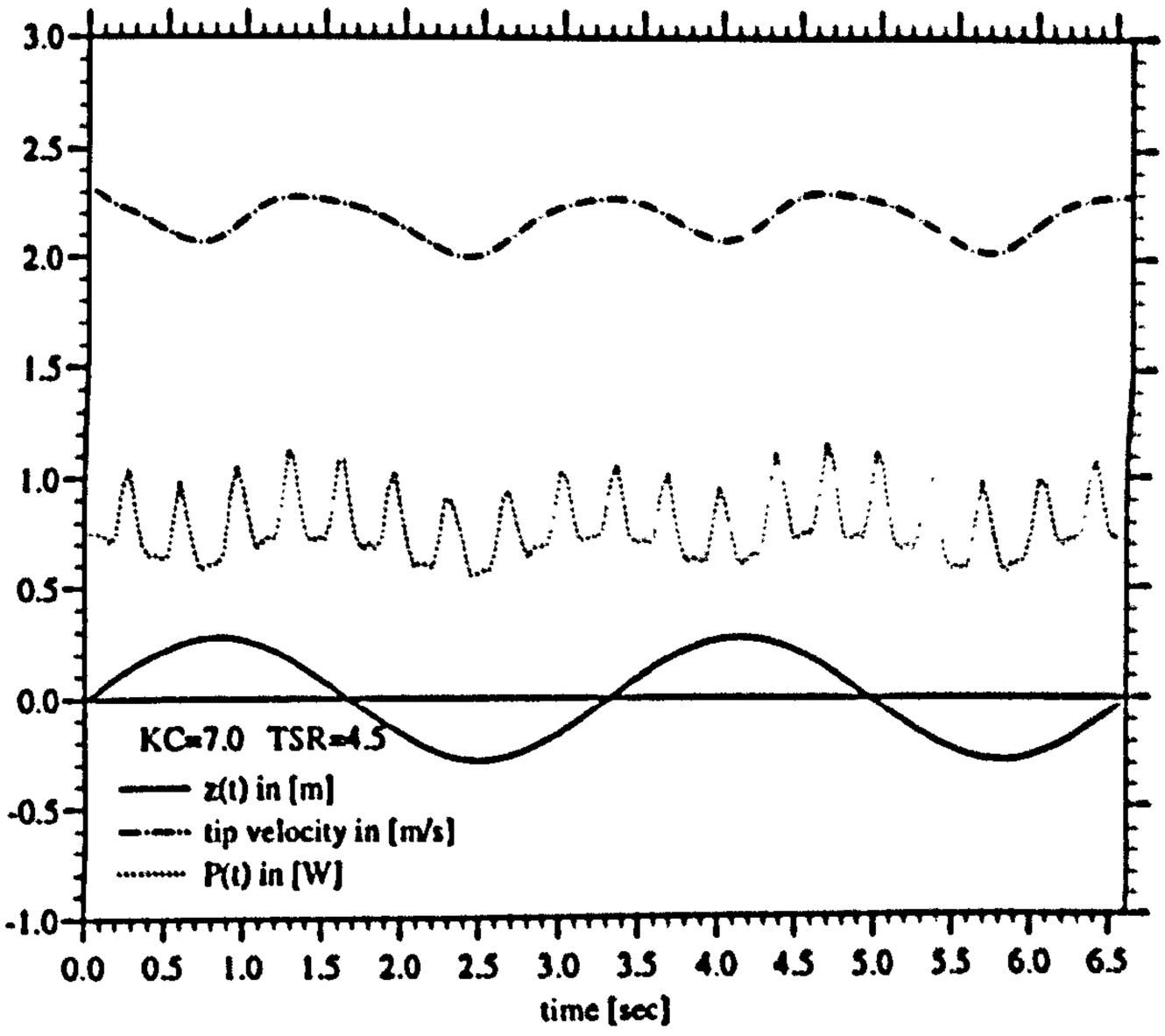

Figure 3.85: Measured Time Variation of $z(t)$, $U_t(t)$, $P(t)$

, which resulted from the circumferentially uneven contact surface between the brake rotor and stator. Some attempts were made to rearrange the brake so that a more uniform braking action could be achieved. However, within the limitations of the experimental apparatus designed these attempts were unsuccessful. In part the problem was accentuated by the small amounts of braking that could be applied in the experiment so that the brake rotor was not worn in to great enough an extent to self-rectify the problem. It was found that, nevertheless, that in spite of the resulting 'jerky' brake action the rotor did maintain a mean rotational speed which was constant over a flow cycle. The problem did, therefore, not fundamentally disqualify the experimental method. It did however mean that in the measurements the load cell signal needed to be sampled at high enough a frequency to record the torque fluctuations.

The deviation of the cyclic mean turbine power $\overline{P}_{turbine}$ between the successive flow cycles shown is around 1.5% which is a representative value for measurements carried out at low brake settings. For the measurements in which larger amounts of braking were applied the variation of $\overline{P}_{turbine}$ between flow cycles increased typically to around 8% for the 4-bladed rotor, which to some extent was due to the uneven brake action.

For the measurement shown in figure (3.86) the mean cyclic loss torque due to

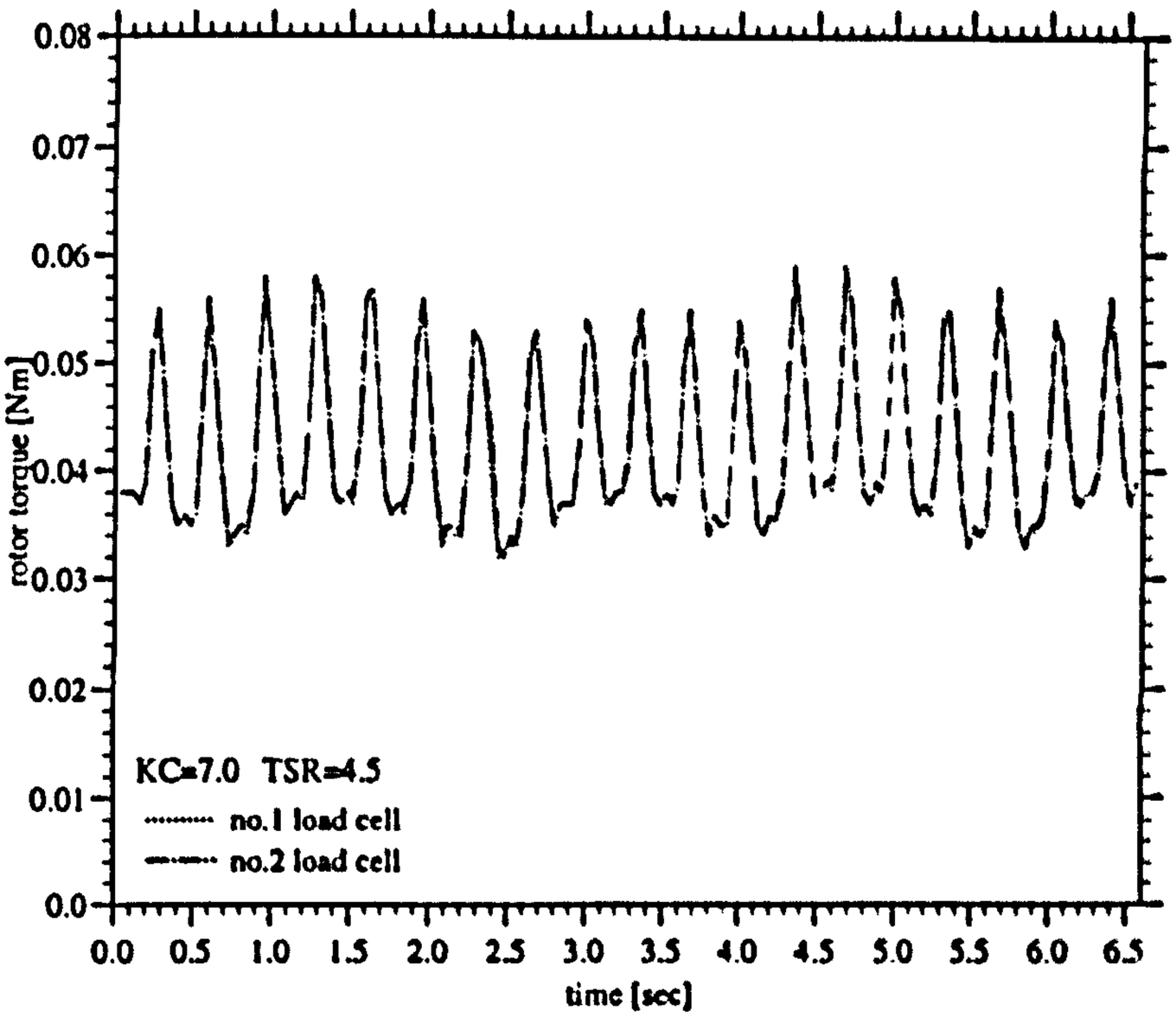

Figure 3.86: Measured Torque $T(t)$

mechanical friction and rotor drag losses estimated in the deceleration test measured approximately 77 % of T_{rotor}. This indicates the sensitivity of the measured $P(t)$ and, therefore, the deduced mean cyclic power coefficient $\overline{C_P}$ at higher rotational speeds to fluid losses which at typical test RPM are significantly greater than the mechanical friction of the device.

Figures (3.87) and (3.88) show the variation of $z(t)$, $U_t(t)$,$P(t)$ in respective units and T_{rotor} in [Nm] for the 4-bladed rotor operating at a KC of 4.0 and a tip speed ratio of 4.0, which was achieved for a higher amount of applied braking torque. Peak values of $U_t(t)$ vary by approximately 6% from the cyclic mean value which is similar in extent to the higher KC case considered above. The magnitudes of $\overline{P}_{turbine}$ derived for the two sequential flow cycles shown varied by 5%. For this particular measurement the mean loss torque was estimated to be around 47% of T_{rotor}, which is a somewhat smaller proportion than at the larger KC but still a significant proportion of the overall torque. It is evident, therefore, that the degree to which the estimated power depends on the fluid losses varies strongly with KC and the amount of applied braking.

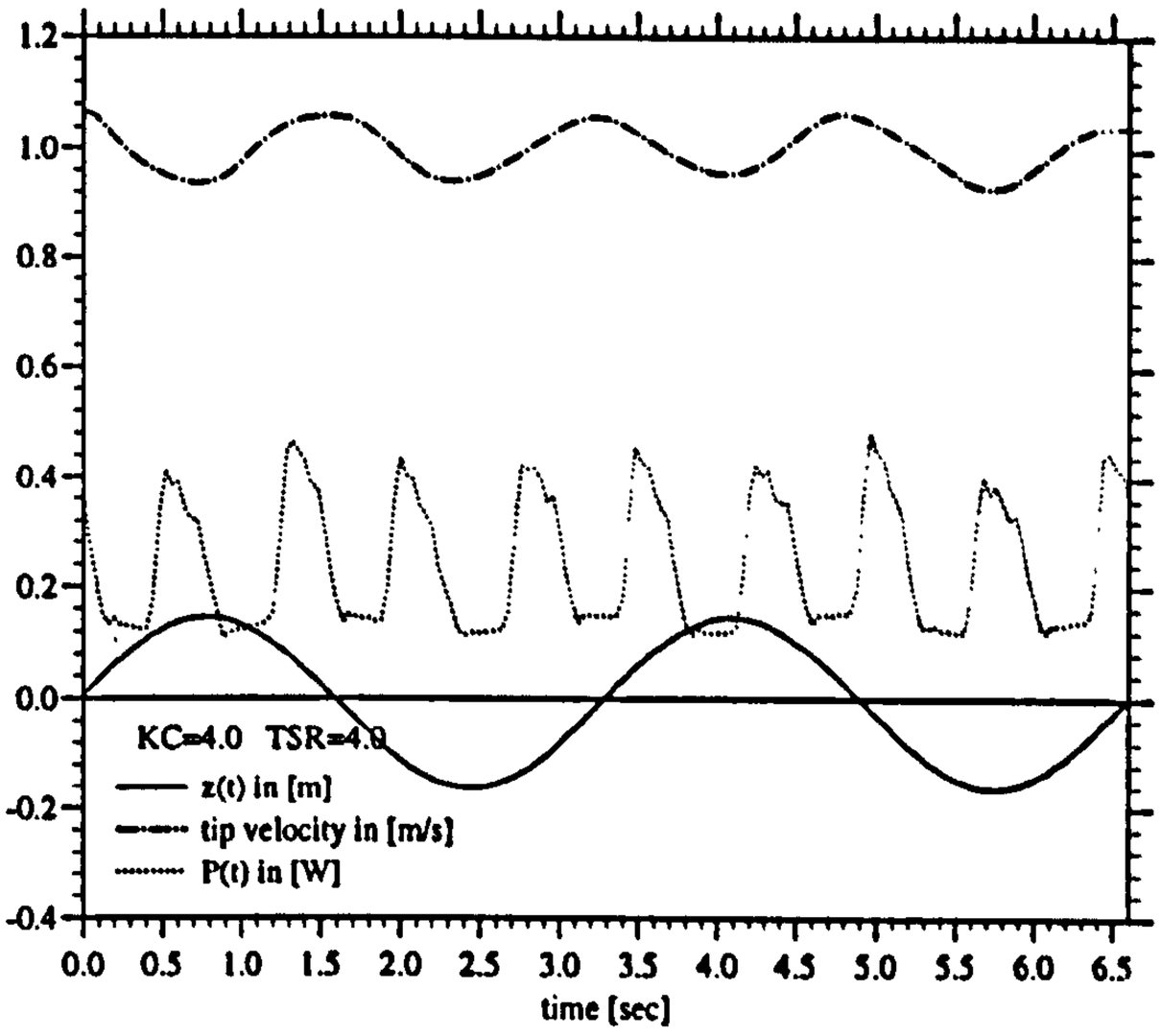

Figure 3.87: Measured Time Variation of $z(t)$, $U_t(t)$, $P(t)$

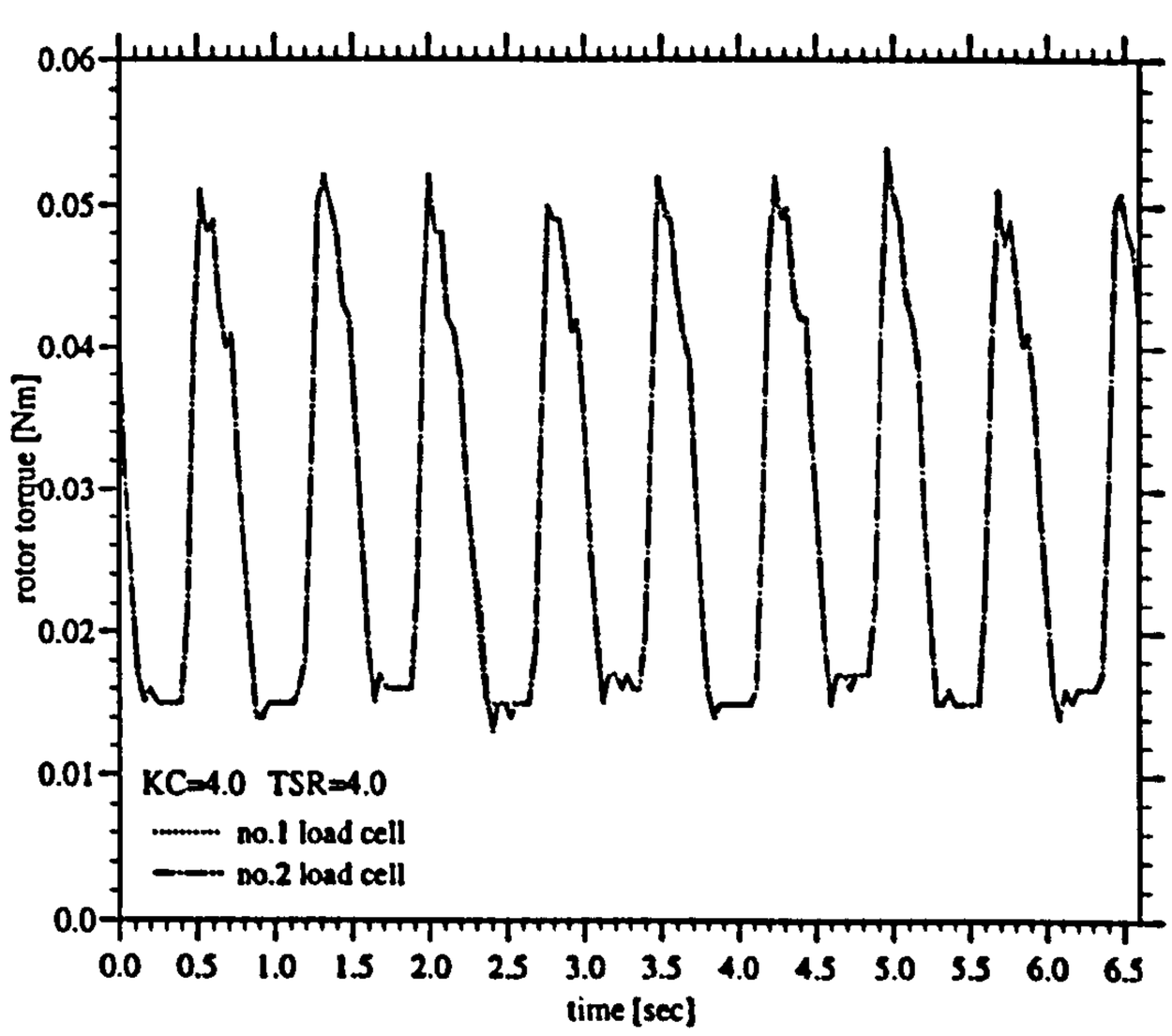

Figure 3.88: Measured Time Variation of $T(t)$

Figures (3.89) - (3.91) show the variation of the mean cyclic power coefficient $\overline{C_P}$ with tip speed ratio Λ at different values of KC calculated for the three different rotor configurations which were tested. The data shown was derived from the power measurements carried out in the U-tube water tank by averaging the values of $\overline{C_P}$, individually formulated for each flow cycle, over the number of cycles of a particular measurement.

The highest values of Λ achieved in the tests corresponded to the lowest brake setting and it it evident that the 2 and 3-bladed rotors tended to operate up to a higher maximum value of Λ than the 4-bladed rotor. The largest amount of applied braking for which the turbine maintained rotation at an invariant mean cyclic rotational speed produced the lowest values of Λ for which data is shown. It is, therefore, unlikely that at the lowest values of Λ the rotor is completely stalled over a significant portion of the flow cycle for any of the data points shown in the above figures. Full rotor stall was usually fairly evident in the experiment since the rotor visibly decelerated to a complete stand still.

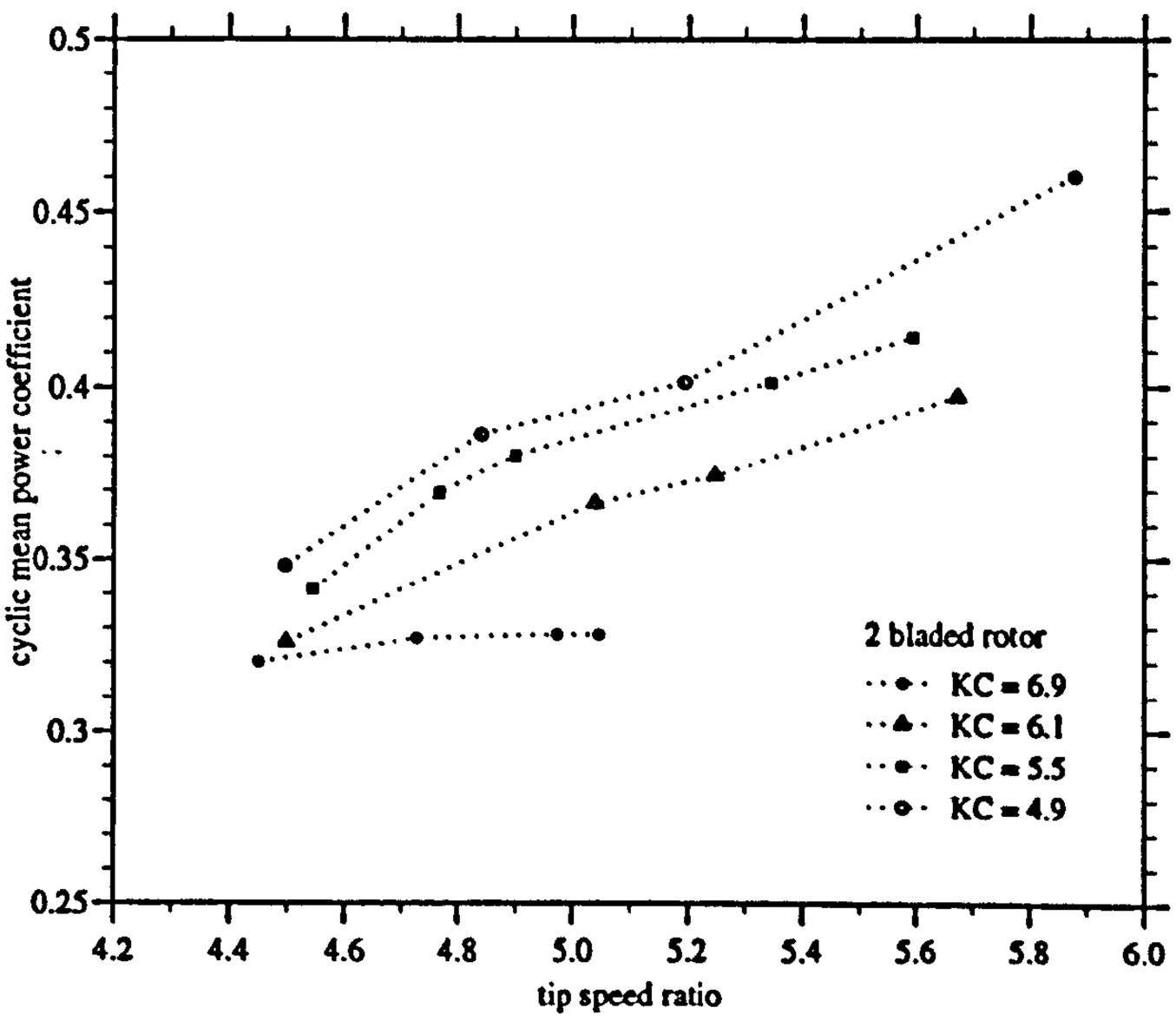

Figure 3.89: Measured $\bar{C}_P$ vs. Λ For 2-Bladed Rotor

At the largest value of KC shown the upper limit for Λ recorded for the 2-bladed rotor was limited because the RPM was too high to be reliably recorded to acceptable accuracy by the implemented technique of RPM measurement. The data presented for the 4-bladed rotor suggests that for the KC values tested between 7.2 and 5.9 the turbine performance was not a strong function of Λ in the

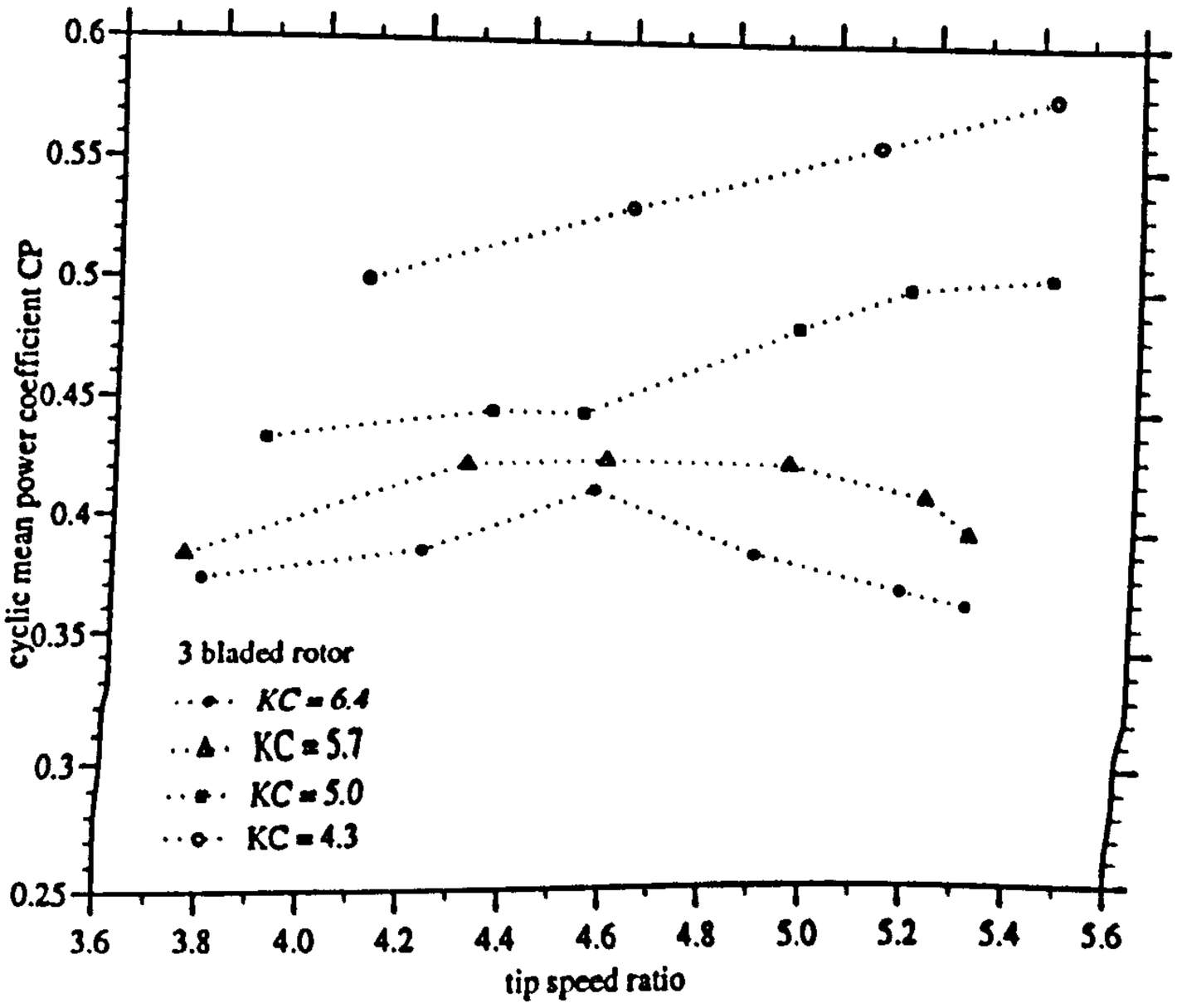

Figure 3.90: Measured $\bar{C}_P$ vs. Λ For 3-Bladed Rotor

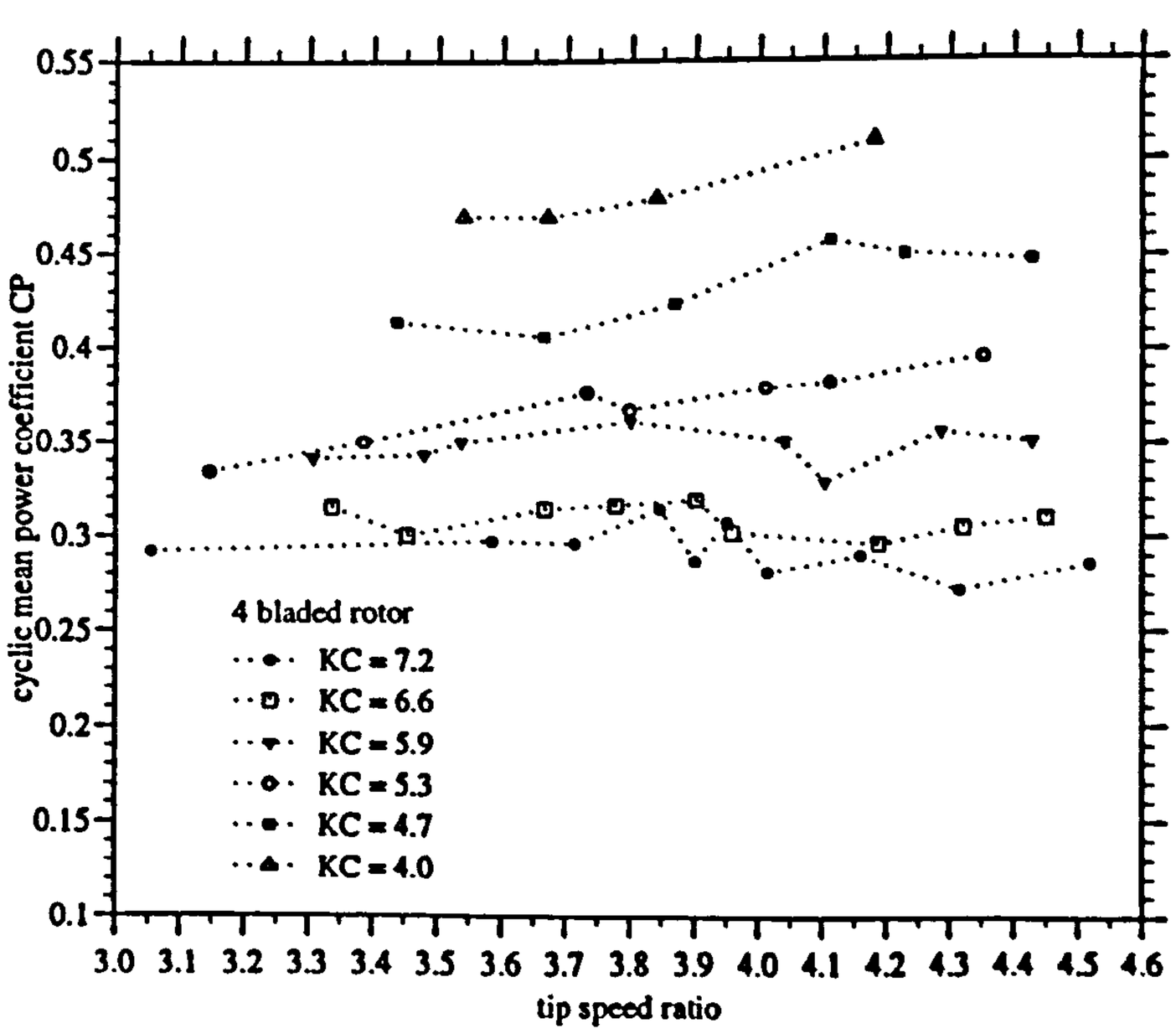

Figure 3.91: Measured $\bar{C}_P$ vs. Λ For 4-Bladed Rotor

experimentally documented range. For the smaller KC values shown the data shows a stronger dependency on Λ and to a first approximation $\overline{C_P}$ may be considered to vary near linearly with Λ over the range covered in the experiment. $\overline{C_P}$ data shown for the 3-bladed rotor suggests that for the larger values of KC explored the turbine actually operated at tip speed ratios for which the turbine efficiency is near optimum, which in the following denoted as Λ_{opt}. In the illustrated measurements at smaller KC the achieved values of Λ are evidently somewhat lower than Λ_{opt}. For the 2-bladed rotor the range of KC flows experimentally studied in the U-tube was somewhat limited since at low KC the amount of energy converted from the flow was too small to allow measurements which comprised reasonable amounts of applied braking. The data of figure (3.89) recorded in the KC range between 4.9 and 6.1 which shows relatively large $\partial\overline{C_P}/\partial\Lambda$ at all values of Λ suggested that the operational tip speed ratios recorded were in all cases below Λ_{opt}.

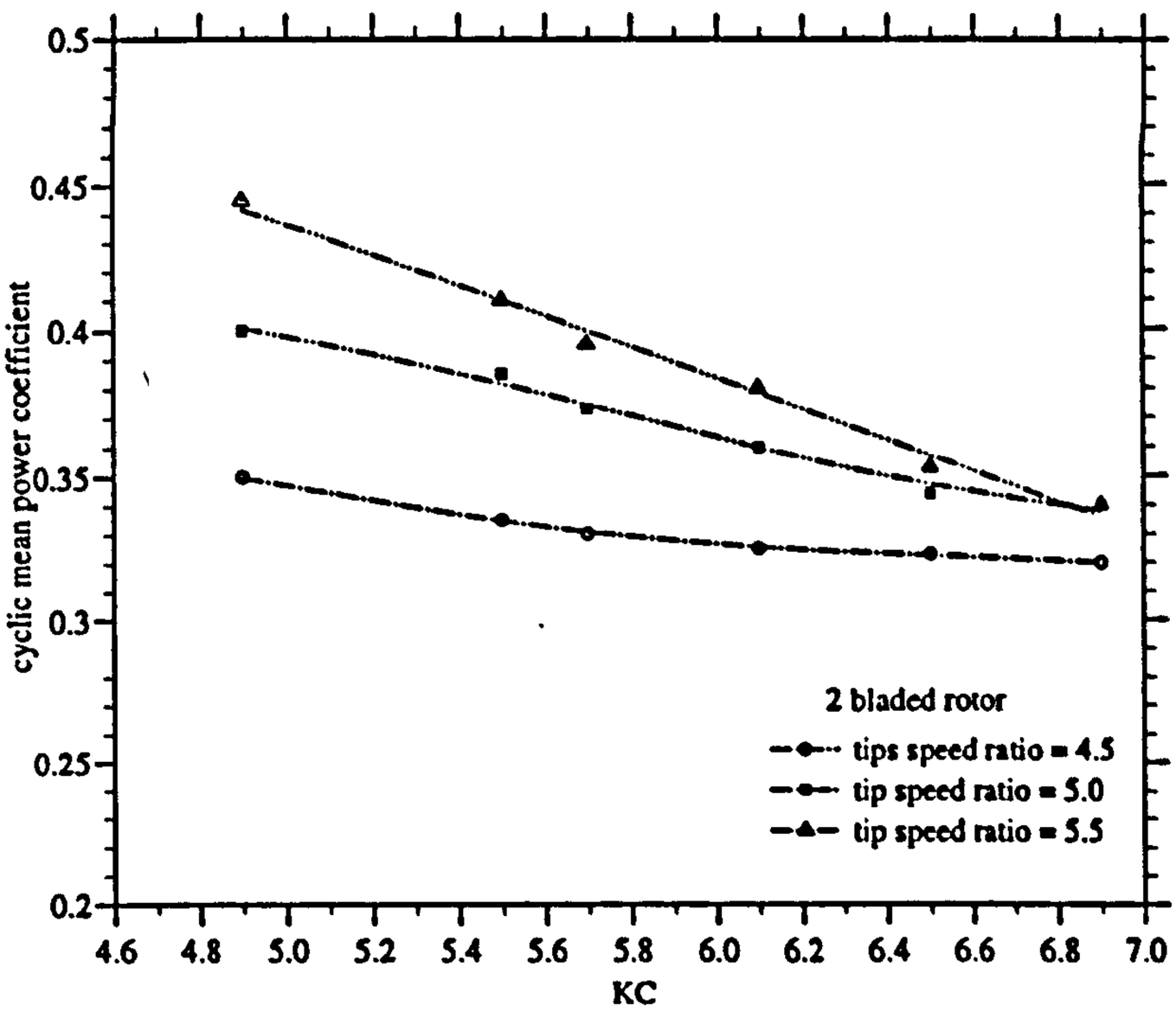

Figure 3.92: Measured $\bar{C}_P$ vs. KC For 2-Bladed Rotor

The curves presented above were interpolated to allow the measured $\overline{C_P}$ data to be studied as a function of KC at different tip speed ratios. Figures (3.92) - (3.94) show the resulting variations for the 3 tested rotors. The graphs for all rotor configurations show a clear increase in $\partial\overline{C_P}/\partial KC$ with Λ. The illustration gives emphasis to the observation that at the smaller values of test KC the rotors were operating below maximum efficiency.

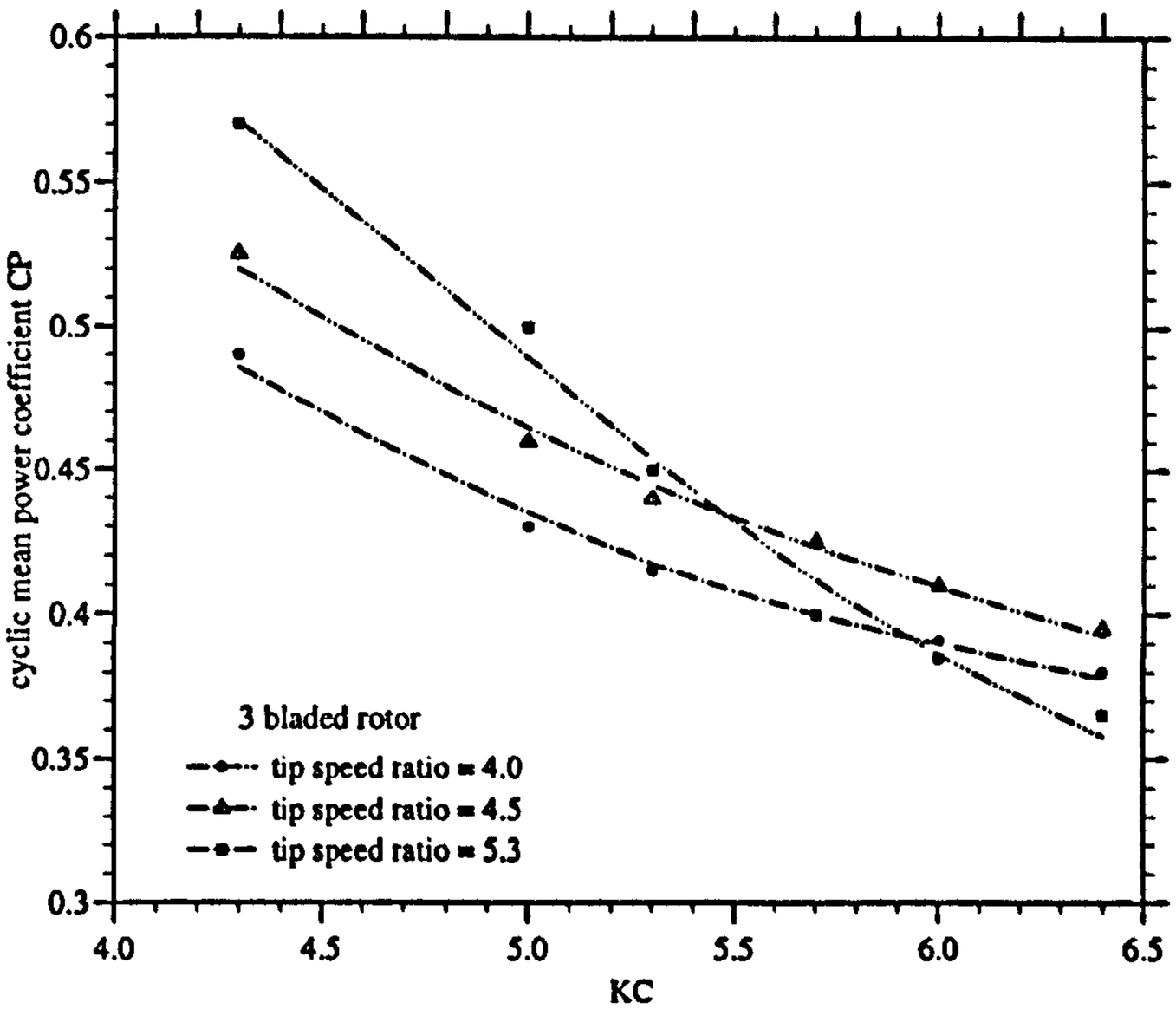

Figure 3.93: Measured $\bar{C}_P$ vs. KC For 3-Bladed Rotor

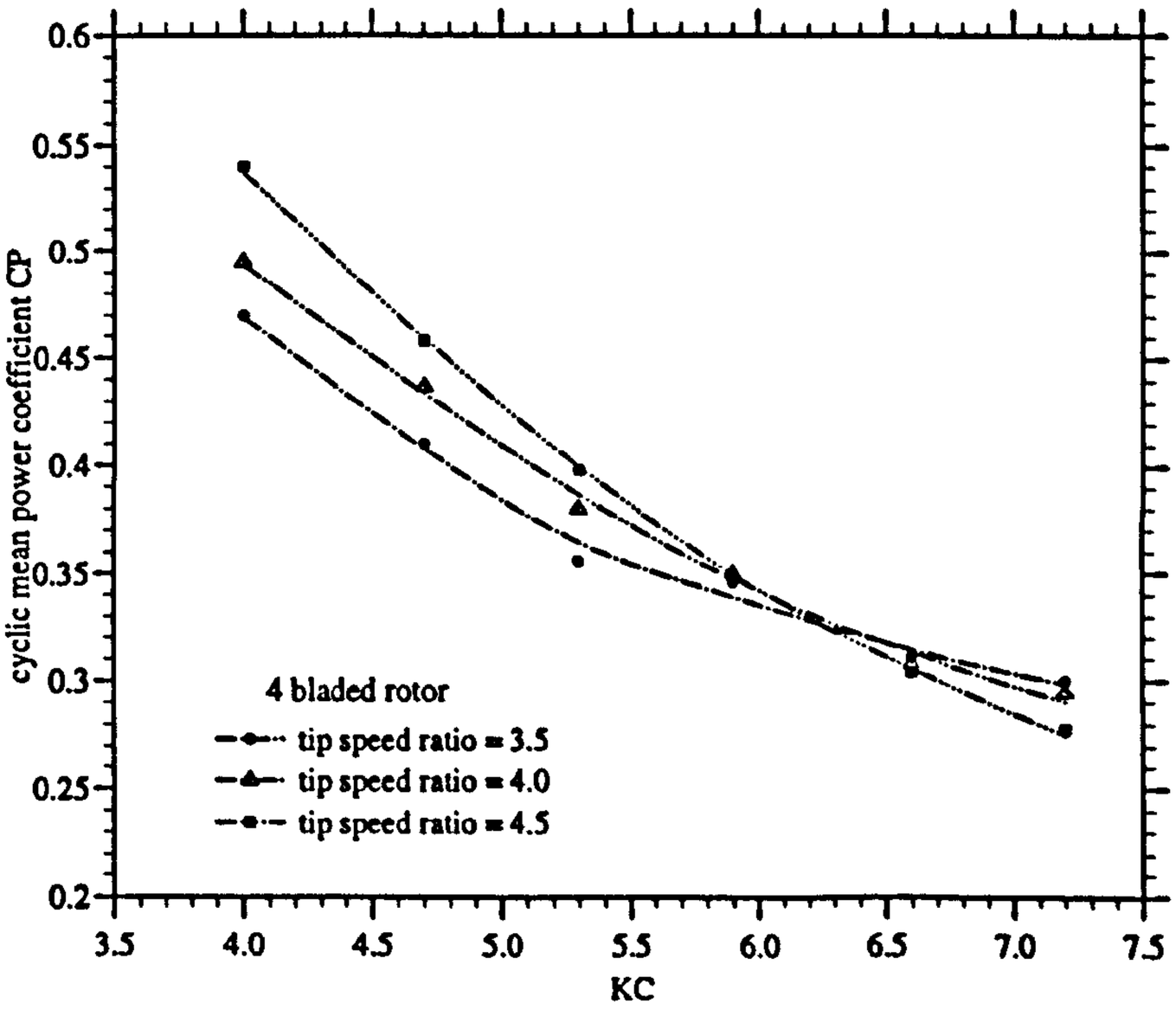

Figure 3.94: Measured $\bar{C}_P$ vs. KC For 4-Bladed Rotor

Clearly, the achieved experimental range of KC and Λ which are the main operational parameters influencing the turbine performance was limited in the U-tube water tank because of the fairly small amounts energy available to the turbine in the flow. Especially for the smaller KC flows the available energy was insufficient for the rotor to sustain rotation against turbine losses and applied braking to an extent that allowed meaningful variation of tip speed. The main restriction in this sense was the fact that in the U-tube water tank the frequency of the oscillation was fixed at the natural frequency of the contained water volume and thus the flow speed could not be increased for any given value of KC.

As described earlier the frequency of the oscillatory motion of the turbine in the large water tank experiments was controllable and could be set considerably higher than the value in the U-tube. It thus could be chosen at each set amplitude so that a reasonable amount of braking could be applied before the turbine stalled. In particular, therefore, the tests carried out in the large water tank were aimed at obtaining data at small KC values which could not be studied in the U-tube water tank. As seen in the following data was recorded at KC values as low as 1.6, which is a flow regime that may be much more interesting to applications of large scale devices operating in real wave flows.

Figures (3.95) - (3.97) show the $\overline{C_P}$ data determined from measurements for the three tested rotor configurations as a function of Λ.

It is evident that in comparison to the tests carried out in the U-tube water tank the turbine could be driven to higher values of Λ. This is due to the higher frequency of the oscillations generated in the large water tank which for a given value of KC cause more energy to be stored in the flywheel. Since the magnitude of applied braking torques in this set-up is comparatively larger than in the U-tube experiments and $\overline{C_P}$ is obtained as an average over a greater number of flow cycles the data scatter is visibly reduced. Considering figures (3.95) - (3.97) it can, in general, be said that the water tank tests give a much clearer indication of Λ_{opt} and the corresponding maximum power coefficient $\overline{C_{Pmax}}$. It may be observed that for all tested configurations Λ_{opt} as well as $\overline{C_{Pmax}}$ are functions of KC.

Figures (3.98) - (3.100) show the variation of $\overline{C_P}$ with KC for a number of different Λ. A non-linear dependency is evident particularly at high tip speeds in small KC flows.

Importantly, it may also be noted that for small values of KC values of $\overline{C_P}$ greater than unity were measured. This qualitatively supports the results of the numerical analysis given earlier, which showed that theoretically cyclic power coefficients greater than unity may be expected in small KC flows.

In order to ascertain any frequency dependency of the experimental $\overline{C_P}$ data

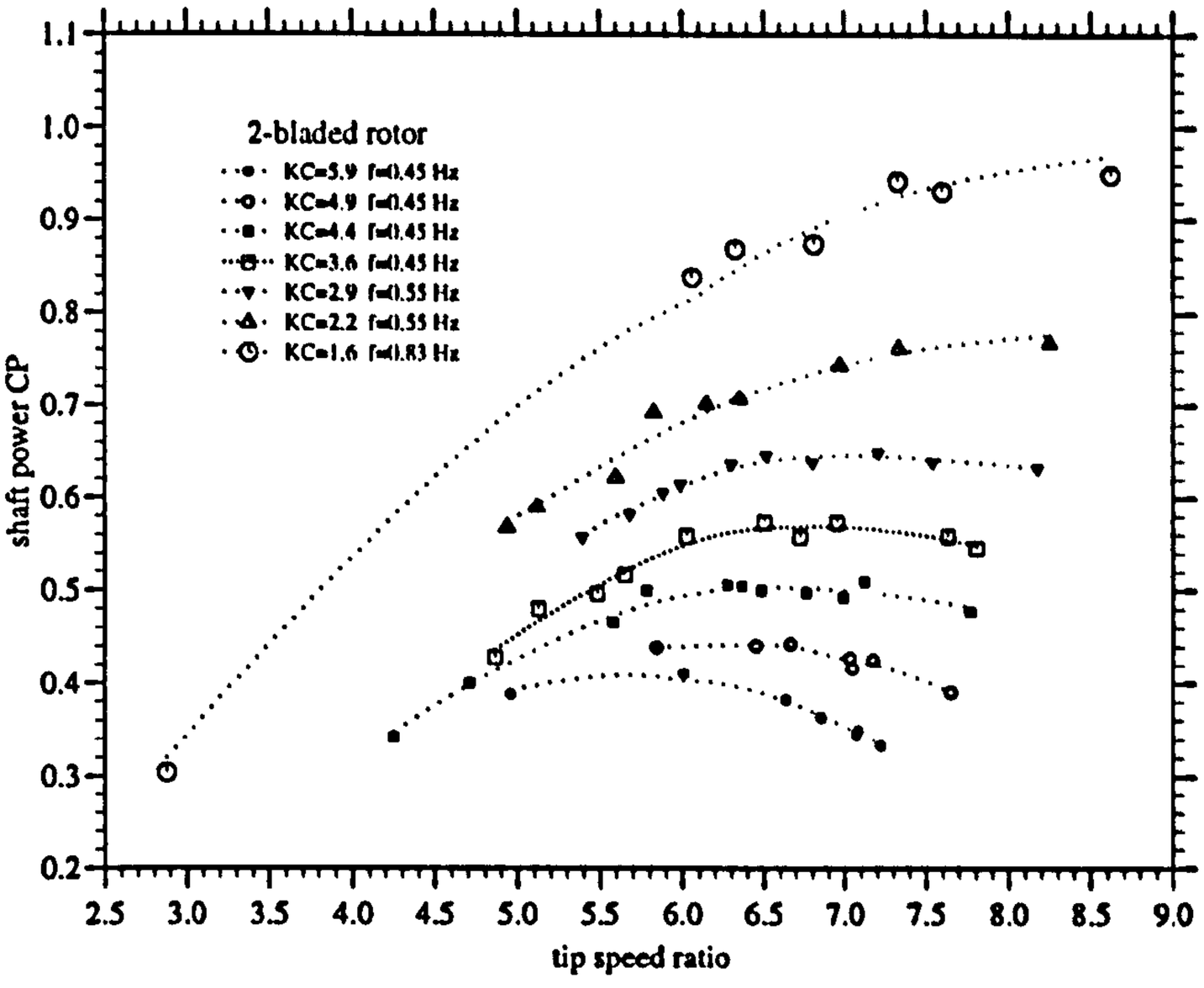

Figure 3.95: Measured $\bar{C_P}$ vs. Λ For 2-Bladed Rotor

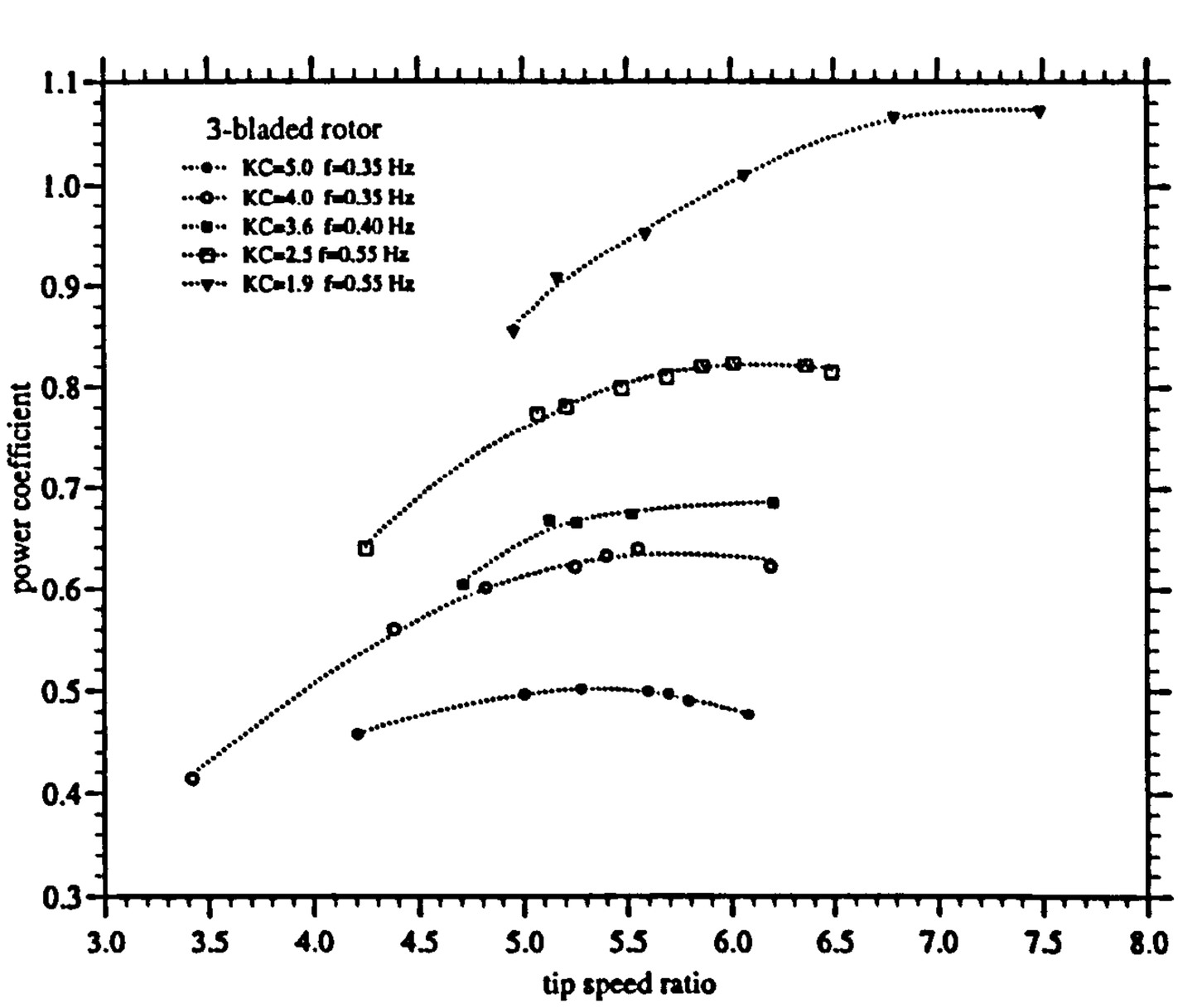

Figure 3.96: Measured $\bar{C_P}$ vs. Λ For 3-Bladed Rotor

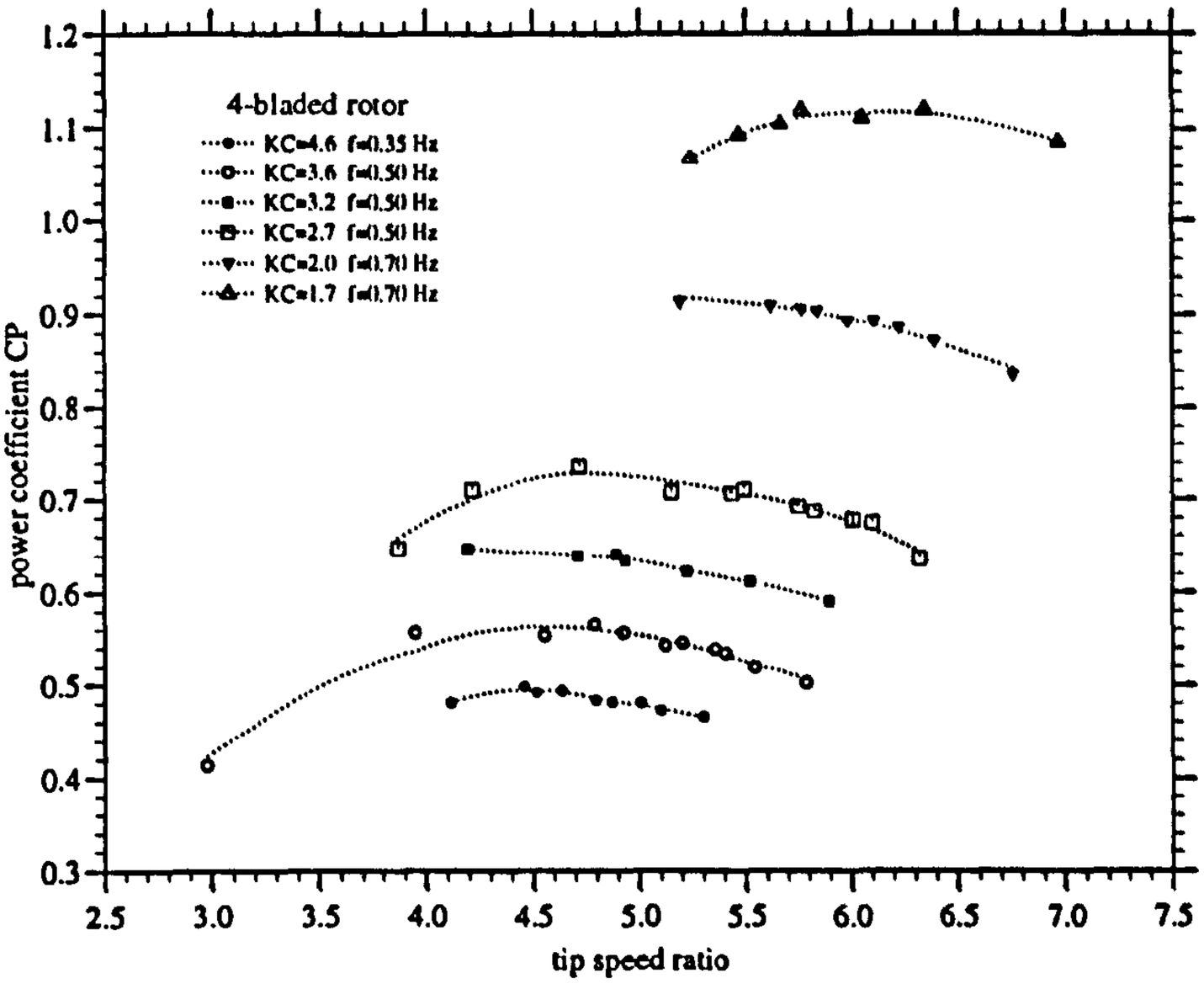

Figure 3.97: Measured $\bar{C}_P$ vs. Λ For 4-Bladed Rotor

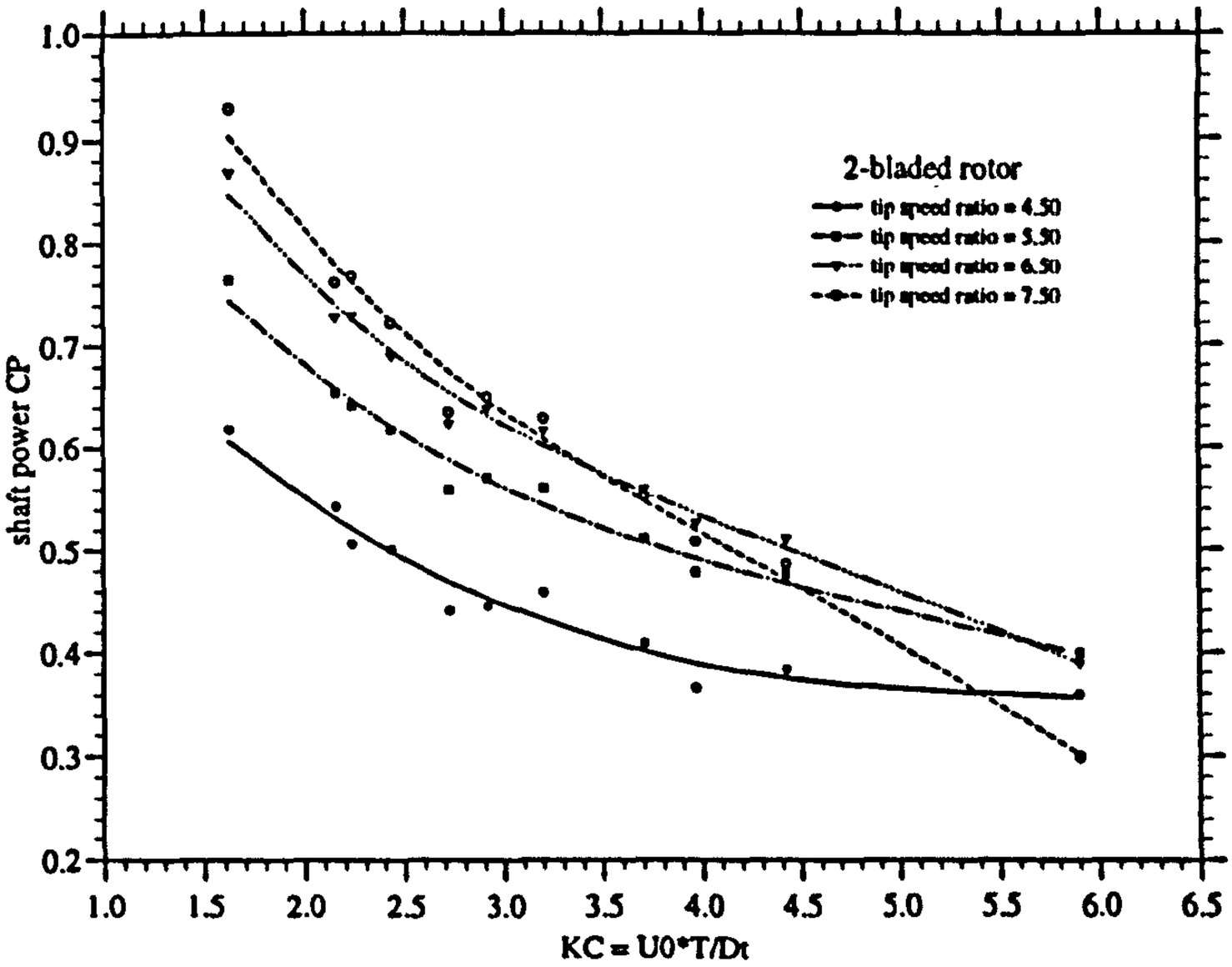

Figure 3.98: Measured $\bar{C}_P$ vs. KC For 2-Bladed Rotor

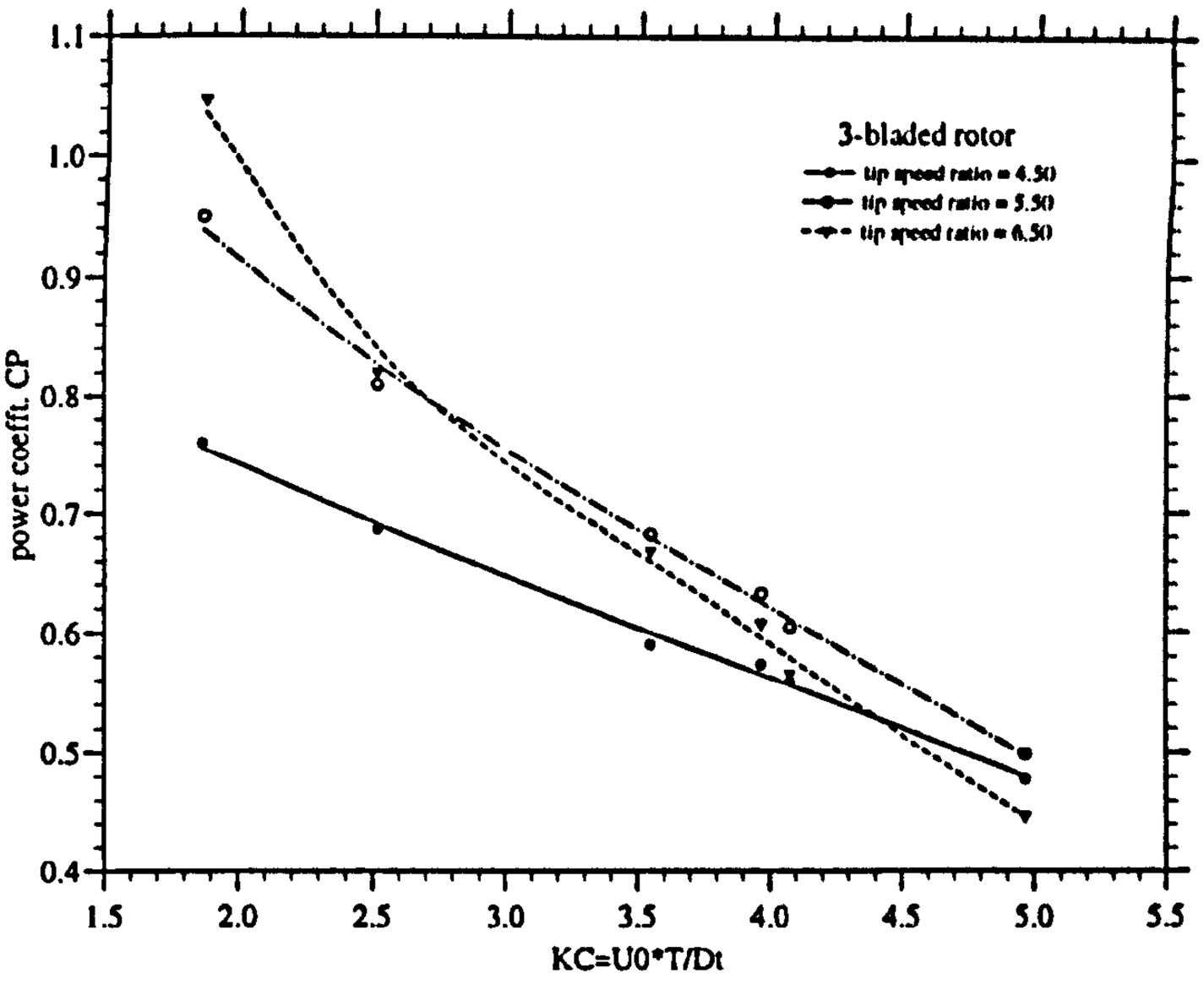

Figure 3.99: Measured $\bar{C}_P$ vs. KC For 3-Bladed Rotor

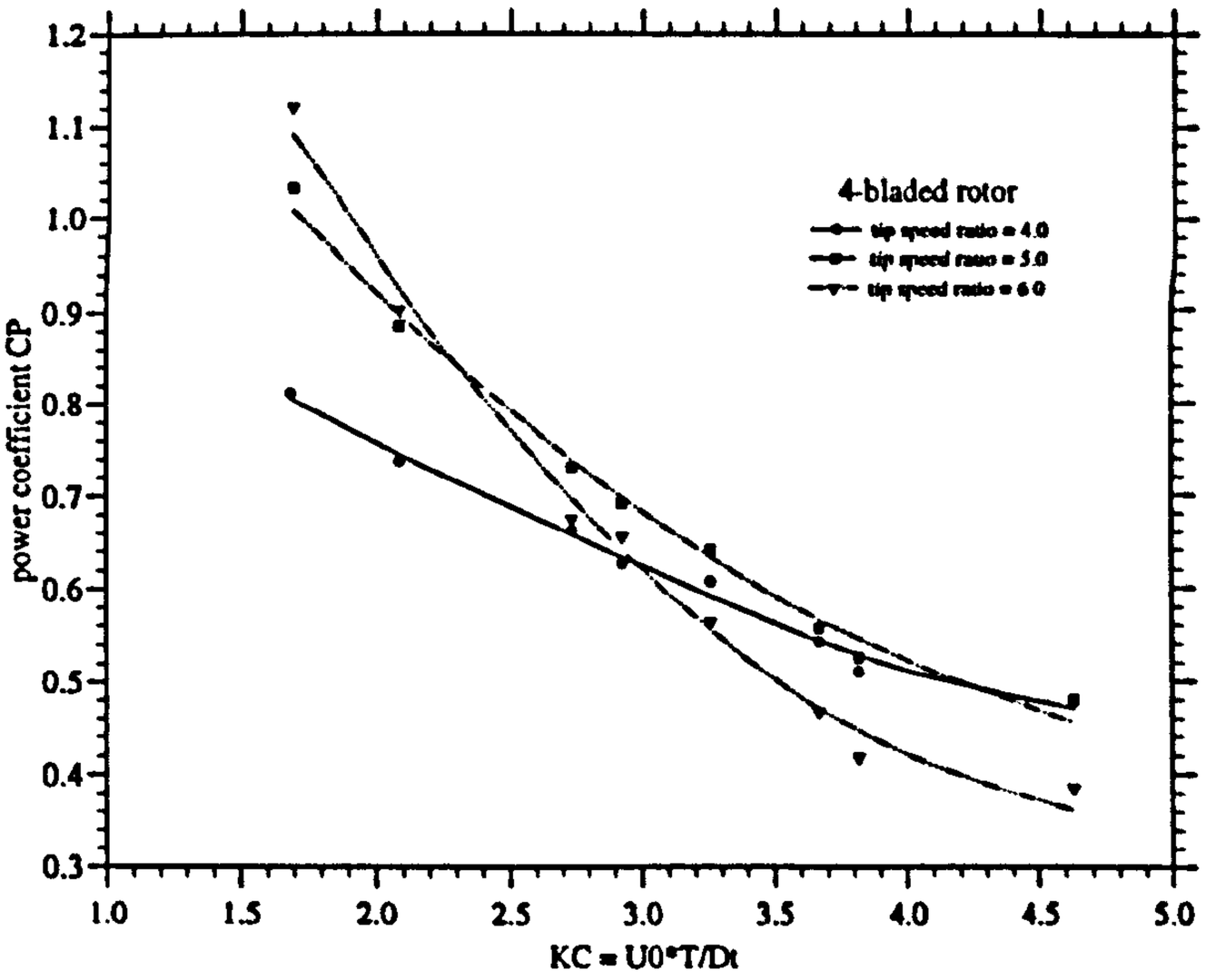

Figure 3.100: Measured $\bar{C}_P$ vs. KC For 4-Bladed Rotor

which may relate to changes in the blade Reynolds number or unsteady flow effects measurements were carried out in which the frequency of oscillations was changed for a fixed value of KC. Figure (3.101) compares the $\overline{C_P}$ data measured for the 2-bladed rotor at a number of KC values. The presentation suggests that any frequency effects on $\overline{C_P}$ lie within the scatter of the experimental data over the test range covered. Further, this graph illustrates the good repeatability of the measurements carried out in the large water tank.

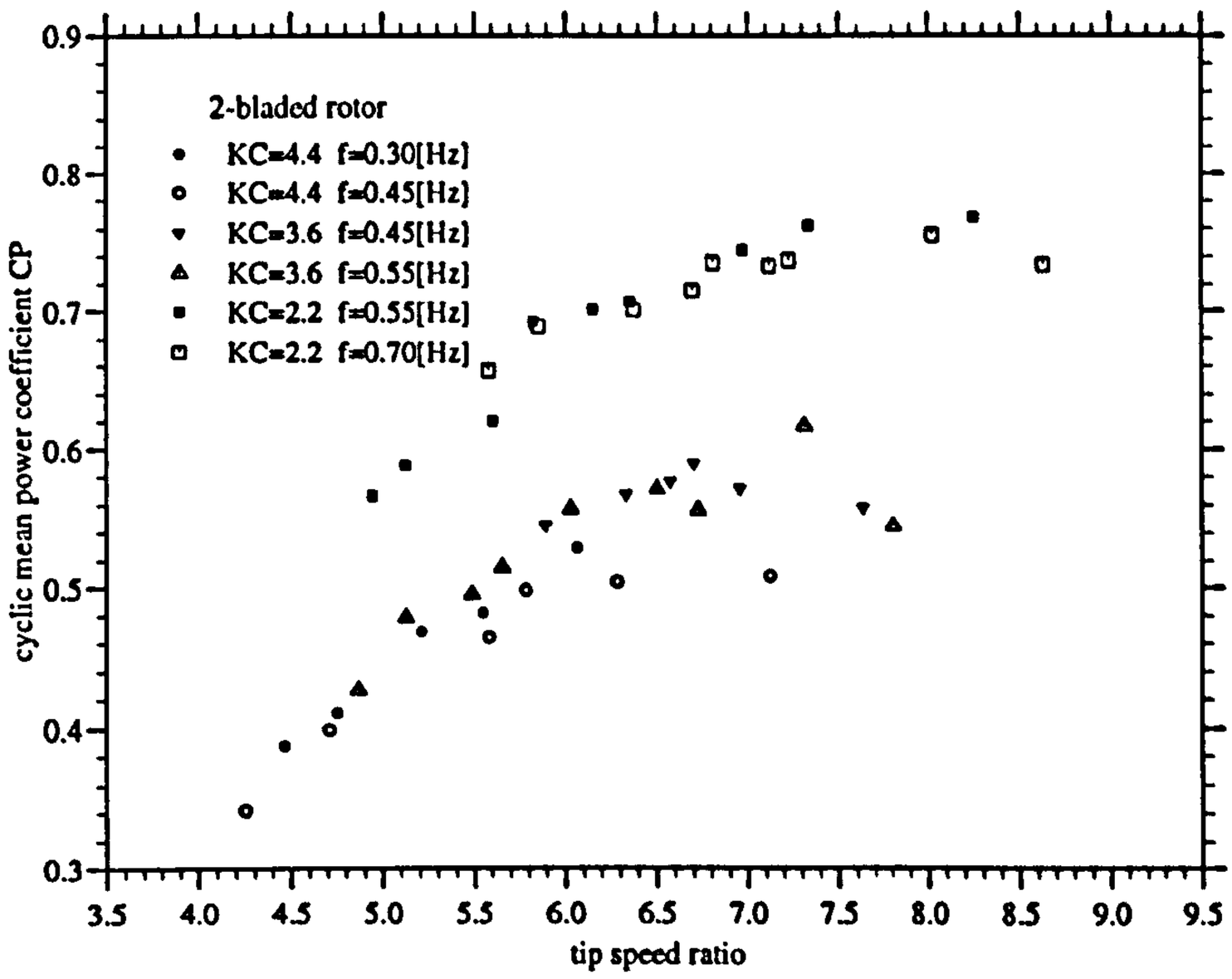

Figure 3.101: Measured $\bar{C_P}$ vs. Λ For 2-Bladed Rotor

Figures (3.102) - (3.104) below give a graphical comparison of $\overline{C_P}$ measured in the U-tube and the large water tank for the three rotor configurations at respective values achieved in both experimental set-ups. The illustration suggests good agreement of the data sets and any variation is considered to be within the limits of typical data scatter. This indicates that in the U-tube testing there was little blockage effect on $\overline{C_P}$ to be accounted for within the sensitivity of the measurement and adds confidence in the procedure for including rotor losses in the calculations of $\overline{C_P}$.

Figure (3.105) provides some quantification of the variation of Λ_{opt} derived from the experimental data measured in the U-tube and large water tank experiments. The data shown in this figures has been obtained by interpolation of a quadratic regression performed on the $\overline{C_P}$ versus Λ curves of figures (3.92) -

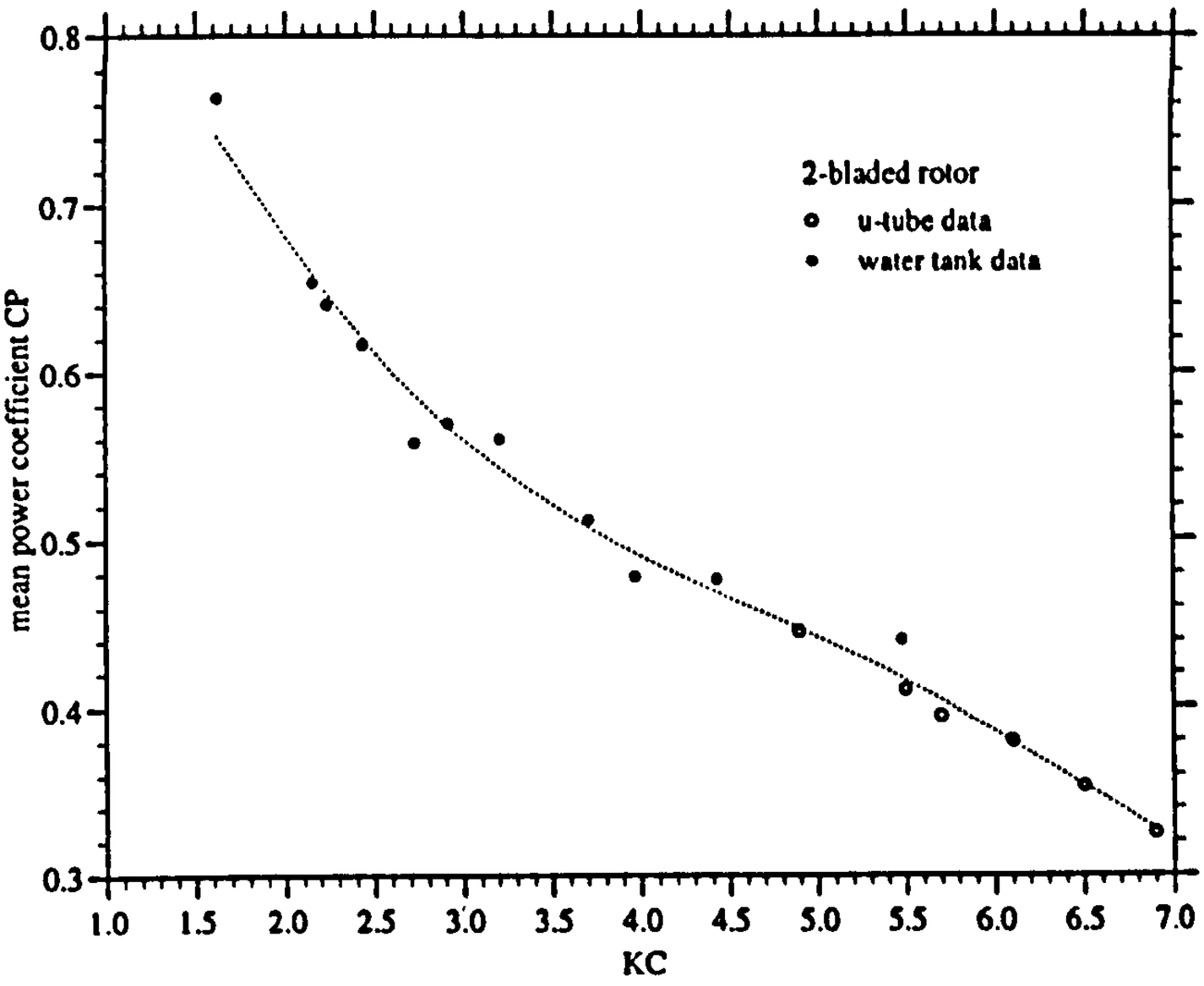

Figure 3.102: U-tube And Large Water Tank Data For 2-Bladed Rotor

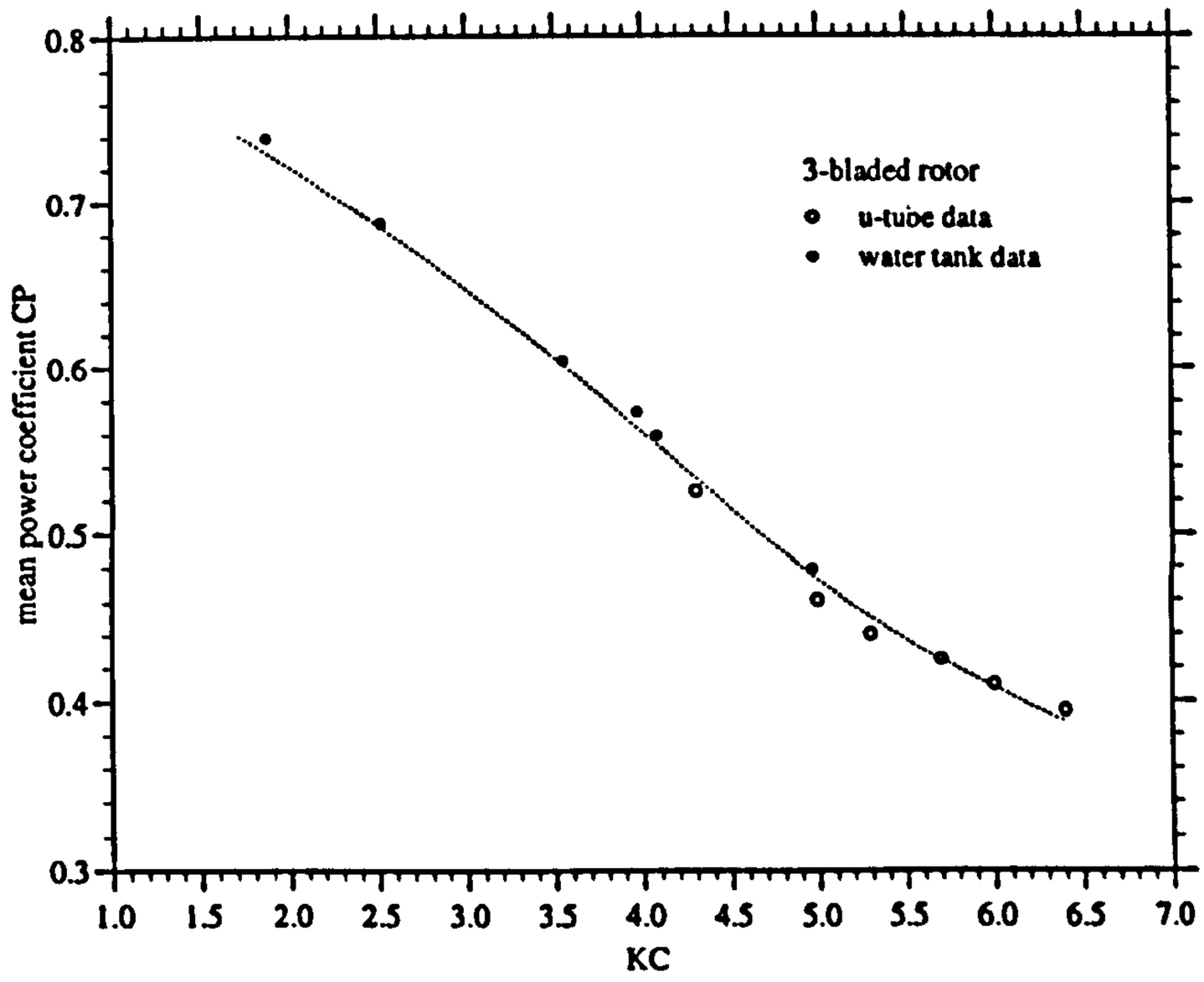

Figure 3.103: U-tube And Large Water Tank Data For 3-Bladed Rotor

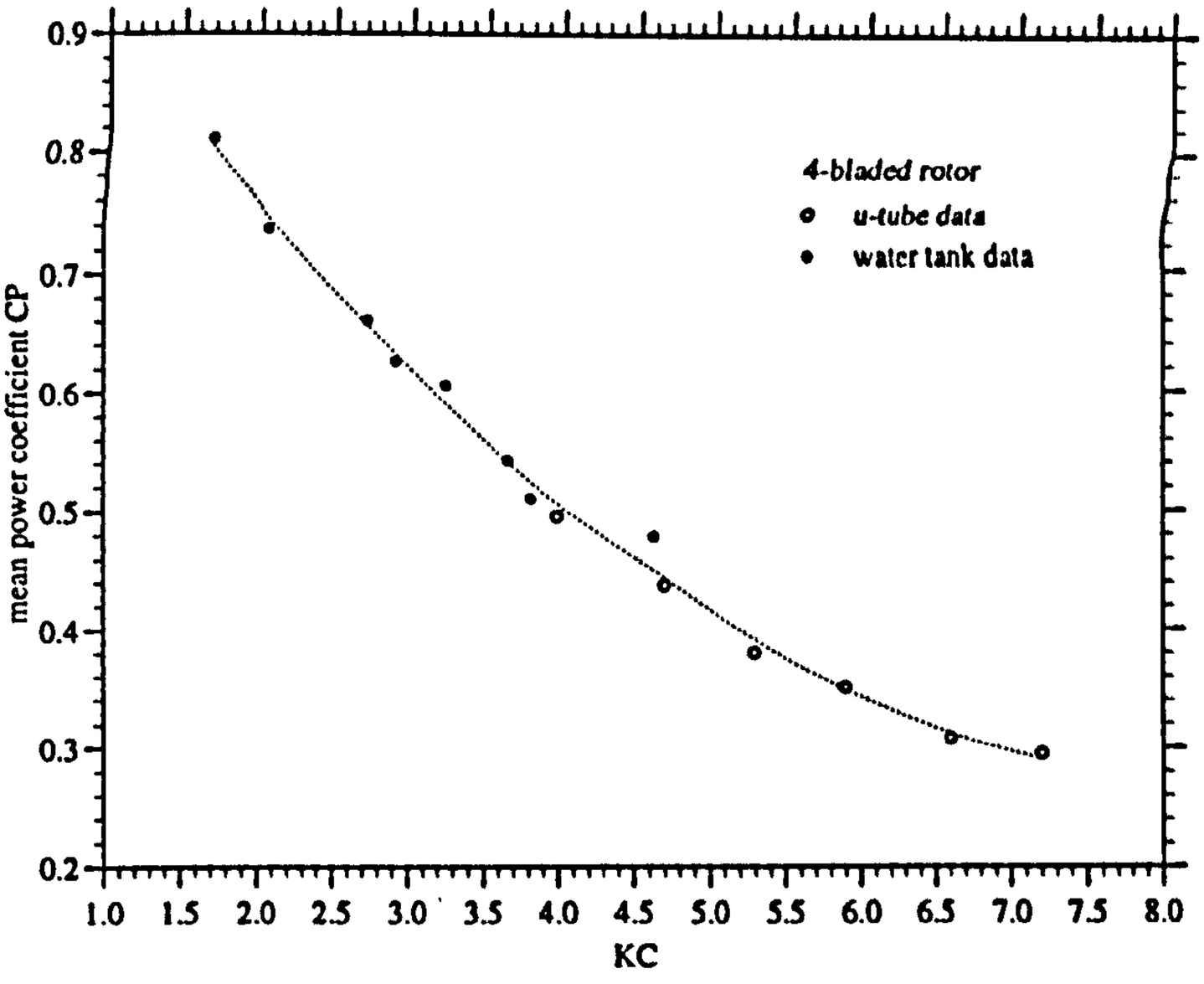

Figure 3.104: U-tube And Large Water Tank Data For 4-Bladed Rotor

(3.97) and is, therefore, to some extent subjective.

Comparing the curves for the different rotor configurations shown in figure (3.105) below a strong non-linear dependency of Λ_{opt} on the rotor tip solidity σ is apparent. At small values of KC it can be seen that $\partial\Lambda_{opt}/\partial KC$ is significantly greater than for the larger values of KC.

In the interpretation of this illustration it is important to note that in contrast to the inviscid actuator disc analysis derived earlier, in which $\overline{C_{Pmax}}$ and Λ_{opt} are affected only by the strength of the wake induced back flow, the (measured) Λ_{opt} values deduced from the experimental power measurements may be affected by partial rotor stall. The occurrence of blade stalling may be expected to cause Λ_{opt} estimated from the power measurements to be higher than the value predicted from the actuator disc theory.

In order to at least qualitatively comment on the extent to which the experimental Λ_{opt} data is affected by rotor stall, an attempt has been made to derive the dependency of notional blade tip and root incidences on Λ: The maximum cyclic blade tip incidence $\hat{\alpha}_t$ is related to the cyclic peak tangential velocity ΩR_T and the peak axial velocity through the rotor plane $\hat{U}_D$, which is assumed to be uniform along the bladed span by

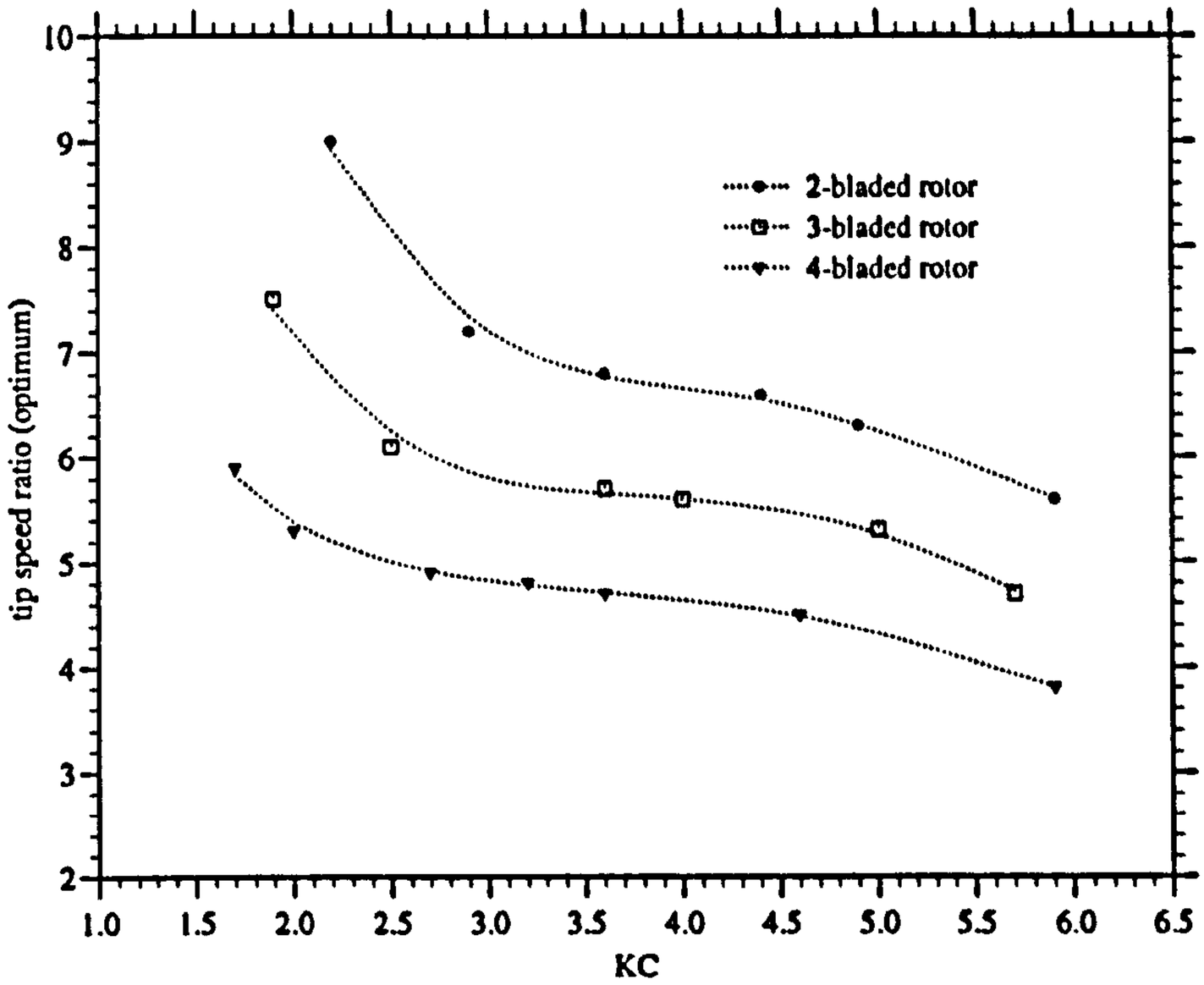

Figure 3.105: Λ_{opt} vs. KC

$$tan\hat{\alpha}_t = \frac{\hat{U}_D}{\Omega R_T} \tag{3.65}$$

The definition of Λ chosen for the presentation of the experimental data is based on the peak free stream velocity U_0. It was shown in the previous section that according to the actuator disc theory $\overline{C_{P_{max}}}$ occurs irrespective of KC when $\hat{U}_D = 0.72U_0$. Using this relation it follows that

$$\hat{\alpha}_t = atan\left(0.72\Lambda^{-1}\right) \tag{3.66}$$

Given that the axial velocity is assumed to be uniform across the rotor disc area the maximum cyclic blade root incidence is

$$\hat{\alpha}_r = atan\left(\frac{0.72\Lambda^{-1}}{h}\right) \tag{3.67}$$

Figure (3.106) below shows the estimated variation of maximum tip and root incidences with Λ. Also indicated is the maximum incidence for which a NACA0018 aerofoil section may be expected to have attached flow at a Reynolds number of 1.6e5 which is at the upper end of the Reynolds number range typically achieved in testing.

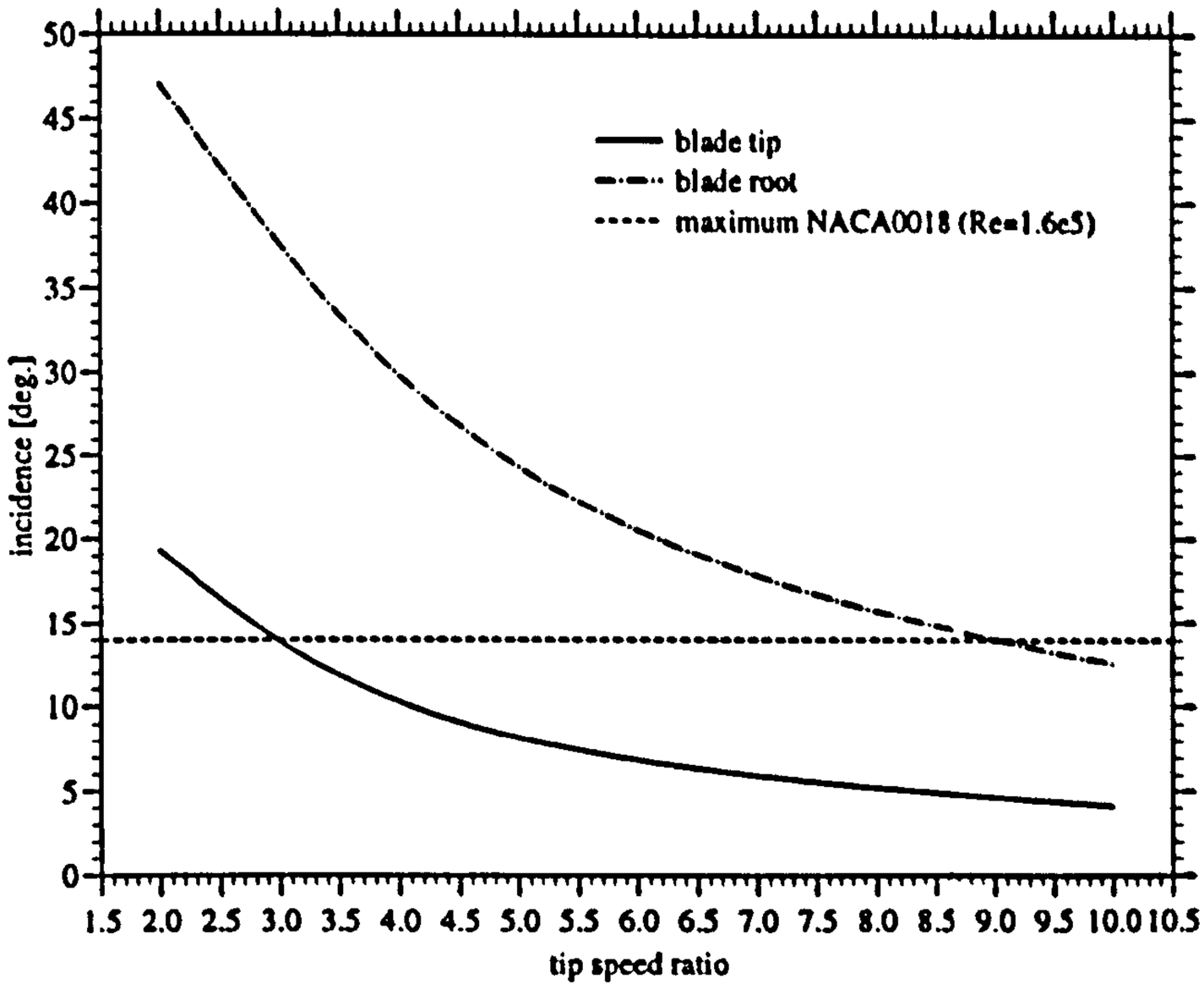

Figure 3.106: Estimated Values of α For Λ_{opt}

It is clear from this figure that blade sections close to the root would from 2 dimensional aerofoil theory be expected to operate in stall for parts of a flow cycle for most experimentally achieved values of Λ. The tip regions of the blades, which contribute strongest to the overall rotor power and from which the majority of the bound circulation is shed into the wake, can be anticipated to be relatively free of stall for values of Λ greater than approximately 3.0-3.5 . Returning to figure (3.105) it can be seen that with the exception of the largest values of Λ_{opt} occurring at small KC flows for the 2- and 3-bladed rotors nearly all values of Λ_{opt} are likely to be affected by partial blade stall. It is evident, therefore, that for a given KC the values of Λ_{opt} derived for the three rotor configurations depends to a varying degree on partial blade stall.

Neglected in the above argument are dynamic stall effects and the effects of three dimensionalities of flow on the suction side of a rotating blade operating at high angle of attack that have been documented in the previous report chapter for a ducted Wells turbine operating in unidirectional steady flow. In particular the stall delay effect may be expected to significantly postpone the stall of the blade root regions to lower tip speed ratios than the above two dimensional arguments suggest and cause the measured turbine efficiency to be somewhat higher than would be predicted from 2-D aerofoil data. The stall delay effect was for the ducted turbine shown to be stronger for higher solidity Wells turbine rotors.

This result implies that of the tested unducted Wells turbine rotors the measured $\bar{C}_P$ values for the 4-bladed rotor should be affected most strongly by stall delay.

According to the actuator disc theory developed in the previous section the maximum power coefficient at a given KC is dependent on $\sigma\Lambda$. Figure (3.107) below shows the variation of $\sigma\Lambda_{opt}$ with KC for the data deduced from the power measurements and for comparison the theoretically predicted curve which was computed from the relevant expressions given by the actuator disc theory. There is an indication that for small KC number flows the experimental curves indeed converge as is predicted by the theory. This is an indication that the flow structure at small KC is well described by the actuator disc theory. However, even at the lower values of KC the $\sigma\Lambda_{opt}$ data derived from the actuator disc theory is considerably lower than the experimental data. As seen in the improved numerical model even at small KC there is some convection of the vorticity, which reduces the phase shift between the resultant axial velocity through the rotor $U_D(t)$ and the free stream velocity $U(t)$. The net effect of this is an increase of $\sigma\Lambda_{opt}$ which may go some way towards explaining the noted difference between the experimental data and the actuator disc theory which does not allow for convection.

At the larger KC values the Λ_{opt} versus KC curves are not collapsed by multiplication with the rotor tip solidity, which suggests that the wake dynamics are less well represented by a concentrated vortex ring fixed in the plane of rotation.

In part this may also be attributed to the importance of viscous effects which as discussed above are likely to introduce a solidity dependency of Λ_{opt}. Further, this behaviour may be an indication of the importance of cascade effects, which are unaccounted for in the actuator disc theory. There is a linear cascade effect on the local blade lift coefficient C_L which for 90 degrees stagger angle is given by

$$C_L = C_{L_0}\left(\frac{2s}{\pi c}\right) tan\left(\frac{\pi c}{2s}\right) \tag{3.68}$$

where C_{L_0} is the lift coefficient for an isolated aerofoil section and s is the blade pitch. The corresponding shedding rate of bound circulation using the actuator disc theory is

$$\frac{d\Gamma(t)}{dt} = \pi\sigma\Lambda U_0\left(\frac{2s}{\pi c}\right) tan\left(\frac{\pi c}{2s}\right)\left(U(t) - \frac{\Gamma}{2R_T}\right) \tag{3.69}$$

The solution of this differential equation will produce an explicit dependency of $\overline{C_P}$ on $(2s)/(\pi c)$ which is related to the rotor tip solidity. As a result $\sigma\Lambda_{opt}$ will also be a function of $(2s)/(\pi c)$and may be expected to vary for rotors of different

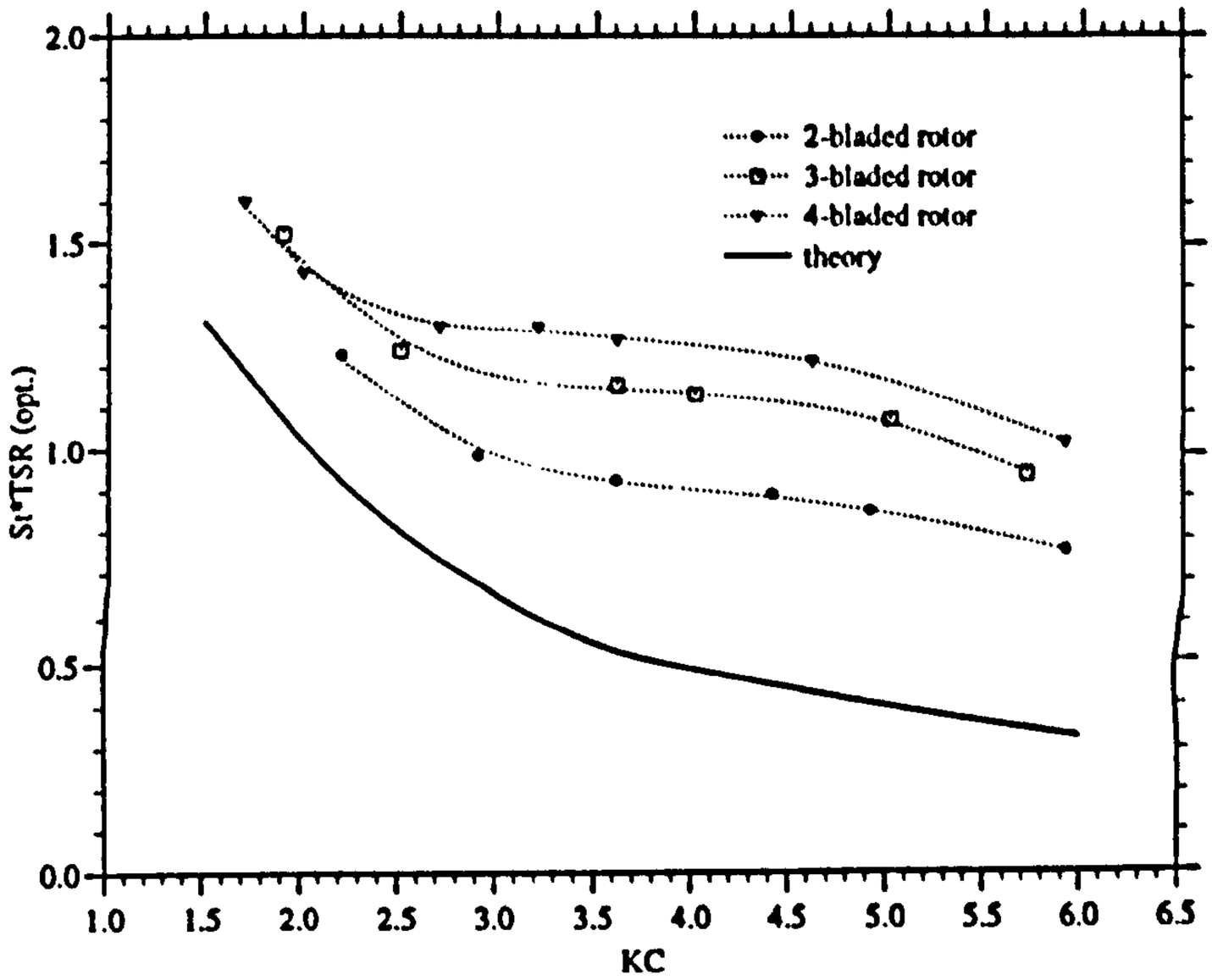

Figure 3.107: $\sigma\Lambda$ vs. KC

solidities.

The comparison of $\overline{C_{Pmax}}$ estimated from the measured data and values predicted from the actuator disc theory which is shown for the three rotor solidities in figure (3.108) also suggests a dependency on the rotor tip solidity σ. Within the data scatter no clear trend can be deduced.To some extent this is due to the subjective inter and extrapolations required in some cases to obtain estimates for uncertainty introduced into the data presented that results from the subjectivity of the $\overline{C_P}$ inter- and extrapolations required to obtain estimates of Λ_{opt}. This is especially the case for the 2- and 3-bladed rotors operating in small KC number flows for which Λ_{opt} was not actually achieved in the experiments.

Qualitatively there is good agreement between the experimental and theoretical data. The experimental data clearly supports the conclusion of the numerical analysis that $\overline{C_{Pmax}}$ is inversely proportional to KC and can achieve values greater than unity.

The quantitative the agreement is less good. At larger KC the theory over predicts the experimentally measured performance by approximately 20% while at smaller values of KC the extent over prediction rises to approximately 50%.

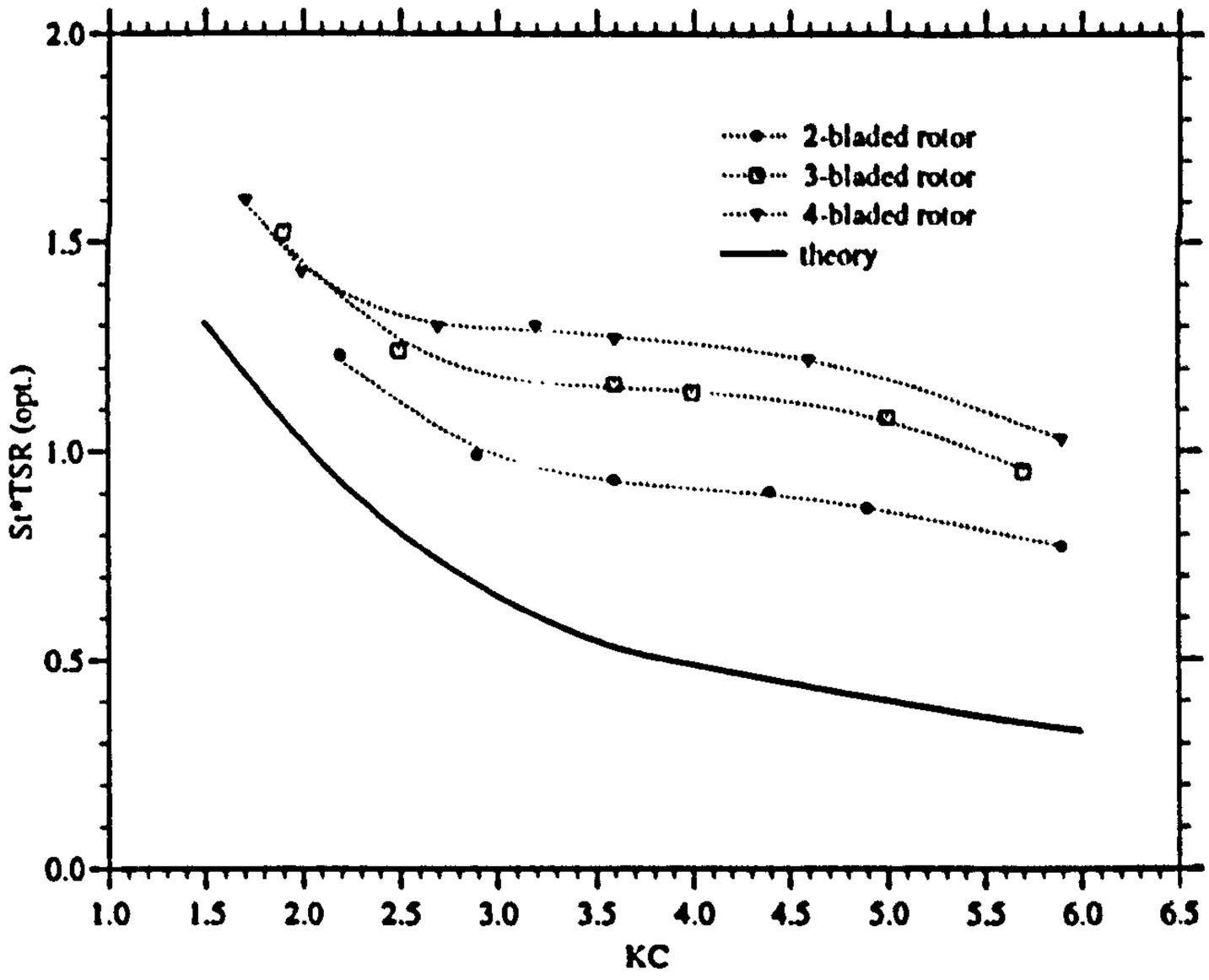

Figure 3.107: $\sigma\Lambda$ vs. KC

solidities.

The comparison of $\overline{C_{Pmax}}$ estimated from the measured data and values predicted from the actuator disc theory which is shown for the three rotor solidities in figure (3.108) also suggests a dependency on the rotor tip solidity σ. Within the data scatter no clear trend can be deduced.To some extent this is due to the subjective inter and extrapolations required in some cases to obtain estimates for uncertainty introduced into the data presented *that results from the subjectivity* of the $\overline{C_P}$ inter- and extrapolations required to obtain estimates of Λ_{opt}. This is especially the case for the 2- and 3-bladed rotors operating in small KC number flows for which Λ_{opt} was not actually achieved in the experiments.

Qualitatively there is good agreement between the experimental and theoretical data. The experimental data clearly supports the conclusion of the numerical analysis that $\overline{C_{Pmax}}$ is inversely proportional to KC and can achieve values greater than unity.

The quantitative the agreement is less good. At larger KC the theory over predicts the experimentally measured performance by approximately 20% while at smaller values of KC the extent over prediction rises to approximately 50%.

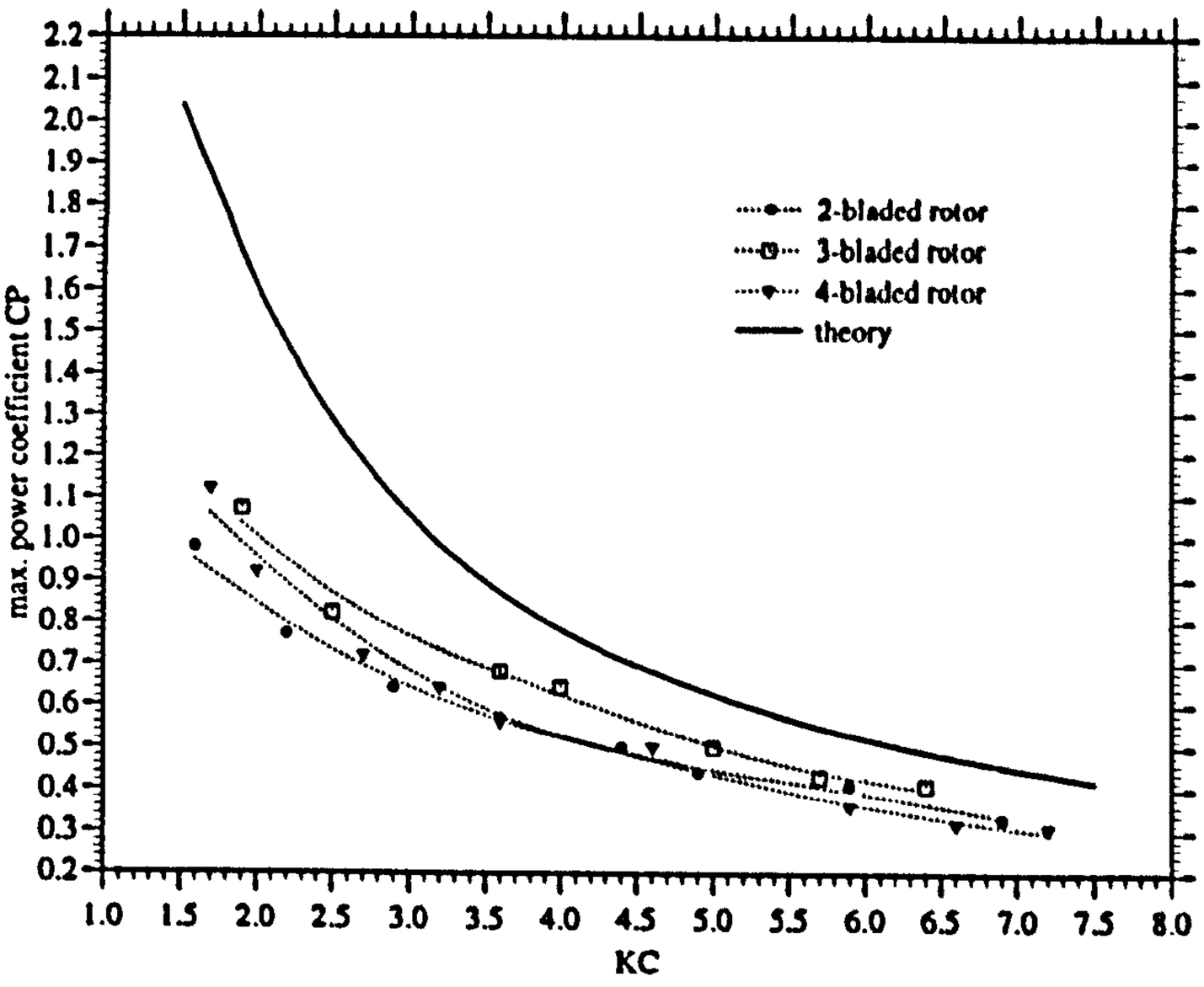

Figure 3.108: $\overline{C_{Pmax}}$ vs. KC (Measured & Actuator Disc Theory)

At larger values of KC the quantitative discrepancies are likely to relate to inadequacies of the numerical model which does not model the wake convection and, therefore, is likely to over predict the back flow induced by the wake which enhances the flow through the rotor.

At the smaller values of KC the idealisations of the numerical model are expected to more representative of the physical flow so that the discrepancies in these cases are more likely to stem from experimental error. Clearly, however, because of the small scale of the experiment the recordable quantities that determine the rotor performance were very small. As a result the system losses and in particular the fluid losses of the rotor blades were as shown earlier very significant. The main source of experimental ambiguity, therefore, is thought to relate to the loss correction applied for the hydrodynamic drag, which was determined from deceleration tests in initially still fluid and has been described earlier. This experimental ambiguity is related to the interference effects between the rotor blades in the deceleration tests, which were not accounted for. In particular, there are two main points of concern which possibly caused the actual fluid losses incurred by the turbine rotor during the power measurements to be somewhat higher than the applied fluid loss correction and which are discussed below:

It is apparent that in the deceleration tests the individual rotor blades were

forced to travel into the wake of the adjacent blades where the velocity is significantly reduced from the free stream value, as the rotor was spun in nominally still fluid. Clearly because of this lower incident velocity the blade drag effectively measured in the deceleration tests may be expected to be lower than if the blade was rotating in undisturbed flow. This effect is dependent on the blade spacing and is, therefore, strongest for the 4-bladed rotor. Figure (3.109) shows the measured torque per rotor blade as a function of the blade spacing for the three tested rotors and provides an illustration of the considerable extent of this effect for a number of rotational speeds.

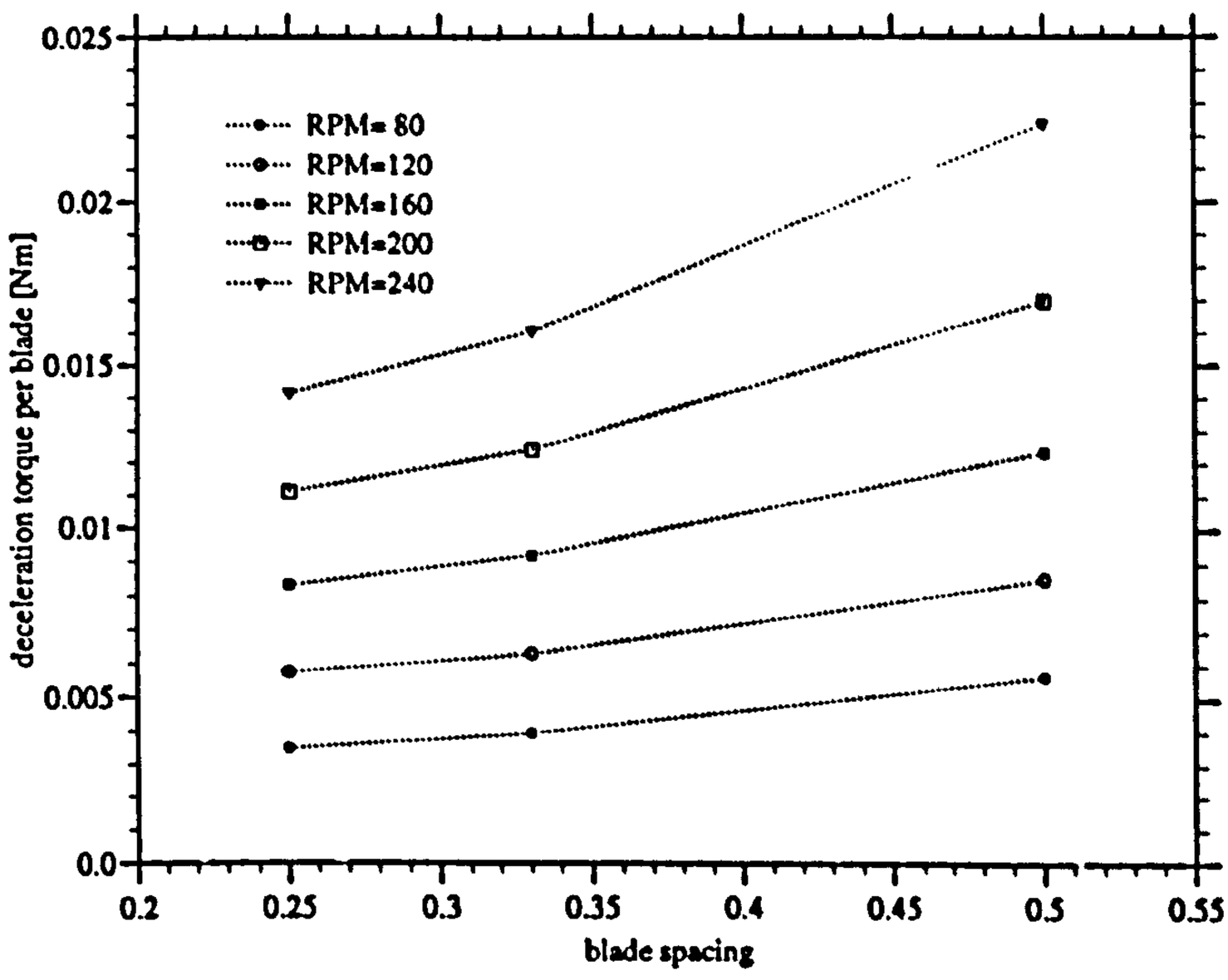

Figure 3.109: T_{decel} vs. Blade Spacing

Ideally, to compensate for this effect one would like the 'no-blade' case which would correspond to an infinite blade spacing. Unfortunately, it is not clear how these curves should be extrapolated for this case and, therefore, the required correction could not be applied.

In addition to the above effect the velocity which is effectively incident to the blade is reduced further because the still fluid is gradually accelerated by the surface friction of the spinning blades.

For very high tip speed operation, which would have occurred in the power measurements towards the end of a flow cycle when the free stream reverses direc-

tion the applied deceleration torques to account for the hydrodynamic losses are likely to be accurate. However, at lower tip speed operation the adjacent blades are less likely to intercept the wake of the adjacent blades and, therefore, would be expected to be see a higher apparent velocity than at the same tip speed in the deceleration tests.

Further, neglected in the deceleration test are increases in the the sectional profile drag due to lift which especially at low tip speed ratios is considerable.

On the whole, therefore, it is likely that the applied corrections for the hydrodynamic drag losses which are not accounted for in the actuator disc theory over a full flow cycle are somewhat lower than those actually experienced by the tested rotors. This is considered to be the main cause for the quantitative discrepancies between theoretical and experimental values of $\overline{C_{Pmax}}$ noted above.

3.7 Concluding Remarks

Flow visualisation experiments were successfully carried out at model scale to provide a qualitative insight into the flow mechanisms that govern the hydrodynamic performance of unducted Wells turbines in small KC oscillatory flows.

These flow visualisations showed that in oscillatory flow the spiral rotor wake of an unducted Wells turbine in small KC flows shows a strong tendency to roll up and remain close to the plane of blade rotation during its formation on one half of the cycle. As a result the idealisation of the rotor wake as a concentrated vortex ring adopted in the numerical modelling is considered legitimate for small KC flows.

During the return half of a flow cycle strong interactions between the rolled up rotor wake and the flow through the rotor itself were apparent and are evidence that the flow augmentation effect of the rotor wake proposed in the numerical model also occur in the physical flow.

The flow visualisations did not produce any evidence that the stream wise convection of the rotor wake is unidirectionally biased as was possible in the improved numerical model due to the paring of sequentially shed vortex rings. The flow pattern observed suggested that over a full flow cycle the wake structure varies symmetrically in time between two sequential half cycles.

A model scale experimental set-up was designed and constructed to measure the shaft power of a number of mono plane Wells turbine rotors operating in sinu-

soidally alternating water tank flows. The experiment was configured to provide some validation for the theoretical analysis of the Wells turbine performance in small to moderate KC flows which was derived earlier.

It was found that at these small scales the system losses, of which the hydrodynamic drag of the rotor formed a mayor part, were considerable. The hydrodynamic losses were assessed by deceleration runs in still fluid and were included as a loss correction in the measured shaft power in order to allow for a more valid comparison between the experimental and theoretical work.

The results of the experimental shaft power measurements confirmed that the mean cyclic power coefficient of unducted Wells turbines operating in small KC flows can be greater than unity due to the induced back flow of the rotor wake.

Further, the shaft power measurements provided some experimental validation of the theoretical result that the cyclic power coefficient is inverse proportional to KC.

There is good qualitative agreement between the experimental and theoretical data recorded for the variation of the cyclic power coefficient over the tested range of small amplitude flows with KC. This gives some confidence in the approximations made in the theoretical analysis of the unducted Wells turbine performance and suggests that the main relevant flow mechanisms have been identified.
The quantitative discrepancies which were noted between the shaft power predicted by the numerical model and that measured experimentally are, to a large extent, considered to be due to scale effects and are likely to result from underestimating the drag losses of the rotor which are large at these small experimental scales.

Chapter 4

Conclusion

4.1 The Wells Turbine Performance in Ducted Unidirectional Flow

An experiment was successfully designed and carried out which has provided a fundamental study of the aerodynamic characteristics of a rotating Wells turbine blade that define the rotor performance characteristics in steady, unidirectional ducted flow relevant to the Wells turbine operation in typical OWC wave power devices. The chosen experimental approach of measuring chord wise *Cp* distributions at a number of radial blade stations has allowed a more direct experimental validation of the basic blade element theory and the linear cascade theories conventionally used for the performance prediction of the ducted Wells turbines than was to date possible from the experimental shaft power measurement experiments carried out by other researchers.

It was found from this experimental work that at high tip speed ratio operation the aerodynamic performance of the rotating blades of a typical ducted Wells turbine rotor can be qualitatively and quantitatively well described by the conventionally applied blade element and static cascade theories.

However, at low tip speed ratio operation when the local blade incidences were high the experimental results showed that these theoretical concepts are less useful in predicting the aerodynamic behaviour of the rotating blades especially near the blade root. In particular it was found that the rotating blade sections showed higher levels of post-stall lift than would be expected from the measured sectional characteristics of the static blade. This was related to a significant low pressure region of the downwind blade surface. The stall delay phenomenon which is usually ascribed to radial flows in the blade boundary layers could be inferred as and explanation for this behaviour because a strong qualitative resemblance was noted between the measured post-stall *Cp* distributions on the instrumented

rotating blade of the ducted Wells turbine and those *Cp* distributions published for analogous measurements performed on unducted wind turbine rotors which showed signs of stall delay.

Further, the experimental work showed that for a high-solidity Wells turbine operating at low tip speed ratios there are strong non-linear interactions between cascade- and the stall delay effects.

In the case of a high-solidity Wells turbine, it was also found that the effective local blade incidences are considerably different from the local 'geometric' incidences, conventionally derived from the radial equilibrium approach neglecting wake effects, because of the the axial and swirl velocities induced by the rotor wake in the rotor plane.

It may be concluded from this part of the thesis work that a comprehensive performance analysis of the Wells turbine in unidirectional steady flow must account for rotational effects in the boundary layer flow of the rotor blades as well as the axial- and swirl velocities induced by the rotor wake.

4.1.1 Further Work

The current work has provided a basic insight into the importance of the stall delay effect to the aerodynamic performance of the Wells turbine in steady unidirectional flow.

The model scale Reynolds number for the rotor blades in the experimental work was approximately 1/4 of the Reynolds number at which the Wells turbine blades would typically operate in current prototype OWC wave power devices. There is some ambiguity about how the noted stall delay effect scales with the blade Reynolds number. The variation of the stall delay phenomenon with the effects of scale is being investigated on a number of full scale wind turbine rotors (see eg. Huyer (1996)). The results of these investigations may be taken as a guidance. However, because of the importance of solidity effects for the Wells turbine the results of these studies may only have limited relevance. In order to achieve quantitatively more directly applicable data it may be desirable to repeat the experimental work carried out as part of the current research at higher Reynolds numbers. These may be achieved using the existing experimental set-up by increasing the blade rotational speed or by increasing the blade chord.

It may be of further interest to conduct experimental investigations equivalent to those carried out in steady flow as part of the current work on an instrumented blade of an actual full-scale Wells turbine rotor operating in an oscillatory air

flow. In this investigation the unsteady flow effect of dynamic stall is likely to be important and it is probable that it will interact with the largely steady stall delay effect. This type of experimental investigation would have to account for the unsteadiness of the blade surface pressures. As a result a sequential pressure scanning system such as the one designed for the wind tunnel study that formed part of the current research work would be inadequate. Instead an simultaneous pressure scanning system would be required for this type of investigation.

Moreover, at full scale the tip Ma of Wells turbine blades is often high enough for compressibility effects to be present over a certain portion of the rotating blades. The current experimental set-up was specifically designed to avoid these effects and can, therefore, not comment on their importance. For wind turbine rotors compressibility effects are of no consequence since the tip speeds of large wind turbine rotors are never high enough for the blades to enter this flow regime. More useful information on the effects of compressibility may be found from research work carried out for axial flow turbomachinery. In any case this subject should be separately investigated for the Wells turbine. An experimental investigation could, however, in principle follow the experimental set-up of the current work designed for incompressible flow.

Finally, it may be of interest to conduct a full 3 dimensional Navier-Stokes computation for the flow over a rotating Wells turbine blade in steady ducted flow to provide a comparative numerical study of the stall behaviour that was a main subject of the current experimental work.

4.2 The Wells Turbine Hydrodynamic Performance in Unducted Oscillatory Flow

A theory similar to the existing actuator disc theory for unidirectional steady flow was developed to assess the ideal hydrodynamic efficiency of the Wells turbine in unducted small to moderate KC oscillatory flow. For this novel application of the Wells turbine no method of performance analysis had previously existed. This theory models the wake simplistically as a vortex ring which for small amplitude flow oscillations was assumed to lie in the plane of rotation since the extent of stream wise convection of wake vorticity is small.

The theory revealed that the peak cyclic efficiency of the rotor is inversely proportional to KC and can attain values greater than unity if the rotor efficiency (power coefficient) is based on the peak axial energy flux through an area equal to the swept area of the turbine rotor that would occur in the undisturbed free

stream. It was concluded that the values of peak efficiencies greater than unity are related to the back flow induced by the rotor wake, which over part of the flow cycle augments the flow through the rotor disc. Further, it was also shown that the axial back flow factor based on the peak induced back flow and the maximum incident flow velocity for which the peak cyclic efficiency is achieved is equal to 0.72 and is independent of KC.

A more sophisticated numerical model was also developed as an extension of the actuator disc theory. This model which modelled the rotor wake by concentrated vortex rings allowed the importance of the rotor wake convection to some extent to be studied. It was found that for small KC flows the stream wise convection of the nascent vortex rings is indeed small as was assumed in the simpler actuator disc theory, while at moderate KC it is more significant. The improved numerical model also revealed that particularly at moderate KC a wake structure can evolve that produces a unidirectionally biased stream wise convection and hence a non-zero mean axial force acting on the rotor.

Flow visualisation studies were conducted in a U-tube water tank using an unducted Wells turbine rotor and provided an insight into the previously undocumented flow mechanisms that govern the hydrodynamic performance of the Wells turbine in unducted oscillatory flow. These studies revealed that in oscillatory flows the wake roll-up is a defining feature of the wake development and hence provided some justification for the idealisation of the rotor wake as concentrated vortex rings as adopted in the numerical studies.

A number of water tank experiments were designed and carried out to measure the shaft power of unducted Wells turbine rotors in small to moderate KC oscillatory flow at small scale to provide some validation for the theoretical performance analysis developed. These experimental investigations confirmed that the cyclic efficiency of an unducted Wells turbine rotor is inversely proportional to KC and that power coefficients greater than unity can be achieved due to the induced back flow of the rotor wake.

4.3 Further Work

The actuator disc type theory does, in its presented state, not account for cascade effects or the sectional characteristics of the rotor blade aerofoils. In particular, the blade stall has been neglected. Clearly these effects are likely to be important for a more comprehensive performance prediction of an unducted Wells turbine in oscillatory low KC flow. They could, however, be incorporated in both numerical models developed in the current work by substituting the appropriate

expressions for the blade force coefficients, which should utilise the documented fluid dynamic characteristics of rotating Wells turbine blades in steady, ducted flow such as e.g. the stall delay phenomenon.

The assumptions made in the derivation of the numerical models clearly limits the validity of these models to small KC flows where the stream wise convection is small. For moderate KC flows the stream wise convection of wake vorticity is significant and can not be neglected in the analysis of the flow through the Wells turbine rotor. This could be seen from the results of flow computations using the more sophisticated of the two numerical models developed in course of the current research work. As the stream wise convection of vorticity shed from the rotor becomes more significant the wake roll-up is unlikely to become a defining feature of the flow until the free stream flow is close to the point of reversal. In order to more realistically model this type of flow it may be of interest to modify the improved numerical model to allow for a less forced roll-up which occurs towards the end of each sequential half cycle. This may be achieved by shedding a number of vortex rings at different span wise positions of the rotor after each computational time step. In order to maintain computational efficiency an amalgamation scheme may be introduced for these vortex rings once they have moved away from the near field of the rotor.

An even more realistic simulation of the wake development may be performed using computationally more expensive methods. Numerical work of this kind could progress the limited attempts that were made as part of the current work to adopt an existing vortex lattice code set up for unidirectional unsteady flow to the more complicated oscillatory flow situation in which the effects of flow reversal on the rotor wake need to be modelled. A main task of this work would be to promote numerical stability of the method as the wake panels begin to roll up and are swept back towards the rotor.

The experimental work carried out may usefully be extended in future by conducting more exhaustive flow visualisations at small KC, which should show more conclusively if the unidirectionally biased stream wise convection of wake vorticity revealed by the numerical computations can occur. These flow visualisations could be supplemented by axial force measurements which would produce more direct evidence of any mean axial force related to biased stream wise convection. In fact, the flow visualisation experiments could be set up to allow not only qualitative flow field analysis but also a quantitative analysis of the flow velocities through the plane of rotation using e.g the Particle Image Velocimetry (PIV) technique.

Further experimental work using a similar experimental technique as that adopted in the current work to measure the shaft power should be carried out at

larger scale in order to reduce the quantitative ambiguities that in the current work were incurred because the rotor losses were large compared with the applied braking torque. This could be achieved using the existing experimental apparatus by increasing the rotor diameter. Clearly, as the rotor diameter is increased the constraint effects of the U-tube water tank of the Aeronautics department of Imperial college, in which some of the current experimental work was carried out, become more important so that truly unducted flow behaviour may only be achieved in a large enough water tank (such as the departmental still water tank). In this way the rotor torque could be increased significantly so that particularly at small KC the accuracy of the power measurement could be considerably improved. Future work may also provide a more detailed quantification of the rotor fluid dynamic losses which could include acceleration as well as deceleration tests in still water.

More generally, it would be of interest to test the unducted Wells turbine in a wave flow in an arrangement which more closely resembled the envisaged applications as an offshore/near shore wave power device. This work could establish to what extent the performance of an unducted Wells turbine in a real wave flow, in which the turbine would convert the power from the orbital fluid flow beneath the waves, deviates from that demonstrated in the numerical and experimental work performed for strictly axial flow as part of the current research project

Research Achievements:

The main achievements of the thesis work are:

- Through experimental measurements of the surface static pressures on a rotating Wells turbine blade, it has been shown that the stall delay effect is important for the stall behaviour of the Wells turbine in steady flow and that, for high solidity rotors, this effect strongly interacts with cascade effects.

- A basic physical understanding of the Wells turbine performance in unducted oscillatory flow of small and moderate flow amplitude to diameter ratios has been gained through the development of a novel numerical model and experimental measurements at small scale.

Chapter 5

References

Abbot I. And Von Doenhoff H. (1959)
'Theory of wing sections',
New York: Dover

Al – Hukail Y.O.I (1993)
'Roll damping due to vortex shedding from slender ship hulls in forward motion',
Ph.D. Thesis, Department of Aeronautics, Imperial College, London

Barnsley M.J. And Wellicombe J.F. (1989)
'Design and testing of a horizontal axis wind turbine model for the investigation of stall regulation aerodynamics'
EWEC'89, Conference Publication, Glasgow

Barnsley M.J. And Wellicombe J.F. (1991)
'Wind tunnel investigation of stall aerodynamics for a 1.0 [m] horizontal axis rotor',
EWEC'91, Conference Publication, Amsterdam

Bishop H.W. And Harvey R.P. (1981)
'The use of the air turbine as a power take off mechanism in wave energy converters'
2nd. International Symposium on Wave and Tidal Energy

de Bernardinis B. (1980)
'Unsteady axisymmetric flow by the method of discrete vortices',
Ph.D. Thesis, Department of Aeronautics, Imperial College, London

de Bernardinis B., Graham J.M.R. And Parker K.H. (1981)
'Oscillatory flow around discs and through orifices',
J. Fluid Mech., vol.102

Brown C.E. And Michael W.H. (1955)
'On slender delta wings with leading-edge separation'
N.A.C.A Tech. Note 3430

Duncan W.J. Thom A.S. And Young A.D. (1960)
'Mechanics of Fluids' 2nd edition
Edward Arnold, London

Eastman N., N.Jacobs And Sherman A. (1937)
'Airfoil section characteristics as affected by variations of the Reynolds number',
NACA report no. 568

Glauert H. (1947)
'The elements of aerofoil and airscrew theory',
Cambridge University Press 2nd edition

Graham J.M.R (1977)
'Vortex Shedding from sharp edges',
Imperial College Aero. Rep. 77-06

Graham J.M.R (1980)
'The forces on sharp-edged cylinders in oscillatory flow at low Keulegan-Carpenter numbers',
J. Fluid Mech., vol.97 , part1

Graham J.M.R And Brown C.J (1991)
'The effect of turbine rotation on maximum lift coefficient',
Proc. XII BWEA/EWEC Conf. , Glasgow

Graham J.M.R. And Pesmajoglou S. (1994)
'Prediction of unsteady yaw response of a wind turbine in yaw',
Proc. XVI BWEA Conference , Sterling

Grant A.D (1978)
'Development of a wave-powered marine distress beacon',
Proc. Wave and Tidal Energy Symposium, Canterbury ,UK

Grant R.J. And Johnson C.G. (1979)
'Performance tests on a single stage Wells turbine',
CEGB Memo., MM/MECH/TF207,

Grant R.J., Johnson C.G. And Sturge D.P. (1981)

'Performance of Wells turbine for use in a wave energy system',
I.E.E. Conference Publication no. 192

Himmelskamp H. (1945)
'Profile investigations on a rotating airscrew',
Ph.d. dissertation, Goettingen

Horlock J.H. (1958)
'Axial flow compressors',
Butterworth and Co. , Oxford

Huyer S.A., Simms D. And Robinson M.C. (1996)
'Unsteady aerodynamics associated with a horizontal-axis wind turbine',
AIAA Journal, vol. 34 , no. 7

Katz J. And Plotkin A. (1991)
'Low - speed aerodynamics: from wing theory to panel methods',
Mc-Graw-Hill New York London

Kuehtz S (1996)
'Experimental investigation of oscillatory flow around circular cylinders at low beta numbers ',
Ph.D. Thesis, Department of Aeronautics, Imperial College, London

Lamb H.H. (1932)
'Hydrodynamics' 6th edition
Cambridge University Press

Lewis A.W. (1993)
'Wave Energy - A European Review'
Proc. of European Wave Energy Symposium, Edinburgh

Lowson M.V. (1973)
'The separated flows on slender wings in unsteady motion'
A.R.C., R&M 3448

McCroskey W.J. (1971)
'Measurements of boundary layer transition, separation and streamline direction on rotating blades',
NASA TN D-6321

Milborrow D.J. (1985)
'Changes in airfoil characteristics due to radial flow on rotating blades',

Proc. of 7th BWEA Wind Energy Conference

Montgomerie B. (1985)
'Unsteady aerodynamics applied to the horizontal axis wind turbine disk ',
12th. Meeting of Experts - Calculation methods for WECS - KFA Juclich

Neals A.N. (1993)
'Air turbines for use with alternating flows - the choices',
Proc. of European Wave Energy Symposium, Edinburgh

Ragunathan S., Tan C.P., Wells N.A.J., Mc.Ilhagger D.S. (1981)
'Efficiency, starting torque and prevention of run-away with Wells self- rectifying turbines',
2nd. International Symposium on Wave and Tidal Energy

Ragunathan S. And Tan C.P. (1982)
'Performance of the Wells turbine at starting',
Journal of Energy, vol.6

Ragunathan S. And Tan C.P. (1983)
'Aerodynamic performance of a Wells air turbine'
Journal of Energy, vol.7, no.3

Ragunathan S. And Tan C.P. (1985)
'Effect of frequency of air flow on the performance of the Wells turbine',
Int. Journal of Heat & Fluid Flow, vol.6, no.2

Ragunathan S., Tan C.P., Ombaka O. (1986)
'Performance of the Wells self-rectifying air turbine',
Aeronautical Journal

Raghunathan S. (1995)
'The Wells air turbine for wave energy conversion',
Progress in Aerospace Sciences, Elsevier Science Ltd.

Rawlinson – Smith R.I. And HalesR.L. (1990)
'Computational study of stalled rotor performance',
Proc. of the 12th BWEA Wind Energy Conference

Ronsten G. (1991)
'Static pressure measurements on a rotating and non-rotating 2.375 [m] wind turbine blade- comparison with 2-D calculations',
EWEC'91, Conference Publication, Amsterdam

Sarpkaya T. (1975)
'Forces on cylinders and spheres in a sinusoidally oscillating fluid',
A.S.M.E, Jnl. Appl. Mechanics, vol. 42

Schlichting H. (1979)
'Boundary-layer theory', 7th edition
McGraw-Hill

Singh S. (1979)
'Forces on bodies in oscillatory flow',
Ph.D. Thesis, Department of Aeronautics, Imperial College, London

Snel H., Houwink R., Boschers J., Peters W.J., VanBussel G.J.W., Bruining A., (1993)
'Sectional prediction of 3D-effects for stalled flow on rotor blades and comparison
with measurements',
Proc. EWEC , Travemuende

Sturge D.P. (1977)
' A turbine for an oscillating water column wave power system',
CEGB Memo., MM/MECH/TA4

Thorpe T.W. (1995)
' An assessment of the ART OSPREY wave energy device',
ETSU final report ETSU-R-90

Viterna And L.H. Janetzke D.C. (1982)
'Theoretical and experimental power from large wind turbines',
NASA report, DOE/NASA/20320-41

Weinig F. (1935)
'Die Stroemung um Schaufeln von Turbomaschinen',
J.A. Bart, Leipzig

Whittaker T.J.T (1992)
'Small-Scale Low Cost Wave Power Devices',
Phase2 Report, ETSU-WV-1680

Whittaker T.J.T McPeake F.A. Barr A.G. (1985)
'The Development and testing of a wave-activated navigation buoy with a Wells
turbine',
Transactions of the ASME, vol. 107

Wood D.H. (1991)
'A three-dimensional analysis of stall delay on a horizontal axis wind turbine',
Journal of Wind Engineering and Industrial Aerodynamics, no.37